

Copyright
by
Orlando José Ortega Pérez
2002

The Dissertation Committee for Orlando José Ortega Pérez

Certifies that this is the approved version of the following dissertation:

**Fracture-size Scaling and Stratigraphic Controls on Fracture
Intensity**

Committee:



Randall A. Marrett, Supervisor



Stephen E. Laubach



Robert K. Goldhammer



Jon E. Olson



John M. Sharp



Earle F. McBride

**Fracture-size Scaling and Stratigraphic Controls on Fracture
Intensity**

by

Orlando José Ortega Pérez, B.S., M.S.

Dissertation

Presented to the Faculty of the Graduate School of
The University of Texas at Austin
in Partial Fulfillment
of the Requirements
for the Degree of

Doctor of Philosophy

**The University of Texas at Austin
May, 2002**

Dedication

To the memory of my father

Acknowledgements

Most ideas contained in this document originated during long conversations with Randy and Steve whose knowledge and experience in fracture systems characterization are the foundations of this work. Thank you also for being friends and for your continued support throughout my time at UT. Thanks to Jon for instructive discussions on rock mechanics explanations to empirical observations. Thanks to Bob for helping me with the Cupido platform stratigraphy and synsedimentary tectonics. Thanks to Jack for critical questioning of fundamental aspects of natural fracture systems and teaching me that there are always more questions after an answer, thanks to Earle for superb classes on sandstone petrography, critical questioning, assistance, and advice throughout all my time at UT.

I would also like to thank a number of people that provided technical support, or shared their ideas and experiences. Thanks are due to: Julia Gale for excellent discussions on fracture scaling, Robert Reed for Scanning Electron Microscope Cathodoluminescence work, Faustino Monroy for helping collect fracture data in Mexico as well as interesting discussions on Cupido platform diagenesis, Wayne Narr for critical questioning of conclusions and for providing access to cores and maps from Rangely Field, Kitty Milliken for discussions on Weber Formation diagenesis and for sharing preliminary probe results on Weber Formation sandstones cementation, Ron Nelson for interesting discussions about

the implications of my research work for the hydrocarbon industry, Robert Folk for discussions on carbonate petrography and diagenesis, Scott Hamlin for suggesting the study of OBK-1 well cores and facilitating access to core and data from the Ozona Gas Field. Thanks are also due to Amos Salvador, Bill Fisher, Mark Cloos, René Manceda, Xiomara Márquez, Sigrid Clift, Scott Tinker, Eloise Doherty, Leonel Gómez, John Hooker, Brad Reid, Bryan Pairsh, Robert Sanchez, and Dennis Trombatore.

This work was financed by the Texas Advanced Research Program grant 003658-011, The Bureau of Economic Geology Fracture Research and Application Consortium and The Department of Geological Sciences through Research and Teaching Assistantships, The San Antonio Foundation Fellowship Program, and Phillips Petroleum Scholarship Program.

Thanks Paul, Lori, Mulugeta, Leonard, Caren, Lisa, Trish, Michael, Jorge.

Fracture-size Scaling and Stratigraphic Controls on Fracture Intensity

Publication No. _____

Orlando José Ortega Pérez, Ph.D.
The University of Texas at Austin, 2002

Supervisor: Randall A. Marrett

Scaling techniques offer an opportunity to solve subsurface fracture-sampling problems by extrapolating fracture properties from sub-millimeter-scales to scales important for economic applications. Although extrapolation of fracture length and aperture distributions across observation scales is fraught with potential errors, sampling of opening-mode kinematic apertures along scanlines using new fracture-aperture measuring tools produces consistent power-law aperture distributions from the micron-scale to outcrop-scale. One-dimensional sampling avoids fracture connectivity issues inherent to traditional two-dimensional length sampling methods. Sampling artifacts and mechanical layer effects can be diagnosed and accounted for, and extrapolation of power-law fracture intensities from the sub-millimeter scale up to the length scale of mechanical layers is feasible. Tests were performed in turbidite beds of the Ozona

Sandstone, Texas, eolian Weber Formation sandstones, Colorado, and Lower Cretaceous carbonates of the Sierra Madre Oriental (SMO), Mexico.

Outcrop studies in Weber Formation sandstones provided an opportunity to characterize well-exposed macrofracture systems as potential analogues for subsurface fractured reservoirs at Rangely Field. However, differences in stratigraphy and diagenetic history between surface and subsurface do not allow the direct extrapolation of these results to subsurface, reinforcing the idea that local data are necessary for fracture system characterization even in cases where long geologic time has passed between the time of sedimentation and the time of deformation that brought potential outcrop analogs to the surface.

Another way to predict fracture properties in the subsurface is to analyze the relationships between fracture attributes and the geologic parameters of the rock volume that govern fracturing. Fracture-fill prediction using relative volumes of cement phases precipitated during and after fracture timing shows an empirical relationship with sedimentary facies in Weber Formation sandstones. Multivariate analysis of unbiased fracture intensity in SMO carbonates suggests that degree of dolomitization and position of a bed at the top of a stratigraphic cycle are the most important controls on fracture intensity in these rocks. Mud content has only a modest control on fracture intensity and bed thickness has the least control on fracture intensity, suggesting that published work concluding that fracture intensity is strongly governed by bed thickness may be biased by scale or sampling effects.

Table of Contents

List of Tables	xv
List of Figures	xvii
INTRODUCTION	1
CHAPTER 1: FRACTURE SIZE SCALING AND SAMPLING ARTIFACTS	11
Ozona Sandstone	11
Introduction	11
Location and geologic context	15
Core description for the Ozona Blakeney Kruger No 1 well	17
Macroscopic Structural analysis.....	22
Fracture size data from cores	28
Microfracture classification and measurement	32
Microfracture orientations.....	35
Orientation weighting method.....	36
Microfracture and macrofracture orientation comparisons	37
Fracture-size distributions	41
Aperture distributions.....	44
Length distributions.....	46
Aperture-length relationship	46
Extent of power-law scaling.....	49
Topological transformations of fracture-size distributions	54
Theoretical relationships	55
Testing conversions of fracture data from two- to one- dimensional domains.....	60
Censoring artifacts.....	62
Use of scaling methods for subsurface fracture characteriza-tion	65

Conclusions	66
CHAPTER 2: OUTCROP ANALOGS AND SUBSURFACE FRACTURE SYSTEM CHARACTERIZATION	69
Weber Sandstone.....	69
Introduction	69
Location of study area	75
Structural style.....	78
Weber Formation.....	79
Rangely Field	80
Data collection and data analysis methods.....	84
Outcrop macrofracture data.....	84
Outcrop macrofracture orientation data	85
Outcrop macrofracture length data.....	86
Outcrop macrofracture aperture data.....	90
Subsurface macrofracture data	92
Microfracture data	94
Analysis of fracture size distributions	102
Sedimentary facies and diagenesis data	105
Fracture quality data.....	106
Mechanical layer thickness data.....	110
Results -Outcrop.....	112
Outcrop fracture orientations	112
Outcrop fracture size distributions	114
Outcrop aperture distributions.....	114
Outcrop length distributions.....	120
Test of topology effect on large-scale end of length distributions ..	122
Test of effect of fracture connectivity on length distributions	125
Aperture-length distributions	128
Tests of outcrop micro- and macrofracture data extrapolation	131

Test of macrofracture strike prediction using microfracture strike...	131
Test of micro- and macrofracture size distributions extrapolations ..	135
Results -Subsurface	140
Subsurface macrofracture orientation	140
Macrofracture orientation prediction using microfractures.....	142
Test of microfracture orientation reproducibility	143
Subsurface microfracture aperture distributions	146
Subsurface microfracture length distributions	147
Fracturing and diagenesis	150
Diagenetic history	151
Subsurface fracture quality results	161
Fracture quality and sedimentary facies.....	163
Mechanical stratigraphy	164
Fracture connectivity	171
Computer-generated fracture patterns	172
Subsurface macrofracture size predictions using microfracture data	175
Fracture pattern simulations	177
Discussion of results.....	181
Fracture orientations and fracture timing	181
Fracture size distributions sampling effects	183
Mechanical layer effect on fracture length distributions.....	183
Connectivity effect on fracture length distributions.....	186
Mechanical layer effect on fracture aperture distributions.....	189
Mechanical layer control on maximum fracture size.	191
Prediction of macrofracture orientation using microfracture data	192
Prediction of macrofracture size distribution using microfracture data	193
Use of subsurface microfractures for subsurface macrofracture characterization	196

Fracturing and diagenesis.....	198
Subsurface fracture quality assessment.....	202
Fracture trace pattern simulations	203
Conclusions	204
CHAPTER 3: SEDIMENTARY AND STRATIGRAPHIC CONTROLS ON FRACTURE INTENSITY	208
Cupido Platform	208
Introduction	208
Previous work.....	209
Location of study area	211
Structural context	215
Stratigraphic context	222
Sedimentary Facies in Cupido Formation	225
Open-marine mudstones.....	227
Bioclastic-intraclastic wackestones and packstones	228
Oolitic-peloidal grainstones	230
Bivalve banks and bioherms	231
Cryptalgal laminites	233
Intraclastic breccias	234
Cyclicality	235
Diagenesis	237
Fracture data collection and Analysis	242
Fracture size data.....	245
Fracture timing determination.....	248
Data organization and analysis.....	251
Linear weighted regressions and multivariate analysis.....	252
Fracture orientations.....	254
La Escalera	255
Las Palmas.....	260

El Chorro	263
Iturbide	265
Fracture timing	270
Fracture timing in the SMO	271
Fracturing and diagenesis	280
Normalized fracture intensity	286
Calculation of normalized fracture intensity	290
Sampling and topology artifacts	295
Calculation of normalized fracture-intensity uncertainties	303
Normalized fracture intensity results	306
La Escalera	308
Las Palmas	312
El Chorro	317
Iturbide	318
Sedimentary facies control on fracture intensity	325
El Chorro	327
La Escalera	331
Las Palmas	334
Iturbide	336
Sedimentary environment of deposition and fracture intensity	337
Bed thickness control on fracture intensity	341
Mechanical bed thickness	343
Normalized fracture intensity and mechanical bed thickness ..	344
La Escalera	345
Iturbide	347
Las Palmas	349
El Chorro	351
A possible explanation for the apparent bed thickness/fracture intensity relation	356

Average fracture intensity of fractures that span the bed thickness ..	359
Dolomitization control on fracture intensity	365
Las Palmas.....	367
La Escalera	369
El Chorro	371
Cyclostratigraphic control on fracture intensity.....	373
Correlation between stratigraphic variables	378
Multivariate Analysis	380
Multiple linear regression.....	383
Conclusions	388
Appendices	394
Appendix 1.A: Opening mode fracture scaling literature review	394
Appendix 1.B: OBK-1 Samples and petrography	395
Appendix 1.C: OBK-1 Fracture orientation data	396
Appendix 1.D: OBK-1 Fracture size data	396
Appendix 2.A: Weber samples and petrography	396
Appendix 2.B: Weber fracture data.....	397
Appendix 3.A: Cupido/Tamaulipas beds studied and samples	397
Appendix 3.B.:Cupido/Tamaulipas petrographic descriptions	398
Appendix 3.C.: Cupido/Tamaulipas fracture orientation data	398
Appendix 3.D.: Cupido/Tamaulipas fracture size data	399
Appendix 3.E.: Cupido/Tamaulipas fracture aperture distributions	399
Appendix 3.F.: Cupido/Tamaulipas normalized fracture intensity error analysis	400
Appendix 3.G.: Cupido/Tamaulipas stratigraphic columns	402
References	403
Vita.....	427

List of Tables

Table 1.1. Data summary of OBK-1 SEM-CL collages studied.	31
Table 1-2. OBK-1 power law cumulative aperture distribution parameters.	52
Table 1.3. Relationships between parameters of power law distributions for fractures that do not span the mechanical layer thickness.	58
Table 1.4. Relationships between parameters of power-law distributions for large fractures.	59
Table 2.1. Summary of outcrop data sets Weber Formation study.	77
Table 2.2. Summary of Weber Formation core data, Rangely Field, Colorado....	93
Table 2.3 Summary of SEM-CL work on surface and subsurface Weber samples.	97
Table 2.4. Diagenetic history of the Weber Sandstone for the Piceance Basin. .	152
Table 2.5. Reservoir-scale fracture size predictions based on microfracture size distribution results.	176
Table 3.1. Summary of number of fracture data collected and scanline lengths in beds studied.	307
Table 3.2. Power law parameters, La Escalera Canyon.	309
Table 3.3. Normalized fracture intensity, La Escalera Canyon.....	310
Table 3.4. Power law parameters, Las Palmas Canyon.....	315
Table 3.5. Normalized fracture intensity, Las Palmas Canyon.	316
Table 3.6. Power law parameters, El Chorro Canyon.	319
Table 3.7. Normalized fracture intensity, El Chorro Canyon.	320

Table 3.8. Power law parameters, Iturbide Anticline.....	323
Table 3.9. Normalized fracture intensity, Iturbide Anticline.	324
Table 3.10. Summary output of multiple linear regression analysis for total fracture intensity and stratigraphic variables.	385
Table 3.11. Summary output of multiple linear regression analysis for combined sets A, B and C fracture intensity and stratigraphic variables.	387
Table 3.12. Summary output of multiple linear regression analysis for combined sets AB intensity and stratigraphic variables.....	389
Table 3.13. Summary output of multiple linear regression analysis for set C intensity and stratigraphic variables.	390
Table 3.14. Summary output of multiple linear regression analysis for total fracture intensity and stratigraphic variables, La Escalera Canyon.	391

List of Figures

Figure 1.1. Location map for OBK-1 well	16
Figure 1.2. Reassembled core pieces from OBK-1 well.....	18
Figure 1.3. Core sketch, OBK-1, segment D.	21
Figure 1.4. Kinematic analysis of structures in OBK-1 cores.....	23
Figure 1.5. Shale injections in wedge-shaped veins.....	25
Figure 1.6. Crosscutting relationships in OBK-1 well.	26
Figure 1.7. Comparison of petrographic and SEM-CL photomicrographs.....	30
Figure 1.8. Comparison of macrofracture and microfracture strikes in OBK-1 well.....	38
Figure 1.9. Rose diagrams for different portions of collage 4448.	40
Figure 1.10. Cumulative fracture aperture distributions for OBK-1 well.....	45
Figure 1.11. Microfracture length distribution, OBK-1 upper sandstone, sample 4448.....	47
Figure 1.12. Aperture-length plot for upper bed in OBK-1 core.	50
Figure 1.13. Log-log plots of aperture vs. cumulative fracture frequency in OBK-1 well.	53
Figure 1.14. Comparison of calculated and observed topologic transformations using Marrett's (1996) equations.	61
Figure 1.15. Censoring effects on fracture length distribution.	63
Figure 2.1. Weber Sandstone study areas.	76
Figure 2.2. Stratigraphic chart for Weber study area.	81

Figure 2.3. Weber Formation thickness variations in northwestern Colorado.....	82
Figure 2.4. Fracture length and aperture measurement.	88
Figure 2.5. Portion of SEM-CL photomicrograph collage L15-5618c(43-54).	96
Figure 2.6. Microfracture trace map from SEM-CL photomicrograph collage L15-5618c(43-54).	99
Figure 2.7. Macrofracture orientations in Weber Formation study area.	113
Figure 2.8. Fracture aperture distributions from Disappointment Draw area.	115
Figure 2.9. Fracture aperture distributions from Disappointment Gulch 1 and Skull Creek areas.....	118
Figure 2.10. Fracture aperture distributions from Disappointment Gulch 2 and 3 areas.....	119
Figure 2.11. Length distributions for ENE striking fractures at North Disappointment and Skull Creek pavements.	121
Figure 2.12. Fracture length distributions for large and small observation domains in South Disappointment pavement.....	123
Figure 2.13. Effect of fracture connectivity on fracture length distributions, North Disappointment pavement.	127
Figure 2.14. Fracture aperture vs. fracture length for Weber sandstone outcrops.....	130
Figure 2.15. Test of macrofracture strike prediction using microfracture orientations, Disappointment Gulch area.	133
Figure 2.16. Test of macrofracture strike prediction using microfracture orientation, North and South Disappointment pavements.	134

Figure 2.17. Microfracture size distributions for South Disappointment area....	136
Figure 2.18. Microfracture and macrofracture length distributions, South Disappointment pavement.....	138
Figure 2.19. Micro- and macrofracture aperture distribution from Weber Fm. outcrops.	139
Figure 2.20. Comparison of rose diagrams for macro- and microfracture strikes, Larson 15X B well.....	144
Figure 2.21. Test of reproducibility for microfracture strike analysis Larson 15X B well.	145
Figure 2.22. Microfracture aperture distributions from two different depths in Larson 15X B well.	148
Figure 2.23. Microfracture length distributions from the same samples as Fig 2.22.....	149
Figure 2.24. Regional distribution of quartz cement in samples of Weber Formation.	154
Figure 2.25. Photomicrographs of macrofracture in sample w-15, Weber Formation outcrops.	157
Figure 2.26. Ankerite-filled fractures in Rangely Field, Colorado.	159
Figure 2.27. Degradation values in Larsen 15X B well cores.....	162
Figure 2.28. Sedimentary facies and degradation values in Larson15X B well.	165
Figure 2.29. Distribution of eolian and fluvial facies in surface and subsurface Weber Formation.....	167
Figure 2.30. Field-based mechanical layer subdivision of Weber Sandstone.....	169

Figure 2.31. North-south stratigraphic section across Rangely Field.	170
Figure 2.32. Fracture connectivity of pavements in the study area.....	173
Figure 2.33. Possible fluid-flow units for Weber Sandstone reservoir based on fracture quality and sedimentary facies distribution.	174
Figure 2.34. Observed and software-predicted fracture patterns for Skull Creek pavement.....	179
Figure 2.35. Fracture pattern simulations for depths 1712 m and 1738 m, Larson 15X B well.	180
Figure 2.36. Field-based mechanical layer thickness estimation, Weber Formation, South Disappointment and Skull Creek areas.	187
Figure 3.1. Location of Cupido Platform study area on a map of the geologic provinces of Mexico.....	212
Figure 3.2. Barremian-Aptian paleogeographic map showing localities studied.	214
Figure 3.3. Major structural elements of the SMO near the Monterrey salient. .	216
Figure 3.4. Landsat image of the Monterrey salient in the Sierra Madre Oriental.....	217
Figure 3.5. NNE-SSW cross section through Monterrey Salient illustrating structural style.	218
Figure 3.6. Fold axes and p planes of folds studied.	221
Figure 3.7. Cross section along Santa Rosa Canyon.....	223
Figure 3.8. NW-SE stratigraphic section across the Cupido-Tamaulipas platform system.	224

Figure 3.9. Examples of typical sedimentary facies in Cupido and Tamaulipas Inferior formations.	226
Figure 3.10. Photomicrographs of dolomite occurrence in shallow-water facies of Cupido Formation.	239
Figure 3.11. Variation of facies, bed thickness and dolomite content in database.	243
Figure 3.12. Segment of scanline for aperture-data collection in dolostone bed 3, La Escalera Canyon.	246
Figure 3.13. Fracture-aperture comparator used in Cupido Platform study.	247
Figure 3.14. Equal area, lower hemisphere stereographic projections of fracture orientations at La Escalera locality.	256
Figure 3.16. Equal area, lower hemisphere stereographic projections of fracture orientations at Las Palmas locality.	261
Figure 3.17. Equal area, lower hemisphere stereographic projections of fracture orientations at El Chorro locality.	264
Figure 3.18. Equal area, lower hemisphere stereographic projections of fracture orientations at Iturbide locality.	266
Figure 3.19. View of the base of a carbonate mudstone bed showing transform veins and stylolites in Tamaulipas Inferior Formation.	269
Figure 3.20. Unfolded fracture orientation data, San Blas Anticline.	272
Figure 3.21. Unfolded fracture orientation data, El Chorro Anticline.	274
Figure 3.22. Unfolded fracture orientation data, Iturbide Anticline.	276
Figure 3.23. Collapse breccia at Las Palmas Canyon.	278

Figure 3.37. Total normalized fracture intensity and interpreted sedimentary environment of deposition.....	339
Figure 3.38. Bed thickness control on fracture intensity, dolostone beds, La Escalera Canyon.....	346
Figure 3.39. Bed thickness control on fracture intensity, open marine mudstones, Iturbide Anticline.....	348
Figure 3.40. Normalized fracture intensity and bed thickness, limestones, Las Palmas Canyon.....	350
Figure 3.41. Normalized fracture intensity and bed thickness, dolostones, Las Palmas Canyon.....	352
Figure 3.42. Normalized fracture intensity and bed thickness, grainstones, El Chorro Canyon.....	353
Figure 3.43. Normalized fracture intensity and bed thickness in dolostones, El Chorro Canyon.....	355
Figure. 3.44 A and B. Apparent increase of fracture intensity with decrease in bed thickness.....	358
Figure 3.44 (continued). Length effect and bed-thickness/spacing modeling results.....	360
Figure 3.44 (continued). Comparison of normalized and non-normalized fracture intensity calculations for beds at Iturbide locality.....	362
Figure 3.45. Control of dolomite content on fracture intensity, Las Palmas Canyon.....	368

Figure 3.46. Control of dolomite content on fracture intensity, La Escalera Canyon.	370
Figure 3.47. Control of dolomite content on fracture intensity, El Chorro Canyon.	372
Figure 3.48. Schematic distribution of fracture intensity and degree of dolomitization in peritidal and subtidal parasequences at La Escalera Canyon.	374
Figure 3.49. Fracture intensity and dolomite distribution in peritidal and subtidal parasequences at Las Palmas Canyon.	375
Figure 3.50. Correlation analysis between stratigraphic variables.....	379
Figure 3.51. Correlation test between bed thickness and other stratigraphic variables	381

INTRODUCTION

Fractures are perhaps the most common structure in rocks, from the microscopic scale to the planetary scale. Fractures can introduce changes of a number of properties in natural materials, like mechanical strength, hydraulic conductivity, elastic wave velocity, and chemical reactivity.

Important research effort has focused on adequately describing natural fracture systems, predicting their characteristics, and evaluating their effects on physical and chemical properties of natural materials. Understanding of natural fracture systems has accelerated as awareness of the effects of rock fractures on human-related activities increases, and as progress is made collecting fracture data and developing both analytical and numerical methods for understanding the data. Cross-disciplinary and integrated studies have produced breakthroughs in the understanding of fundamental properties of fracture systems. However, multiple aspects of natural fracture characterization and modeling are still in their infancy.

The description of a fracture system requires addressing fracture orientation, fracture size, fracture abundance, fracture connectivity, spatial distribution, and fracture fill. Surface fracture system characterization is challenging due to limitations of fractured rock exposure, poor understanding of the relevant measurable attributes of fractures, and lack of adequate measuring tools. Another significant limitation of surface fracture system description is the

fact that we observe only the external surfaces of outcrops and ignore most of what occurs in 3D. Subsurface rock fracture characterization is even more difficult due to limited sampling of fractures at the scale important for most practical applications. Currently available remote exploration tools are still limited in their spectrum of resolution and in the depth and lateral extent of investigation (e.g., seismic and well-log tools). Progress is being made to improve these tools for the detection and evaluation of some key properties of fracture systems (e.g., fracture orientation), but we still lack remote tools to acquire information about fracture size distribution, fracture fill and connectivity and most importantly we lack hard data to calibrate these indirect measurements.

Fracture mechanics techniques, including analytical, laboratory-based, and numerical modeling, offer an opportunity to understand how fractures form, propagate and interact with each other, as well as provide insight on the propensity to fracture as loading conditions change during the evolution of geologic materials. Computer-based numerical models have successfully produced realistic fracture patterns and some spatial properties of fracture systems. However, at present, numerical fracture mechanics models have difficulties modeling fracture propagation over a wide range of scales at the same time, so they cannot address the observed existence of fractures at scale ranges from microscopic to planetary.

One method used to embrace the range of scales covered by natural fractures for statistical description and prediction of fracture sizes is scaling. The objective of scaling is to describe and understand the relationships of events or

features (e.g., fractures) at different sampling scales. One aim of research on scaling of natural objects is to predict the properties of these objects at a scale unavailable or difficult to sample. Fracture scaling has been a topic of active research during the last two decades, and the results derived from this effort have been used in a number of practical applications, including water and hydrocarbon exploration and management, waste disposal, evaluation and management of mineral resources, and civil engineering projects.

Most scaling studies of opening-mode fractures have suggested that fracture size distributions follow power-law scaling (Appendix 1.A). However, some studies have suggested that power-law scaling changes across observation scales (Nicol et al., 1996; Marrett, 1996; Ackermann and Schlische, 1997; Ortega and Marrett, 2000, Borgos et al., 2000). The majority of fracture studies have used data from joints in rock surface exposures (Baecher et al., 1977; Priest and Hudson, 1981; Segall and Pollard, 1983; Rouleau and Gale, 1985; Castaing et al., 1996; Odling, 1997, 1999; Gillespie et al., 2001; and numerous publications on fractal dimension of joint patterns using box-counting methods), fewer studies have addressed veins (McCaffrey et al., 1994; Sanderson et al., 1994; Clark et al., 1995; Gross and Engelder, 1995; Vermilye and Scholz, 1995; Johnston and McCaffrey, 1996; Marrett, 1997; Marrett et al., 1999; Ortega and Marrett, 2000; Gillespie et al., 2001), and an important number do not specify the type of fracture studied (Baecher and Lanney, 1978; Gudmundson, 1987; Barton and Hsieh, 1989; Barton and Zoback, 1990; Hatton et al., 1993; Belfield and Sovich, 1995; Belfield 1998).

The majority of opening-mode fracture-scaling studies have focused on the scaling properties of fracture length, particularly in two-dimensional exposures (Appendix 1.A, Bonnet et al., 2001, and references therein), and only a small number of studies include scaling properties of opening-mode fracture apertures (Barton and Hsieh, 1989; Barton and Zoback, 1990; McCaffrey et al., 1994; Sanderson et al., 1994; Clark et al., 1995; Belfield and Sovich, 1995; Gross and Engelder, 1995; Marrett, 1997; Marrett and Laubach, 1997; Laubach et al., 1998; Ortega et al., 1998; Belfield, 1998; Marrett et al., 1999). From this select group only a small portion has used information from subsurface fracture systems (Barton and Zoback, 1990; Sanderson et al., 1994; Belfield and Sovich, 1995; Laubach et al., 1998; Ortega et al., 1998; Belfield, 1998; Marrett et al., 1999).

Fracture-size scaling techniques have proved to be fraught with potential errors (Davy, 1993; Bonnet et al., 2001). Errors introduced in fracture scaling results include errors due to sampling difficulties (Einstein and Baecher, 1983; Segall and Pollard, 1983; Barton and Zoback, 1992; Clark et al., 1995; Ortega and Marrett, 2000), poor understanding of fracture attribute definitions (Gudmundson, 1987; Ortega and Marrett, 2000), changing standards for fracture attribute measurement (Gudmundson, 1987; Heffer and Bevan, 1990; Castaing et al., 1996; Ouillon et al., 1996), inadequate tools to measure fracture size (Barton and Hsieh, 1989; Belfield and Sovich, 1995), possible effects of lower and upper limits to scaling properties (Henderson et al., 1994; Hatton et al., 1994; Odling et al., 1999; Ortega and Marrett, 2000; Bonnet et al., 2001), statistical undersampling (Priest and Hudson, 1976; Berkowitz and Adler, 1998; Main, 2000), finite size effects

(Pickering et al., 1995; Ouillon et al., 1996), spatial distribution effects (Ackermann and Schlische, 1997; Borgos et al., 2000; Ortega, chapter 3), and topologic artifacts (Warburton, 1980; Westaway, 1994; Marrett, 1996; Borgos et al., 2000). Some errors are systematic so there is potential for filtering them out of biased fracture size distributions, as well as understanding the physical and mathematical laws that explain their occurrence. However, many errors are non-systematic and arise from mixing unrelated fracture populations, inconsistencies in measurements of fracture sizes at various scales of observation, insufficient data collection, and probably some still unknown effects.

Many published studies about fracture scaling lack sufficient detail on the sampling methodology used and physical boundaries of the fracture system studied to understand the resulting artifacts (Bonnet et al., 2001, and references therein). Additionally, most fracture data are not included in the publications, making it difficult to use these data for experimenting with potential techniques to eliminate artifacts or explain their occurrence. A poor understanding of scaling artifacts has generated confusion and multiple interpretations for the same data set, and frequently reinterpretation of the data under new assumptions leads to very different conclusions about the extent of power law fracture-size scaling in rocks. Important challenges in fracture scaling studies include: designing efficient methods of fracture sampling for two-dimensional domains, evaluating the reliability and practical usefulness of fracture scaling predictions, understanding the mechanisms that introduce artifacts in observed fracture size distributions, and

designing analytical methods to filter out artifacts from the underlying signal of the size distribution.

The first chapter of this dissertation uses unusually high quality subsurface data to address some of the issues introduced above. Fracture aperture will be the focus of these scaling studies because fracture length in interconnecting fractures is more challenging to define uniquely. Fracture measurements at two overlapping scales of observation will test the best model and applicability of extrapolated aperture scaling. Choosing *a priori* a minimum fracture size for measurement that is not limited by resolution will minimize truncation artifacts. Censoring artifacts on fracture length scaling will be evaluated using a fracture map containing thousands of fractures and studying progressively smaller areas of observation. Topologic artifacts will be examined by comparing the fracture size distribution of two mechanical layers with different thickness, and finally, published topologic conversion relationships will be tested from one-dimensional and two-dimensional sampling of the same fracture system containing thousands of fractures.

The use of microfracture orientation to predict macrofracture orientation will be tested in both the first and second chapters of this dissertation using fracture systems in sandstone. The second chapter will analyze fracture scaling from excellent outcrops of a fractured formation, and outcrop-based results will be compared with subsurface fracture properties predicted using microfracture information. Some effects of mechanical layer thickness on the upper limits of fracture scaling will become apparent by considering regional variations of the

mechanical layer thickness. Additionally, different definitions of fracture length in interconnected fracture networks will shed some light on fracture swarm organization, fracture connectivity, and possible explanations for apparent non-power-law scaling reported in the literature.

Another important property of fracture systems is their spatial distribution. Average spacing has been the most common tool applied to describe fracture spatial organization. However, average fracture spacing has little meaning without specifying the fracture-detection threshold. As mentioned above, fractures exist across wide scales of observation; therefore, a change in the scale of observation is bound to produce changes in the threshold of fracture detection and consequently in apparent average spacing. Most studies of fracture spacing fail to specify the threshold used for fracture spacing measurements (Harris et al., 1960; Price, 1966; McQuillan, 1973; Priest and Hudson, 1976; Hudson and Priest, 1979; Ladeira and Price, 1981; Rouleau and Gale, 1985; Lerche and Narr, 1986; Huang and Angelier, 1989; Narr and Suppe, 1991; Gillespie et al., 1993; Gross, 1993; Mandal et al., 1994; Gross et al., 1995; Wu and Pollard, 1995; Gross and Engelder, 1995; Becker and Gross, 1996; Pascal et al., 1997; Ji and Saruwatari, 1998; Bai and Pollard, 2000; Eyal et al., 2001). In Chapter 3, I show evidence that this practice may have introduced a systematic scale bias and resulted in questionable conclusions about the relationship between bed thickness and fracture spacing.

Probably the three most significant fracture properties influencing fluid flow through fractured rock are the portion of fractures occupied by residual

porosity, its variation with observational scale, and its interconnectivity. Cement precipitation in open fractures decreases fracture permeability. Quantification and prediction of fracture fill in a fracture network is very important for realistic modeling of fluid-flow through fractures. Petrographic techniques allow classification of different cement phases in sedimentary rock according to their timing relative to fracturing (Laubach, 1988; Laubach et al., 1995; Laubach, 1997; Laubach et al., 2000). Postkinematic cements precipitate after opening of fractures and can seal large fractures that would otherwise be important conduits for fluid flow (Laubach, 1997; Laubach et al., 2000). Synkinematic cements precipitate as fractures propagate and their apertures increase (Laubach et al., 1995; Laubach, 1997). Synkinematic cements often produce mineral bridges and trails of fluid inclusions in the fracture fill, but commonly leave abundant residual porosity in fractures. Cement bridges across fractures are possibly capable of keeping fractures open in the subsurface, even after fluid pressure no longer props fractures open. On the other hand, synkinematic cements tend to seal microfractures, possibly because rates of cementation commonly can keep pace with the opening rate of such small fractures. Identification of relationships between cement phases and microfractures helps classify cement timing with respect to fracture timing, even if no large fractures are directly observed. Similarly, treating the matrix pore system at the conclusion of fracturing as a surrogate for fracture porosity, the fluid-flow quality of fractures can be evaluated (Laubach et al., 2000).

The second chapter of this dissertation applies the fracture quality methodology of Laubach et al. (2000) to subsurface data from the same oil producing units for which scaling analyses were carried out. The distribution of zones with high potential for open fractures shows an empirical correlation with sedimentary facies, which consequently can be used to assess where fractures might be important to exploration strategies, selection of completion intervals, and reservoir management. A subdivision of the stratigraphic sequence into fracture-enhanced fluid-flow units is proposed on the basis of stratigraphic information and potential open fracture occurrence. Quality ranks for these flow units can be established on the basis of reserve calculations and permeability.

In the third chapter, scaling techniques are used to obtain scale-unbiased estimates of fracture intensity in carbonate beds of the Sierra Madre Oriental, Mexico and to compare them with possible stratigraphic controls. Das Gupta (1978) applied multivariate methods to analyze geologic effects on fracture intensity in carbonate outcrops near Alberta, Canada, but variable scales of observation possibly affected fracture intensity estimates and undercut comparison of fracture intensities among beds. Normalized fracture intensity for carbonate beds in the Sierra Madre Oriental allowed consistent comparison of fracture intensities between beds with different lithology, bed thickness, mud content, sedimentary facies, degree of dolomitization, and position in fifth-order stratigraphic cycles. Bivariate and multivariate analyses of the data described the relative importance of stratigraphic and diagenetic controls on fracture intensity. Concentration of the analysis on pre-folding fractures, and restricting observations

to one structural domain in each study area minimized structural control on fracture intensity and emphasized stratigraphic effects. Study of fracture intensity distribution in a cyclostratigraphic context provided a link between fracture properties (e.g., fracture intensity) with a predictive genetic-stratigraphic model. A model for the distribution of fracture properties in a sequence stratigraphic cycle provides a tool for fracture property prediction using remote exploration tools through links between stratigraphic models and geophysical exploration methods (e.g., seismic stratigraphy, well log interpretation).

CHAPTER 1: FRACTURE SIZE SCALING AND SAMPLING ARTIFACTS

Ozona Sandstone

INTRODUCTION

Fracture scaling techniques have become one of the standard tools to characterize natural fracture systems (Bonnet, 2001). Scaling techniques provide a means by which fracture attributes (e.g., length and aperture size) at one scale of observation can potentially be predicted using information from the same fracture system at a different scale of observation that is more amenable for characterization. The potential predictive capability of fracture scaling techniques has significant practical applications. For example, adequate characterization of subsurface fracture systems is difficult because complete sampling of large conductive fractures dominating fluid flow is impossible in the subsurface. Large fractures in subsurface are often widely spaced and have much larger dimensions than the diameter of vertical boreholes, so the probabilities of encountering such fractures in a given mechanical layer are small and even when they are intersected only fragmentary data can be collected (Narr, 1991). Even horizontal wellbores on specific orientation and length can only sample a fraction of the large fractures, because the length of most fractures will not reach far enough along strike to cross the borehole. Fracture scaling techniques offer an opportunity to solve part of the subsurface fracture-sampling problem because microscopic fractures in

conventional subsurface samples are abundant, can readily be sampled, and can be used to predict macroscopic fracture properties.

With a few possible exceptions (Baecher et al., 1977; Baecher and Lanney, 1978; Priest and Hudson, 1981; Rouleau and Gale, 1985; Gillespie et al., 2001), there is now consensus that natural fracture aperture and length typically follow power-law scaling (Appendix 1.A). However, it is still questionable the extent (or size range) of this power law scaling. Excellent fracture size data sets indicate that fracture-size power law scaling may extend for over four orders of magnitude in size (Marrett et al., 1999). However, most examples of natural fracture size distributions span a few orders of magnitude in size and are affected by artifacts that prevent uniform power-law scaling in the entire range of sizes measured (Pickering et al., 1995). Typically, the smallest and largest fractures of an observed size distribution deviate from the pattern shown by other fractures. Deviations at the small-scale end of the size distribution may result from incomplete observations for features near the threshold of resolution (i.e., truncation artifacts; Baecher and Lanney, 1978; Segall and Pollard, 1983; Barton and Hsieh, 1989; Barton and Zoback, 1992; Pickering et al., 1995; Odling, 1997). Deviations at the large-scale end of the distributions have been explained by a number of effects including censoring (Laslett, 1982; Barton and Zoback, 1992; Pickering et al., 1995; Odling, 1997), resolution problems near fracture tips (Pickering et al., 1995), mechanical boundary effects (Ortega and Marrett, 2000), sampling topology changes (Heffer and Bevan, 1990; Marrett, 1996), fracture spatial distribution (Ackermann and Schlische, 1997; Bonnet et al., 2000), and

integration of a power-law fracture density function over a limited observation area (i.e., finite range effect; Bonnet et al., 2001, and references therein).

Artifacts in fracture-size distributions are often the source of errors in estimation of the underlying size distribution for a fracture population. It is possible that some published fracture-size distributions interpreted as non-power law are in reality power-law distributions affected by severe sampling artifacts (e.g., Priest and Hudson, 1981). Artifacts can be particularly important in fracture-length distributions, where censoring is commonly present and where severe truncation can affect a wide range of sizes (e.g., Ortega and Marrett, 2000). Artifacts can also be significant in size distributions based on sparse data or data spanning less than two orders of magnitude in size (Bonnet et al., 2001).

In the first part of this chapter, I investigate the extent of power-law scaling at two different but overlapping scales of observation in a well-controlled fracture array for which resolution problems are minimized. Fracture aperture is used to quantify fractures instead of fracture length and observations are made along a scanline instead of within a two-dimensional surface. The accuracy of fracture length data sets is typically limited by the problem of identifying fracture tips where fractures connect or branch (Ortega and Marrett, 2000). However, use of one-dimensional observation domains avoids complications related with two-dimensional measurement issues (e.g., choosing a representative aperture for a fracture in cross section).

Although one-dimensional collection of aperture data has proved adequate for fracture-aperture scaling studies (Marrett et al., 1999), continuous scanlines

typically intersect relatively few fractures. Two-dimensional observation domains contain more abundant fractures than one-dimensional domains but the criteria to collect two-dimensional data are questionable. Marrett (1996) derived formulas to transform fracture size distribution parameters based on observations in one topological domain (e.g., two-dimensional) to another (e.g., one-dimensional or three-dimensional). I will test for the first time the validity of these transformations using real data. Assumptions made by Marrett's (1996) topologic transformation formulas include simple geometry for fractures, spatial distributions uncorrelated with fracture size, isolated fractures, and lack of censoring artifacts. Marrett's (1996) formulas may not be applicable to a fracture array under investigation if these assumptions are severely violated (e.g. Borgos et al., 2000).

In the second part of this chapter, description of the fracture array and the mechanical layers thickness allows investigation of mechanical boundary and topologic effects on observed fracture size distributions. Unusual cores recovered from the Ozona Sandstone, a gas-producing formation in West Texas, contain numerous macrofractures suitable for fracture scaling studies. The use of Scanning Electron Microscope Cathodoluminescence images (SEM-CL) allowed the collection of fracture size data, bridging the microscopic scale with core-scale observations. Also significant is the fact that the fractures developed in the subsurface and have apertures preserved by mineral fill, which adds to the reliability of aperture measurements. As noted in the general introduction of this

work, there are no previous examples of scaling studies based on abundant subsurface macrofracture and microfracture data.

LOCATION AND GEOLOGIC CONTEXT

The Ozona Gas Field occupies parts of Crockett, Terrell, and Val Verde Counties in West Texas (Fig. 1.1). This gas accumulation is limited by the lateral extent of producible sandstone of Late Pennsylvanian—Early Permian age. The Ozona Canyon sandstones are interpreted as slope- and basin-floor submarine-fan deposits (Hamlin, 1999). Structural position of wells shows little correlation with well productivity, and locally enhanced porosity and permeability determine success of wells in this gas-saturated tight-sandstone reservoir (Hamlin et al., 1995). The spatial distribution of channel and fan-lobe sandstone bodies and their diagenetic history, combined with the presence and abundance of open fractures, are key parameters for drilling success in this field (Hamlin et al., 1995; Hamlin, 1999).

The Ozona Blakeney Kruger No 1 (OBK-1) well explored for gas in a step-out location from the main Ozona Gas Field. The well is located in the periphery of the Ozona Gas Field, Crockett County, southwest Texas, about 50 km to the west of the southeast corner of the county, near the county line (Fig. 1.1). The OBK-1 well has produced gas in commercial quantities from a smaller accumulation separated from the main Ozona Gas Field. The nature of the hydrocarbon trap is not well understood because of lack of local structural and

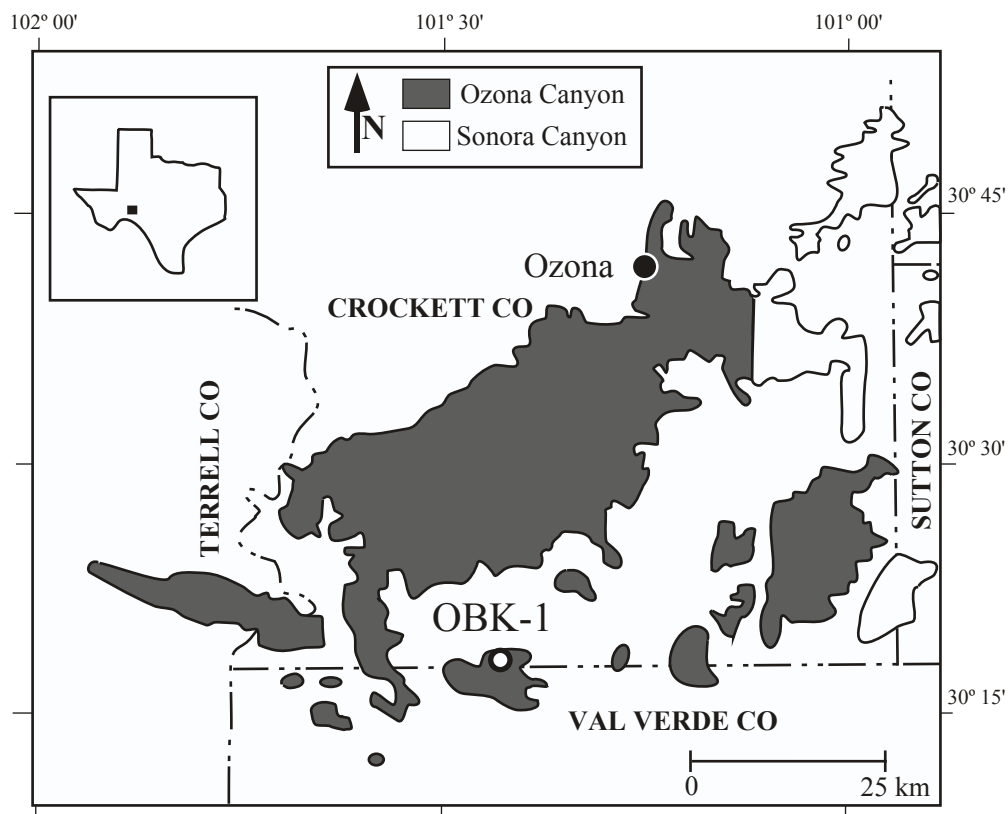


Figure 1.1. Map showing location of OBK-1 well in Ozona and Sonora Gas Fields (modified from Hamlin et al., 1995). Hatched and stipled areas indicate the extent of deep-water sand bodies producing hydrocarbons near Ozona, Crockett County, Texas.

stratigraphic information, but a large fault intercepted by the well suggests that the trap might be partly structural.

CORE DESCRIPTION FOR THE OZONA BLAKENEY KRUGER NO 1 WELL

The approximately vertical Ozona Blakeney Kruger No 1 well intercepted a reverse fault and in the footwall encountered a repeated section of the Ozona Sandstone (Hamlin, 1997 personal communication). Approximately 4 m of core recovered from the faulted section show steeply dipping beds affected by intense fracturing and minor faulting. This unusual situation of a vertical core drilled through steeply dipping beds provides an unintentional bed-parallel core through these reservoir sandstones.

Cores from the Ozona Blakeney Kruger No 1 are especially well suited for scaling analysis of opening-mode fractures. Meter-long segments of two sandstone layers were recovered from these cores. Abundant quartz- and calcite-filled fractures present in the sandstones form high angles with both bedding and the borehole, providing an opportunity to obtain abundant subsurface macrofracture information, equivalent to a horizontal well in flat lying beds, recommended for reliable scaling studies (Bonnet et al., 2001).

Core pieces were carefully reassembled to restore them to their correct relative positions. After reassembling the core, most segments showed enough physical continuity to allow systematic collection of orientation measurements and kinematic data from the veins and faults (Fig. 1.2). The core is not oriented, however, a relative orientation of the best-preserved pieces is possible.



Figure 1.2. Reassembled core pieces from OBK-1 well. A recovery factor of 87% allows a good to very good quality of the fit of the pieces. White bags contain shale rubble with abundant slip surfaces. Scale bar on top is approximately 20 cms long. The scale on the side is graduated in twentieths of feet (3.28 feet = 1 m).

Sedimentary structures are abundant in the sandstone layers and helped in the determination of geopetal direction in beds.

Faults are also present in the core and are particularly abundant in shale intervals. The tops and bottoms of the sandstone beds are flexural-slip surfaces in shale. The steeply dipping beds, abundance of fractures, oblique faults, and flexural-slip surfaces in the core suggest that these beds were affected by tectonic deformation associated with the reservoir-scale fault that the OBK-1 well intercepted.

Meter-long portions of two steeply dipping sandstone beds having different thicknesses provide independent opportunities to test fundamental scaling properties of subsurface fracture systems and evaluate the effect of bed thickness on fracture scaling. Calcite- and quartz-filled opening-mode fractures abound in both sandstone layers. The high fracture intensity in the beds allowed the collection of over a hundred fracture aperture measurements from each bed. Fracture lengths were also measured, but in most cases the value recorded is a minimum estimate because most macrofractures extend beyond the boundaries of the core.

The stratigraphically higher sandstone layer in the core is 5.5 cm thick, and its top and base are preserved in the core as flexural-slip surfaces. Flexural-slip surfaces within the adjacent shale layers are sub-parallel to the stratification and show abundant slickensides and tool marks. The stratigraphically lower sandstone bed is thicker than the upper sandstone but its complete thickness cannot be determined because it exceeds the diameter of the core and one of the

sandstone-shale contacts was not recovered in the core. Some large veins in the lower sandstone layer contain preserved fracture porosity.

Sandstone beds studied are fine-grained and poorly to moderately well sorted. Petrographic analyses of thin sections cut parallel and perpendicular to the stratification are summarized in Appendix 1.B. The lower sandstone is a subarkose—lithic arkose and contains abundant feldspar grains (~14% of total volume of rock, TVR), and some rock fragments (7% TVR). The original intergranular porosity has been reduced by quartz precipitation (10% TVR), non-ferroan calcite (6% TVR), ferroan calcite (3% TVR) and illite-smectite (~1% TVR).

The upper sandstone is a litharenite and contains abundant rock fragments (19% TVR), and some feldspars (5% TVR). Sedimentary rock fragments are the most common (12% TVR), but also chert and low-grade metamorphic rock fragments are present in significant quantities (7% TVR). Most of the original porosity was occupied by compaction-induced pseudomatrix, quartz cement in the form of quartz overgrowths (8% TVR), non-ferroan calcite (3% TVR), ferroan calcite (6% TVR) and illite-smectite (~1% TVR). Infiltrated clay matrix and dead oil also contributed to fill original pore space in this sandstone.

The pieces of core from which thin sections were made for microfracture analysis were carefully described and oriented (Fig. 1.3). Relative orientations of faults and opening-mode fractures in the OBK-1 cores were measured with respect to a reference mark and bedding. Cores were arranged continuously from top to bottom and north was assumed to be parallel to bedding, perpendicular to

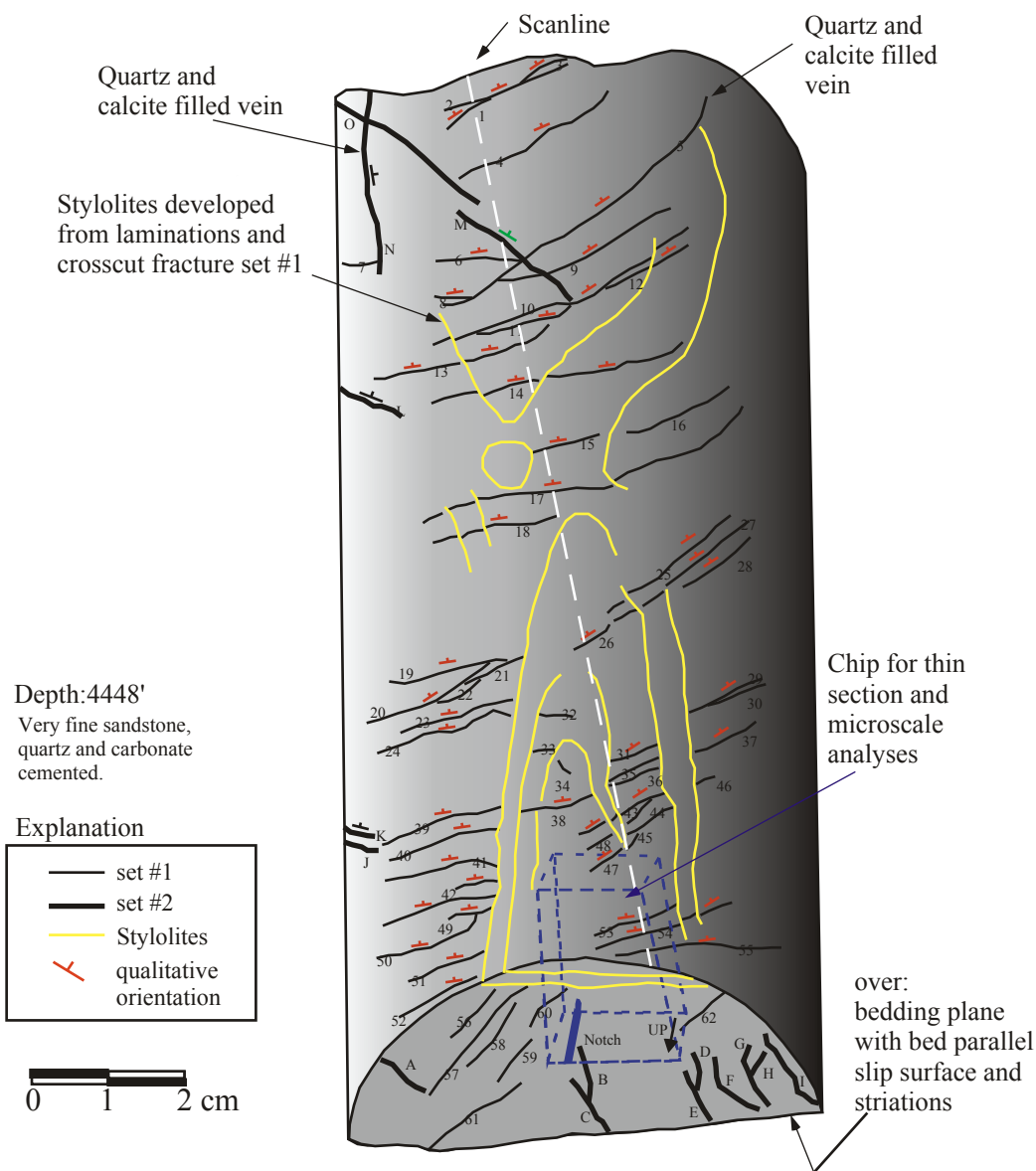


Figure 1.3. Core sketch, OBK-1, segment D. Diagram indicates location of chip cut for thin section preparation with a notch to record orientation. An additional mark was added to the chip to indicate which side should be glued to the glass of the thin section. Set #1 fractures are serially labeled with numbers and set #2 fractures are labeled with letters.

the core axis, and 90° clockwise from the up direction in the cores. Dip values were measured with respect to bedding surfaces. Abundant sedimentary structures in sandstones were used to distinguish the base from the top of the beds in order to obtain a unique north direction. Opening mode fracture and fault orientations were recorded in core logs, diagrams, and summarized in tables (Appendix 1.C).

Crosscutting relationships between faults and opening mode fractures were also carefully recorded to interpret the relative timing of fracturing. Slickensides and slickenfibers abound on slip planes, aiding in the interpretation of fault kinematics.

MACROSCOPIC STRUCTURAL ANALYSIS

Three fault sets, two opening-mode fracture sets and one set of bed-parallel stylolites are present in the cores. Faults are the most common structures in shale intervals and opening-mode fractures and stylolites are common in sandstone.

The oldest structures affecting these rocks are faults that contract bedding (currently normal faults), grouped as set 1 (Fig. 1.4 E). Kinematic analyses of these faults suggest that they formed by bed-parallel contraction and bed-normal extension. This fault set might be linked to tectonic events in the Ouachita thrustbelt and on the Central Basin Platform that were partly contemporaneous with Ozona Sandstone deposition (Hamlin, 1999). A second event of bed-parallel contraction formed two sets of conjugate faults (fault sets 2 and 3) sub-parallel to the stratification (Fig. 1.4 C and 1.4 D). These faults clearly crosscut fault set 1.

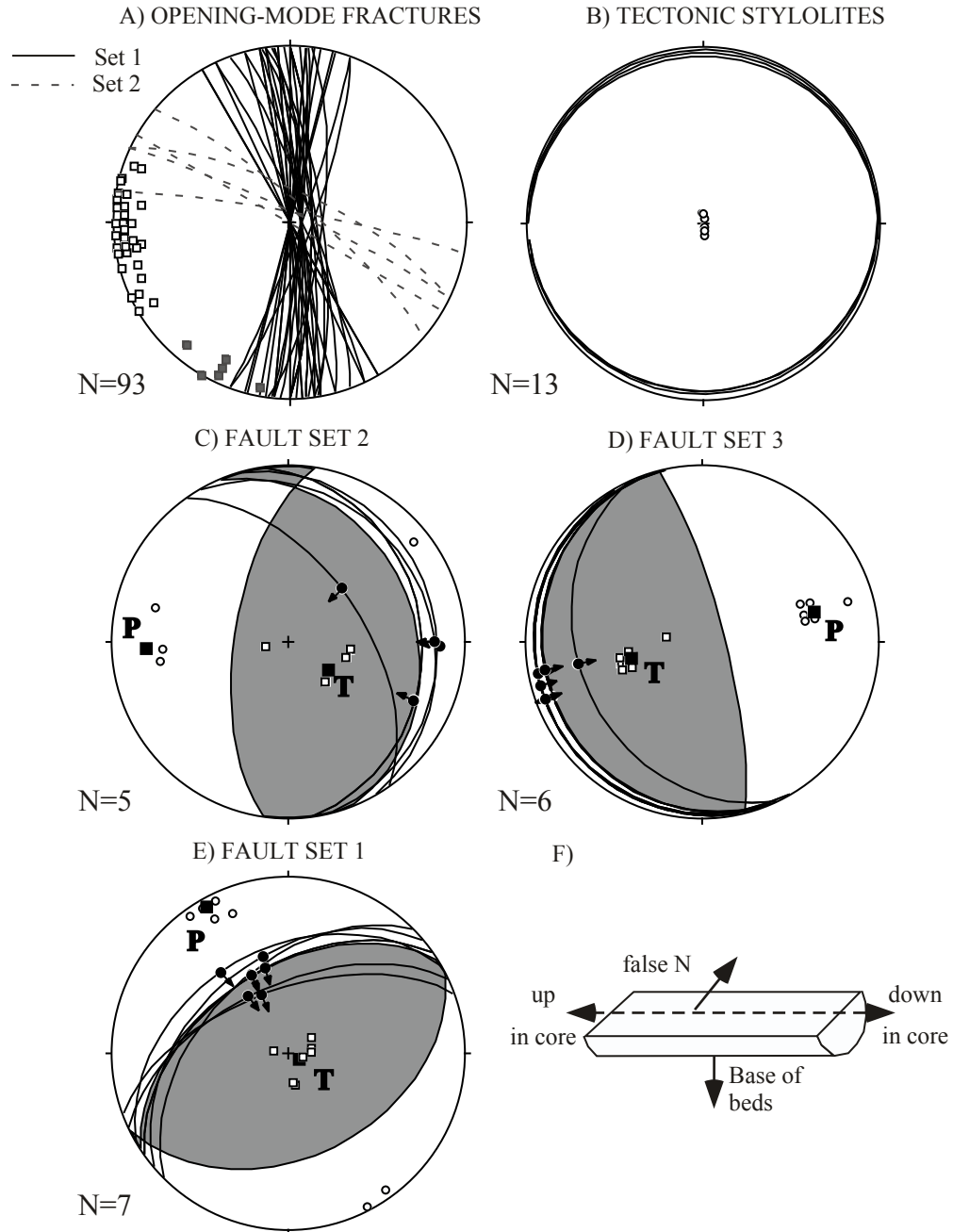


Figure 1.4. Kinematic analysis of structures in OBK-1 cores (following Marrett and Allmendinger, 1990; bedding is horizontal). White-filled circles are contraction axes and white filled squares are extension axes for individual structures. Solid squares are principal axes of contraction (P) and extension (T) for fault sets. Solid circles with arrows show trend and plunge of slip lineations and direction of foot-wall motion. F) Sketch of coordinate system assumed for orientation measurement of cores.

Fault sets 2 and 3 probably represent flexural-slip surfaces that formed during tilting of the beds.

Opening-mode fractures sets 1 and 2 form high angles with bedding (Fig. 1.4 A). Currently sub-horizontal opening-mode fractures are consistent with bed-parallel extension, and sub-horizontal, possibly post-flexure, contraction. Vein abundance is high in the near-vertical beds studied but low in sub-horizontal beds in other cores from the same well, suggesting that vein formation was related to the localized flexure that produced the steeply dipping beds. Clay material from adjacent shale beds was injected along some large veins that reached the boundaries of sandstone beds and helped prop open large fractures (Fig. 1.5).

A secondary opening-mode fracture set is also present in the core (Fig. 1.4A), forming a high angle with bedding and moderate angle with opening-mode fracture set 1. Limited crosscutting relationships examined petrographically suggest that fracture set 2 might be an older burial-related fracture set, which rotated during tilting of the beds to a near-vertical orientation.

Layer-parallel stylolites (Fig. 1.4B) both cut and are cut by set 1 veins. This suggests they were contemporaneous with the veins, which in turn were associated with tilting and faulting of the Ozona sandstones.

Opening-mode fracture set 1 clearly crosscuts fault set 1 (Fig. 1.6 A) and probably was partly contemporaneous with or postdated fault sets 2 and 3, because vein traces show on flexural slip surfaces crosscutting slickensides and slickenfibers (Fig. 1.6 B). This suggests that contraction parallel to bedding occurred first, producing reverse faults (fault set 1), followed by flexural-slip and

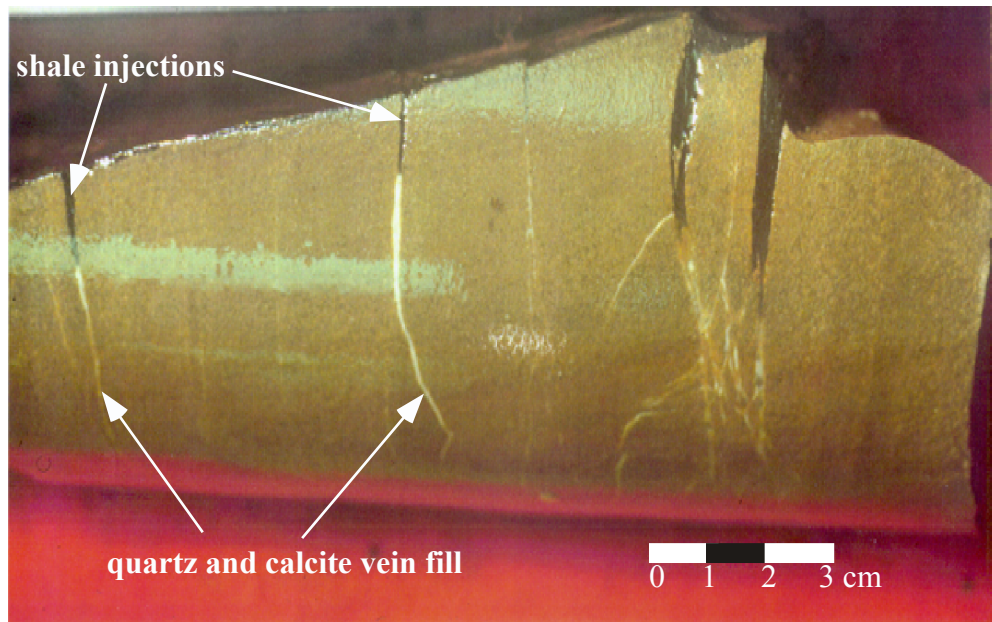


Figure 1.5. Shale injections in wedge-shaped veins. Top of core piece is bedding of one of the sub-vertical sandstone beds in the OBK-1 core (1358 m depth). The narrowest parts of the fractures are lined with quartz and younger calcite fill.

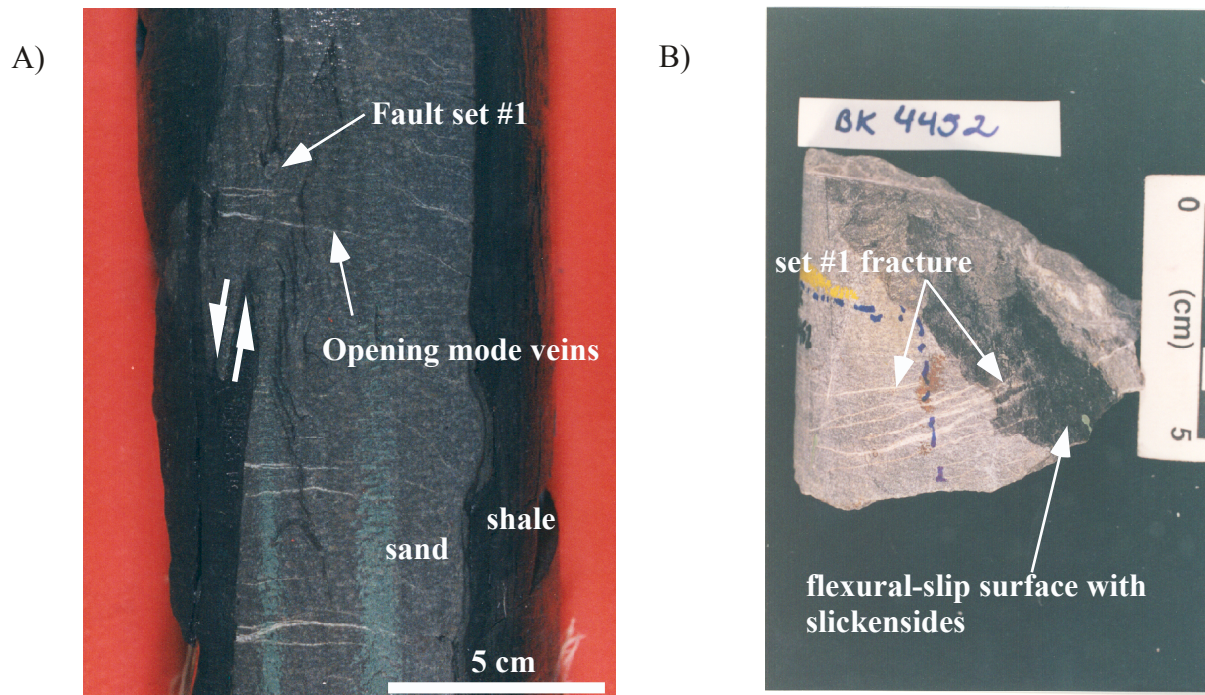


Figure 1.6. Crosscutting relationships in OBK-1 well. A) Opening-mode veins of fracture set 1 crosscut fault set 1 in upper sandstone bed (1356 m depth). B) Vein traces of set 1 cut across flexural slip surfaces (fault sets 2 and 3, 1357.3 m depth).

possibly rotation of beds to a vertical position, and contemporaneous or younger opening mode veins that crosscut all fault sets. Opening-mode veins could have formed then under sub-horizontal maximum contraction that was directed perpendicular to rotated beds.

Sub-horizontal beds are dominant in the Ozona Gas Field (Hamlin, 1999). Steeply dipping beds occur in the OBK-1 well near a fault towards the southern boundary of the field. Given the kinematics for fault and opening-mode fractures and the crosscutting relationships, it is possible to propose a genetic explanation for the steeply dipping beds, veins and faults. The steep dips might represent fault-tip related folding or “drag” folding. Given that sub-horizontal beds surround the domain of steeply dipping beds, then the fold axis probably is sub-horizontal and strike-parallel to the steeply dipping beds. This means that the veins of set 1 are parallel to the fold axis. Fractures parallel to the fold axis are consistent with models of outer-arc extension during fold formation.

According to Hamlin et al. (1995) fractures striking northeastward have the most favorable orientation to remain open, given the present state of stress in the subsurface of the Val Verde Basin. However, fractures with apertures smaller than 0.5 mm are mostly occluded by mineral fill, although fractures having apertures larger than 0.5 mm typically are partly filled but tend to have some remnant porosity. Stretched crystal fibers of quartz (Ramsay and Huber, 1987) are common in these fractures, and might hold fractures open even under unfavorable present-day stress conditions.

FRACTURE SIZE DATA FROM CORES

Fracture apertures were measured along scanlines drawn perpendicular to the main vein set (set 1) orientation in both sandstone layers. Apertures were measured using a comparator with lines of different calibrated widths. The minimum fracture aperture measurable with this tool was 50 μm . Apertures down to 50 microns size are recognizable with the naked eye and clearly visible with a hand lens. Chapter 3 of this dissertation contains an example of the latest design of these measuring tools, and an explanation of how to construct and use one. Fracture measurements were recorded in tables and were input to a spreadsheet for scaling analysis.

Only isolated fractures (i.e., with no visible connections to other fractures) were selected for measurement of fracture lengths from cores. Physical fracture connectivity introduces uncertainty to the measurement of fracture length (Ortega and Marrett, 2000), so connected fractures (i.e. fractures that intercept, abut or branch from other fractures) were disregarded. Using these criteria, only a few fractures were chosen for measurement. The apertures of these fractures were recorded in order to study fracture length-aperture relationships.

MICROFRACTURE IMAGING

In sandstones, the interpretation of microfractures from Scanning Electron Microscope Cathodoluminescence (SEM-CL) collages has proved advantageous over petrographic microfracture interpretation (Laubach and Milliken, 1996;

Laubach, 1997; Milliken and Laubach, 2000). Microfractures in sandstones tend to be filled with quartz that precipitates in optical continuity with the quartz in the grains and cement, so the microfractures are generally invisible to plane- or cross-polarized light under petrographic microscope. Fluid inclusion planes were the only evidence for these microstructures before the use of cathodoluminescence techniques, and some authors attempted to use fluid-inclusion plane orientation measurements for macrofracture orientation prediction or structural analyses in general (Bonham, 1957; Laubach, 1988, 1989; Onasch, 1990). From SEM-CL images, the identification, measurement, and interpretation of microstructures is commonly feasible because of contrast in luminescence between quartz grains and quartz cement that fills most microfractures. Laubach (1997) provided the fundamentals of SEM-CL imaging and described the equipment used in this study. The advantages of SEM-CL imaging for microfracture analysis in sandstones can be appreciated by comparing SEM-CL photomosaics with petrographic photomosaics of the same area of a thin section (Fig. 1.7).

Microfractures in the Ozona sandstone were observed in SEM-CL images from three sandstone samples (R. Reed, unpublished, Bureau of Economic Geology archives, The University of Texas at Austin). Individual SEM-CL panchromatic photos were stitched together to form photocollages. Photocollages were collected from layer-parallel thin sections along transects having an arbitrary direction. The shape and size of the mosaics were designed to study specific fracture-system-characterization problems (Table 1.1).

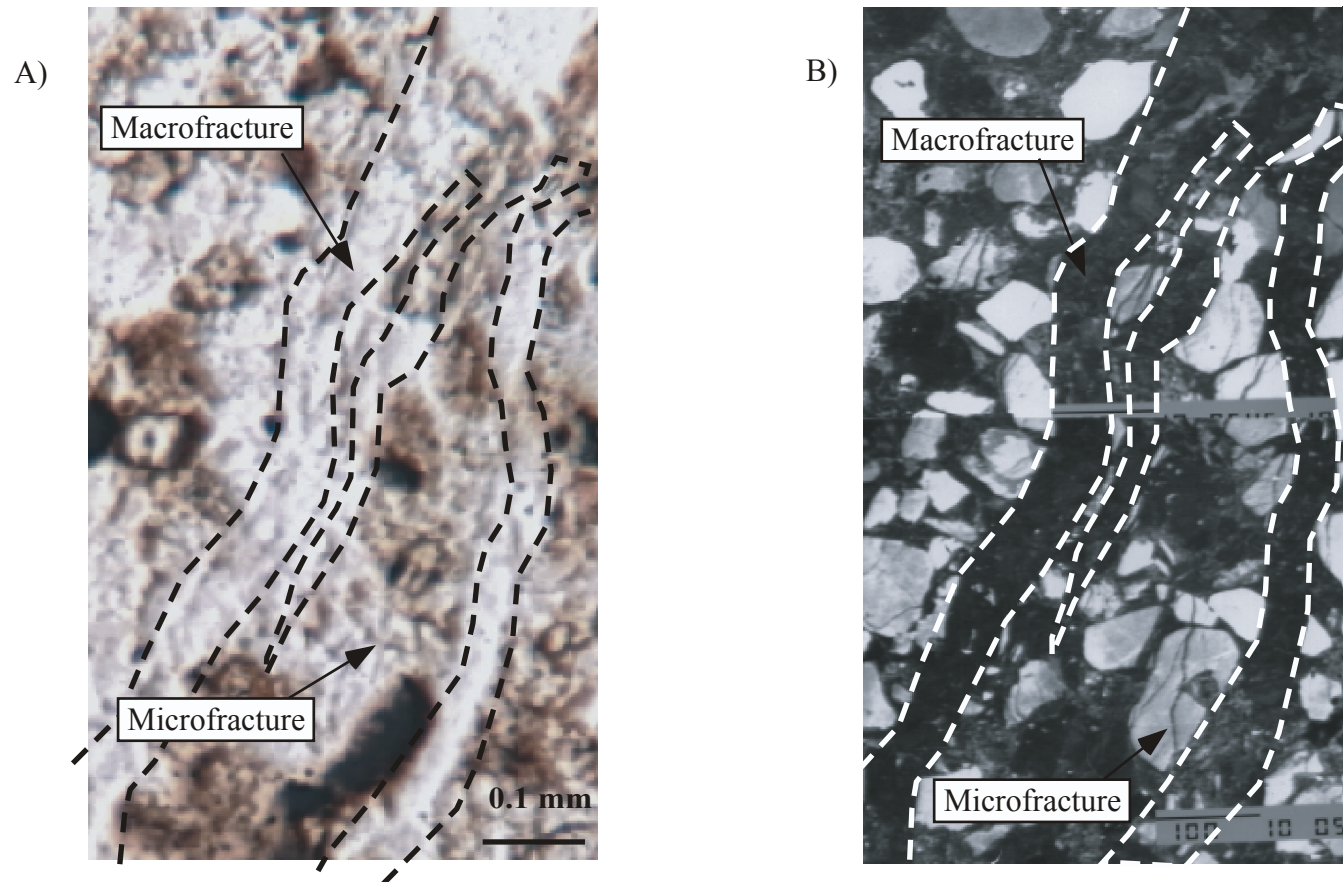


Figure 1.7. Comparison of petrographic photomicrograph and SEM-CL collages. One macrofracture and one microfracture have been identified in both images. A) Plane polarized light, B) SEM-CL image. Note improvement in the definition of grain boundaries, macrofracture walls, and especially unequivocal identification of transgranular microfracture in B. Scale in SEM-CL image is 100 microns.

Table 1.1. Data summary of OBK-1 SEM-CL collages studied.

Collage	Area (mm ²)	Number of photos	Orientation*	Magnification	Purpose
4448	20.6	102	6	200 X	Artifacts, Scaling
4449	4.8	73	198	350 X	Scaling
4455	8.9	62	180	200 X	Scaling

* : Azimuth of reference direction in collages relative to reference direction in cores

MICROFRACTURE CLASSIFICATION AND MEASUREMENT

SEM-CL images show a variety of microstructure morphologies and details of quartz cement and framework grains in sandstones (Laubach, 1997). Laubach (1997) pointed out the potential use of SEM-CL imaging techniques for systematic analysis and classification of microstructures.

Microstructures in OBK-1 SEM-CL collages can be separated in two groups: opening-mode microfractures with straight walls and microstructures with irregular/wavy traces. Both groups of microstructures have preferred orientations in the collage. Opening-mode microfractures primarily affect framework grains and show up best in quartz grains. These microfractures are bounded by sharply-defined walls, have straight and continuous traces, and are often arranged in en echelon patterns. They show an important variation in aperture size (0.001-0.1 mm) and limited orientation variability. All observed examples are filled with dark gray or non-luminescent quartz cement.

Irregular and wavy microstructures are common in the matrix, sedimentary rock fragments, feldspars, and cement. Some cut quartz grains where they commonly show jagged traces, which usually continue into the matrix and cement in braided patterns. These microstructures show diffuse walls and their exact width is difficult to measure. The variability in strike is also more significant in these microstructures than in the opening-mode microfractures. Crushed grains and sheared grains are often associated with these microstructures. I preliminarily interpret these microstructures as either microfaults, cataclastic

zones, pressure-solution seams, or unknown structures that generate changes in the cathodoluminescence of intergranular areas (e.g., different events of cementation within intergranular volume). These microstructures were not systematically measured or studied further in this work.

Opening-mode microfractures were classified following the Laubach (1997) classification, as modified by Ortega and Marrett (2000). Microfractures studied include transgranular microfractures (IA+ class in Laubach, 1997 classification; suitability A in Ortega and Marrett, 2000), trans-cement microfractures (IA microfractures in Laubach, 1997; suitability A microfractures in Ortega and Marrett, 2000), and microfractures where the cement in the microfractures and around the grains appears to be a uniform and continuous phase (e.g., Reed and Laubach, 1996; suitability B in Ortega and Marrett, 2000). Uncertainty in the use of microfractures as proxies of macrofractures in the same volume of rock decreases by restricting attention to transgranular and trans-cement microfractures (reliabilities IA+ and IA in Laubach, 1997), because these fractures must have formed after grain deposition. However, these microfractures are typically the least abundant and their number in a given SEM-CL collage can be insufficient for scaling analyses. Suitability B microfractures (Ortega and Marrett, 2000) were included in the database for fracture scaling purposes. Occurrence of the same cement phase inside microfractures and in intergranular pores suggests a post-depositional and synchronous timing for microfracture opening and cement precipitation. Suitability B microfractures often show similar orientation as transgranular and trans-cement microfractures, have straight walls,

and are not arranged in radial (grain-crushing) patterns. Common orientation, morphology, cement fill, and crosscutting relationships with cement suggest a post-depositional origin for these high- and moderate-suitability fractures. Common orientation suggests that they formed as a response to the same remotely imposed stress field. Here we assume that suitability A and suitability B microfractures are genetically related to the macrofractures in the same volume of rock. No attempt was made to analyze other kinds of microstructures.

Panchromatic SEM-CL photocollages were scanned to create digital versions. Interpretation of microstructures from digital images was done using commercially available software (Canvas 5TM). Only opening-mode microfractures were digitized. Every suitability A and B microfracture in the collage was digitized using a four-vertex polygon. The first vertex is at one tip of the microfracture, the second is on one of the walls at the location of maximum aperture. The third vertex is located at the remaining fracture tip, and the last vertex is on the other wall of the microfracture at the location of the maximum aperture.

Microstructural measurements (i.e., strike, length, and aperture) were made using a C⁺⁺ console program (Appendix 4.A). Microstructure length corresponds to the perimeter of the digitized polygon (i.e., sum of line lengths between vertices defining the microfracture) divided by two. The maximum kinematic aperture corresponds to the maximum opening displacement between the fracture walls. Microstructural apertures are calculated by measuring the distance between digitized vertices two and four in digital photocollages. This

displacement is usually preserved by mineral fill precipitated during and/or after fracture opening.

Microstructure strike is the azimuth of the line joining the tips of the microfracture. However, for statistical analysis of microfracture orientation, the orientation of each polygon side (referred to below as a fracture segment) was used.

MICROFRACTURE ORIENTATIONS

Recent studies using SEM-CL imaging techniques have shown that micro- and macrofracture orientations in sandstones are commonly comparable (Laubach, 1997; Ortega and Marrett, 2000). Systematic microfracture strike analyses from oriented subsurface samples can reliably be used to predict the orientation of macrofractures in the same volume of rock. The technique has now been tested in outcrops (Ortega and Marrett, 2000), oriented core (Laubach, 1997; Ortega and Marrett, 2000), and sidewall core samples (Laubach and Doherty, 1999). The technique could be adopted as a standard for macrofracture strike determination in sandstone reservoirs (Laubach et al., 2000).

Special care is required to properly orient samples for macrofracture strike prediction using microfracture orientation measurements. Experience shows that sample misorientation is one of the most important sources of error in microfracture orientation measurements. Also, a microfracture classification scheme is necessary to separate inherited microfractures (i.e. fractures that came with the grain) from post-depositional microfractures (Laubach, 1997) and further

isolate those with the highest probability to be related to macrofractures (Laubach, 1997; Ortega and Marrett, 2000).

Special characteristics of the OBK-1 core permitted collecting abundant and reliable macrofracture and fault orientation data, but this situation is not the general case for subsurface rock samples. A total of 93 opening-mode macrofracture orientations and 17 fault orientations were measured from the whole core. However, 244 microfracture strikes were collected from only 3.7 mm² of a thin section from the upper bed. These results suggest that the use of microfracture strike for prediction of macrofracture strike can provide abundant fracture orientation information even on a bed-by-bed basis. This method is particularly useful in situations where oriented (or orientable) subsurface samples are available, but scarce natural macrofracture strikes have been detected. Uncertainty about interpretation of sparse macrofracture strike data may further increase where complex structural patterns are present (e.g., multiple fracture sets, bed-to-bed changes in dominant macrofracture strike) and where it is difficult to distinguish induced from natural fractures.

Orientation weighting method

Sizes and strikes of microfractures were processed with a C⁺⁺ console program (FracStrikeW) to separate microfractures into sets based on preferred orientations. The program FracStrikeW performs a weighted orientation analysis on microfracture segments. The weighting consists of summing the lengths of microfracture segments that fall in the same orientation range. This weighting

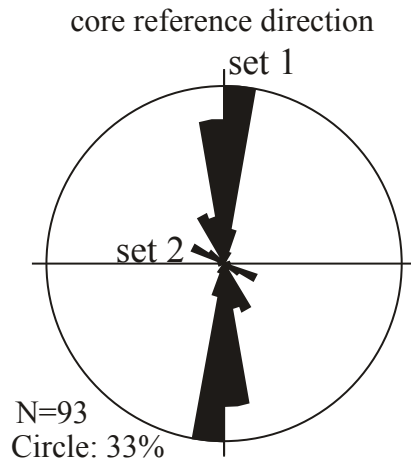
method places more importance on longer fractures, which are more certainly related to the macrofractures. The weighting factor consists on multiplying the number of observations on a certain strike range by the sum of the lengths of the microfractures having a strike in such orientation range. Microfracture lengths are multiplied by 100 and reduced to whole numbers to calculate the number of observations in the orientation range. For example, the strike of a 0.012 mm long microfracture would weight as one observation, whereas a microfracture 0.156 mm long would contribute with 15 observations to this microfracture strike range.

The program also determines the number of fracture sets present by identifying the modes and minima of the fracture strike distribution. All microfractures with average orientation between two given strike distribution minima belong to the same set. Microfractures of each set are then saved to a separate file for other analyses.

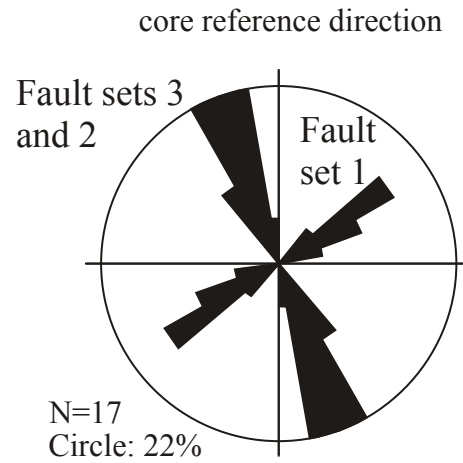
Microfracture and macrofracture orientation comparisons

Opening mode microfracture strikes resemble macrofracture strikes in the OBK-1 core (Fig. 1.8). A difference of approximately 10 degrees in the strike maxima can be attributed to possible errors in orienting the thin section and the SEM-CL collages. However, this difference may also be explained by differences in strike commonly reported between small en echelon fractures and large through-going fractures developed by linkage of en echelon fractures (Ramsay, 1980; Laubach, 1991; Davis and Reynolds, 1996).

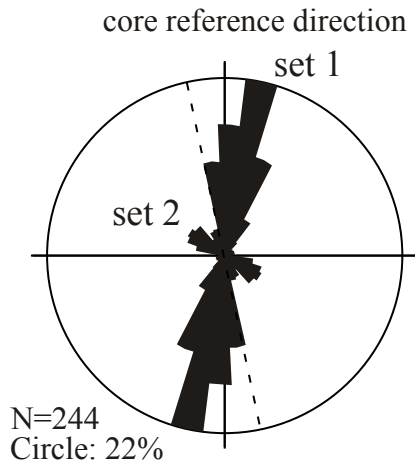
Macrofracture Opening-mode strikes



Fault strikes



Microfractures Opening-mode strikes



Wavy and irregular micro-structure strikes

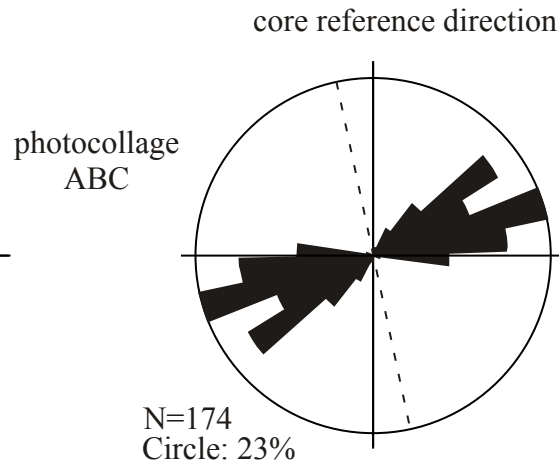


Figure 1.8. Comparison of macrofracture and microfracture strikes in OBK-1 well. Macrofracture data come from whole core measurements and microfracture data come only from SEMCL photocollage ABC (sample 4448), approximately 3.7 mm² surface area. Dashed line indicates SEM-CL reference direction

Irregular and wavy microstructures show strikes similar to fault set 1 (Fig. 1.8). Few or none of the irregular and wavy microstructures show strikes similar to fault sets 2 and 3, but these faults formed at a very small angle with the stratification and their expected abundance in bed-parallel thin sections is low. Also, fault sets 2 and 3 are macroscopically restricted to shale intervals and their absence in sandstone layers supports their interpreted flexural-slip origin. One possibility is that the irregular and wavy microstructures are small examples of fault set 1, but another possibility is that they are pressure-solution seams associated with macroscopic stylolites observed in the sandstones. However, at this observation scale pressure-solution related microstructures might be indistinguishable from shear-microfractures possibly related to faults. Lack of closed microstructures favors an association with dipping planes. More research might help understand the relationships of irregular and wavy microstructures with faults and stylolites.

A test was carried out to evaluate the reproducibility of microfracture orientations in different areas of a large SEMCL collage from sample 4448. Microfracture strike was evaluated in five areas ranging from 3.7 to 5.1 mm² (Fig. 1.9). Results show that the dominant fracture sets can be detected regardless of the spatial location of the collage. However, the relative importance of the two dominant fracture sets varies. Collages ABC, JKLM and NOPQ adequately predict that fracture set 1 is the most important macrofracture set in this sandstone bed. But, mosaics DEF and GHI suggest that fracture set 2 is more important.

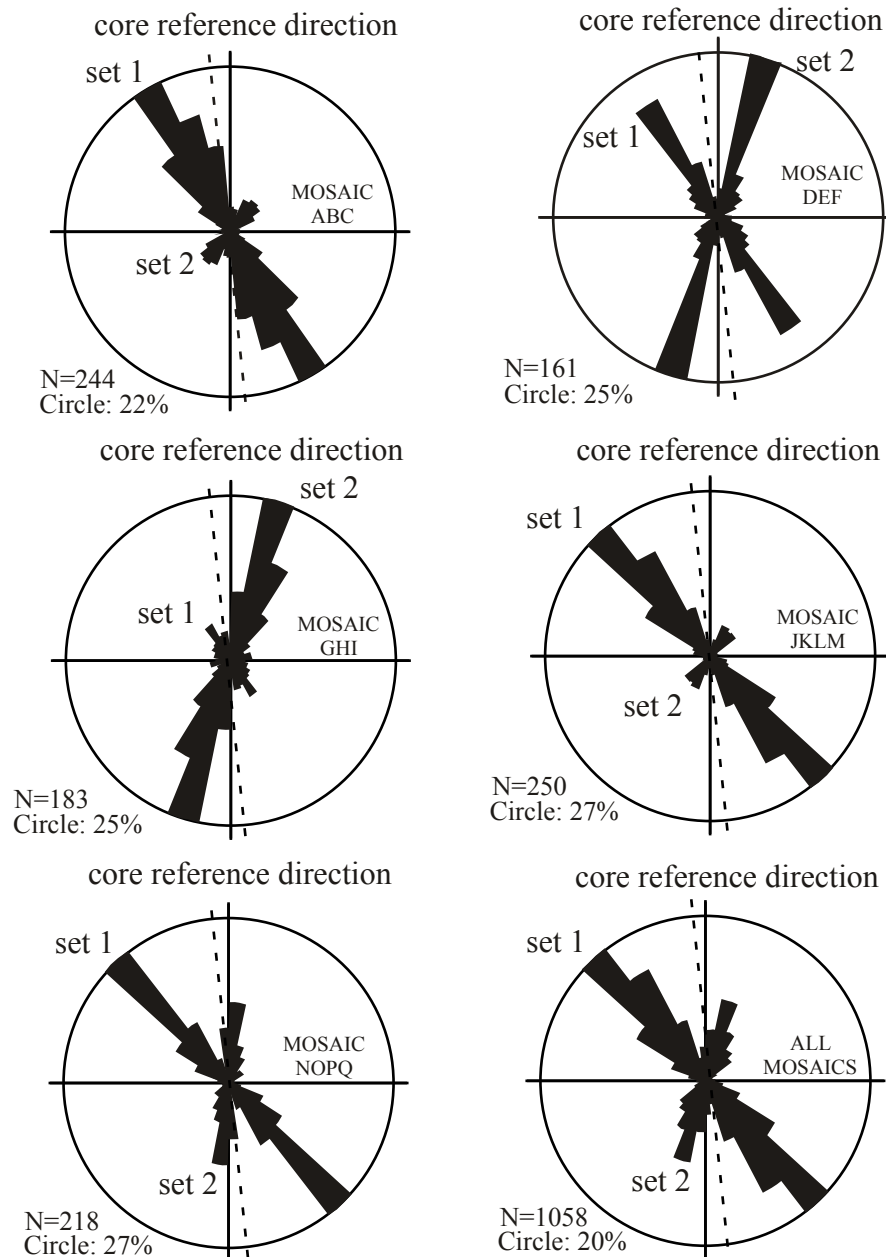


Figure 1.9. Rose diagrams for different portions of collage 4448. In all collages the same two opening-mode microfracture sets can be recognized but their relative importance varies. Set 1 in Mosaic GHI is a secondary set with respect to a swarm of transgranular microfractures of set 2. Dashed lined indicates SEM-CL reference line and core reference direction is false north (Fig.1.4).

Differences in the apparent importance of fracture sets can be explained by clustering of microfractures into swarms of one or both sets in the collages. Visual inspection of collages suggests that imaged areas smaller than about 1.5 mm² may not be sufficient to predict macrofracture orientations reliably. In some individual photographs (~0.25 mm²) there are no microfractures with suitability A or better. The fracture intensity in this bed is considerably higher than commonly observed in flat-lying beds in subsurface rocks. Flat lying beds with lower fracture abundance than the units studied may require imaged areas significantly larger than 1.5 mm².

FRACTURE-SIZE DISTRIBUTIONS

Many opening-mode fracture systems show an organization of fracture sizes such that their cumulative size distribution can be described by a simple power-law relationship (Gudmundson, 1987; Wong et al., 1989; Heffer and Bevan, 1990; Barton and Zoback, 1992; Gillespie et al., 1993; Hatton et al., 1994; Sanderson et al., 1994; Belfield and Sovich, 1995; Clark et al., 1995, Gross and Engelder, 1995; Johnson and McCaffrey, 1996; Marrett, 1997; Ortega et al., 1998, 1999, Marrett et al 1999; Ortega and Marrett, 2000). A power-law of the form:

$$N = ab^{-c} \quad (1.1)$$

best describes the aperture-size distribution observed; where N is the cumulative number of fractures larger than a certain aperture b , and a and c are constants referred to as the coefficient and exponent of the fracture-aperture distribution, respectively, and vary with the size of the observation domain. The exponent c is

also commonly called the fractal dimension of the distribution. The coefficient a is a measure of the abundance of fractures in the observation domain.

Cumulative fracture-length distributions are similarly best described by power-laws:

$$N = hl^{-e} \quad (1.2)$$

where l is the fracture length, and h and e are the coefficient and exponent of the power-law distribution.

From (1.1) and (1.2) it follows that:

$$ab^{-c} = hl^{-e} \quad (1.3)$$

which has the form of:

$$b = gl^m \quad (1.4)$$

implying a power-law relationship between aperture and length where g and m are the coefficient and exponent of a third power law.

The relationship between the power-law exponents is easily obtained from substituting (1.4) into (1.3):

$$ag^{-c}l^{-cm} = hl^{-e}$$

giving the simple formula:

$$e = cm \quad (1.5)$$

Additionally, the coefficients of the aperture and length size distributions are also related by a simple relationship:

$$h = ag^{-c} \quad (1.6)$$

All these relationships were first derived theoretically by Marrett (1996), but high-quality fracture data sets are required to test the validity of these theoretical relationships.

Real data sets often show deviations from a power law size distribution. Sampling truncation (Baecher and Lanney, 1978; Pickering et al., 1995) is produced by the progressive loss of sampling resolution toward smaller fracture sizes, because smaller fractures are more difficult to identify and differentiate from the matrix of the rock. The effect of sampling truncation is to underestimate the total number of fractures having small sizes. This sampling artifact particularly affects the collection of opening-mode fracture data in rocks where the material cementing the fractures is similar to the bulk composition of the rock (e.g., sandstones with quartz-filled fractures).

Another sampling artifact affecting fracture measurements is censoring (Baecher and Lanney, 1978; Laslett, 1982; Barton and Zoback, 1992; Pickering et al., 1995). Censoring artifacts are introduced when the total size of some fractures are too large to be measured accurately, for example where a fracture extends beyond the boundaries set up for fracture data collection. This artifact is commonly observed in fracture-length measurements. Longer fractures have greater probability of continuing beyond the limits of an observation area than do shorter fractures, and are preferentially affected by censoring. Recorded sizes for fractures affected by censoring are smaller than their true size; consequently, censoring results in an apparent increase in the exponent of the power-law for the longest fractures.

Aperture distributions

Macro- and microfracture apertures were measured along scanlines perpendicular to fracture set 1 in the cores and SEM-CL collages to study their statistical distribution (Appendix 1.D). Censoring artifacts do not affect aperture data collected along scanlines unless the scanlines terminate at a fracture or include gaps of incomplete exposure or core recovery. Truncation artifacts were avoided by choosing a minimum fracture-size to be measured that was above the resolution of the measuring tool, as estimated independently. For photomicrographs the resolution depends primarily on the quality of the photographs in the collage, but also greatly depends on the composition of the rock. The presence of highly luminescent minerals reduces the effective resolution.

Aperture distributions for the Ozona sandstone suggest that a power-law model best explains the variation of fracture abundance as a function of fracture size for both macro- and microfracture aperture populations (Fig. 1.10). However, macrofractures of the upper bed show a distribution that appears to follow two different power laws. In this bed, the cumulative number of fracture apertures smaller than approximately 0.3 mm follows a power law of exponent -0.626 , and larger fractures can be best modeled by a power law of exponent -1.668 .

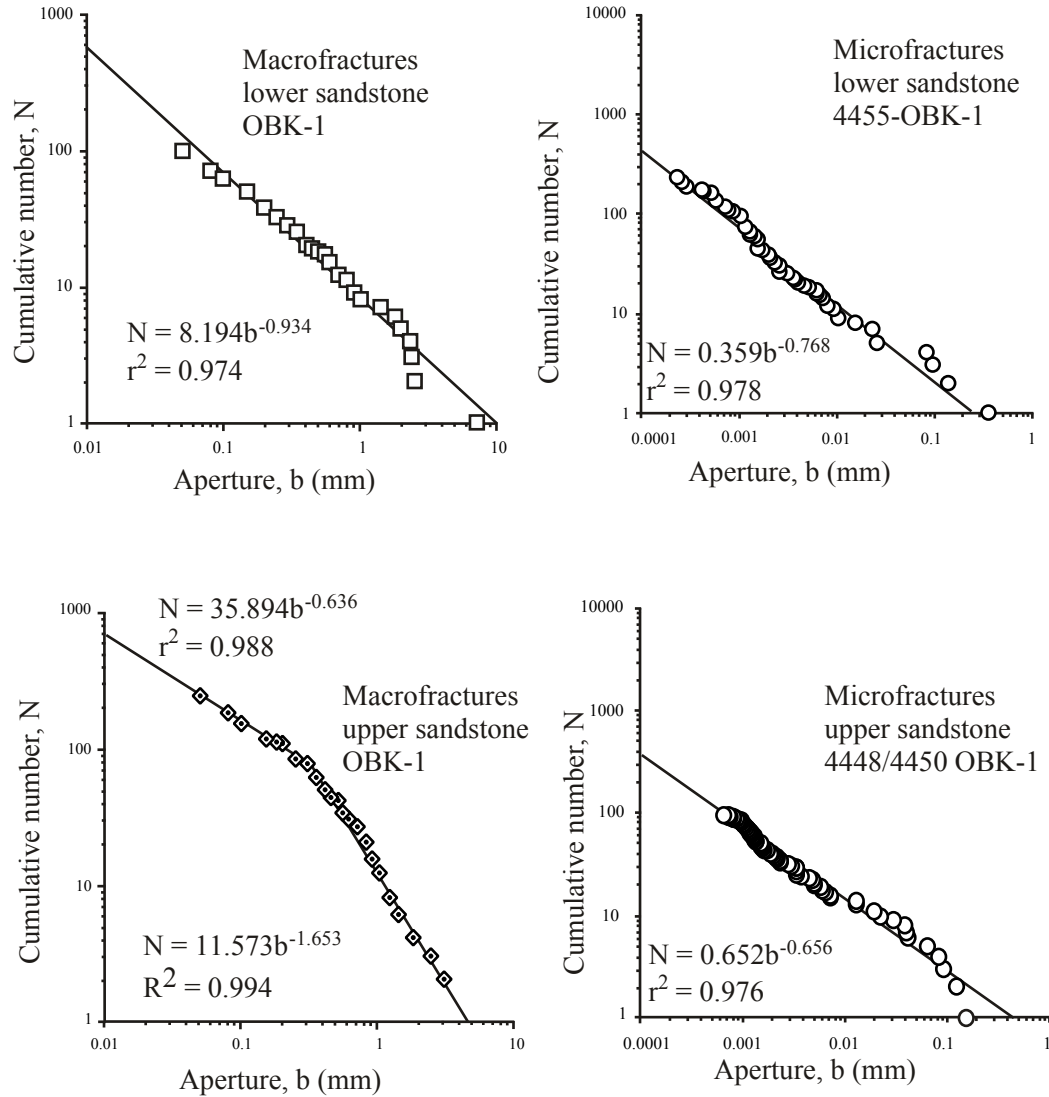


Figure 1.10. Cumulative fracture aperture distributions for OBK-1 well. Power law models adequately explain the cumulative size distributions observed. For each observational scale the power law model explains the abundance of aperture sizes over one and a half orders of magnitude. The smallest fracture size in each distribution is the minimum aperture size reliably detected with the observation tools available. Parameters in equations come from least-squares regressions to all data, except macrofracture distribution in upper bed, which has two segments with a boundary around 0.3 mm (see text).

Length distributions

Fracture length distributions are more problematic than aperture distributions because identification of the tips of fractures can be difficult wherever two or more fractures connect. The determination of fracture length can be based on a set of geometric criteria to assure interpretation consistency (Ortega and Marrett, 2000), but these criteria are at best simplistic solutions to a problem that requires understanding of complex geometries for the fractures that grow interactively.

Systematic collection of macrofracture length data from cores was not possible because the traces of the majority of fractures visible with the naked eye extend beyond the core. Fracture length measurements were also impaired because adjacent shale layers covered the surfaces of the sandstone beds.

Length distributions were obtained only from microfractures of collage 4448. The two-dimensional sampling yields a power-law exponent consistent with commonly reported values (Bonnet et al., 2001; Fig. 1.11). Fractures shorter than 50 microns have been ignored for power law regression. Grain size in sample 4448 vary from 0.05 to 0.120 mm, consequently most reliable microfractures (i.e., transgranular and trans-cement) are longer than 0.05 mm.

Aperture-length relationship

It is possible that most fractures observed at the macroscopic scale in part reflect growth by connection between individual fractures that initially grew

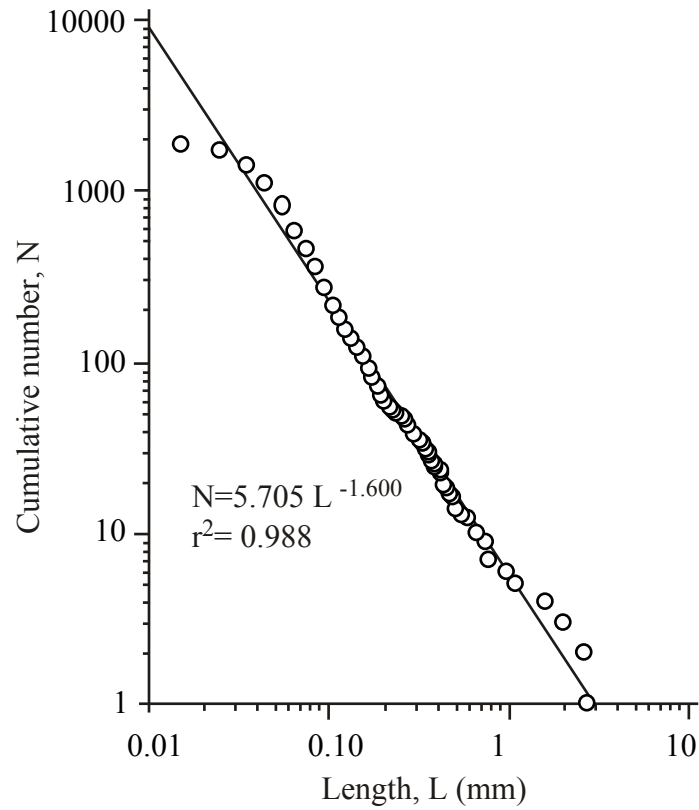


Figure 1.11. Microfracture length distribution, OBK-1 upper sandstone, sample 4448. A power law is a good model for this distribution, spanning approximately two orders of magnitude in size. Power-law regression fit to fractures larger than average grain size in sample. Approximately 2000 microfractures were measured to make this plot.

independently and ultimately linked to make a larger fracture. En-echelon arrays of fractures, for example, would tend to produce a larger interconnected fracture as deformation progresses (e.g. Olson and Pollard, 1991).

Moros (1999) showed that the majority of fractures he studied are characterized by locally variable apertures, but in general local aperture is between the maximum aperture and half of the maximum aperture for the majority of the trace length for most fractures.

Measurement of fracture apertures and lengths at different scales of observation allowed study of scaling relationships between these parameters. Two scales of observation were used: bed-scale (upper bed in OBK-1 core), and SEMCL-scale (20.6 mm² collage from thin section 4448). Only isolated fractures for which both tips could be identified were selected for the study. Isolated fractures have no visible connection with other fractures in the observation domain studied.

Theoretical predictions based on power-law scaling for apertures and lengths suggest that aperture and length are related by a power-law relationship (equation 1.4; Marrett, 1996). The power-law exponent of the aperture/length relationship (m) is a measure of the variation of aperture with length through observation scales. If $m > 1$, it would be possible to have fractures with an aperture larger than the length at certain (large) scales of observation. If $m = 1$, aperture and length are linearly proportional and their aspect ratio (aspect ratio = aperture/length) remains constant for any scale of observation. If $m < 1$, apertures

represent progressively smaller proportions of length as the scale of observation increases.

Aperture-length plots of the data collected show high scatter, suggesting that the results are at best statistical and probably depend on a number of other variables not considered in the study (Fig. 1.12). The plot suggests that aperture and length are positively correlated and follow a power law of exponent close to 1 (0.884). A linear relationship between aperture and length is an adequate model for the aperture-length relationship in these rocks, at least within the scales of observation studied. OBK-1 fractures are approximately 100 times longer than they are wide.

Moros (1999) found that a power-law relationship is the best model to explain fracture aperture vs. length relationships in a study of fractures from nine sandstone units, based on SEM-CL, petrographic microscope, and hand-lens observations. Moros (1999) found that the best model for all data is a power law of exponent ~ 0.75 for average and maximum apertures. This exponent is smaller than the exponent found in this study (0.88), but Moros (1999) found a similar exponent (0.85) for a sub-population of linked fractures. Also, Moros (1999) found that aperture-length aspect ratios are approximately 0.080 to 0.0125. These aspect ratio values are in agreement with the values obtained from OBK-1 data.

Extent of power-law scaling

Macro- and microfracture aperture distributions in the OBK-1 sandstone beds follow a power-law and suggest that the abundance of fractures of a certain

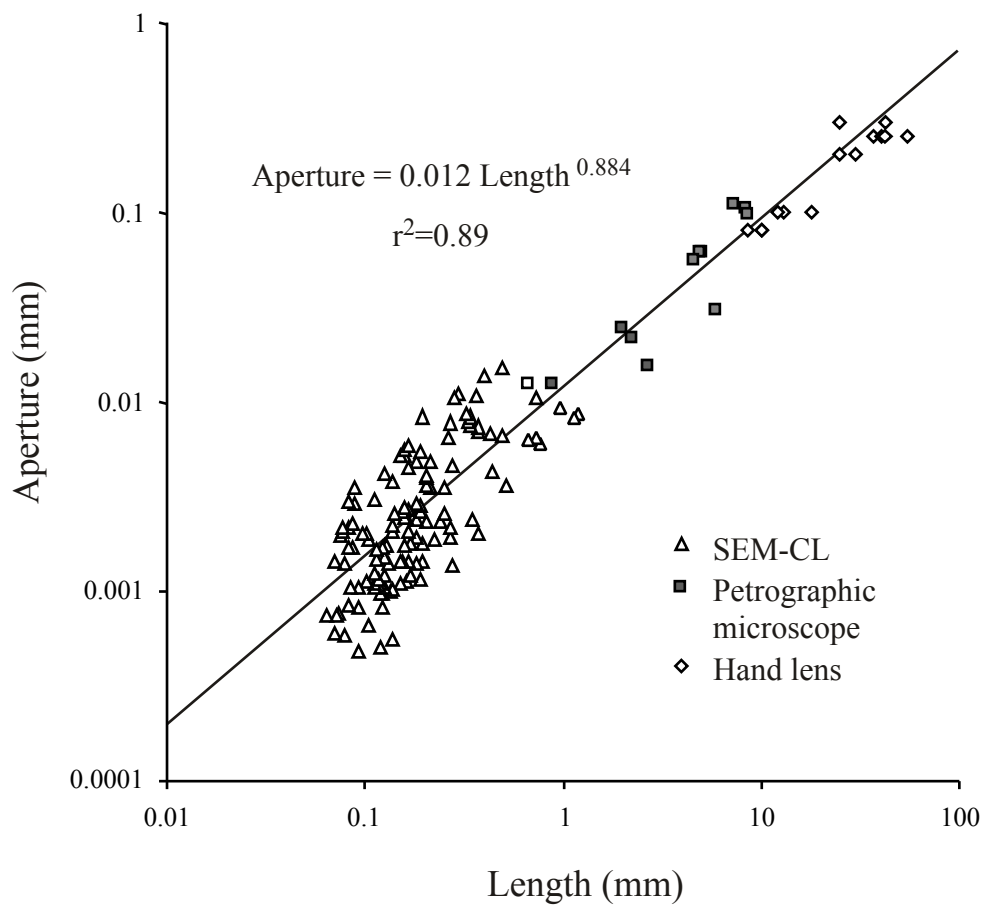


Figure 1.12. Aperture-length plot for upper bed in OBK-1 core. There is up to an order of magnitude variation in aperture for a given length value, particularly for microfractures observed with SEM-CL. A power-law regression is a good model for nearly three orders of magnitude variation in fracture size and gives a coefficient of determination $r^2=0.89$.

size or larger can be predicted for one scale on the basis of observations at a different scale. Also, the size of the largest fracture (b_{max}) in a finite observation domain can be predicted setting $N=1$ in equation (1) and solving for b to get:

$$b_{max} = a^{\frac{1}{c}}$$

In order to compare the size distributions at different scales of observation (e.g., macro- and microscale) a normalization methodology is necessary. This normalization is obtained by dividing the cumulative number by the size of the observation domain (Table 1.2). For example, in the case of scanlines the size of the observation domain is the total length of the scanline. The normalization process allows direct comparison of microfracture and macrofracture abundance. After normalizing fracture abundance by the size of the observation domain, we can evaluate the number of microscopic-scale fractures missed during macroscopic-scale observations. This exercise demonstrates the truncation effect on fracture size distributions (Pickering et al., 1995).

Systematic measurement of fracture apertures from core and SEM-CL images from samples of the Ozona Sandstone showed that the aperture distributions of micro- and macrofractures could be modeled by a single power-law for almost five orders of magnitude in fracture size (Ortega et al., 1998). These results were obtained from the analysis of the lower bed in the OBK-1 core and they are included here as part of this dissertation (Fig. 1.13). The method was repeated with data from the upper bed and similar results were obtained. However, in the upper bed, the prediction of macrofracture apertures is accurate

Table 1-2. OBK-1 power law cumulative aperture distribution parameters for sand studied. S is the scanline length, and a and c are aperture distribution parameters (equation 1.1).

Unit (Thickness)	Scale	S (mm)	a (mm ^{1-c})	c
Upper bed (55 mm)	Macro 1D	1500	35.894	0.636
	Macro 2D	1500	11.573	1.653
	Micro	23.63	0.652	0.656
Lower bed (>100 mm)	Macro	555	8.194	0.934
	Micro	18.61	0.3591	0.768

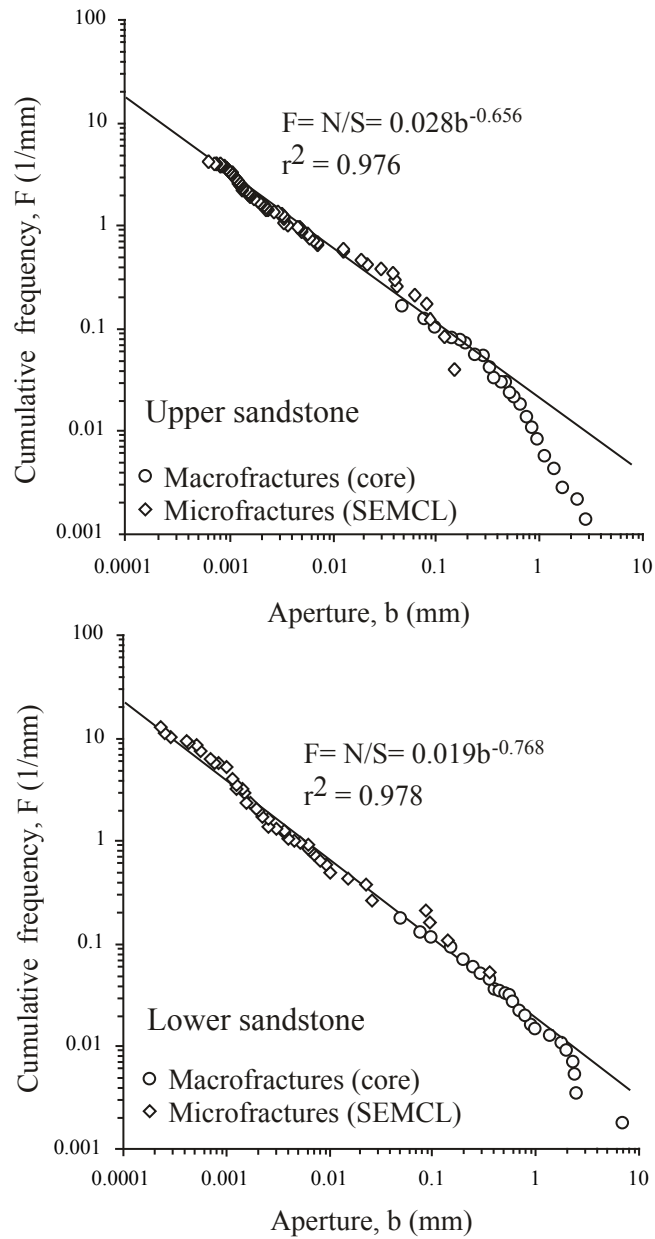


Figure 1.13. Log-log plots of aperture vs. cumulative fracture frequency in OBK-1 well. Power-law fits to microfracture aperture data adequately predict normalized macrofracture aperture distributions. Deviations at large apertures may be produced by topology artifacts. S is the scanline length in mm.

only up to apertures of approximately 0.3 mm (Fig. 1.13). Due to the larger exponent interpreted for fractures having larger apertures, their abundance cannot be directly predicted from extrapolation of the microfracture power-law. One possibility is simply that large fractures are proportionally less abundant than microfractures in this layer, however, other possibilities include artifacts produced by sampling topology changes (see section on topology artifacts below), and other effects (Bonnet et al., 2001).

The results from OBK-1 suggest that the prediction of macrofracture aperture abundance using microfracture size distributions is possible. Ortega and Marrett (2000) arrived at a similar conclusion after studying micro- and macrofracture length-size distributions in sandstones of the Mesaverde Group in New Mexico. If these observations are routinely corroborated in other rocks and in a number of localities, the organization of fracture sizes in a fracture system might be suitable for quantitative characterization using simple observational methods at the microscopic scale. This size organization may also reflect fundamental mechanical properties of natural fracture systems, strain magnitudes, and stage of development of fracture systems (Walmann et al., 1996).

TOPOLOGICAL TRANSFORMATIONS OF FRACTURE-SIZE DISTRIBUTIONS

Collection of fracture aperture data in one-dimensional domains (scanlines) has proved to be adequate for describing the size distributions of fracture systems in various lithologies and geologic conditions (Marrett et al., 1999). Fracture size distributions from two-dimensional observation domains are

more challenging because they are more affected by sampling artifacts and measurement of fracture attributes in two dimensions is fraught with problems. However, two-dimensional observation areas intersect more fractures than scanlines of comparable length scale. Comparison of two-dimensional data to one-dimensional data requires accounting for the topologic dimensions of the observation domains, the parameters of the fracture size distribution and the geometry of the fractures. Different fracture-geometry models imply different conversion formulas. If censoring problems are minimized, two-dimensional data can be used to estimate equivalent one-dimensional size distributions, even from relatively small observation areas. An understanding of these topologic transformations is important when estimating and managing of economic resources associated with fracture systems.

Theoretical relationships

Marrett (1996) derived the formulae to convert fracture size distributions between observation domains of different topology, assuming simple fracture geometry, one fracture set of constant orientation, spatial distributions uncorrelated with fracture size, and only isolated fractures. The probability (P) of observing a fracture in a fracture-perpendicular scanline through a three-dimensional volume containing the fracture is proportional to the fracture area:

$$P \propto l^2$$

In a population of elliptical fractures, the number of one-dimensionally sampled fractures will also be proportional to the fracture length:

$$\frac{dN_{1D}}{db} = \frac{dN_{3D}}{db} \frac{\pi l^2}{4\lambda} \quad (1.7)$$

where dN_{1D} is the number of fractures of area $\pi l^2/4\lambda$ sampled in a scanline, b is the fracture aperture, dN_{3D} is the number of fractures of area $\pi l^2/4\lambda$ in a volume, l is the length of the fracture and λ is the ellipticity of the fracture surface ($\lambda = l/h$, where l is the bed-parallel fracture length and h is the fracture height).

Equation (1.7) suggests that larger fractures will have a better chance to be sampled in lower-dimensional domains than smaller fractures, but typically large fracture abundance in the three dimensional volume is lower than smaller fractures abundance.

Now, substituting (1.1) and (1.4) in (1.7):

$$a_1 \frac{db^{-c_1}}{db} = a_3 \frac{db^{-c_3}}{db} \frac{\pi b^{\frac{2}{m}}}{4\lambda g^{\frac{2}{m}}} \quad (1.8)$$

where the number next to the exponent signifies the dimension of the observation domain; that is, “1” for one dimensional and “3” for three dimensional. Further reduction of (1.8) gives:

$$\frac{-4\lambda}{\pi} a_1 c_1 g^{\frac{2}{m}} b^{-c_1-1} = -a_3 c_3 b^{-c_3-1+\frac{2}{m}} \quad (1.9)$$

Equating aperture exponents we obtain:

$$c_3 = c_1 + \frac{2}{m} \quad (1.10)$$

and equating the coefficients we obtain a relationship between the power-law coefficients in three- and one-dimensional samples:

$$\frac{4\lambda}{\pi} a_1 c_1 g^{\frac{2}{m}} = a_3 c_3 \quad (1.11)$$

Other relationships between power-law exponents and coefficients of three dimensional fracture populations as determined in two-dimensional or one-dimensional observation domains are summarized in Table 1.3.

The previous relationships are not valid for large fractures that span the mechanical thickness of a layer in which the fractures are contained. These fractures have a higher probability of being sampled than predicted by the formulas. Corbett et al. (1987) introduced the concept of mechanical layer thickness for fracturing characterizing different fracture intensities in exposed units of the Austin Chalk in Texas. Mechanical boundaries of a fractured layer can be identified by systematic terminations of fractures at certain stratigraphic levels. A common observation is that fractures terminate at the stratification surfaces bounding a bed or group of beds and do not generally propagate into the adjacent layers.

Layer-perpendicular fractures that span the thickness of a mechanical layer will be sampled in any layer-parallel two-dimensional domain selected for data collection. The probability of intersecting these fractures using fracture-perpendicular scanlines is proportional to the length of the fractures rather than fracture area.

Following a similar procedure as the one used above for fractures that do not reach the mechanical thickness, we can derive the relationships between power law coefficients and exponents in 3D, 2D and 1D (Marrett, 1996; Table 1.4).

Table 1.3. Relationships between parameters of power law distributions in three-, two-, and one-dimensional domains for fractures that do not span the mechanical layer thickness.

Aperture power-law exponents	Length power-law exponents	Aperture power-law coefficients	Length power-law coefficients
$c_3 = c_2 + 1/m$	$e_3 = e_2 + 1$	$a_3 c_3 = \lambda a_2 c_2 g^{1/m}$	$h_3 e_3 = \lambda h_2 e_2$
$c_3 = c_1 + 2/m$	$e_3 = e_1 + 2$	$a_3 c_3 = 4\lambda a_1 c_1 g^{2/m}/\pi$	$h_3 e_3 = 4\lambda h_1 e_1/\pi$
$c_1 = c_2 - 1/m$	$e_1 = e_2 - 1$	$a_1 c_1 = \pi a_2 c_2 g^{-1/m}$	$h_1 e_1 = \pi h_2 e_2/4$

Table 1.4. Relationships between parameters of power-law distributions in three-, two-, and one-dimensional domains for large fractures.

Aperture power-law exponents	Length power-law exponents	Aperture power-law coefficients	Length power-law coefficients
$c_3 = c_2$	$e_3 = e_2$	$a_3 c_3 = a_2 c_2$	$h_3 e_3 = h_2 e_2$
$c_3 = c_1 + 1/m$	$e_3 = e_1 + 1$	$a_3 c_3 = a_1 c_1 g^{1/m}$	$h_3 e_3 = h_1 e_1$
$c_1 = c_2 - 1/m$	$e_1 = e_2 - 1$	$a_1 c_1 = a_2 c_2 g^{-1/m}$	$h_1 e_1 = h_2 e_2$

Testing conversions of fracture data from two- to one-dimensional domains.

Two- and one-dimensionally sampled data were collected from a large collage of SEMCL photographs of sample 4448 to test the validity of the formulas in Table 1.3 with real fracture-size populations.

The power law from a one-dimensionally sampled size distribution of kinematic apertures measured along a scanline was used to estimate the equivalent two-dimensionally sampled size distribution using the formulas. Collection of abundant fracture aperture data from a portion of the large photocollage was used to observe two-dimensional fracture size distribution. Predicted and observed 2D fracture aperture distributions were then qualitatively compared (Fig. 1.14). Predicted exponents and coefficients depend on the relationship between apertures and lengths (Fig. 1.12) and the geometry assumed for the fractures. In this exercise, average two-dimensional apertures were chosen for testing topologic conversion relationships. The average aperture is the best representation of aperture of a fracture for these purposes, because the aperture collected along a scanline is arbitrarily located along the fracture and statistically closest to the average aperture than to the maximum kinematic aperture. Predicted and observed two-dimensional distributions are reasonably similar if sampling artifacts at large and small size ends of the distributions are ignored (Fig. 1.14).

This is the first time that topologic predictions have been tested with aperture data. Ortega and Marrett (2000) attempted a similar exercise using fracture length data but their results were ambiguous, not only because of the

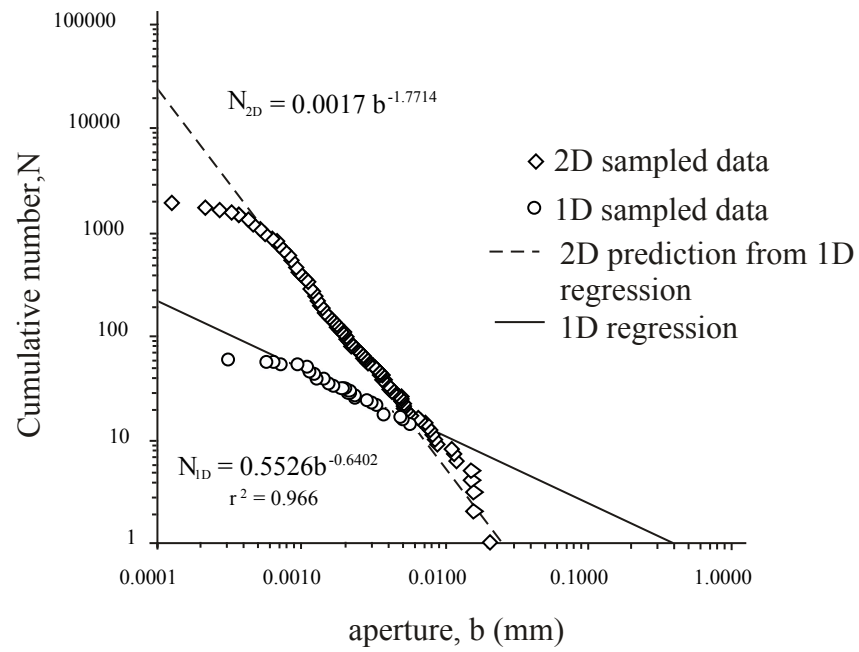


Figure 1.14. Comparison of two-dimensionally sampled aperture data and predictions from one-dimensionally sampled data using Marrett's (1996) topologic conversions.

difficulties inherent to fracture length measurements but also because of observation area limitations.

CENSORING ARTIFACTS

The collage from sample 4448 was chosen for a systematic study of censoring effects on fracture size distributions. Three sub-areas were chosen from the collage, which represent 80%, 50% and 20% of the total collage area. The areas maintain the same length as the whole collage but their width changes to fit the percentage area reduction. The lengths of all areas are roughly perpendicular to the strike of fracture set 1 and consequently censoring effects are expected. Moreover, censoring effects should become progressively more pronounced as the proportion of the collage interrogated decreases.

Two-dimensional fracture length distributions for the total collage area and progressively smaller portions of it are shown in Fig 1.15. Fractures affected by censoring have been indicated with white-filled symbols in each distribution, allowing control of those fractures whose lengths were not completely sampled in each area. The results of the analysis suggest that censoring modified the original fracture-size distribution in at least the following ways:

- 1) An increase in the apparent exponent of the power-law distribution for fracture lengths approaching the width of the observation area.
- 2) The longest fractures have the highest probability of being affected by censoring. All fractures longer than 1 mm were affected by censoring when the area of the collage was reduced to 80%. However, an

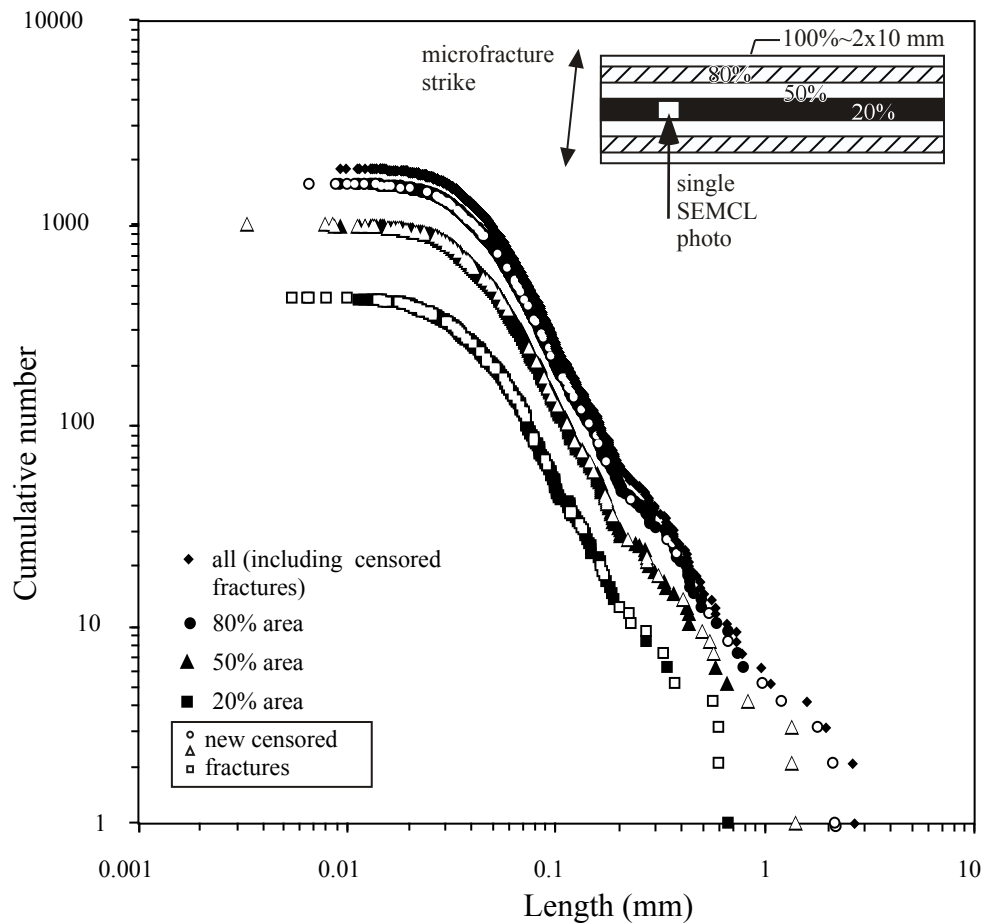


Figure 1.15. Censoring effects on fracture length distribution. OBK-1 sample 4448. The diagram in the upper right hand corner illustrates the methodology used to select smaller areas from the original SEM-CL collage. The small rectangle indicates the approximate size of an individual SEM-CL photo in the collage. Censored fractures are indicated with white-filled symbols in smaller-area length distributions. Note the parallelism of the distributions for intermediate fracture lengths regardless of the size of the observation domain.

important number of shorter fractures were also affected by censoring, possibly because they are more abundant. Note that in the 80% area distribution, a number of censored fractures fall in the smaller fracture length part of the distributions (< 1 mm long).

- 3) As area reduction progresses, a more noticeable truncation effect appears in the distributions toward the small-scale fracture range. This effect can explain why some length distributions based on scarce data have been interpreted as non power law.
- 4) Progressively more censored distributions contain a progressively smaller segment that remains parallel to the original fracture-size distribution. The boundaries of the linear segment of the underlying power law are the length scale of the observation area (e.g., photocollage width) and the greatest length unaffected by truncation.
- 5) The range of scales affected by truncation remains constant as the area analyzed becomes smaller because the resolution of the photocollage does not change. However, truncation artifacts become apparently more pronounced as progressively smaller areas are analyzed. This effect can be explained as a consequence of having consistent resolution limit (i.e. truncation scale) and progressively smaller fracture size range in the distribution.
- 6) Determination of the boundaries of the linear segment of the size distribution is important to obtain the underlying power law distribution for the entire population. Analyses of the fracture size

distribution in progressively smaller domains may help determine the small-scale boundary of the rectilinear segment in size distributions.

USE OF SCALING METHODS FOR SUBSURFACE FRACTURE CHARACTERIZATION

Subsurface-fracture sampling problems make the approach of using scaling techniques for fractured system characterization interesting. Abundant microfractures in small pieces of rock can provide information about the orientation and size distributions of macrofractures on a bed-by-bed basis. However, the extrapolation of fracture properties across several orders of magnitude in size is fraught with potential hazard. Deeper understanding of the relationships between microfractures and macrofractures, as well as the effects of sampling topology, mechanical boundaries, local structures and changes in mechanical properties are important to reliably perform these extrapolations and to recognize when they are futile or effective.

Further research to understand the relationships between microfractures and macrofractures might lead to techniques of predictable mechanical stratigraphy and prediction of spatial distribution of fractures in subsurface. Macrofracture maps based on microfracture information from subsurface samples would provide valuable geologic constraints for fractured reservoir modeling.

Marrett (1996) proposed mathematical relationships to describe some aggregate properties of fracture systems, assuming power-law scaling for apertures and lengths in a given volume of fractured rock. Aggregate fracture

properties such as surface area, strain, porosity, permeability, and shear-wave anisotropy were estimated assuming simple fracture geometry for each fracture set. These are potentially useful variables to predict, especially if they can be estimated on the basis of small samples retrieved from the subsurface. However, whether such estimates are accurate enough to be useful in practice remain to be seen.

CONCLUSIONS

The study of microscopic and macroscopic fracture systems from the Ozona Sandstone revealed:

- 1) Veins in the OBK-1 well are probably associated with local tectonic deformation that produced tilting of beds observed in cores. Sub-horizontal veins probably formed during sub-horizontal contraction of tilted beds, based on crosscutting relationships between veins and older structures. Large veins (> 2 mm aperture) retained some fracture porosity and their occurrence may enhance permeability gas recovery in tight Ozona Sandstone reservoirs.

- 2) SEM-CL imaging of sandstones revealed abundant microfractures with persistent orientations sub-parallel with observed macrofractures in core.

- 3) Power-law models best describe microfracture and macrofracture aperture size distributions from the OBK-1 well. Microfracture length distribution from a large collage of sample 4448 is also best modeled using a power law.

- 4) Opening-mode fracture aperture and length are positively correlated but significant dispersion characterizes this relationship. An aperture-length

relationship in OBK-1 sandstones suggests that as fractures get longer, their apertures increase at a slower pace. In other words, small-scale fractures have larger aperture-length ratios than large-scale fractures.

5) Power-law aperture scaling of microfractures and macrofractures in two beds of the OBK-1 well support the idea that scaling techniques applied to microfracture size distributions can be used to predict macrofracture sizes in the same volume of rock, at least up to the scale of the mechanical layer thickness.

6) In the upper bed, extrapolation of the power-law regression to microfracture apertures predicts the macrofracture aperture distribution up to a scale of 0.3 mm aperture. Fractures having 0.3 mm apertures or larger have average lengths in the order of 4 cm, approaching the thickness of the mechanical layer. Fractures that span the mechanical layer thickness will produce a two-dimensional topologic artifact when sampled along scanlines. Topologic artifacts produce an increase in the slope of the macrofracture size distribution and can be difficult to separate from other effects affecting the large-scale portion of a fracture size distribution (Pickering et al., 1995).

7) In the lower bed, power-law regression to microfracture apertures predicts the macrofracture size distribution up to a scale of 2 mm apertures. If topologic artifacts produce the observed increase in slope of the fracture size distribution at the large-scale end of the plot, then we can predict that the thickness of the lower bed is approximately 30 cm, based on the aperture-length relationship.

8) Tests of topologic transformation equations in Marrett (1996) using abundant microfracture data from sample 4448 demonstrate that topologic conversions from one-dimensionally to two-dimensionally sampled size distributions agree with observations. Results suggest, however, that collection of microfracture size data in two-dimensional sampling domains and conversion of these size distributions to one-dimensional size distributions is possible. Abundant two-dimensionally (i.e. map view) sampled microfracture data can be collected from small portions of a thin section and their size distributions converted to one-dimensional (i.e. scanline) equivalents. One-dimensional data sets are more amenable for subsurface fracture characterization and offer information directly applicable to borehole applications.

9) Qualitative analyses of censoring artifacts from progressively smaller areas of an SEM-CL photocollage reveal the impact of censoring on observed size distributions. As expected, the largest fractures have the highest probability of being affected by censoring. Censored lengths produce an apparent increase in the slope of the size distribution. As areas investigated get smaller, the linear segment of the size distribution least affected by artifacts, gets smaller. Truncation artifacts represent a larger proportion of the size distribution revealing the resolution scale of the observation domain.

10) The linear portion of the power law in progressively smaller areas of the collage maintains the same slope, suggesting that the underlying power law of the distribution can be obtained from any sufficiently large data set if the portion of the distribution unaffected by artifacts can be identified.

CHAPTER 2: OUTCROP ANALOGS AND SUBSURFACE FRACTURE SYSTEM CHARACTERIZATION

Weber Sandstone

INTRODUCTION

Significant volumes of hydrocarbons are trapped in reservoirs classified as fractured reservoirs. Fractured reservoirs are characterized by low-porosity and low-permeability matrix, requiring the permeability provided by natural fractures to meet economic thresholds (Aguilera, 1980). However, fractured reservoirs are often marginally economical because of our limited understanding of natural fracture systems in general, lack of adequate methods to characterize fracture systems, and use of fluid flow modeling software that cannot manage fundamental properties of the fracture system. Constant demand for more and cleaner fuels attracts interest to these complex hydrocarbon reservoirs, especially in the continental U.S., as a secure energy source. The characterization of fractured reservoirs is challenging because the fractures responsible for the improved permeability of the reservoir are difficult to sample. Reservoir-scale fractures typically are below seismic resolution, form high angle with stratification and are characterized by wide spacings compared with borehole diameter, which make their sampling infrequent using conventional vertical boreholes. The difficulties faced trying to sample subsurface fractures are collectively called the subsurface fracture-sampling problem (Laubach et al., 2000).

The literature contains many examples of fracture studies based on surface information whose results have been extrapolated to subsurface conditions to solve subsurface fracture characterization problems (Rauch, 1984; McCoy and Young, 1992; Hoover and Rauch, 1989; Guo et al., 1999). However, use of remote sensing and outcrop analogues for subsurface fracture characterization is dangerous because stratigraphic characteristics, tectonic, burial, and diagenetic histories are potentially different between outcrop areas and subsurface.

For example, characterization studies of fracture systems in outcrops of Upper Cretaceous units along the Rocky Mountains, which produce hydrocarbons in a number of basins in that region, may be biased by significant differences in the diagenetic and burial histories between outcrop and subsurface locations (e.g., Dutton and Willis, 1998; Ortega and Marrett, 2000). The Laramide deformation in the eastern Rocky Mountains region occurred during the Paleogene (Berg, 1962; Cross, 1986) and probably affected the diagenesis of Upper Cretaceous rocks since very early in their burial history. These diagenetic processes were probably very different in uplifted areas (e.g., near present outcrop locations) compared with areas in subsurface locations in the foreland (e.g., hydrocarbon accumulation sites). The main difference between outcrop and basin localities is often the duration of residence of the rock at high temperature, which is thought to be a primary control on cement volume production (e.g. quartz cement, Lander and Walderhaug, 1999). We can expect that fractures forming in considerably different host rocks and subsurface environments will show differences in morphology, intensity, cement fill, timing, and orientation. To justify the use of

outcrop analogues for the characterization of subsurface fracture systems of Upper Cretaceous rocks of the Rocky Mountain region, fracture patterns in outcrop need to be linked to the progress of diagenetic reactions in the outcrop and compared to (readily sampled) diagenetic reaction products in the subsurface (Laubach et al., 2000).

Excellent outcrops of Permian-Pennsylvanian Weber Formation sandstones in northwestern Colorado and abundant core data from Rangely Field wells located only a few tens of kilometers from these outcrops offer an excellent opportunity to compare and contrast surface and subsurface fracture systems in a sedimentary unit deposited at least 200 m.y. before the Laramide orogeny, the deformation event responsible for the structural configuration that we observe today in northwestern Colorado (Hansen, 1986).

Rangely Field is one of the largest fractured reservoirs in North America and has been producing oil for over 50 years, mainly from Weber Formation sandstones (Hefner and Barrow, 1992). However, the effect of natural fractures in oil production and enhanced recovery from Weber sandstones at Rangely has been only recently acknowledged in the literature (Hild and Wackowski, 1998). Little is known about the subsurface fracture systems in Weber Formation sandstones at Rangely Field (Larson, 1975; W. Narr, 1997 unpublished) probably because of scarce tools available for natural fracture characterization and almost certainly because of subsurface fracture sampling problems.

It is tempting to extrapolate the results of recent fracture studies in outcrops of the area (Silliphant et al., 2000; Wilkins et al., 2001; Wilkins and

Gross, in press) to subsurface Weber Formation characterization, but the diagenetic and stratigraphic characteristics of the units studied in these outcrops may impair a direct application of these results to subsurface reservoirs. Indeed, Larson (1975) pointed out that fracture orientations in outcrops of younger units than the Weber Formation in the surroundings of Rangely Field differ from fracture orientations found in oriented cores.

In order to test the viability of extrapolation of Weber outcrop fracture studies to subsurface Weber reservoir rocks, samples from surface and subsurface Weber sandstones were analyzed to investigate their diagenetic history and petrographic characteristics. Field data and published literature (e.g., Fryberger, 1979; Koelmel, 1986; Bowker and Jackson, 1989) helped establishing differences and similarities in Weber sandstone stratigraphy between outcrops and subsurface. Significant changes in stratigraphy, diagenesis, and petrographic characteristics between Weber outcrops and subsurface Weber rocks prevented a direct extrapolation of outcrop data to subsurface conditions, supporting the idea that local data must be used to characterize fracture systems in the subsurface, even when timing of deposition and deformation of reservoir units are separated by hundreds of millions of years.

Use of local data for the characterization of subsurface fracture systems is difficult because of macrofracture sampling problems. However, microfractures are often abundant even in small volumes of rock (Laubach, 1997). Excellent exposures of Weber sandstone in northwestern Colorado were selected to test the hypothesis that micro- and macrofractures are different size fractions of the same

fracture system in the rock and that they have similar orientation and size scaling properties (Ortega et al., 1998; Laubach et al., 2000). If this hypothesis is valid, microfracture data can potentially be used for macrofracture property prediction in the subsurface, helping solve the subsurface fracture-sampling problem. The study of microfractures in sandstones was possible using a Scanning Electron Microscope Cathodoluminescence device (SEM-CL). SEM-CL can image quartz-filled microfractures in sandstones that are otherwise invisible (Laubach, 1997).

Positive results of testing the technique of micro- to macrofracture extrapolation with outcrop micro- and macrofracture data supported the application of the technique using core samples of Weber Formation from Rangely Field. It will be shown that microfracture attribute analyses augmented fracture information in Weber sandstones at Rangely. Local macrofracture information derived from microfracture data can be incorporated into reservoir-scale fracture patterns to improve fractured reservoir simulation.

Extrapolation of fracture attributes across scales of observation from the microscopic scale to the scale important for reservoir characterization is risky. One way in which we can reduce the uncertainty of these extrapolations is by identifying and understanding scale-dependent processes and sampling artifacts on fracture system characterization (Pickering et al., 1995; Bonnet et al., 2001). For example, the thickness of the volume of rock in which fractures propagate may represent limits for extrapolation of some microfracture attributes. It is a common observation that joints and veins systematically terminate against some stratigraphic surfaces in a sequence of layered rocks. Identification of mechanical

stratigraphic units in Weber Formation allowed testing the hypothesis that mechanical thickness affects fracture size distributions and that these effects are at least partly produced by sampling artifacts (Marrett, 1996). Sampling topology effects are purely geometrical and do not imply fundamental changes in fracture growth processes. However, data from one of the outcrop pavements studied suggests that fracture linkage can facilitate continuity of fracture size distributions beyond the scale of the mechanical layer thickness.

Another objective of this work was to apply new empirical methods of fracture-fill prediction (Laubach et al., 2000) to subsurface fracture systems in Weber Formation sandstones and to incorporate this type of information into fracture pattern simulations for the reservoir. Fracture fill information should be a component of fluid flow modeling because the degree to which fractures are potential conduits for flow depends on the proportion of the fracture not occupied by cement. A classification of cement timing with respect to fracture opening (Laubach et al., 1995) and conventional point counting techniques allow a qualitative evaluation of the intervals in the stratigraphic succession prone to contain filled or at least partly open fractures. Furthermore, comparing the distribution of fracture fill and the distribution of sedimentary facies in Weber Formation stratigraphy revealed that fracture quality and sedimentary facies may be related. Application of fracture quality assessment techniques (Laubach et al., 1995) supports a subdivision of the reservoir into flow units using the degree of fracture openness as a basis for discriminating fracture-controlled and matrix-controlled fluid flow units. This information may be used to choose single or dual

porosity models for reservoir simulation and may help targeting high fracture-quality intervals within seemingly homogeneous reservoirs.

Finally, a visualization of fracture connectivity in subsurface Weber sandstones was based on microfracture predictions of macrofracture orientations, size distribution information from microfractures, and fracture quality from rock-matrix surrogates. The integrated model was first tested in outcrops and then applied to two intervals in one well of Rangely Field, illustrating the potential of these techniques for fractured reservoir characterization and management.

LOCATION OF STUDY AREA

The study area is located in northwestern Colorado, to the north and northeast of the town of Rangely (Fig. 2.1). Surface data were collected from outcrops of Weber Formation near Dinosaur National Monument, and subsurface data were obtained from cores recovered from Rangely Field (Fig. 2.1). The fracture outcrop database includes macrofracture data from three two-dimensional observation domains (i.e., bed-parallel pavements), four one-dimensional observation domains (i.e., bed-parallel scanlines), and microfracture data from SEM-CL photomicrograph collages (Table 2.1). Two of the pavements studied are from the Disappointment Draw Monocline, in a 20-km-long gently east-southeast dipping limb (10° - 20°) at the eastern edge of the Uinta Mountains. The third pavement is located on the southern limb of Skull Creek Anticline, approximately 15 km to the southwest of Disappointment Draw Monocline (Fig. 2.1).

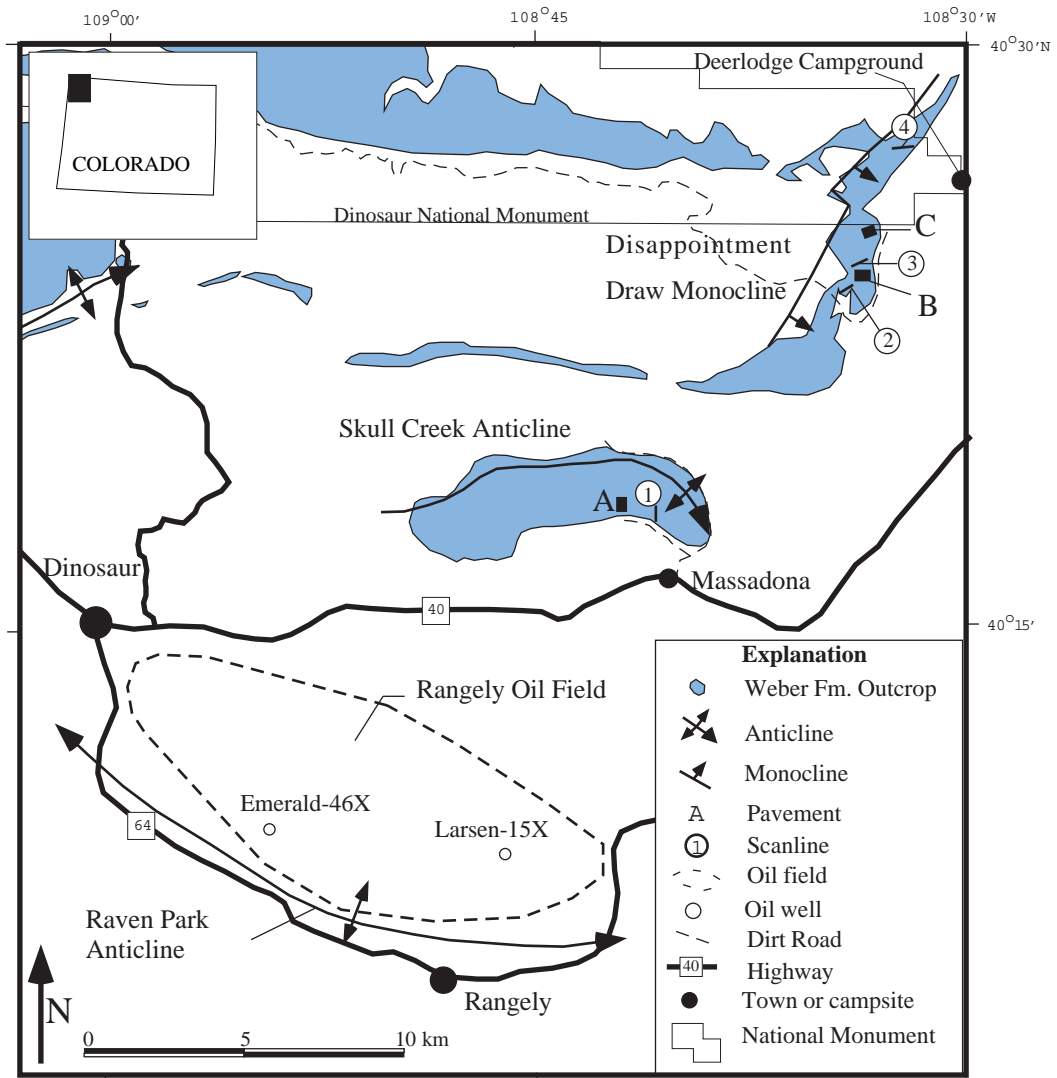


Figure 2.1. Weber Sandstone study areas. Two-dimensional and one-dimensional macrofracture outcrop data were collected in Disappointment Draw Monocline and Skull Creek Anticline. Weber Sandstone subsurface data were obtained from cores of two wells in Rangely Field. Pavements and scanlines studied in the field are indicated by symbols and numbers (see text for details).

Table 2.1. Summary of outcrop data sets (see Fig 2.1 for location). Also indicated are the samples selected for microfracture analyses.

Name of data set	Label (Fig 2.1)	Domain 2D or 1D	Area/length (m ² or m)	Strike/dip or trend/plunge	Layer thickness	Fractures measured	Fracture attribute	Size range (mm)	SEM-CL sample
North Pavement Disappointment	C	2D	637	40, 11	?	1475	length	10-3030	
South Pavement Disappointment	B	2D	1654 3558	15, 10	~6 m	1540	length	15-6830	w-043-97
Skull Creek Pavement	A	2D	69	70, 30	~4 m	1295	length	10-4920	
North Scanline Disappointment	4	1D	208.5	200, 5	>100 m (?)	362	aperture	0.1-995	w-045-97
		1D	9.2	40, 5	?	183	aperture	0.1-7	
Disappointment Gulch Scanline	3	1D	15.6	70, 11	?	137	aperture	0.1-3.2	w-036-97
		1D	74.3	50, 6	?	383	aperture	0.1-20	
South Scanline Disappointment	2	1D	87	55, 6	~6 m	224	aperture	0.15-270	
Skull Creek Scanline	1	1D	18	180, 29	?	150	aperture	0.1-20	

Three of the scanlines are located along Disappointment Draw Monocline. Two of these scanlines are located on pavement tops (North and South Disappointment scanlines) and one scanline is located along a small creek near South Disappointment pavement (Disappointment Gulch). The fourth scanline is located in the southern limb of Skull Creek Anticline, near the pavement studied in the same structure.

STRUCTURAL STYLE

The study area is characterized by basement-involved thrusting (Narr, 1993; Narr and Suppe, (1994). Narr and Suppe (1994) used examples from the eastern Rocky Mountains (including the study area) to demonstrate the applicability of their fault-fault-fold triple junction model to interpret basement-involved structures. Several published cross sections of anticlines in the area illustrate the structural style (Harding and Lowell, 1979; Stone, 1986). Seismic sections across Rangely Field (Stone, 1986) show that the Park Raven Anticline structure (i.e. closure for Rangely Field) is asymmetric, with a steeper limb in the south-southwest.

Narr and Suppe (1994) showed a cross section through Willow Creek Anticline, the western continuation of Skull Creek Anticline (Fig. 2.1), with good control from wells drilled on the structure, and described its structural style as a drape fold formed above a triple fault-fault-fold junction that evolved to a fault-bend fold. Novoa et al. (1998) described the geometry of Disappointment Monocline as a map-view example of monoclinal interference fold.

WEBER FORMATION

Weber Formation sandstones were deposited during the Permian-Pennsylvanian time, covering portions of the Piceance, Uinta, and Sandwash basins (De Voto et al., 1986). The Weber Formation was primarily deposited in an eolian environment that graded laterally to fluvial sediments (Fryberger, 1979). Regional stratigraphic changes in northwestern Colorado have been studied by a number of authors who have also shown the implications of these stratigraphic changes for oil and gas exploration and hydrogeology (Fryberger, 1979; Fryberger and Koelmel, 1986; De Voto et al., 1986; Geldon, 1986; Bowker and Jackson, 1989; Hefner and Barrow, 1992).

The Weber Sandstone is partly time correlative with the Tensleep Sandstone in Wyoming (Fryberger, 1979). The Weber Formation is dominantly composed of sandstones, siltstones, and shales (Larson, 1975), although a few thin and discontinuous carbonate layers have also been described (Fryberger, 1979). These carbonate layers were interpreted as deposited in shallow marine conditions by Mallory (1975), but Fryberger (1979) demonstrated a fresh-water origin and continental sedimentary environment. Relative proportions of each lithotype in Weber Formation vary regionally due to lateral and vertical changes of dominant environment of deposition and proximity to sediment source areas (Geldon, 1986; Bowker and Jackson, 1989). However, sandstones typically constitute more than 50% of the unit in the study area (Bissel, 1964; Geldon, 1986). Weber sandstones partly overlie and change laterally into redbeds of the

Maroon Formation, for which a fluvial sedimentary environment has been proposed (Fryberger and Koelmel, 1986). Maroon and Weber formations are overlain by Permian age sediments of the Park City and State Bridge formations (Sheldon, 1963; Bowker and Jackson, 1989; Fig. 2.2).

Weber Formation thickness varies regionally from 0 to more than 450 m (Geldon, 1986; Fig. 2.3), and from 200 m to 400 m in the study area (Fryberger and Koelmel, 1986). Major depocenters of Weber sandstones developed in the Yampa Platform area, around Dinosaur National Monument, and in the Sandwash basin area (Geldon, 1986).

The Uncompahgre Uplift, approximately 60 km to the south of the study area, was the main source of sediments for the Weber Formation, but other elevated areas to the east provided secondary sediment sources for the sediments (Koelmel, 1986). Sandstones vary in their composition depending largely on the environment of deposition and the distance to the sediment-source area (Bowker and Jackson, 1989).

RANGELY FIELD

Rangely Field is the largest oil field in the U.S. Rocky Mountain area (Fryberger and Koelmel, 1986), with an estimated 1.6 billions of barrels of oil originally in place (Hefner and Barrow, 1992). The oil in Rangely Field accumulated in a four-way closure trap (Raven Park anticline, Fig 2.1) with clear surface expression. Sandstones of the Weber Formation comprise the most

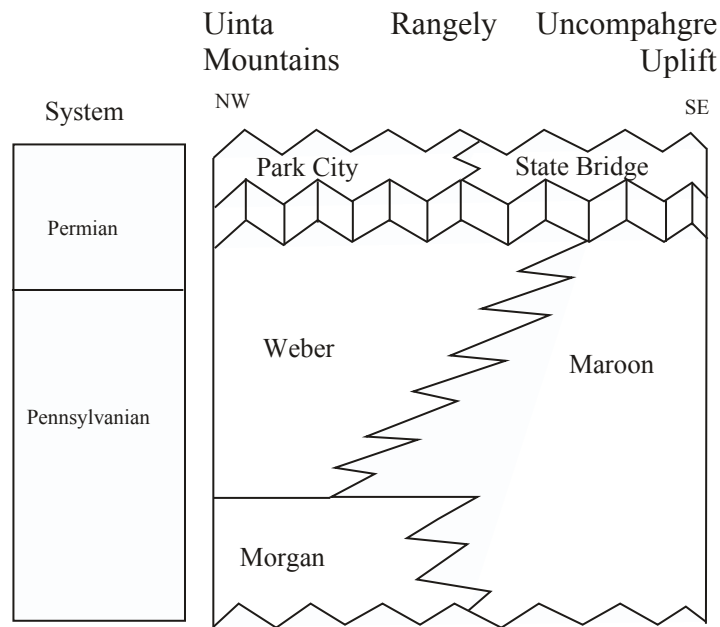


Figure 2.2. Northwest-southeast Permo-Pennsylvanian stratigraphic chart for the study area. Dominantly eolian Weber Formation sandstones change to alluvial Maroon Formation sandstones and shales toward uplifted areas. Vertical bars indicate missing section before deposition of Park City and State Bridge sediments (modified from Bowker and Jackson, 1989; Hefner and Barrow, 1992).

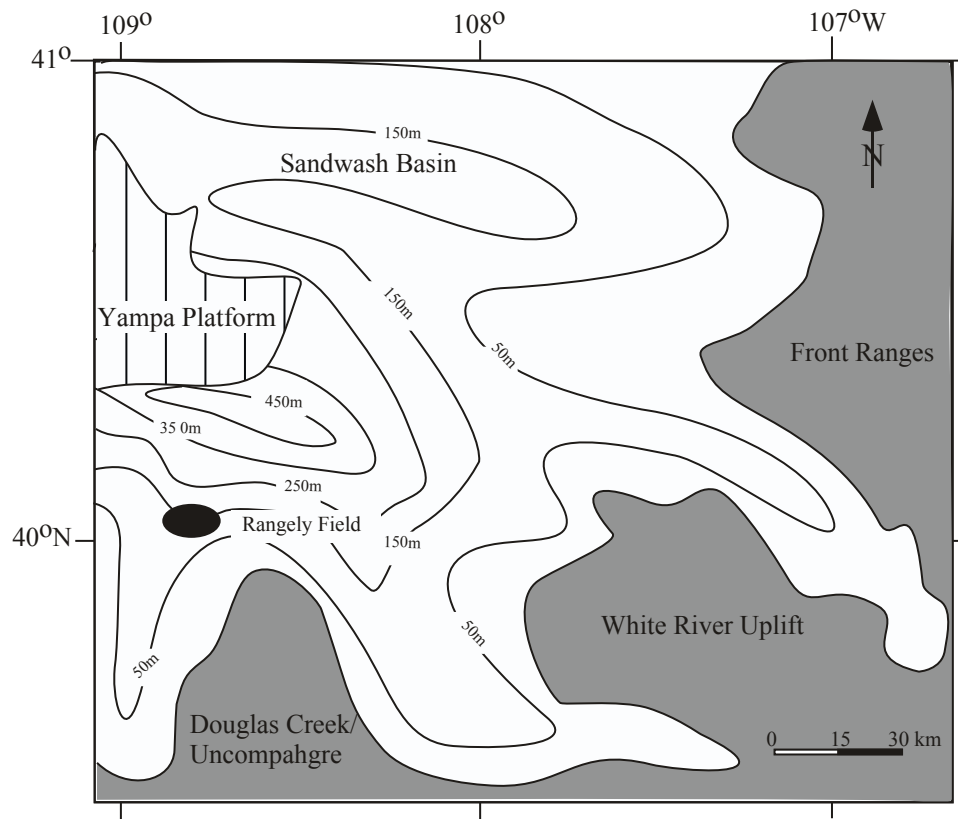


Figure 2.3. Weber Formation thickness variations in northwestern Colorado (modified from Geldon, 1986). Approximate location of Rangely field is indicated by a black ellipse. Ruled area represents eastern termination of the Uinta Mountains, where Weber sandstones are presently exposed or have been eroded. Gray areas represent interpreted Weber Formation sediment source areas.

important reservoir in Rangely Field (Hervey and Iakovakis, 1991; Hefner and Barrow, 1992). Sedimentological and petrophysical studies suggest that sandstone composition and average grain size largely determine fluid-flow behavior in the Weber reservoir (Bowker and Jackson, 1989). Cross-laminated, fine-grained, subarkosic, sandstones deposited in an eolian environment are the best reservoir facies with approximately 12% (TVR) average porosity, and permeability from 0.4 to 2 md (Bowker and Jackson, 1989). Structureless eolian interdune sandstones are generally poor reservoir facies with 7% (TVR) average porosity and 0.2 md permeability (Bowker and Jackson, 1989). Grey to red, arkosic, fluvial sandstones and siltstones have the lowest reservoir quality and are considered seals for fluid flow (Bowker and Jackson, 1989). Fluvial sequences occur in fining upward cycles with channel-fill sands overlain by over bank facies (Bowker and Jackson, 1989).

Although sedimentary facies are important for reservoir quality assessment, natural fractures significantly affect permeability in the Weber reservoir (Hild and Wackowski, 1998). Major faults in the field have affected fluid flow during enhanced recovery operations (Bowker and Jackson, 1989; Bowker and Shuler, 1991) and natural open fractures are a possible explanation for premature breakthrough times of fluids injected into the reservoir (Hild and Wackowski, 1998). A better understanding of the natural fracture system in subsurface Weber sandstones would help design better strategies for continuing efforts to extract hydrocarbons from this prolific reservoir. Fracture intensity distribution, fracture orientation, fracture spacing, mechanical stratigraphy, and

estimates of cement filling fracture porosity would help locate injectors and producers for more effective flooding of the reservoir and enhanced recovery. During enhanced hydrocarbon recovery, fractures must sometimes be avoided and other times targeted. For example, well injector locations ideally must be located away from fluid flow fairways to avoid rapid communication between wells. Conversely, producers should intersect fractured zones in order to extract hydrocarbons and injection fluids effectively.

DATA COLLECTION AND DATA ANALYSIS METHODS

Outcrop macrofracture data

Excellent exposures of Weber Formation fractured sandstones in and around Dinosaur National Monument, Utah and Colorado, offer an ideal opportunity to study the size, orientation, and spatial distribution of fracture systems in the same stratigraphic unit over large areas, and in cross sectional exposure along canyons. The quality of the outcrops is good to excellent and large pavement patches covering areas from hundreds to thousands square meters are common. Abundant two-dimensional fracture data can be collected from these large pavements. The pavements are generally devoid of soil cover with the exception of isolated bushes or grass growing along erosional grooves. Lichen cover is ubiquitous on the pavements and affects detection of fractures shorter than 20 cm in length. However, in the pavements selected for study, there is little chance of missing any fracture longer than 1 m during data collection.

Exceptionally well-exposed areas in some pavements and along streams allow collection of one-dimensional data along scanlines. Areas adequate for scanline collection have width dimensions of tens of meters to hundreds of meters. Scanlines were set perpendicular to the fracture set of interest to minimize geometrical effects on fracture measurement (Terzaghi, 1965).

Outcrop macrofracture orientation data

Macrofracture orientation data were collected from outcrops using a Brunton compass. Areas used for outcrop fracture orientation data collection are located in gently dipping Weber sandstone beds (10° - 20° at Disappointment Draw, 20° - 30° at Skull Creek, Fig. 2.1). The majority of macrofractures observed in outcrops form a high angle with stratification. Fracture dips generally exceed 80° so fractures were treated as vertical planes and only fracture strikes were recorded. Macrofracture strike data were collected along scanlines and on pavements. At pavement localities, the orientation of a fracture set was estimated as the average strike of fractures in fracture swarms. After determining the average strike and strike dispersion of fractures belonging to one set, fractures were simply counted to obtain an estimate of the proportion of fractures belonging to each set (Appendix 2.B). Fracture orientation data collected from scanlines are restricted to the set selected for measurement. Regular measurement of fracture strike along the scanline confirmed the selection of one fracture set for fracture aperture and spacing measurement. Fracture strike results are biased by the orientation of the scanline or elongation of the pavements (Mauldon et al., 2001).

Macrofracture strike data were plotted in rose diagrams and displayed in maps to analyze regional variations in fracture strike. Fracture orientation diagrams can be compared with bedding attitude and the orientation of fold axes in the area. Correlation of fracture attitude with local structure orientations can suggest (but not demonstrate) a structural origin for the fractures. Similarities of fracture orientation in markedly different structures at different localities may indicate that fractures postdate the structures. Restoration of bedding planes to a horizontal position can show that fracture orientations are similar in both limbs of folds and at different localities in the study area, suggesting that fractures formed before folding.

Outcrop macrofracture length data

The measurement of fracture length depends on the identification of fracture tips (Ortega and Marrett, 2000). Most fractures studied on Weber Formation pavements are isolated and their tips can be identified without ambiguity. However, some fractures are connected (hard link) or their terminations partly overlap (soft link). Measurement of lengths for interconnected fractures is difficult. Fracture segments are defined here as the smallest fracture branching off a connected network and having one or two connections at the end. Some fractures terminate against other fractures with curved terminations (Olson and Pollard, 1989), and others terminate abruptly forming “T- shape” connections (Odling, 1992). Fractures with abrupt terminations can be either branches stemming away from a larger fracture or small fractures bridging larger fractures.

Collection of fracture length data from the pavements studied included measurement of isolated fractures and fracture segments (Appendix 2.B). Below are definitions for isolated fractures, fracture segments, and interconnected fractures and methods adopted to measure their lengths:

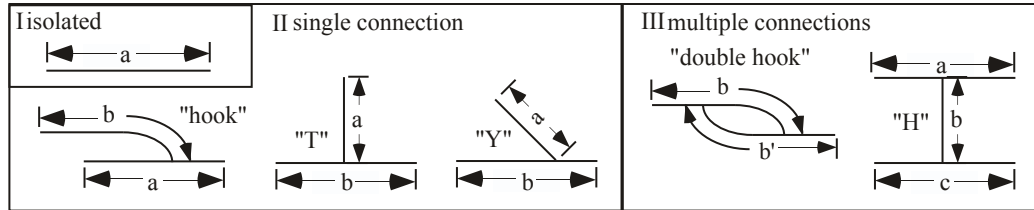
Isolated fracture length:

Isolated fractures have two free tips not connected with any other fracture in the observation domain. The length of isolated fractures is taken to be the distance between the fracture tips.

Fracture segment length:

All fracture branches of interconnected fractures were considered as separate fracture segments. The connection types observed were: II (hook, T- or Y-shape), III abc (H-shape), and III bb' (double hook) terminations (Ortega and Marrett, 2000, Fig. 2.4A). At each fracture connection up to three but generally two individual fracture segments were measured, with a tip at the connection point. If the termination is T-shaped then two segments were measured; the through-going fracture and the connecting fracture. If the connection is H-shaped, three segments were measured; the two through-going fractures and the bridging fracture between them. If fractures terminate in a double hook (Type III bb') then two segments were measured with tips at the connection points of the hook terminations.

A)



B)

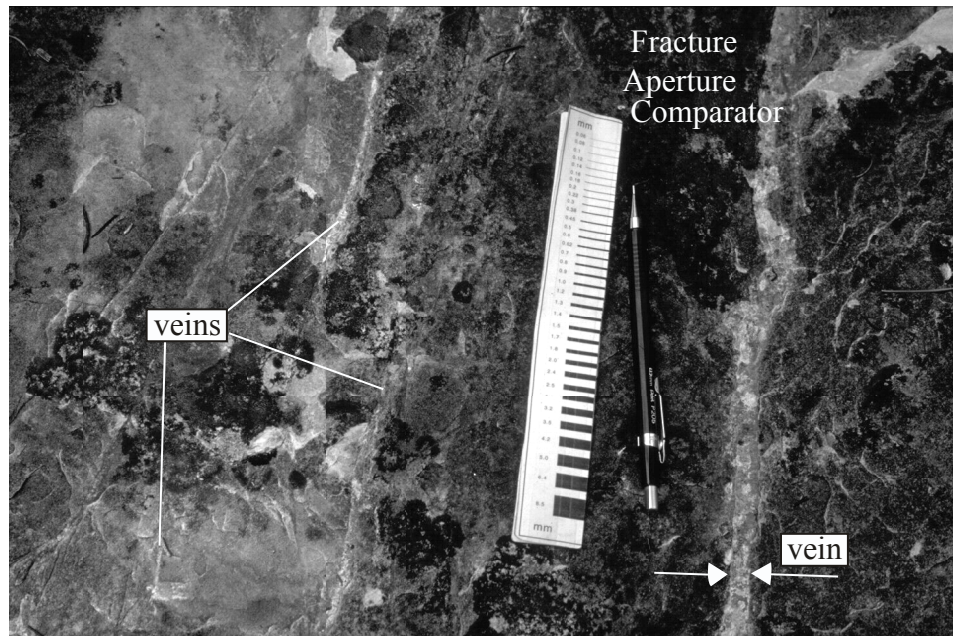


Figure 2.4. Fracture length and aperture measurement. A) Types of fracture connections observed in the field (modified from Ortega and Marrett, 2000). Individual fracture segments are indicated by letters, and fracture tips are indicated by fracture arrows. Total connected fractures length is the sum of fracture segments lengths. B) Fracture aperture comparator used to collect fracture size data from Weber sandstones. The narrowest line in the comparator is 60 mm wide and the widest is 5.5 mm. This tool allows effective collection of aperture data spanning two orders of magnitude in size.

Interconnected fracture length:

One method to measure interconnected fractures is to consider all branches of the network as separate fractures or fracture segments (see above). This method produces the greatest number of fracture length measurements and fracture lengths are minimized. A completely opposite method of measurement of interconnected fractures is to consider the length of interconnected fractures as the sum of all connected fracture segments visible at a given scale of observation. This method produces the least number of fracture length measurements and the fracture lengths are maximized.

Fracture length distributions from 637 m² of Weber Sandstone pavement at North Disappointment Draw were analyzed considering two contrasting methods to determine the length of interconnected fractures. First, all isolated fractures and fracture segments were measured; and second, all isolated fractures and interconnected fractures were analyzed. During fracture length measurement, only isolated fractures or fracture segment lengths were considered. The connected fracture segments were classified in the field and the fractures to which a fracture segment connects was also noted. This method allowed the calculation of the length of interconnected fracture groups as the sum of the lengths of fracture segments.

At South Disappointment pavement, fracture length data were collected at two scales of observation. A small portion of the pavement (914 m²) was selected to collect length data ranging in size from few centimeters to a few meters, and a large area (1654 m²) of the pavement was selected to collect fracture lengths

longer than one meter. All fractures shorter than one meter were ignored in the large area of the pavement.

Outcrop macrofracture aperture data

The literature contains only a few examples of opening-mode fracture aperture size distributions (Barton and Hsieh, 1989; Barton and Zoback, 1990; McCaffrey et al., 1994; Sanderson et al., 1994; Gross and Engelder, 1995; Belfield and Sovich, 1995; Clark et al., 1995; Marrett, 1997; Marrett and Laubach, 1997; Belfield, 1998; Ortega et al., 1998; Marrett et al., 1999; Gillespie et al., 2001). Fracture aperture size characterization has been a challenge because fracture apertures are difficult to measure with confidence in the field, especially without adequate measuring tools, and because many fracture studies have focused on *in situ* characterization of unmineralized fractures for which an estimate of the aperture may be problematic (Barton and Hsieh, 1989). During the course of this work new instruments for reliable aperture measurement in outcrops were developed (Fig. 2.4B). Measurement of fracture aperture using these tools is fast and accurate, allowing collection of abundant aperture data spanning several orders of magnitude, from tens of microns to tens of centimeters in size in the Weber Sandstone.

Two-dimensional sampling of fracture apertures in outcrops is difficult and time consuming. On one hand, the measurement of fracture aperture in two dimensions is non-trivial because the cross section morphology of fractures can be fairly complex, particularly where fractures interconnect (Vermilye and

Scholz, 1995; Moros, 1999). On the other hand, deciding what constitutes a single fracture where fractures interconnect also complicates the measurement of fracture aperture in two-dimensional domains. In contrast, fracture aperture measurement along scanlines is convenient because we can limit our measurement to the fractures that intercept the scanline, avoiding connectivity questions inherent to two-dimensional sampling.

The majority of well-exposed pavements in the study area are characterized by weathered fractures with small apertures. The fracture fill in most of these fractures at the upper pavement surface has been leached-out leaving a deep groove in the pavement, which is commonly filled with sediment and oxide cements. The measurement of fracture aperture in these areas is difficult but it is not believed to affect the form of the aperture distribution (Barton and Hsieh, 1989). Some areas on the pavements and along small canyons or streams in the study area were best suited for one-dimensional aperture data collection. In these areas fractures are filled with carbonate cements and their kinematic apertures can be measured with confidence. The kinematic aperture is the distance between the fracture walls measured perpendicular to the fracture.

Macrofracture apertures and spacing data were collected along scanlines forming high angle with fracture strike (Appendix 2.B). Scanline orientation was maintained constant but sometimes the presence of covered patches along the scanline trajectory obliged me to step-out. The scanlines at North and South Disappointment are composed of a series of scanline segments. Each successive scanline segment is added by following a long fracture along strike and selecting

an area where the scanline can continue with no covered areas. The scanline at Disappointment Gulch is composed of three long segments (1, 2, and 3), which sample different portions of the Weber Sandstone stratigraphy along a stream that cuts across Disappointment Draw Monocline. Disappointment Gulch scanline 1 samples the base of the Weber Sandstone, Disappointment Gulch scanline 2 samples the middle part, and the highest in the stratigraphy is Disappointment Gulch scanline 3. Skull Creek scanline is also composed of short parallel scanline segments. These segments do not follow a transect in a continuous succession but are a series of disconnected segments drawn on top of a small and well-exposed pavement.

Macrofracture apertures were measured by comparing their size to a comparator consisting of graduated line widths printed on a piece of paper (Fig. 2.4B). A 10X hand lens was necessary to measure the smallest apertures measurable with the tool (~60 microns wide). Fracture spacings were measured with tape measure and recorded along with fracture apertures (Appendix 2.B). Whether or not the beginning of the scanline was a fracture aperture was also annotated.

Subsurface macrofracture data

Two cores from Rangely Field were selected for subsurface fracture studies (Larson 15X B and Emerald 46X, Fig. 2.1, Table 2.2). The cores analyzed contain scribe knife orientation marks (Kulander et al., 1990), however, at the time of completion of this work no information on the orientation of the scribe

Table 2.2. Summary of Weber Formation core data, Rangely Field, Colorado. PSL: principal scribe knife line (Kulander et al., 1990), S: number of samples collected, ccw: counter clockwise.

Well	Core length S=samples	Samples for SEM-CL	Single notch orientation
Larson 15X B	701' (213 m) S=23	L15-5618C	90° from natural opening-mode mineralized macrofracture
		L15-5702.8	90° from natural opening-mode mineralized macrofracture
Emerald 46X	216.5' (66 m) S=5	WE46-5660.3	45° ccw from natural opening-mode mineralized macrofracture

marks had been found. Nevertheless, scribe marks in cores of Larson 15X B well were unreliable in most of the core due to frequent spin-offs, and ill-defined marks. Consequently, macrofracture orientation measurements were not attempted and only sketches were drawn for potential orientation if reliable scribe-knife orientation data becomes available.

Macrofracture data from cores were scarce due to the low probability of intercepting near vertical and sparse fractures with vertical wells. It is possible that macrofracture-sampling problems in Rangely Field hindered the integration of natural fracture attributes into the characterization of Weber sandstone reservoirs for decades of time (Larson, 1975; Hild and Wackowski, 1998).

An inventory of the fractures found along the core and samples collected can be found in Appendix 2.A. The depth of the macrofracture observation, morphology, attitude with respect to bedding, and strike with respect to the principal scribe knife line were recorded (if possible). The composition of the material filling the fractures was also recorded and a visual estimate of the degree of fracture fill was added to the description of each macrofracture observed in the core. Fractures without recognizable cement fill were also recorded and they were labeled as induced when a clear determination of their origin was possible (Kulander et al., 1990).

Microfracture data

Microfracture data come from analyses of digital SEM-CL photomicrograph collages of thin sections. Robert Reed (unpublished) collected

the SEM-CL photomicrographs, which were later assembled into collages and archived in digital media. SEM-CL can detect subtle changes in the degree of luminescence of quartz. Quartz cement often shows a different color or gray tone from quartz grains, revealing quartz-filled microfractures with unprecedented clarity (Laubach, 1997; Fig. 2.5). Details on sample preparation and operating procedures for SEM-CL work can be found in Milliken (1994) and Laubach (1997).

Samples analyzed for microfracture studies were collected from outcrops and subsurface cores (Table 2.3). There is a macrofracture (joint or vein) in every thin section imaged with SEM-CL. Fractures from outcrops are oriented in reference to true north and the single notch in the thin sections is parallel to the macrofracture trace. Orientation sketches were prepared, indicating the azimuth of single and double notches in the thin sections.

Two cores from Weber Formation reservoir in Rangely Field provided the samples necessary for microfracture characterization in the subsurface. Two kinds of thin sections were prepared from core samples: B-sections (perpendicular to bedding and perpendicular to fractures) were primarily used for petrographic analyses, C-sections (parallel with bedding and perpendicular to steeply dipping fractures) were intended for SEM-CL work but also used for petrographic studies. Four C-sections were selected for SEM-CL imaging and microfracture analyses.

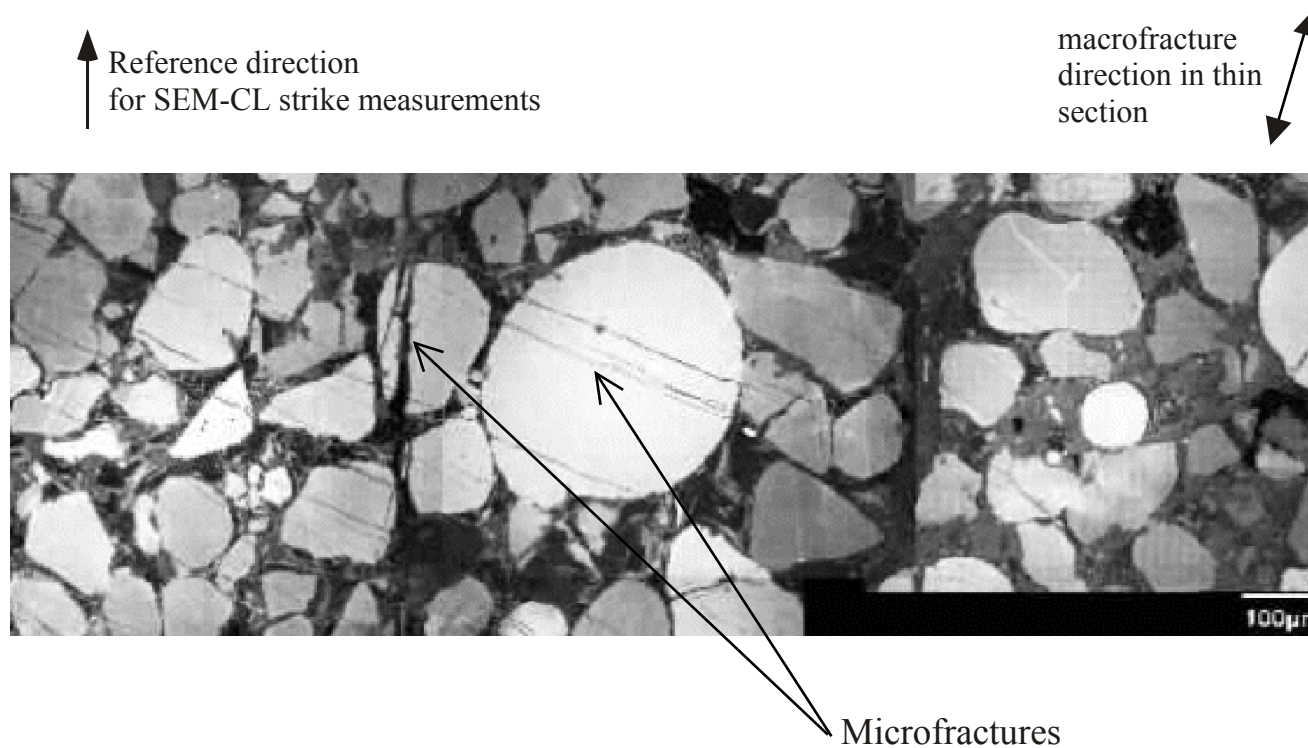


Figure 2.5. Portion of SEM-CL photomicrograph collage L15-5618c(43-54) showing transgranular microfractures that are invisible using conventional petrographic techniques. This photomicrograph collage represents about one square millimeter of a thin section cut from cores of Larsen-15X B well at a depth of 1712 m. If microfractures and macrofractures are different size fractions of the same fracture system, microfracture strikes could be used to predict macrofracture orientation without actually sampling the macrofractures (provided that the photomicrograph collage is oriented). Orientation of this collage is relative to a macrofracture present in the thin section and assumed to strike parallel to the dominant macrofracture strike in the area (Larson, 1975; Narr, unpublished).

Table 2.3 Summary of SEM-CL work on surface and subsurface Weber samples. SEM-CL imaging work by Robert Reed using SEM-CL equipment at the Department of Geological Sciences, The University of Texas at Austin.

Locality	Label (Fig. 2.1)	Samples	SEM-CL collages	Area (mm ²)
South Disappointment	B	w-043-97	w-043-97	4.36
North Disappointment	4	w-045-97	w-045-97	2.47
			w-045-97-2	3.15
Disappointment Gulch	3	w-036-97	w-036-97	4.97
			w-036-97a	1.5
			w-036-97b	0.85
Larsen 15X B	Larsen 15X	L15-5618C	L15-5618c(1-10)	3.55
			L15-5618c(43-54)	3.27
		L15-5702.8	L15-5702.8c	2.62
Emerald 46X	Emerald 46X	WE46-5660.3	we46-5660.3-1	1.23
			we46-5660.3-2	1.28

Criteria for SEM-CL thin section selection included good quality of thin section preparation, sandstone composition, features present in the thin section (e.g., presence of macrofractures) and thin section location within the reservoir (Table 2.2).

Four SEM-CL photomicrograph collages from the Larson 15X B well and two photomicrograph collages from the Emerald 46X well were selected for the characterization of microfractures and for macrofracture-property prediction in Rangely Field. Samples from the subsurface were oriented in reference to the strike of macrofractures observed in the cores or the principal scribe line where present. The single notch in subsurface thin sections is parallel the trace of the macrofracture used for orientation reference. Orientation of subsurface thin sections with respect to true north was not possible primarily because the scribe line orientation data for the cores were not available but also because bad quality of scribe knife marks in cores would have made orientation measurements largely unreliable in portions of the core.

Digital SEM-CL photomicrograph collages were interpreted in a commercial graphics package (Canvas 5TM) to produce microfracture trace maps (J. Hooker, unpublished, archives of the Bureau of Economic Geology, The University of Texas at Austin). Figure 2.6 shows an example of an SEM-CL photomicrograph collage and the fracture map derived from it. Microfractures were digitized using four sided polygons such that the vertices of the polygons correspond to the tips and maximum aperture of the microfracture. The coordinates of these four points can be used to obtain fracture length, aperture,

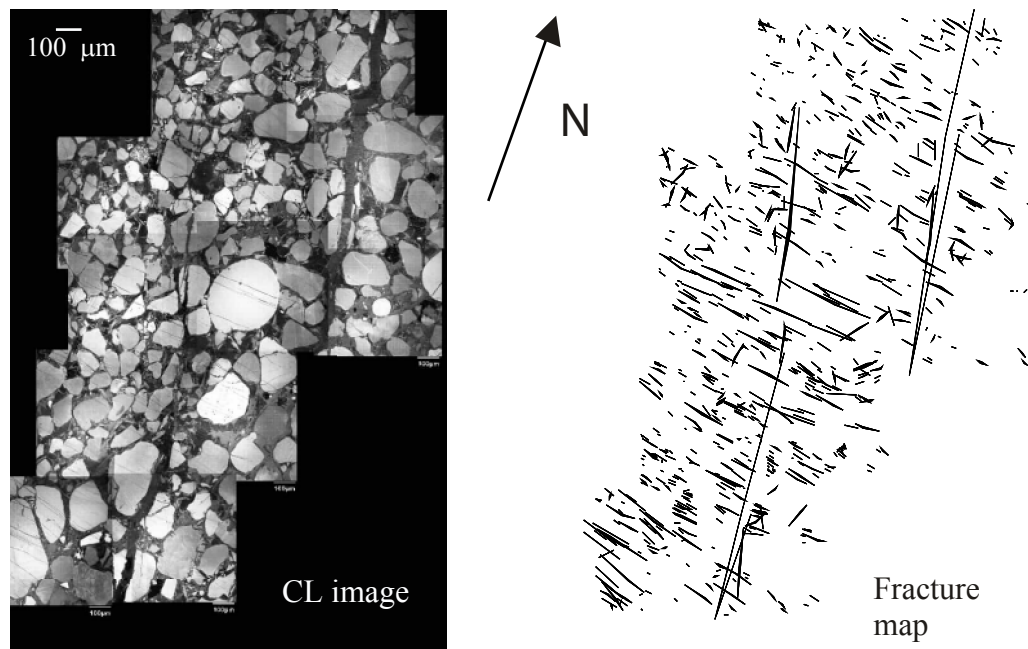


Figure 2.6. SEM-CL photomicrograph collage L15-5618c(43-54) and fracture map from Larson 15X B well thin section at 1712 m depth. This photomicrograph collage covers approximately 4.5 mm² of the thin section.

and orientation by applying simple trigonometric formulas. The coordinates of the polygon vertices were exported in IGES format (Initial Graphics Exchange Specification) from the digitization software for ulterior analyses of microfracture orientation and size distributions.

Resolution tests using the fracture digitization program suggest that microfracture aperture determination from SEM-CL collages is reproducible to fractions of a micron at a magnification of 200X but varies with the magnification used for photomicrograph collection. Interpretation of microfracture length in SEM-CL images can be problematic because the quartz filling microfractures and quartz overgrowths often show similar luminescence. In some cases, microfractures follow the borders of grains and are indistinguishable from grain overgrowths. In other cases, microfractures terminate abruptly in a pore and their possible continuation on the other side of the pore is questionable (Ortega and Marrett, 2000).

Another important aspect of microfracture interpretation is related to a necessary separation of microfracture populations according to their possible relationship with macrofractures present in the rock. Interpretation of the suitability of microfractures (Laubach, 1997; Ortega and Marrett, 2000) as proxies of macrofractures is important because some microfractures observed in SEM-CL images form by processes that do not generate macrofractures (e.g., grain to grain interactions). Laubach (1997) described the criteria that distinguish post-depositional microfractures (microfractures that formed after sediment deposition) from inherited microfractures (microfractures predating grain deposition).

Laubach (1997) also proposed criteria to distinguish microfractures most probably related to macrofractures in the same rock volume from microfractures formed by grain-to-grain interaction during compaction. In the Laubach (1997) classification, transgranular and transcement microfractures are the most reliable for microstructural analysis aimed to unravel macrofracture attributes. However, transgranular and transcement fractures are less abundant than grain-restricted fractures, and in some low fracture intensity rocks large numbers of SEM-CL photomicrographs must be collected before encountering significant numbers of transgranular microfractures. In those cases, similarities in microfracture orientation, morphology, and microfracture cement luminescence can be used to refine the classification of grain-restricted microfractures increasing or decreasing their suitability as proxies of macrofractures. Ortega and Marrett (2000) gave an example of the application of a suitability classification of microfractures for length scaling studies in Mesaverde Group sandstones.

Digitized microfractures were classified and separated into groups of microfractures most probably related to macrofractures, microfractures associated with grain-scale interaction processes, and inherited microfractures (Hooker and Ortega, Fracture Research and Application Consortium, Bureau of Economic Geology, The University of Texas at Austin). IGES files containing the coordinates of the vertices of the four sided polygons were then used as input for C⁺⁺ programs that calculate the microfracture lengths, apertures, tip-to-tip orientations, and lengths and orientations of each side of the polygon that represents the microfracture. Other programs use these data to generate rose

diagrams and to separate microfractures into microfracture sets for fracture size distribution analyses (Appendix 4.A).

Analysis of fracture size distributions

The relative abundance of fracture lengths of different sizes was analyzed using probability distributions (Swan and Sandilands, 1995). The discrete fracture size distribution is a histogram of the frequency of fractures having sizes within a given range (Bonnet et al., 2001; Gillespie et al., 2001). Cumulative size distributions can be obtained by accumulation of length frequencies starting with the largest fracture and progressively adding smaller-size fracture frequencies. Cumulative length distributions obtained by progressive addition of smaller fracture size ranges of the discrete fracture size distribution yield a graph of the observed frequency of fractures of a given size or larger. A mathematically more amenable form of the cumulative number of fracture sizes can be obtained by eliminating the restrictions imposed by binning. This is achieved by sorting the fractures from the largest to the smallest, and numbering them progressively starting with the largest.

The cumulative size distribution can be analyzed graphically using combinations of linear and non-linear axes. Some fracture size distributions have been reported to follow exponential (Snow, 1970; Baecher and Lanney, 1978; Rouleau and Gale, 1985; Priest and Hudson, 1981), or lognormal distributions (Baecher et al., 1977; Baecher and Lanney, 1978; Rouleau and Gale, 1985; Ledècert et al., 1993; Gillespie et al., 2001). Figures and photographs included in

these papers suggest that these authors studied open fractures, with small aperture/length ratio, and spanning the mechanical layer thickness (e.g. surface-related joints), although in some of these studies it is unclear the type of fracture measured. On the other hand, the majority of size distributions reported for veins are interpreted as power law distributions (Appendix 1.A). Power law distributions fall along straight lines if plotted in log-log graphs. The exponent of the power law distribution is the slope of the line in the log-log graph and the power law coefficient is the intercept of the line with a fracture size of 1. The power law exponent gives a measure of the relative proportions of small versus large fractures. A high exponent indicates that there are many small fractures in proportion to large fractures. The power law coefficient indicates the abundance of fractures of a unit size or larger in the observation domain, and is a measure of fracture abundance (i.e., density or intensity) if it is normalized by the size of the observation domain. Cumulative frequency distributions are obtained by normalizing the cumulative number distribution by the size of the observation domain. Cumulative frequency values for a given fracture size can be used to compare fracture intensities from different observation domains.

Although power laws are the best models for mineralized fracture size distributions reported in the literature, the distributions typically show departures from a line in a log-log graph at the small- and large-scale sizes. Departures at the small-scale range of fracture sizes have been interpreted as a result of a progressive loss of completeness in sampling near resolution limit (Segall and Pollard, 1983; Rouleau and Gale, 1985; Huang and Angelier, 1989; Barton and

Zoback, 1990; Pickering et al., 1995; Gross and Engelder, 1995; Odling, 1997; Ortega and Marrett, 2000). Departures at the largest fracture sizes have been attributed to a number of sampling effects that include: censoring (i.e., impossibility of measuring accurate lengths for fractures that extend beyond the limits of the observation domain, Baecher, 1980; Priest and Hudson, 1981; Laslett, 1982; Rouleau and Gale, 1985; Barton and Hsieh, 1989; Barton and Zoback, 1990; Pickering et al., 1995; Odling, 1997), topologic effects (i.e., effective sampling in spatial dimensions different from the dimension of the observation domain, Baecher et al., 1977; Baecher and Lanney, 1978; Warburton, 1980; Marrett, 1996; Berkowitz and Adler, 1998; Gillespie et al., 1999; Ortega and Marrett, 2000; Borgos et al., 2000), finite size effects (i.e., result of integration of discrete power law distributions over finite-size observation domain, Pickering et al., 1995; Bonnet et al., 2001; Burroughs and Tebbens, 2001), other possible effects of finite layer thickness (Hatton et al., 1994; Ortega and Marrett, 2000), and fracture spatial distribution effects (Borgos et al., 2000; Bonnet et al., 2001).

The underlying power law distribution must be extracted from these biased distributions in order to quantitatively describe the size distribution of fractures. Most authors have traditionally selected the linear portion in the middle of the fracture size distribution in log-log plots to obtain the underlying power law from biased distributions. This approach is sometimes justified because the limits of the biased portion of the power law distribution cannot be objectively determined (Main et al., 1999). Ortega and Marrett (2000) proposed a method to

analyze the departure of the fracture size distribution from an ideal power law assuming that the biased portion at both sides of the power law distribution follow an exponential law. Marrett (2000) developed a bias model that assumes that the deviations of the power law distribution at the large and small-scale ends asymptotically approach values in the ordinate and abscissa. Marrett (2000) wrote an ExcelTM program to calculate the parameters of underlying power law distribution with a minimum of 11 data points. Another methodology was proposed by Burroughs and Tebbens (2001) to analyze upper truncated power laws distributions produced by the finite integration of discrete size distributions. In this work we have used Marrett (2000) bias model to obtain the parameters of the underlying power law distribution in most cases. However, in some cases the bias model did not converged and linear segment(s) of the size distribution were subjectively chosen to obtain the power law model for those distributions.

Sedimentary facies and diagenesis data

It is beyond the scope of this work to investigate in detail the sedimentary and diagenetic characteristics of surface and subsurface Weber Formation sandstones. I have used previous observations and interpretations to set the fracture systems studied in sedimentary and diagenetic contexts. Data on Weber Formation sedimentary facies and diagenetic processes were obtained primarily from the literature and complemented with information collected from outcrop and subsurface samples (Appendix 2.A). Important contributions to the understanding of sedimentary facies distribution and diagenetic history in Weber

sandstones were made by Fryberger (1979), Fryberger and Koelmel (1986), and Bowker and Jackson (1989). Fryberger (1979) described in detail the sedimentary facies in Weber Formation sandstones from outcrops and subsurface. Fryberger's (1979) stratigraphic columns for North Disappointment area and the Larson 15 X B well are the basis for the stratigraphic and sedimentary facies information used here.

Samples collected in the field and from cores were sent for conventional and special thin section preparation for SEM-CL imaging. Petrographic descriptions and point counting were done in these samples (Laubach and Schwartz, 1998 unpublished, Appendix 2.A). Petrographic descriptions are succinct but confirmed compositional, textural, and diagenetic information obtained from the literature. Point counting techniques were aimed to address specific questions about the cement phases present in the rock and their proportions, regional variations, porosity, macro- and microfracture fill. The quality of the thin sections for microfracture SEM-CL imaging was also evaluated. Currently, Kitty Milliken (The University of Texas at Austin) leads a thorough petrographic and compositional investigation of Weber Formation sandstones with emphasis on the understanding of ankerite cement distribution and geologic controls on ankerite precipitation.

Fracture quality data

Fracture quality assessment is an empirical method that allows an estimation of the degree to which macrofractures in the rock volume might be

mineral filled or open (Laubach et al., 2000; Laubach, unpublished). The method is based on the assumption that fracture porosity is only one part of the total pore system in the rock and that cement precipitation in pores and in the fractures. The method also assumes that there are no significant differences in the velocity of cement precipitation in the pores of the matrix and the fractures.

Fracture quality determination is quantified with the degradation index (Laubach, 2000). In order to calculate the degradation index it is important to distinguish the timing of cement precipitation relative to fracture opening. According to this timing relationship, cement can be classified as prekinematic, synkinematic and postkinematic (Laubach, 1988; Laubach et al., 1995; Marrett and Laubach, 1997). Prekinematic cements precipitated before fractures formed and are not important for fracture quality determination. However, their occurrence and abundance may determine important mechanical properties of the rock undergoing fracturing. Synkinematic cements precipitated while fractures were propagating (Laubach et al., 1995). These cements can be distinguished because they often line fracture walls and record crack-seal structures (Laubach, 1988; Laubach et al., 1995). Quartz is commonly synkinematic in sandstones (Laubach, 1997), and has the tendency to preserve macrofracture porosity by forming wall-to-wall pillars or bridges. Small-scale fractures are generally filled with synkinematic cement (Laubach 1997; Ortega and Marrett, 2000), and the cement phase filling microfractures can be used to identify synkinematic cements from postkinematic cements without direct observation of macrofractures.

Postkinematic cement precipitated after fractures propagated. Carbonate cements in sandstones tend to be postkinematic (Laubach, 1988; Clift et al., 1997; Laubach 1998, personal communication). Carbonate cements in fractures commonly include calcite, ferroan calcite, and ankerite. Postkinematic cement is generally absent in micron-wide microfractures because these fractures are already sealed by synkinematic cement, but postkinematic cement is found in pores of the rock matrix and in macrofractures. Where observations of macrofracture fill is possible, postkinematic cements precipitate as massive, coarse crystals in the residual fracture porosity left by synkinematic cementation (Laubach, 1988; Laubach et al., 1995). Occasionally, little synkinematic cement is visible in the fractures and fractures are completely filled with postkinematic cement. In these rare cases, it is possible that fluid pressure kept the fracture open during massive post-kinematic cementation.

The degradation index (D) is the ratio of postkinematic cement volume (O) to total pore volume before postkinematic cement precipitation (i.e., the sum of postkinematic cement volume and current porosity (P) volume). This ratio is a measure of pore occlusion by cement phases precipitated after fractures propagated and synkinematic cement precipitated. The formula for degradation is:

$$D = \frac{O}{O + P} \times 100\% \quad (\text{Laubach et al., 2000})$$

The fracture quality estimator assumes that current porosity has not been enhanced by dissolution postdating postkinematic cement. However, if dissolution occurred after postkinematic cement precipitation and dissolution selectively

affected framework grains, this portion of the total porosity should be excluded from the degradation index. If the dissolution affected cement phases precipitated in fractures, no porosity correction is necessary.

Fracture quality data were derived from conventional petrographic point counting of thin sections from Larson 15X B well cores (Laubach and Schwartz, unpublished, Appendix 2.A). Porosity, synkinematic and postkinematic cement proportions were the focus of the thin section point counting procedure. Thin sections were stained for identification of carbonate cement phases. Alizarine red allows the distinction of calcite and dolomite. Potassium ferrocyanide allows the identification of calcite, ferroan calcite, and ankerite. Quartz cement proportion is difficult to determine because quartz cement is typically in the form of overgrowths in optical continuity with grains. However, quartz cement proportion is rarely part of the equation for degradation index calculation because quartz tends to be synkinematic in sandstones (Laubach et al., 1995). The exact reasons why quartz cement is generally synkinematic is still an open question. It is possible that fracture propagation creates fresh quartz surface area and produces changes in fluid pressure/temperature in the rock that promote quartz precipitation along fracture walls from silica-saturated water in subsurface sandstones.

According to fracture mechanics principles, longer fractures will tend to propagate and increase in aperture faster than smaller fractures (Griffith, 1920; Atkinson and Meredith, 1987). If synkinematic precipitation velocity is similar in all pores, then small fractures will tend to be filled by synkinematic cement whereas large fractures may contain proportionally less synkinematic cement.

These predictions have been qualitatively corroborated by visual inspection of fracture porosity in numerous sandstone units (Laubach, 1997; Ortega and Marrett, 2000; Chapter 1 of this work, Laubach personal communication). These observations are also the expected outcome of quartz precipitation models (Lander and Walderhaug, 1999), and indicate that there is a size threshold above which fractures preserve porosity (emergent threshold, Laubach, 1999). A qualitative estimate of the emergent threshold can be made by collecting data on fracture aperture and quantifying the proportion of remnant porosity and postkinematic cement in the fracture. If macrofractures are not available to make this estimation, the average diameter of pores in the matrix retaining porosity before precipitation of postkinematic cements may be used as surrogates of the emergent threshold value in fractures. Models of quartz precipitation (e.g., Lander and Walderhaug, 1999) in fractures promise the possibility of a predictive determination of the emergent threshold in sandstones.

Mechanical layer thickness data

Mechanical stratigraphy is revealed by systematic terminations of fractures at certain stratigraphic surfaces (e.g., Corbett et al, 1987; Becker and Gross, 1996; Ortega and Marrett, 2000; Wilkins and Gross, in press). The boundaries of mechanical stratigraphic units commonly separate volumes of rock with different fracture intensity (Corbett, 1987; Wilkins and Gross, in press). Mudstones are typically good mechanical stratigraphy bounding units, however, changes in mineralogy or texture, interruptions in sedimentation, and sedimentary

structures in beds can also produce mechanical boundaries (Ortega and Marrett, 2000). To date there are no models that predict mechanical stratigraphy based on rock attributes. Direct observation of fracture terminations at certain stratigraphic horizons is necessary for accurate mechanical thickness determinations. Wilkins and Gross (in press) indicate that changes in lithology do not necessarily correlate with mechanical layer boundaries. However, if direct observations of the mechanical stratigraphy of an area are not possible, changes in lithology separating packages of sedimentary layers with relatively homogeneous lithology can be used as a first approach to a mechanical stratigraphic model. Determination of fracture intensity variations in these units may further support the initial mechanical stratigraphic model or provide information to adjust it.

The Weber Formation is a thick stratigraphic unit (up to 400 m thick in the study area) that appears homogeneous in outcrops at Dinosaur National Monument and adjacent areas. However, closer inspection of the sedimentary succession reveals numerous heterogeneous sedimentary bodies often separated by diastems (Fryberger, 1979). Observation of systematic fracture terminations at stratigraphic surfaces in Weber Formation sandstones along canyons in the study area permitted defining an outcrop-scale mechanical stratigraphy for the fracture data collected at North Disappointment, South Disappointment and Skull Creek localities (Table 2.1). A regional-scale first-order approximation of mechanical stratigraphy in the study area was also obtained combining regional stratigraphic studies (Geldon, 1986; Koelmel, 1986) and well log correlations of Weber sandstones at Rangely Field (Bowker and Jackson, 1989).

RESULTS -OUTCROP

Seven localities in the study area were selected for outcrop fracture characterization (Fig. 2-1). In addition to characterizing fracture attributes at these localities, outcrops were also used as a testing ground of the hypothesis that microstructural information can be used for macrofracture prediction. Successful results of these tests were the basis for applying the same techniques to subsurface fractures in Rangely Field. Fractures in outcrops of Weber sandstone were evaluated as potential analogues for subsurface fracture systems at Rangely field. However, stratigraphic and diagenetic history variations do not allow direct application of outcrop results to subsurface conditions. Locally derived data are necessary for fracture system characterization in subsurface.

Outcrop fracture orientations

Figure 2.7 shows the results of macrofracture strike measurements in the study area. Fracture strikes in Figure 2.7 are biased at some localities by the trend of the scanline selected for measurement (Mauldon et al., 2001). For example, fractures striking perpendicular to the trend of a scanline are preferentially encountered and appear as the dominant set in rose diagrams. Orientation data from two-dimensional observation areas are also biased because the shape of the observation domain was chosen to enhance sampling of a fracture set of interest. Consequently, in the rose diagrams of Figure 2.7 the dominant fracture strike is apparent. For example, NW striking fractures were chosen for detailed fracture

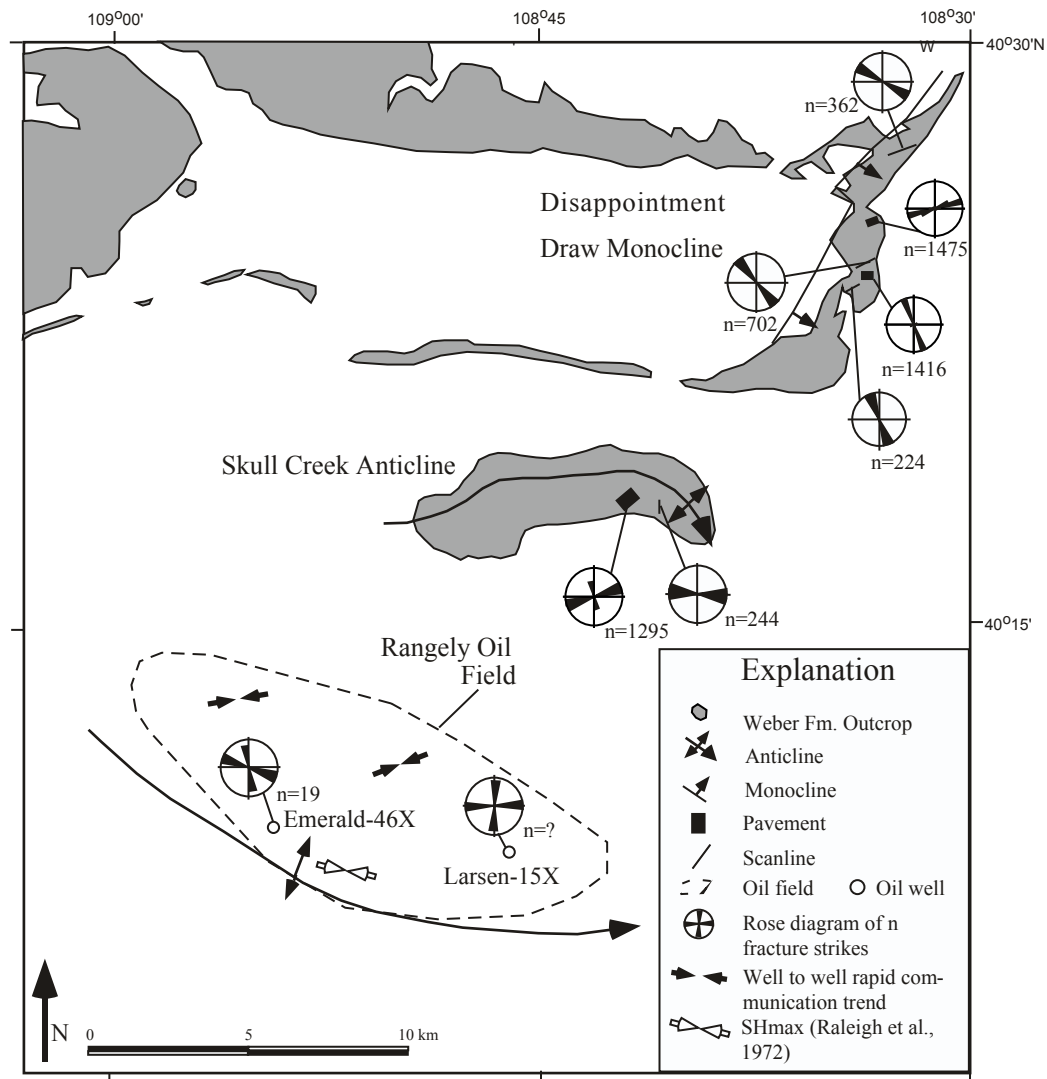


Figure 2.7. Macrofracture orientations in study area. Symbol on map indicates the kind of data collection: from pavements, scanlines, observation stations (solid circles), and subsurface methods (Courtesy of Chevron; Narr, unpublished). Rose diagrams are divided in 10 degree increments. At least one of two fracture sets are present in all localities: ENE-ESE and NW-NNW (See Table 2.1 for localities names, pavement areas, scanline lengths, and observation domain orientations). SHmax: maximum horizontal stress.

size studies in Disappointment South pavement and the rose diagram obtained reflects this orientation as dominant in this pavement. However, highly clustered, fractures in South Disappointment pavement strike NE as distinguished in aerial views, maps (Hansen et al., 1983), and in the field.

Outcrop macrofracture strike results suggest that there are two main fracture sets present in the study area: one set striking ENE-ESE is dominant and another set striking NW-NNW is secondary (Fig. 2.7). Sets with similar orientations have been documented by Wilkins et al. (2001) and Silliphant et al. (2002) in fracture studies of units younger than the Weber Formation in Split Mountain Anticline, Dinosaur National Monument, Utah, approximately 20 km to the northwest of Dinosaur, Colorado.

Outcrop fracture size distributions

Outcrop aperture distributions

Fracture aperture data collected along scanlines at four different localities in outcrops of the Weber Formation suggest that the cumulative frequency of fractures of a given size or larger follow power-law scaling. The fracture aperture distribution obtained for North Disappointment scanline suggests that a power law scaling is the best model for this distribution, which spans four orders of magnitude in size (Fig. 2.8). The largest fracture sampled along this scanline more than 200 m long, has a kinematic aperture of 1 m and is filled with carbonate cement. The maximum aperture observed in this fracture is close to 2 m and the

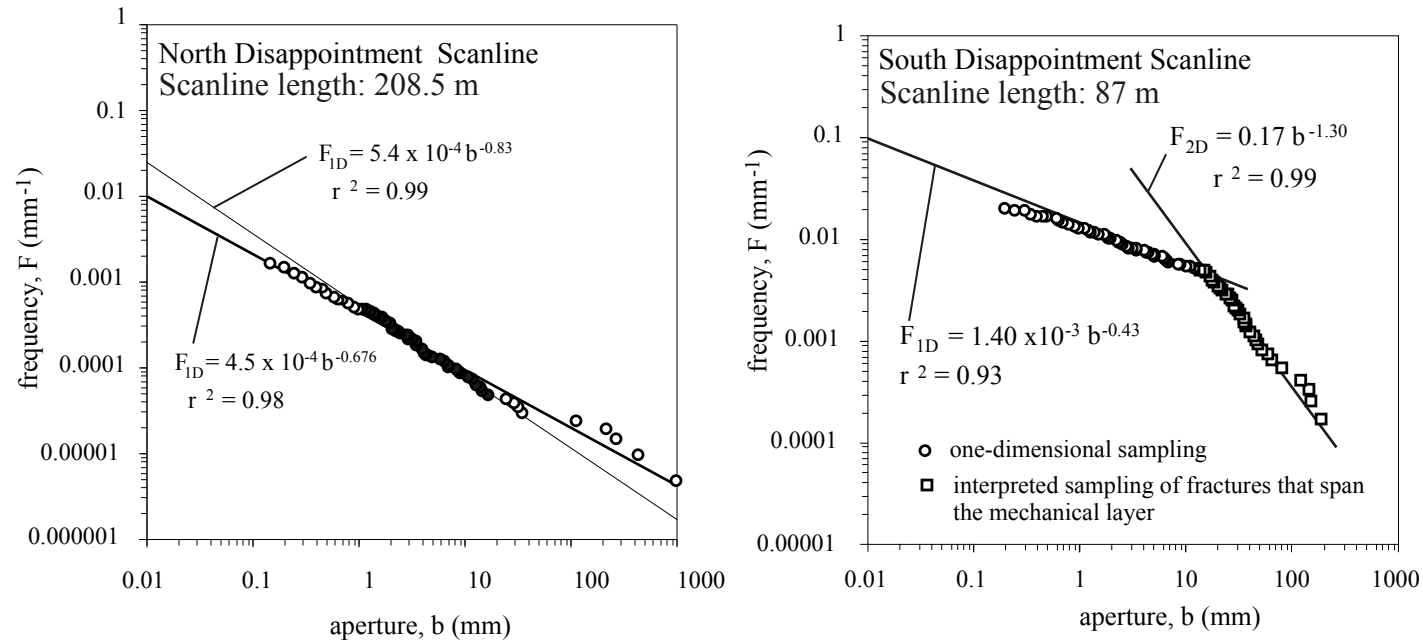


Figure 2.8. Fracture aperture distributions from scanlines in Disappointment Draw area. Two power-law models are shown for North Disappointment scanline data: a bias model regression (heavy line; Marrett, 2000) adequately models the observations for nearly four orders of magnitude in size, the second model is based on selection of the linear segment in the middle of the graph (solid circles). The second model suggests that sampling artifacts affect the small and large scale ends of the distribution. The aperture distribution for South Disappointment scanline shows a sharp change in slope for apertures larger than approximately 15 mm. A bias model regression was used for the entire distribution and adequately fits the low slope portion of the distribution. A power law regression to selected data (squares) fits the steep portion of the distribution. Sampling topology changes (Marrett, 1996) might explain the increase in slope of this portion of the power law distribution.

fracture trace can be followed for approximately 1 km (Marrett and Laubach, personal communication). Other large-aperture fractures were scarce along the scanline but some fractures with apertures of hundreds of millimeters were encountered along the scanline, supporting the idea that the power law distribution may extend up to those scales of observation.

Two power law segments best explain the fracture aperture distribution from South Disappointment scanline (Fig. 2.8). In South Disappointment scanline a bias model fits the majority of small fractures up to a scale of 15 mm aperture, and fractures larger than 15 mm aperture are best modeled by a power law with a steeper slope (i.e., larger absolute magnitude of the power law exponent). The bias power law model yields the best possible coefficient of determination for the distribution observed ($r^2=0.93$, Marrett, 2000). Sampling effects (e.g., topologic sampling artifacts) is the preferred explanation for the change in slope obtained for the large-scale fractures in this distribution. However, finite range artifacts (Pickering et al., 1995; Bonnet et al., 2001), and spatial distribution artifacts (Borgos et al., 2000) could be contributing to the deviation of the distribution from a single power law model in the range of aperture sizes measured. The exponent of the large aperture portion of the power law distribution is -1.3 and the exponent of the bias power law distribution of smaller aperture fractures is -0.43 . These exponents are consistent with sampling in two-dimensional and one-dimensional domains respectively and are in the range commonly observed for fracture size distributions (Bonnet et al., 2001).

The fracture aperture distribution obtained from Disappointment Gulch scanline 1 (Fig. 2.9) can be interpreted as a combination of two power laws, one fitting the small-scale fractures and another power law fitting large scale fractures with a steeper slope in the size distribution (not shown in Fig. 2.9). A dual power law model yields coefficients of determination above 0.97. An exponential regression to all the distribution does not account for the smallest and largest apertures observed and yielded a smaller coefficient of determination (0.86) than power law models (not shown in Fig. 2.9). Another possibility is to model this distribution with a single power law affected by sampling artifacts at the small- and/or large-scale ends of the distribution. A selection of the data in the rectilinear segment in the middle of this power law distribution yields a power law model with an exponent of -0.94 and a coefficient of determination $r^2=0.99$. The exponent of this power-law model is in the range of commonly observed one-dimensionally sampled size distributions (Bonnet et al., 2001) and the coefficient of determination of this model is high, however the selection of the data for the power law regression is somewhat subjective and biased by the behavior of other size distributions published affected by sampling artifacts at the large and small scale ends of the distribution. Finally, a bias model regression suggests a power law with a exponent of -1.36 , which visually makes a good fit to the largest fractures and yields a coefficient of determination $r^2=0.99$.

Fracture aperture distributions from two other scanlines along Disappointment Gulch were also modeled using a bias model function (Fig 2.10). The bias models make a good visual fit to the largest fractures in the distribution,

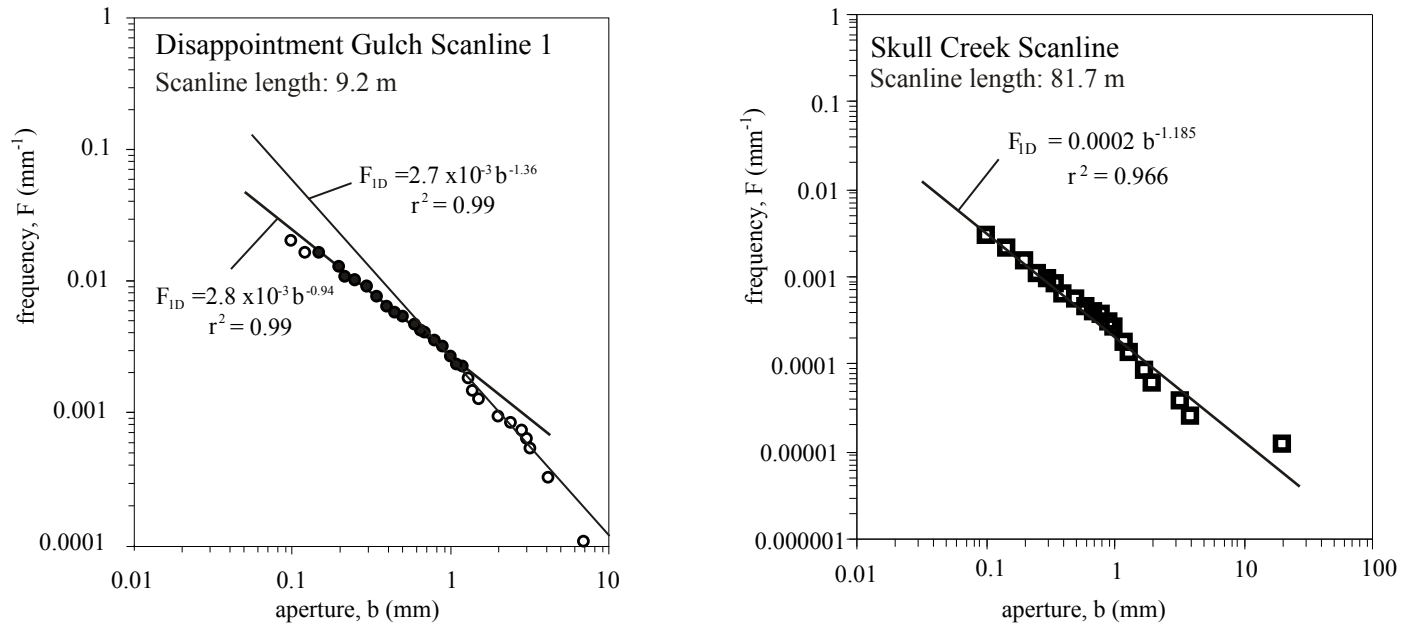


Figure 2.9. Fracture aperture distributions from scanline data at Disappointment Gulch scanline 1 and Skull Creek areas. Both distributions are best explained by power laws spanning approximately an order of magnitude variation in fracture aperture. A bias power law regression model (Marrett, 2000) for Disappointment Gulch scanline 1 data yields an exponent of -1.36. Selection of the linear middle portion of the distribution (solid dots) suggests a lower exponent and sampling artifacts at the small- and large-size ends of the distribution. The aperture size distribution from Skull Creek comes from data collected along multiple disconnected scanlines drawn perpendicular to the dominant set of fractures. Sampling artifacts might be affecting the large scale end of this distribution.

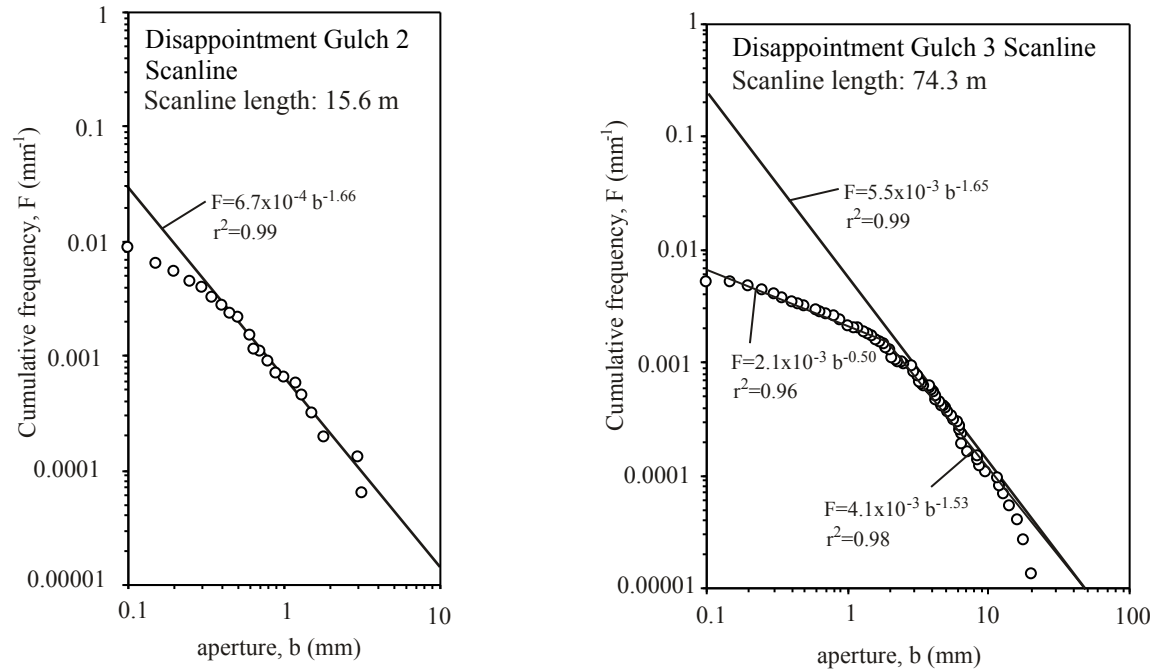


Figure 2.10. Fracture aperture distributions from scanlines 2 and 3 in Disappointment Gulch. Bias model regressions (Marrett, 2000) have been fit to both distributions (heavy lines) yielding power laws with exponents -1.66 and -1.65. Larger and smaller fractures deviate from an ideal power law and may represent sampling artifacts. The aperture distribution from Disappointment Gulch 3 scanline has also been interpreted as composed of two power law segments with exponents -0.50 and -1.53.

similar to the bias model applied to the first scanline in the Disappointment Gulch area. The bias model regression applied to these data suggests an exponent of approximately -1.65 for both distributions. However, the power law model for scanline 2 (middle section of Weber Formation) has a lower power law coefficient than the coefficients of the power law models for scanlines 1 and 3.

Finally, the fracture aperture distribution from multiple parallel scanlines drawn on the top of Skull Creek pavement (Fig. 2.9) produced a power law distribution with a exponent of -1.185 . The scanline segments used to generate this distribution were not collected along a transect like other one-dimensional data shown, but rather the scanlines are multiple parallel segments covering the entire pavement surface. This kind of sampling produces a pseudo-two-dimensional sampling effect for large fracture sizes, some of which may be sampled more than one time in multiple parallel scanline segments (Ortega and Marrett, 2000).

Outcrop length distributions

Fracture length distributions obtained from pavements in the study area were modeled by power law and exponential functions (Fig. 2.11). Neither the power law model nor the exponential model reproduce the observations. Pickering et al. (1995) provided explanations for the departures of fracture length distributions from an ideal power law (see the section above on “Analysis of Fracture Size Data” for references to sampling artifacts). A bias model regression

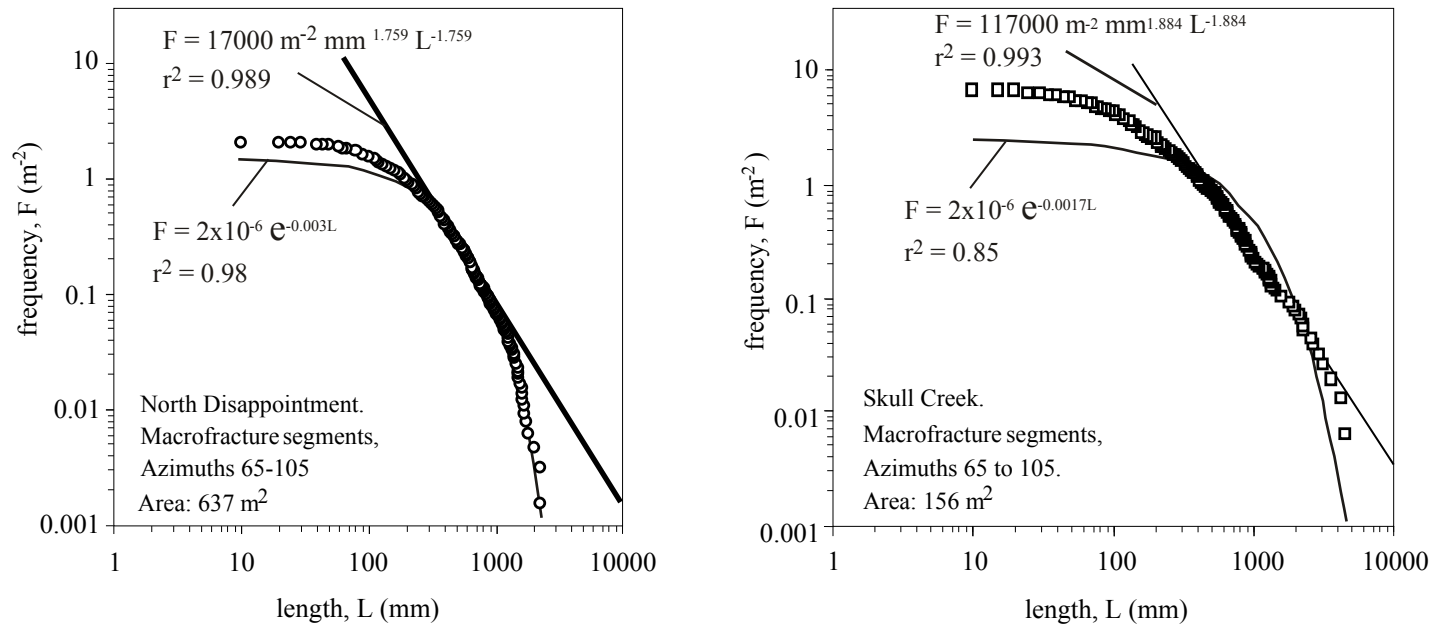


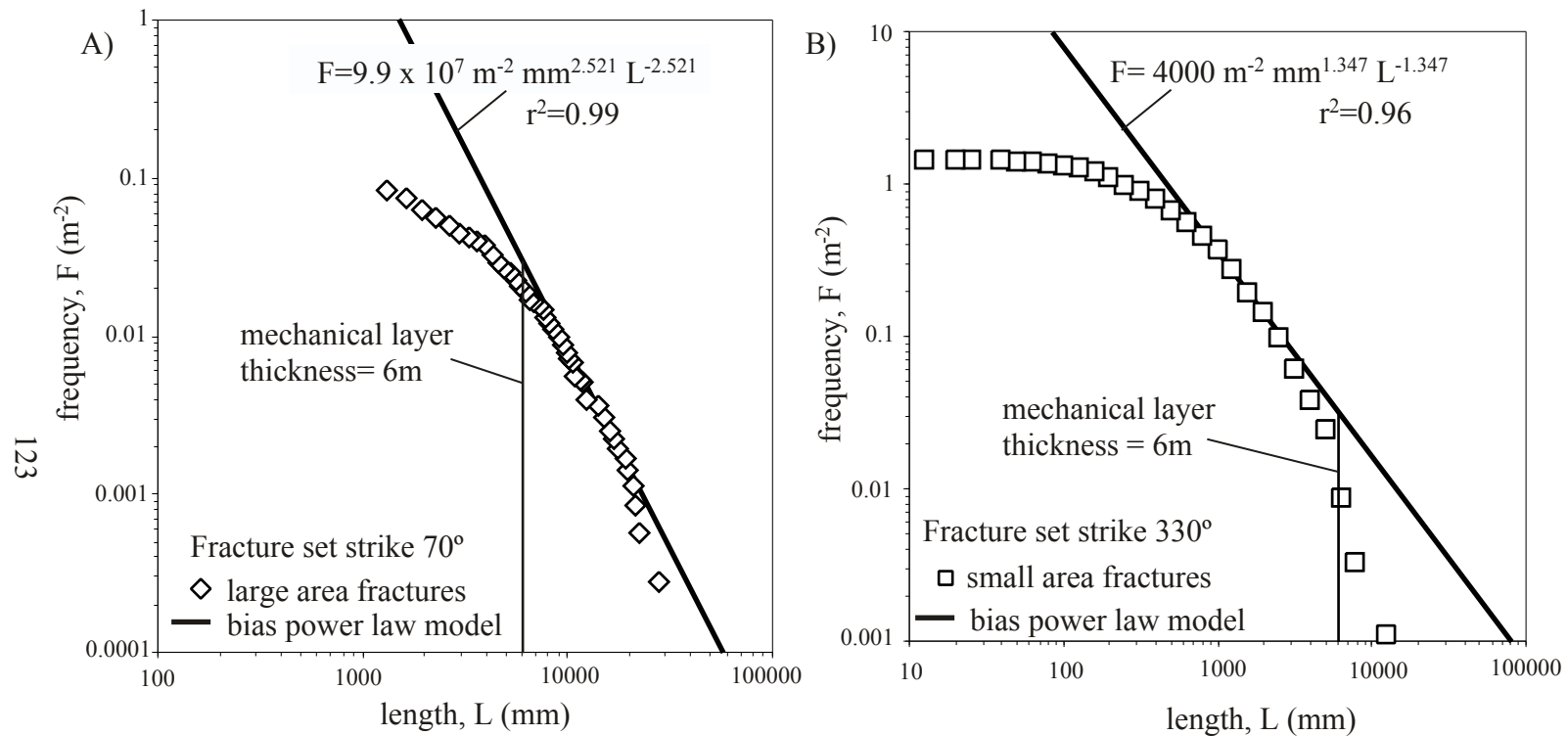
Figure 2.11. Length distributions for ENE striking fractures at North Disappointment and Skull Creek pavements. Thick line represents power-law bias model fit to the distributions. Note that the coefficient of determination is high in both cases. Exponential law fit to all data provides a good model for North Disappointment data, however it fails to account for small fractures observed. Exponential model is not adequate for Skull Creek data. Power-law model is considered a better model for these distributions because sampling artifacts probably caused the departures from power-law models at small and large scales ends of the distribution.

was applied to the length distributions in Figure 2.11 to obtain the underlying power law unaffected by sampling artifacts (Marrett, 2000). The bias power law regressions suggest that true fracture abundance has been underestimated at small and large scales of observation. Exponential models, on the other hand, underestimate the number of the smallest and largest fractures already observed and were considered inadequate models for the length distributions obtained.

Test of topology effect on large-scale end of length distributions

Marrett (1996) derived the formulae for two-dimensional and one-dimensional sampling of a three-dimensional power law fracture size distribution. However, Marrett's (1996) formulas do not take into account other sampling artifacts that may affect the size distributions. For example, Borgos et al. (2000) suggest that Marrett's (1996) formulas are not necessarily applicable to clustered fracture systems. Fracture length data covering the length scale of the estimated mechanical layer in one of the pavements were used to test the effect of the mechanical boundary on the length distributions observed.

Figure 2.12 shows the fracture length distribution for the fracture set with an average strike of 70° (dominant set) in South Disappointment pavement. Only fractures longer than one meter were measured in this area of 3558 m^2 . Also in Figure 2.12 is the fracture length distribution for all macrofractures of the set with an average strike of 330° (cross set) visible with the naked eye and measured from a small observation area of 1654 m^2 . This is a cross set to the dominant set in the area. In both areas, an effort was made to choose an observation domain that



contains the entire lengths of fractures of interest. Choosing such an area in the pavements minimized censoring artifacts on the length distribution (Baecher et al., 1997; Barton and Hsieh, 1989; Barton and Zoback, 1992). Truncation artifacts were minimized in the large observation area by choosing a fracture size that is clearly visible with the naked eye. Truncation artifacts were not avoided in the small observation area.

The thickness of the bed where fractures were measured is approximately 6 m. For penny-shaped fractures with diameters equal to or larger than 6 m there should be a topologic effect in any layer-parallel two-dimensional slice of the rock host. Topologic effects are expected to produce an increase in the slope of the fracture size distribution, because all fractures having length greater than 6 m in the volume covered by the pavement will be sampled and the fractures will effectively have been sampled in three dimensions (Marrett, 1996). Fractures of the large area range in size from one meter to 28 meters including fractures embedded in the layer and fractures that span the mechanical layer. A bias power law model (Marrett, 2000) was fit to the large area fracture size distribution and yielded an exponent of -2.521 . Most of the largest fractures that follow the bias model are longer than 6 m. Fractures smaller than 6 m deviate from the bias model and appear to follow a power law having a lower slope. This change in power law scaling is consistent with sampling topology predictions (Marrett, 1996).

A bias model was also fit to the cross fracture set, yielding a power law exponent of -1.347 . Most of these fractures are shorter than the mechanical layer

thickness and are sampled in two dimensions. Only the three longest fractures in this distribution are longer than the mechanical layer thickness. These three fractures deviate from the bias power law model and follow a steeper slope. These results are also consistent with a topologic effect on sampling. The formulas in Marrett (1996) were derived for randomly distributed isolated fractures and different spatial distributions or interconnected networks can have an effect on the predicted slope of the power law distribution (Borgos et al., 2000). No spatial data were collected from the pavements for an analysis of fracture clustering effects on the fracture length distributions observed. However, fractures measured in the large observation area are dominantly organized in clusters. According to Borgos et al. (2000), fracture-clustering effects decrease the slope of the fracture length distribution for fractures that span the mechanical layer thickness compared with the slope predicted by Marrett's (1996) formulas for a random spatial distribution.

Test of effect of fracture connectivity on length distributions

Fractures on pavements of all localities studied tend to cluster in swarms at different scales of observation. En echelon patterns are common, especially within fracture swarms. Collecting fracture data from fracture swarms containing the largest fractures may produce over-sampling of the fracture sizes in the fracture swarm, whereas measurements in inter-swarm areas may produce undersampling of clustered largest fractures.

The length distribution of isolated fractures and fracture segments were analyzed and compared with the length distribution of isolated fractures and

interconnected fracture groups for the North Disappointment pavement (637 m²) (Fig. 2.13). A bias model regression (Marrett, 2000) was obtained for each length distribution from North Disappointment pavement. Bias models for the two length distributions in Figure 2.13 suggest that essentially the same power law model fits both forms of the data. The size distribution of isolated and interconnected fractures should have a smaller power law exponent, because the number of small fractures is reduced when they are grouped into a few interconnected fracture arrays, resulting in increased size for the longest fractures. However, in this case, the proportion of interconnected fractures in the pavement network is small compared with isolated fractures, and grouping all connected fractures only decreases the number from 1311 isolated fractures and fracture segments to 1234 isolated fractures and connected fracture groups. The difference of 77 fractures is insufficient to produce significant changes in the underlying power law in this case.

The longest fractures in the fracture length distribution for fracture segments and isolated fractures from North Disappointment pavement deviate from the bias power law model. This deviation would be interpreted as a topologic effect on fracture sampling with the longest fractures spanning the mechanical layer thickness and effectively sampled in three-dimensions. However, measuring fractures as the total length of all interconnected segments produces a fracture length distribution in which the effect at the large scale end of the distribution have been minimized.

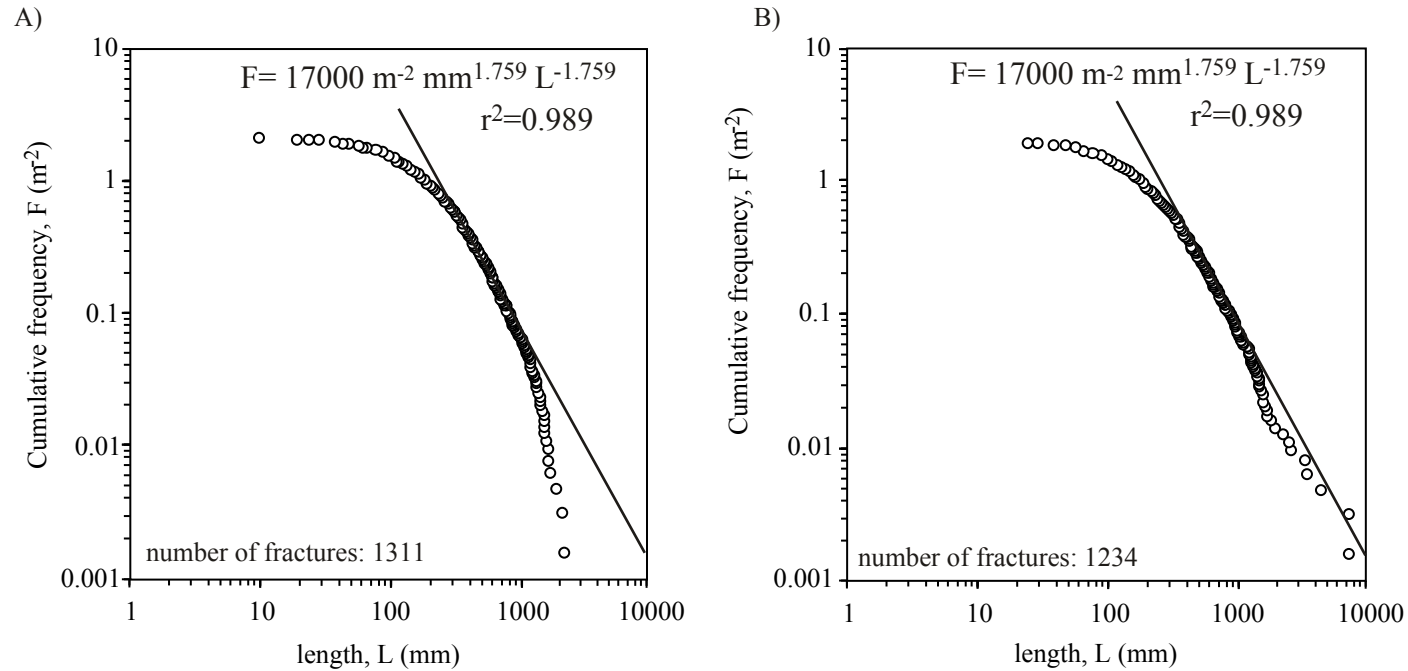


Figure 2.13. Effect of fracture connectivity on fracture length distributions, North Disappointment pavement. Bias model regressions (Marrett, 2000) for both isolated fractures and fracture segments (A), and isolated fractures and connected fractures (B) are indistinguishable. A steep trend for the longest fractures, which could be interpreted as a topologic sampling effect produced by effective three-dimensional sampling of fracture segments that span the mechanical layer, is almost eliminated when the lengths of fractures are considered to be the sum of all connected fracture segments.

The results of this exercise suggest that defining fracture length as the sum of all connected fracture segment lengths produces a distribution with a less pronounced (or possibly corrected) slope at the large-scale end of the distribution than defining fracture lengths as fracture segment lengths. A similar result was obtained for fractures measured in South Disappointment pavement. Consideration of fracture connectivity in the criteria to measure fracture length produce fracture length distributions closer to a power law than to an exponential law. Numerical models based on fracture mechanics theory predict exponential fracture length distributions rather than power law distributions (Olson, 2002, unpublished).

Aperture-length distributions

A number of publications contain data comparing apertures and lengths of opening-mode fractures (Johnston, 1992; Johnston, 1994; Hatton et al., 1994; Vermilye and Scholz, 1995; Walmann et al., 1996; Johnston and McCaffrey, 1996; Marrett and Laubach, 1997; Moros, 1999; Stowell et al., 1999). Aperture-length data analysis requires collection of fracture aperture and fracture length from individual fractures in a fractured rock unit without requiring exhaustive sampling of all the fractures visible at a given scale of observation.

Fracture aperture-length relationships have generally been described as power laws (Appendix 1.A) but linear relationships have also been proposed (Vermilye and Scholz, 1995). Fracture mechanics predicts that fracture length is proportional to the square root of the aperture (Vermilye and Scholz, 1995; Olson,

2002, personal communication). A few authors have inferred changes in aperture-length patterns with scale of observation (e. g., Hatton et al., 1994; Johnston, 1994; McCaffrey, 1994; Stowell et al., 1999) but others did not find adequate support for changes in aperture-length relationships (Marrett and Laubach, 1997; Moros, 1999)

Moros (1999) collected aperture-length data from a number of sandstone and limestone units at various scales of observations and with different types of spatial arrangements. Moros (1999) concluded that fracture aperture-length patterns can be modeled adequately using power laws, and proposed general equations for sandstones and limestones. Moros (1999) also collected information on the variation of fracture aperture along the length of individual fractures and concluded that fractures display a variety of morphologies, although many fractures tend to have relatively constant apertures along their lengths and rather abrupt decreases near the tips. Vermilye and Scholz (1995) reported similar fracture morphology results for single- and multi-segment veins.

Fracture aperture-length relationships were obtained for fractures measured in Weber Formation pavements and scanlines (Fig. 2.14). Aperture-length data from microfracture observations were added to the plot. The data fall in two separate groups (microfractures and macrofractures), with a gap of more than one order of magnitude in the length data. Fractures in this size range are difficult to measure in the field because they are filled with quartz cement and are undistinguishable from the rock matrix. They are also difficult to observe in thin sections because few are present at thin section scale and only small areas of a

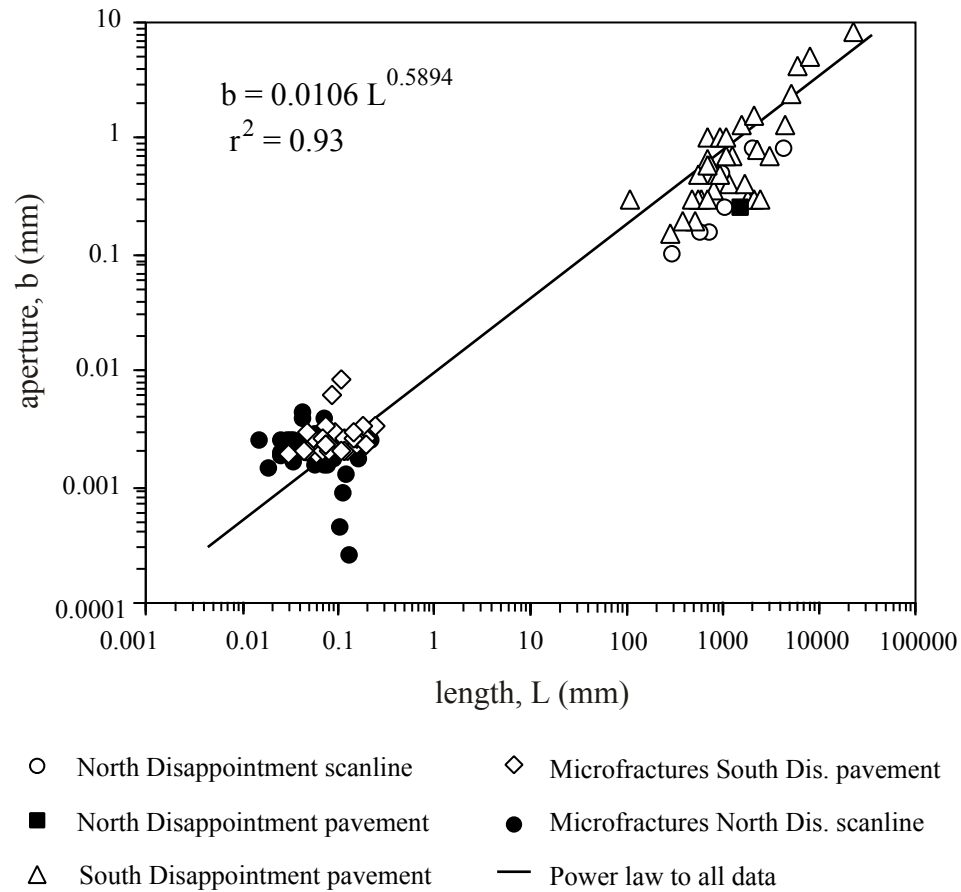


Figure 2.14. Fracture aperture vs fracture length for Weber sandstone outcrops. Outcrop data localities are indicated by different symbols but the power law regression applies to all of the data. The coefficient of the power law regression is similar in magnitude to the one reported by Moros (1999) based on observations from a number of sandstone units. The exponent of the power law is significantly smaller than other exponents reported before for sandstones (0.77, Johnston and McCaffrey, 1996; 0.75, Moros, 1999; 0.88, Chapter 1). A small exponent in the aperture-length relationship suggests that apertures grow slower than lengths.

thin section are practical to image with the SEM-CL. A power law regression to the data in Figure 2.14 yields a coefficient of determination of 0.93 suggesting that a power law model is adequate to explain the aperture-length relationship observed. The exponent of the power law (~ 0.59) obtained is small compared with others reported for sandstones (Moros, 1999; Chapter 1) but is closer to fracture mechanics predictions (Olson, personal communication). This exponent suggests that as fractures propagate, their lengths grow faster than their apertures (i.e., they grow proportionally thinner). Similar predictions of fracture geometry with scale of observation were reported by McCaffrey (1994), Johnston (1994), and Johnston and McCaffrey (1996) in vein studies.

TESTS OF OUTCROP MICRO- AND MACROFRACTURE DATA EXTRAPOLATION

Test of macrofracture strike prediction using microfracture strike

Oriented samples collected in the field were studied with SEM-CL for microfracture orientation. The results of microfracture strike analyses were compared with macrofracture orientations from the same locality. The objective of the comparison was to test the hypothesis that microfracture strike and macrofracture strike are equivalent, in order to justify using microfracture strike as a proxy of macrofracture strike where macrofracture orientation data are scarce, such as the subsurface. This technique (Laubach, 1997) has now been used successfully in a number of subsurface case studies conducted by the Fracture Research and Application Consortium at The University of Texas at Austin

(Laubach et al., 2000). In Rangely Field there is poor control on macrofracture orientation (Narr, 1997 personal communication, Fig 2.7) based on conventional indirect techniques for subsurface macrofracture orientation measurement (e.g., image logs).

Macrofracture orientation prediction tests with microfracture strikes from Weber Formation outcrop samples produced satisfactory results (Figs. 2.15 and 2.16). After correcting microfracture strikes for true orientation, length weighting of microfracture strikes, and selecting the longest 25% of microfractures, the final rose diagram of microfracture strikes reproduced the rose diagram of macrofracture strikes obtained in the field. The rose diagram in Figure 2.15 suggests that the ENE- and NW-striking sets equally dominate these rocks. However, the orientation of the photomicrograph collage favors encountering microfractures of the secondary set orientation and the results are biased. Terzaghi (1965) proposed a method to correct orientation data for observation domain size and orientation. The rose diagram for outcrop macrofractures is also biased because the secondary set was selected for study and the shape of the pavement and data collection favored the secondary set. Equidimensional collages should be more accurate at predicting macrofracture orientation using microfractures. In a general case, photomicrograph collage orientation should be considered for macrofracture orientation prediction and determination of dominant versus secondary sets.

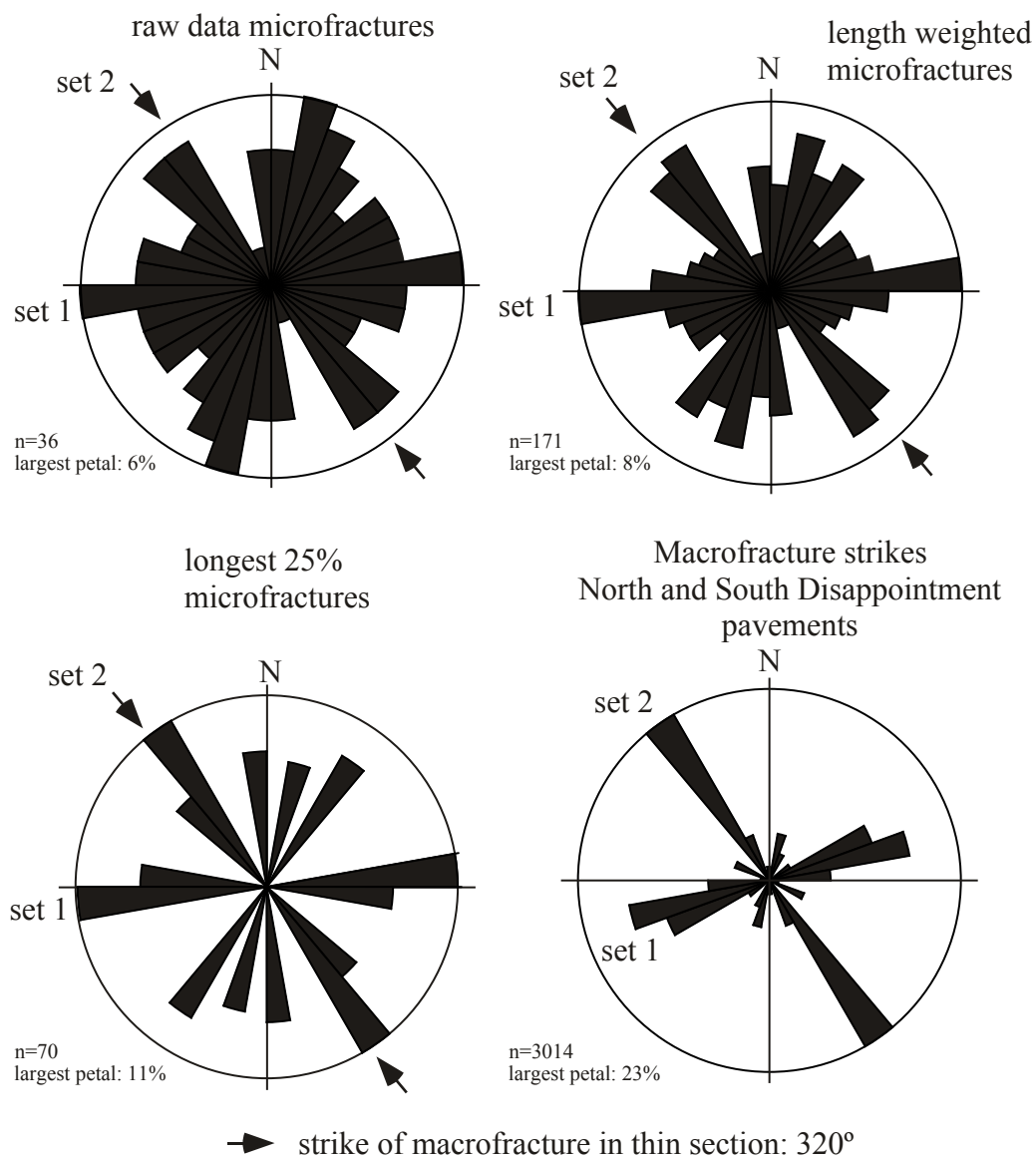


Figure 2.15. Test of macrofracture strike prediction using microfracture orientations, Weber Sandstone, Disappointment Gulch Scanline area, sample w-036-97. The rose diagram for the longest 25% longest microfractures matches the strike of two macrofracture sets in the area. Macrofractures striking 320°-330° were the focus of scaling studies in the scanline from where sample w-036-97 was obtained.

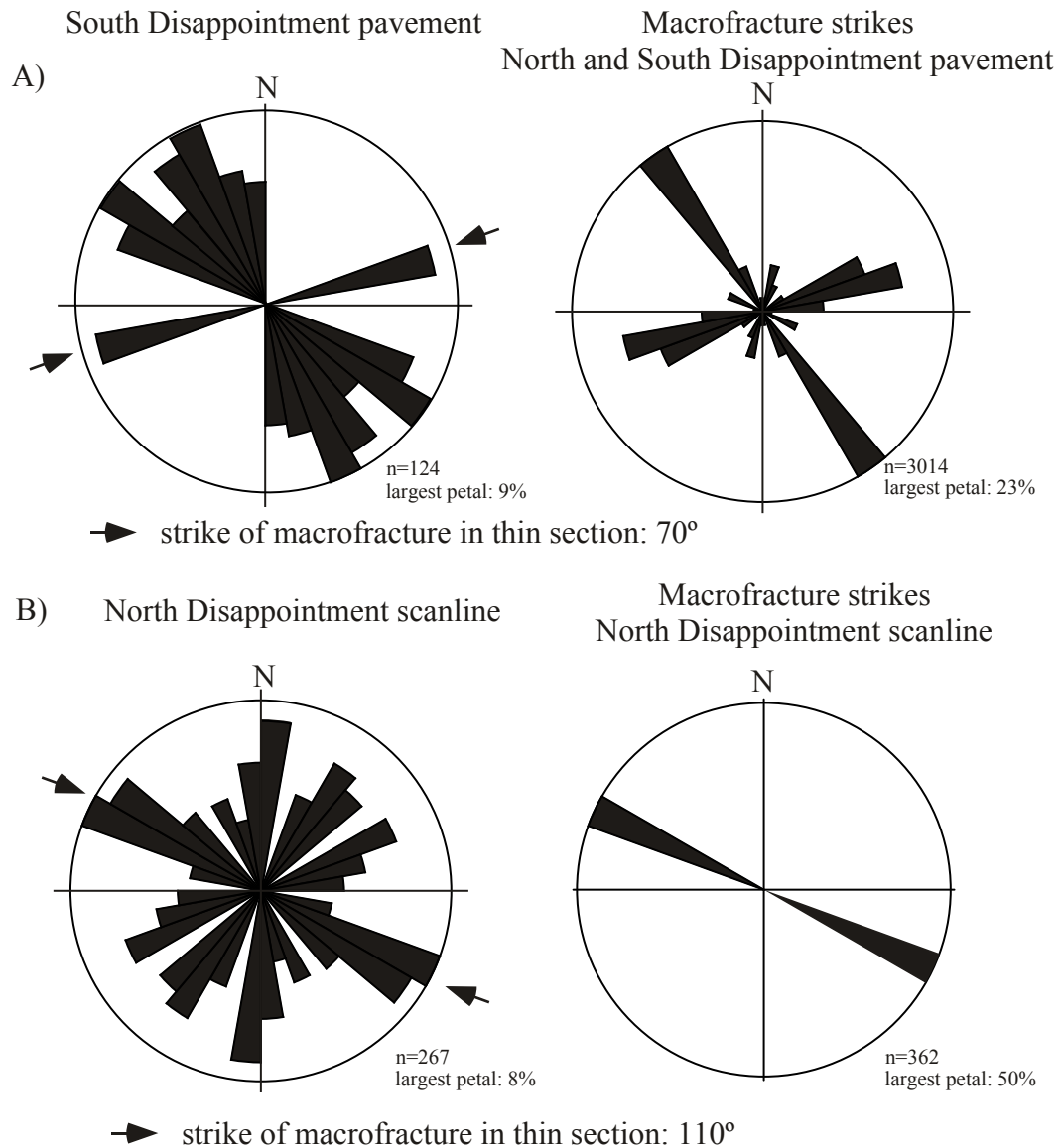


Figure 2.16. Test of macrofracture strike prediction using microfracture orientation, Weber Sandstone, Disappointment Draw area. A) sample w-043-97, and B) sample w-045-97. The rose diagram for the longest 25% of microfractures in each case matches the macrofracture strike in the area. Macrofractures striking 320°-330° were the focus of scaling studies at South Disappointment pavement. Sample w-045-97 was collected from North Disappointment scanline area where apertures of 362 fractures striking ~110° were measured.

Test of micro- and macrofracture size distributions extrapolations

In this section, I use thin sections from outcrop samples and macrofracture field data to test the hypothesis that microfracture size distributions can be used to predict macrofracture size distributions in the same volume of rock. Selected oriented thin sections from outcrop localities were processed for microstructural analysis following the procedure explained in the section on microfracture data collection and methods. Aperture and length distributions were then obtained for the dominant microfracture sets. Two-dimensionally sampled microfracture data from photomicrograph collages produced an adequate number of microfractures for size distribution analysis. However, one-dimensionally sampled data were too scarce and produced unreliable fracture size distributions.

Microfracture length distributions obtained from SEM-CL photomicrograph collages are adequately modeled using power laws (Fig. 2.17). Microfracture length distributions were sampled from two-dimensional observation areas similar to macrofracture length data collected from nearby pavements. The analysis of the microfracture length distributions was restricted to microfractures striking parallel to macrofractures studied in pavements, under the assumption that similarly orientated microfractures and macrofractures are different size fractions of the same fracture system (Laubach, 1997; Ortega et al., 1998; Ortega and Marrett, 2000; Laubach et al., 2000). The extrapolation of microfracture-based power-law length distributions obtained from two samples collected in South Disappointment area to the scale of macrofractures measured

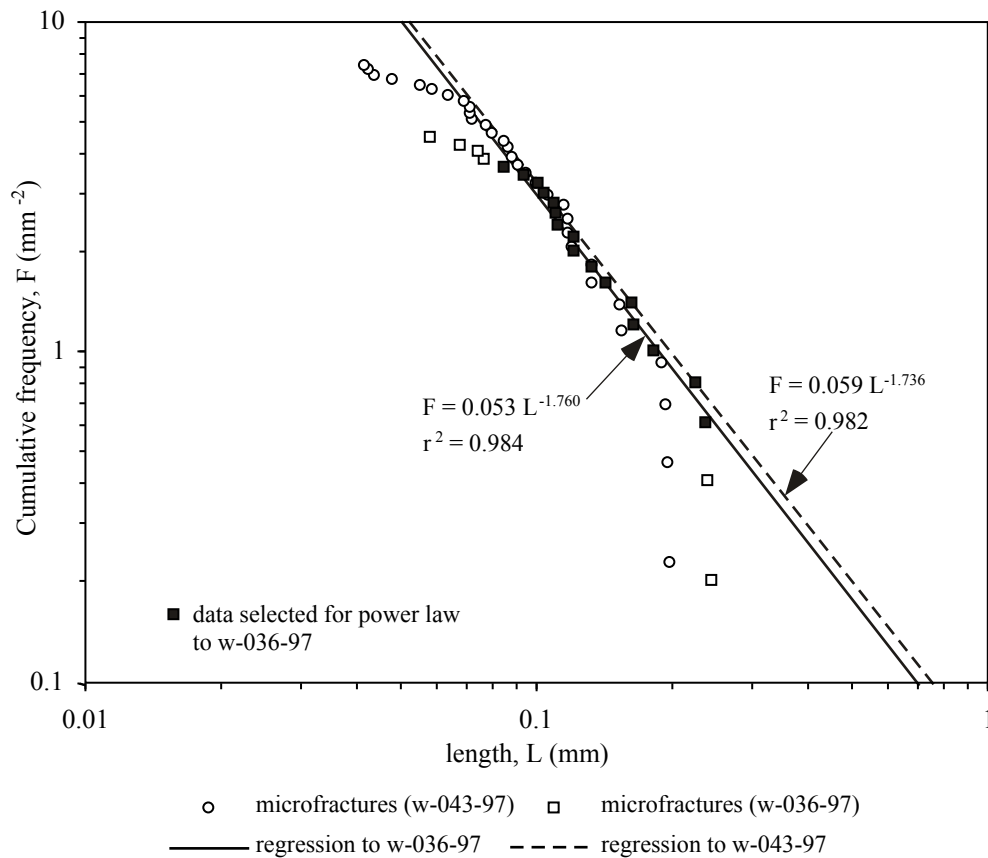


Figure 2.17. Microfracture size distributions for South Disappointment area. Microfracture length distribution for sample w-036-97 is for microfracture set striking 320° in Disappointment Gulch locality. Microfracture length distribution for sample w-043-97, collected from South Disappointment pavement, is for the main set present in SEM-CL photomicrograph collages which also strikes 320° . A bias model regression was fit to data from sample w-043-97 and a simple power law regression was fit to the linear segment in the length distribution from sample w-036-97 because of scarce data.

on pavements adequately predict the observed abundance of macrofractures measured in the area (Fig 2.18).

Test of similar relationships between microfracture and macrofracture aperture distributions were done from localities in the study area where systematic aperture data were collected along scanlines (Fig. 2.19). The fracture sets studied at Disappointment Gulch and North Disappointment localities have similar strikes, but the two localities are separated several kilometers. Scanlines from SEM-CL photomicrograph collages drawn perpendicular to a macrofracture of the same set studied in the field provided limited aperture data to fully test the hypothesis and construct meaningful fracture size distributions. A maximum of six microfractures were intercepted by the scanlines drawn on SEM-CL collages. The maximum scanline length for microfracture analysis was 5.29 mm long and the maximum number of pictures in photomicrograph collages studied was 9.

Extrapolation of macrofracture aperture distributions to the microscopic scale for Disappointment Gulch Scanline 1 adequately matches microfracture intensity calculations from SEM-CL images at that locality. However, results of extrapolation of macrofracture aperture distribution from North Disappointment scanline did not match microfracture intensity calculations and the difference is of approximately two orders of magnitude. In the discussion section of this work I provide some possible explanations for the mismatch of macrofracture and microfracture intensities in North Disappointment area. These results are not conclusive and more data are necessary to discard the hypothesis. However, the results are reproducible and different photomicrograph collages acquired from

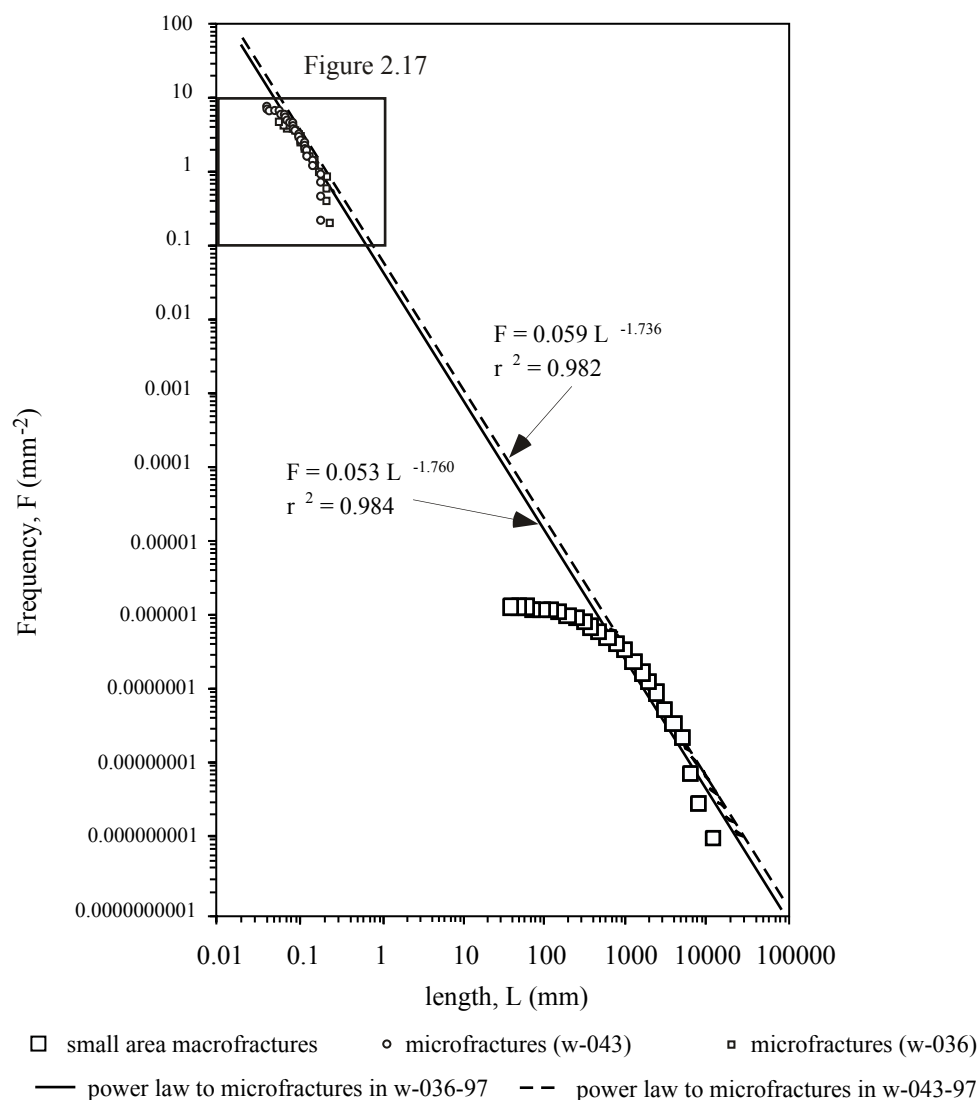


Figure 2.18. Microfracture and macrofracture length distributions, South Disappointment pavement. Power law models fit to microfracture length distributions from two samples in the area (inset, Fig. 2.17) suggest that microfracture length distributions could be used to predict approximate macrofracture length abundance. These extrapolations are fraught with dangers associated with sampling artifacts, microfracture interpretation, classification, and measurement. However, this result adds to previous successful microfracture length extrapolations reported by Ortega and Marrett (2000) for Mesaverde Group sandstones.

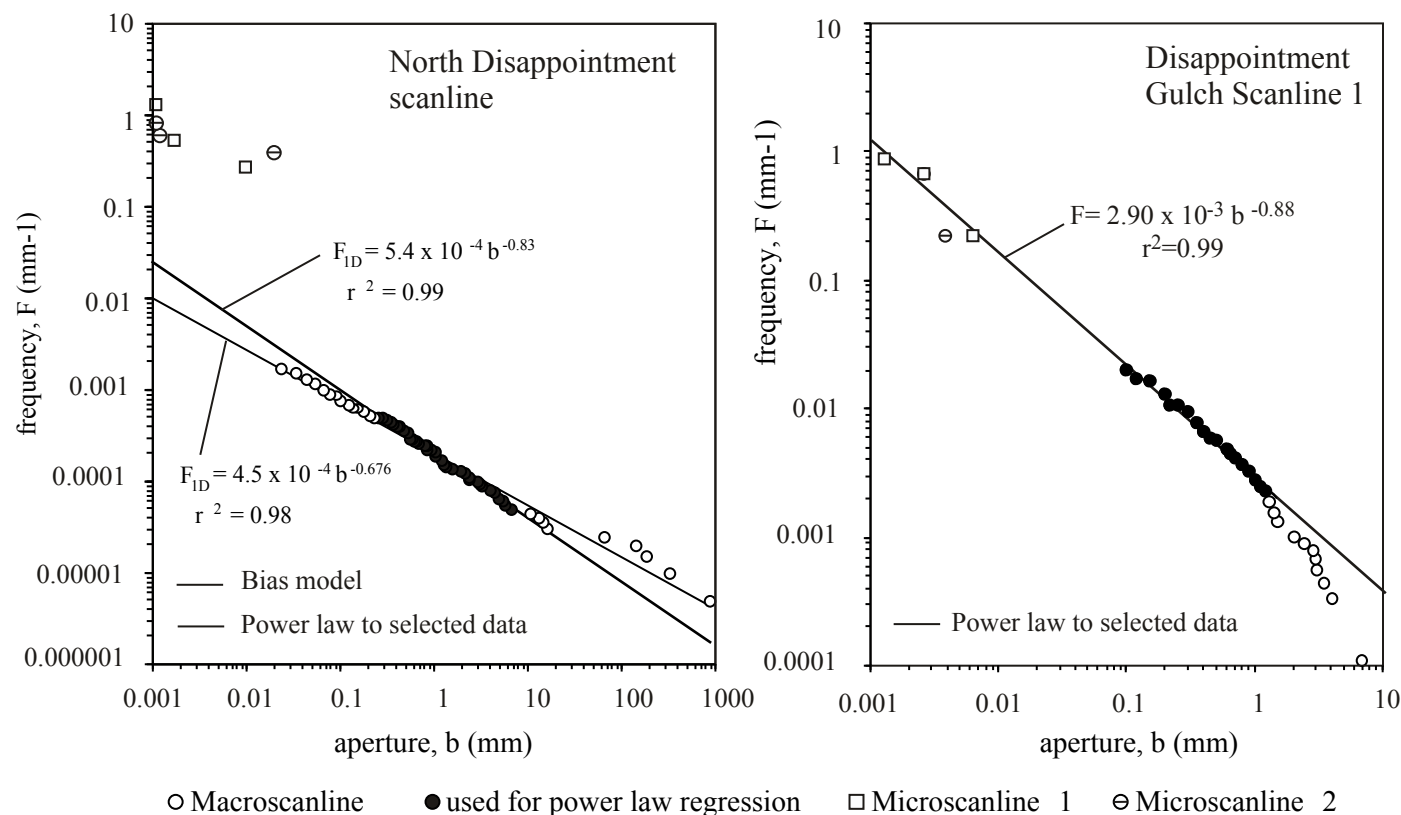


Figure 2.19. Micro- and macrofracture aperture distribution from Weber Fm. outcrops. Bias models or selected portions of the distributions (solid circles) were used to obtain the power law model for these aperture distributions. Extrapolations of macrofracture power law regression down to microscopic scale were successful predicting microfracture abundance at Disappointment Gulch. The area at North Disappointment scanline is characterized by a very low fracture intensity. Microfracture frequency calculation for this area is possibly biased because data were collected from a short SEM-CL traverse with a few microfractures close to a macrofracture.

different areas of the same thin section yielded similar one-dimensional microfracture abundance results.

RESULTS -SUBSURFACE

Subsurface macrofracture orientation

Relatively few macroscopic natural fractures were found in cores of the Weber sandstone at Rangely Field. Most natural fractures observed with the naked eye form a high angle with bedding. No more than one macrofracture was observed at the same depth in the core except for an interval with small parallel en echelon fractures in Larson 15X B well.

The cores studied contain scribe knife marks for orientation (Kulander et al., 1990), however orientating the cores was not possible. Previous subsurface fracture orientation studies at Rangely Field (Larson, 1975; Narr, unpublished) suggest that in the southeastern portion of Rangely Field macrofractures strike east and that there is a secondary fracture set that strikes north (Fig. 2.7). However, these results are based largely on questionable image log interpretations (Narr, personal communication). “Joint-like” fractures in the Emerald 46X well, in the northwestern portion of Rangely Field strike WNW with a secondary set striking NNW (Fig. 2.7, Narr unpublished). Dominant strike of induced fractures (petal-centerline fractures, Kulander et al., 1990) identified in the Emerald 46 X well is aligned with “joint-like” fracture strikes (Narr, unpublished), suggesting (but not demonstrating) that fractures measured from the Emerald 46 X cores could be induced from drilling.

Seismicity analyses from a fault that operationally divides the northwestern and southeastern portions of the field (Raleigh et al., 1972), suggest that the current day maximum horizontal stress strikes east-west. Seismically-derived maximum horizontal stress direction (Raleigh et al., 1972) coincides with the interpreted natural fracture strike in Larson 15X B well and also coincides with well-to-well rapid communication direction in the southeastern portion of Rangely Field. However, this orientation differs from hydraulic fracture strikes in a well of the same area (Fig. 2.7).

Rapid fluid-flow communication directions between wells in the northwestern portion of Rangely Field approximately coincide with hydraulic fracture strike in this area (Fig. 2.7) suggesting that hydraulic fracturing is possibly responsible for rapid fluid-flow directions in the northwestern portion of the field. However, preferred fluid-flow orientations do not match strike of “joint-like” and petal-centerline fractures (Narr, unpublished) from the Emerald 46X well and older reports of macrofracture orientation from the same cores (Larson, 1975). A possible interpretation of the complex strike patterns for natural fractures, induced fractures, and rapid communication directions is that the current state of stress in Rangely Oil Field as well as the current fluid pressure distribution are heterogeneous. The field has been under enhanced recovery since 1958 with a water flood and more recently a CO₂ flood (Hervey and Iakovakis, 1991). Hydraulic fracture treatments have probably altered what could have been the original permeability distribution in the field (Bagzis, 1989) and rapid communication between wells might result from a combination of open hydraulic

fractures, natural fractures and fluid pressure gradients. The southeastern portion of the field is the least productive, and in that area hydraulic fracturing has possibly been less detrimental to the original permeability structure in the field. In this area natural fracture orientations and rapid communication between wells have the most matches (three out of three natural fracture strike/rapid communication matches versus 0 out of two in the northwestern portion of the field). This suggests that the best estimate of natural fracture strike in Rangely Field is ENE-ESE as indicated in the Larson 15X B well (Fig. 2.7, Larson, 1975; Hefner and Barrow, 1992; Narr, 1997 unpublished).

Macrofracture orientation prediction using microfractures

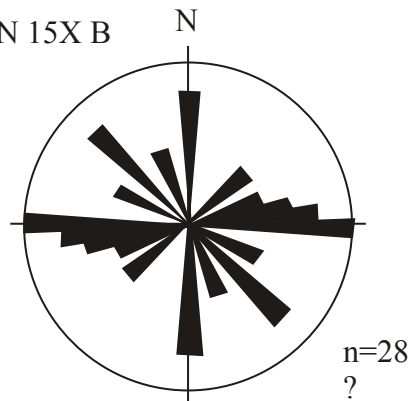
Systematic study of microfracture orientations has proved successful predicting macrofracture orientations in the same volume of rock (Laubach, 1997; Ortega and Marrett, 2000). Oriented samples are required for prediction of macrofracture strike but not oriented samples can also be studied to determine the number of macrofracture sets possibly present and the angular relationships between them. Samples collected for microfracture orientation analysis from the cores of Larson 15X B well and Emerald 46X well are not oriented with respect to true north. However, samples were oriented with respect to observed core macrofracture strike for relative orientation purposes and/or the principal scribe line for possible future orientation (e.g. via paleomagnetic methods) (Table 2.2). Microfracture orientations were originally referred to an arbitrary orientation in the SEM-CL collage and later referred to macrofracture orientations. Analyses of

microfracture strikes from SEM-CL photomicrograph collages of a sample collected at 1712 m depth from Larson 15X B cores show microfractures striking parallel to a macrofracture in the same thin section. If this microfracture set is parallel to the dominant macrofracture set identified in the well (Narr, unpublished), then the dominant microfracture set in the thin section strikes east-west as well. A secondary microfracture set strikes at a high angle with respect to the primary microfracture set and it is also present in the rose diagram for the macrofracture strikes in the well (Fig. 2.20), indicating that microfractures predict the number of macrofracture sets present and the angular relationships between them.

Test of microfracture orientation reproducibility

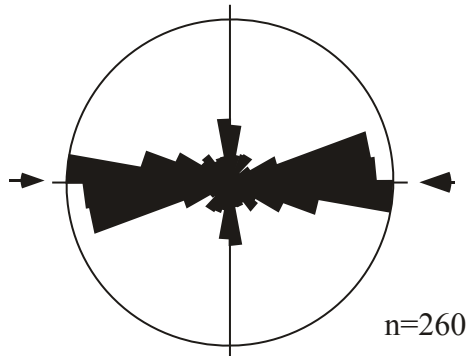
A test was performed in different SEM-CL photomicrograph collages of a single thin section from the Larson 15X B well to evaluate if microfracture orientation analyses are reproducible using different areas of the thin section (Fig. 2.21). The collages selected for the microfracture strike test were L15-5618c(1-10) and L15-5618c(43-54) from thin section L15-5618c (Table 2.3). Statistical analysis of the dominant microfracture set strike in L15-5618c(1-10) yields an average microfracture strike of -49° with a standard deviation of 14° . The average strike for the same dominant microfracture set in L15-5618c(43-54) is -60° with a

LARSON 15X B



Macrofracture strikes
Fractures dipping more than
50 degrees in image logs
(Narr, unpublished)

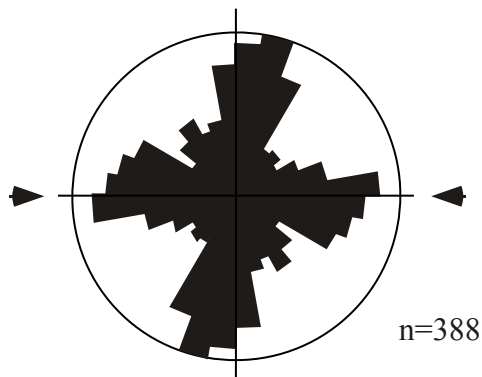
Core depth range: 1711-
1724 m
Core length: 213 m
(potentially orientable)



Microfracture strikes
SEM-CL photomicrograph
collage from thin section
at 1712 m

Area imaged: 3.27 mm²

← strike of macrofracture
in thin section



Microfracture strikes
SEM-CL photomicrograph
collage from thin section at
1738 m

Area imaged: 2.62 mm²

← strike of macrofracture
in thin section

Figure 2.20. Comparison of rose diagrams for macro- and microfracture strikes, Larson 15X B well. The number of fractures measured to construct the macrofracture rose diagram is unknown (Narr, unpublished), but I found 28 natural fractures in the core. In contrast, abundant microfracture orientation data were obtained from small areas of two thin sections. Macro- and microfracture data match in terms of number of fracture sets and relative orientation.

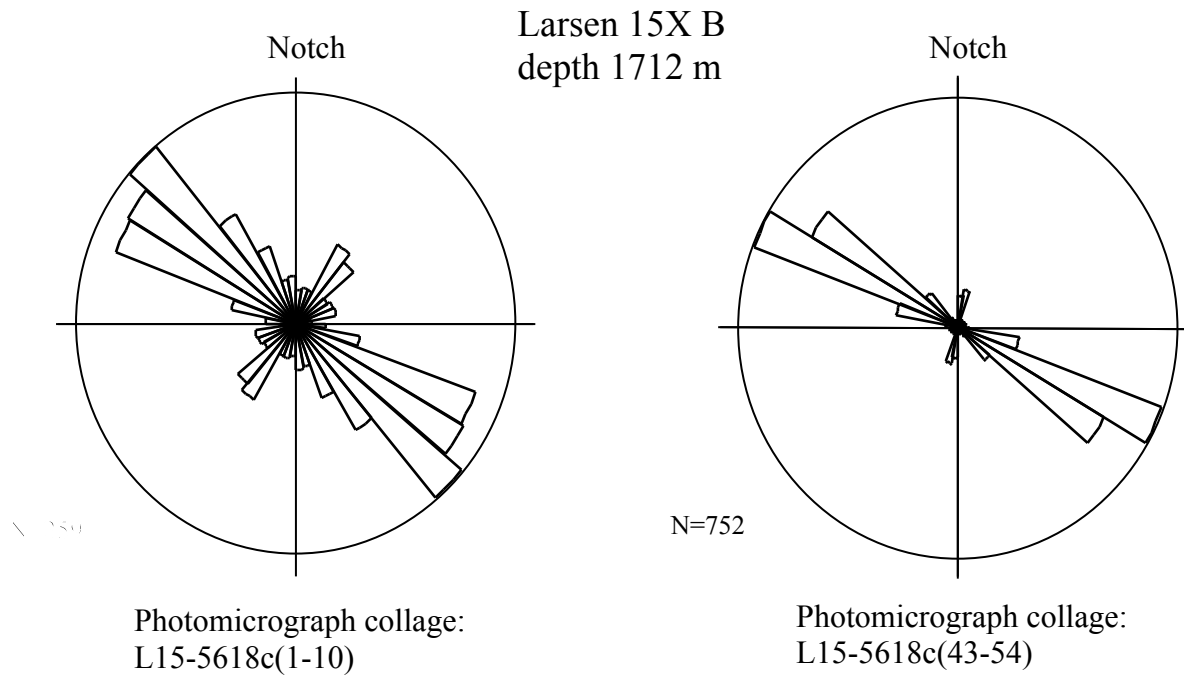


Figure 2.21. Test of reproducibility for microfracture strike analysis in a thin section of Larson 15X B well. Two fracture sets are identified in each case. Changes in the average strike of the dominant and secondary set range from 11 to 29 degrees. Higher reliability and greater number of microfractures reduces microfracture strike dispersion.

standard deviation of 9°. The secondary set in L15-5618c(1-10) has an average strike of 38 with a standard deviation of 7° and the same set in L15-5618c(43-54) yields an average strike of 9 with a standard deviation of 7°. The difference in average strike for the microfracture sets in the two collages selected for the test range from 11 to 29 degrees. The dispersion in the microfracture orientation for photomicrograph collage L15-5618c(1-10) is larger than for collage L15-5618c(43-54). These results suggest that microfracture orientation results are reproducible in different parts of a thin section. The number of fracture sets is similar and angular relationships between sets are also similar. However, differences in average strike of 10° to 30° and amount of strike dispersion indicate that prediction of macrofracture orientation using microfracture orientation should include similar margins of error.

Subsurface microfracture aperture distributions

Subsurface microfracture aperture data come from SEM-CL photomicrograph collages from three samples of Weber Formation in Rangely Field. Two of the samples analyzed come from different depth intervals from the Larson 15X B well (1712 m and 1738 m) and one comes from the Emerald 46X well (1726 m).

Microfractures in SEM-CL collages from these samples were interpreted as four sided polygons and their apertures were calculated using a C⁺⁺ program (Appendix 4.A), following the methodology described in the data collection and

data analysis section. Samples could not be oriented with respect to true north but they were oriented with respect to macrofractures present in the thin sections. The orientations of macrofractures parallel the orientation of microfractures of the dominant or secondary set in the SEMCL collages (Fig. 2.20).

Microfracture aperture distributions for the dominant and secondary sets at two different depths of the Larson 15X B well are shown in Figure 2.22. Bias regression models (Marrett, 2000) fit to the distributions suggest that a power law model is an adequate model for the observations. Truncation artifacts probably produced the departure of the aperture distribution from a power law at the small-scale aperture range. Artifacts at the large-scale end of the aperture distribution are also present, producing an increase in the slope of the aperture distribution of most samples. However, the aperture size distribution for the dominant microfracture set in the sample collected at 1712 m follows the power law model even at the large-scale end of the distribution.

Subsurface microfracture length distributions

The length distributions of microfractures in SEM-CL photomicrograph collages were analyzed using the same methodology used for subsurface microfracture apertures. Figure 2.23 shows the cumulative microfracture length distributions obtained from the same SEM-CL collages used to obtain the microfracture aperture distributions in Figure 2.22. Truncation artifacts are significant in microfracture length distributions. Censoring affects measurement of lengths for microfractures that continue beyond the observation domain within

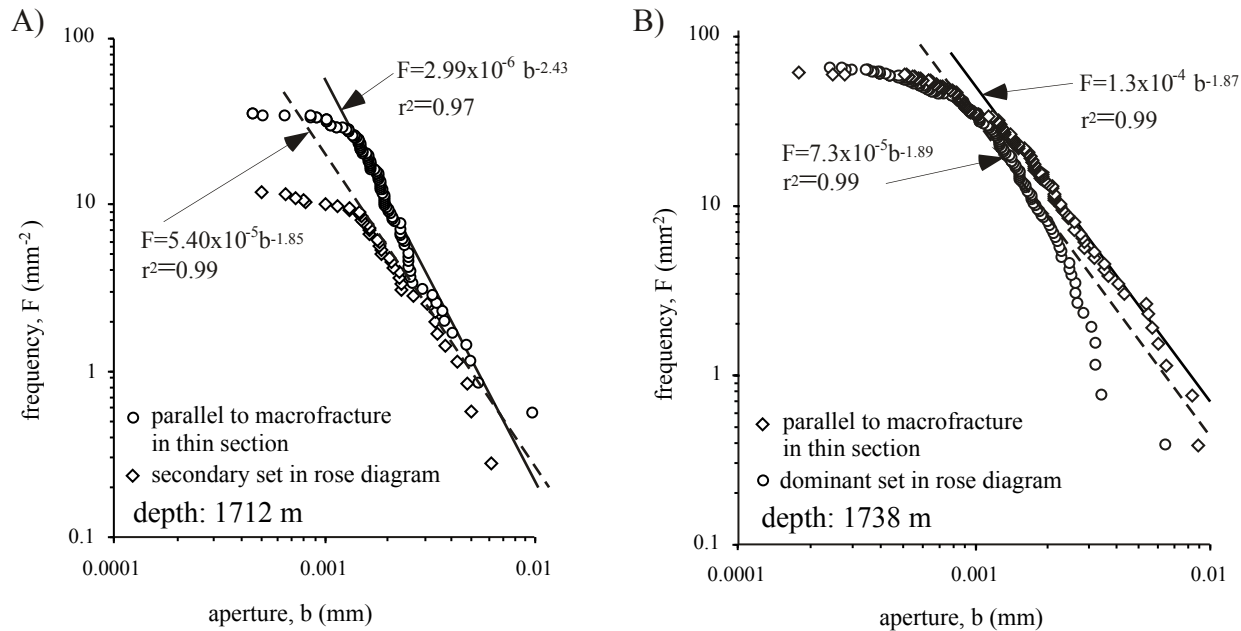


Figure 2.22. Microfracture aperture distributions from two samples collected at different depths in cores of Larson 15X B well. One of the microfracture sets is parallel to a macrofracture in the thin section and the other microfracture set forms a high angle with the former one (Fig 2.20). Bias model regressions (Marrett, 2000) have been applied to all the distributions to obtain the underlying power laws. Power law models in A) are different and suggest that the secondary set may be a primary set at larger scales of observation. Power law models in B) are similar and suggest that the dominant set at microscopic scale is also dominant at reservoir scales.

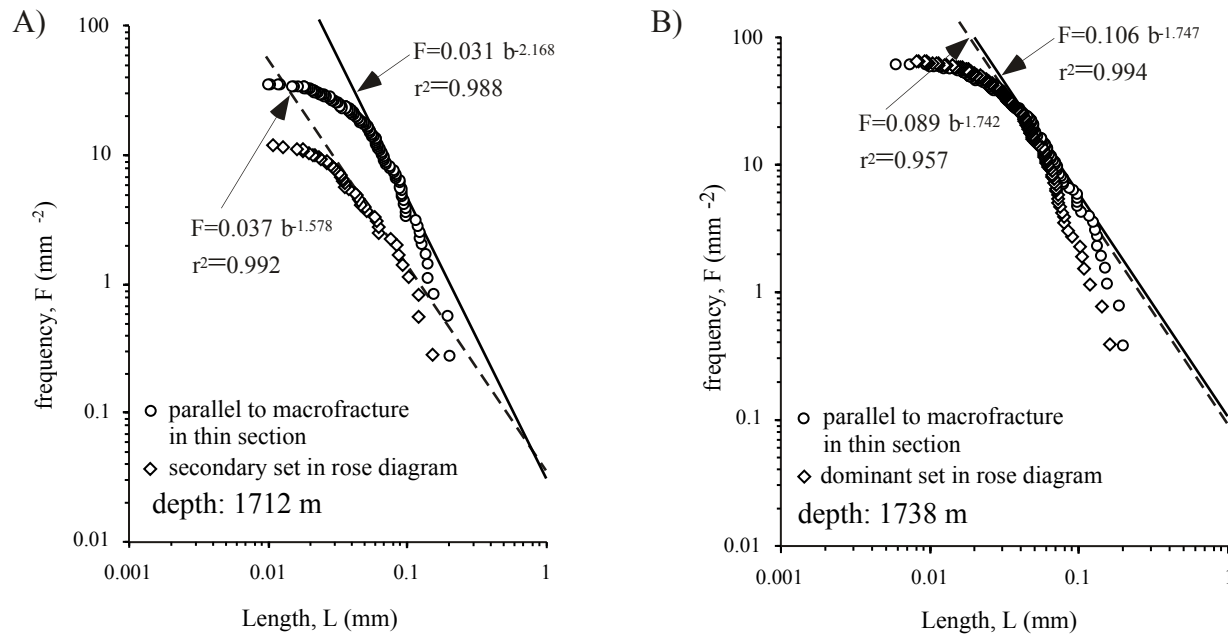


Figure 2.23. Microfracture length distributions from the same samples as Fig 2.22. Bias model regressions (Marrett, 2000) have been applied to these distributions to obtain the underlying power law parameters. As with microfracture aperture distributions, power law models in A) are different. The high exponent in the primary set in A) may be an effect of microfracture data collected within a swarm. Power law models in B) are similar and neither of the sets is more abundant than the other at this observation scale.

the SEM-CL photomicrograph collage, truncate against pores, or whose lengths have been partly missed because they follow the borders of grains, becoming indistinguishable from intergranular quartz cement.

Similar to the microfracture aperture distribution results, the bias power-law model for the dominant set in the thin section from the sample collected at 1712 m depth is characterized by a high exponent (-2.168). In the discussions section I will provide some possible explanations for the anomalously high power law exponent obtained for this fracture set.

FRACTURING AND DIAGENESIS

In the preceding paragraphs I described the results of characterizing the orientation, fracture length, and fracture aperture distributions in fracture systems, pointing out some of the pitfalls and sampling effects that influence the data and interpretations. I also showed the results of testing the hypothesis that microfracture information can be used to predict macrofracture attributes in the same volume of rock.

In the following paragraphs, I summarize the diagenetic history of Weber Formation sandstones using literature sources and then I focus on the description of different cement phases identified in the rock, their timing, regional distribution and proportion variations. I will also show the results of an evaluation of the proportion of cement phases present at different depths in the Larson 15X B well cores (Laubach and Schwartz, 1998 unpublished) and how these proportions can be converted to a fracture degradation index that allows empirical prediction

of subsurface fracture fill. Results of fracture quality predictions will be compared with natural fracture observations from cores.

Diagenetic history

Koelmel (1986) and Fryberger and Koelmel (1986) proposed a paragenetic history for Weber sandstones in the Piceance and Uinta basins (Table 2.4). Following is a brief explanation of the diagenetic stages identified by Koelmel (1986) and their relationship with fracturing, based on petrographic observations of samples collected from surface and subsurface locations (Appendix 2.A), SEM-CL photomicrographs collages observations, and preliminary microprobe results (Milliken, 2002 personal communication).

Early carbonate cements

Two kinds of calcite cement in Weber sandstones were identified by Fryberger and Koelmel (1986) and Koelmel (1986): early and late calcite cements. Early-stage carbonate cements are poikilotopic in habit and are commonly contaminated with detrital and authigenic clays. Koelmel (1986) interpreted that poikilotopic calcite cement precipitated during or soon after the deposition of Weber sandstones. Loose packing is characteristic of shallow burial poikilotopic cements. Poikilotopic cements inhibited quartz overgrowth in calcite patches. Rock material affected by poikilotopic calcite cement tends to weather as pea-size spherical nodules visible on outcrop exposures. Precipitation of early carbonates probably occurred before fracturing (prekinematic cement, Laubach et

Table 2.4. Diagenetic history of the Weber Sandstone for the Piceance Basin (modified from Fryberger and Koelmel, 1986, and Koelmel, 1986).

Timing Sequence (1 is oldest)	Diagenetic event
Stage 1	Carbonate cement (poikilotopic) and infiltrated clay
Stage 2	Quartz overgrowths
Stage 3	1. Calcite cement 2. Ferroan calcite cement 3. Dolomite 4. Ferroan Dolomite 5. Anhydrite 6. Authigenic illite (\pm chlorite, \pm illite/smectite)
Stage 4	Secondary porosity (dissolution of feldspars and authigenic carbonate)
Stage 5	Hydrocarbon migration and asphaltene deposition

Increase in salinity



al., 1995) because quartz cement overgrowths postdate early stage carbonates and line fracture walls in outcrop and subsurface fractures.

Quartz cement

Proportion of quartz cement in sandstones is difficult to quantify using regular petrographic microscope techniques because quartz in overgrowths is in optical continuity with quartz in host grains. Bowker and Jackson (1989) indicated that very few “dust rims” are visible in Weber Formation sandstones and reported that inspection of quartz grains with SEM reveals that most quartz grains are covered with quartz overgrowths.

Quartz cement is present both in the rock matrix and lining fractures in outcrop and subsurface Weber Sandstones. Quartz cement is comparatively lower in outcrop samples than in the subsurface (Fig. 2.24, Appendix 2.A). Small volumes of quartz are present (as overgrowths) lining fractures in outcrops. In outcrops, a variation of crack-seal structures (Ramsay, 1980) are developed and preserved by quartz cement. These crack-seal structures tend to follow grain boundaries instead of cutting across grains in outcrop fractures. Additionally, loose quartz grains with thin quartz overgrowths are present inside the calcite filling outcrop fractures, indicating that calcite in the veins postdated early stages of quartz overgrowths and that the rock had considerable porosity at the time fractures formed. Microfractures in outcrop are filled with quartz cement suggesting that quartz is synkinematic (Laubach et al., 1995). However, some

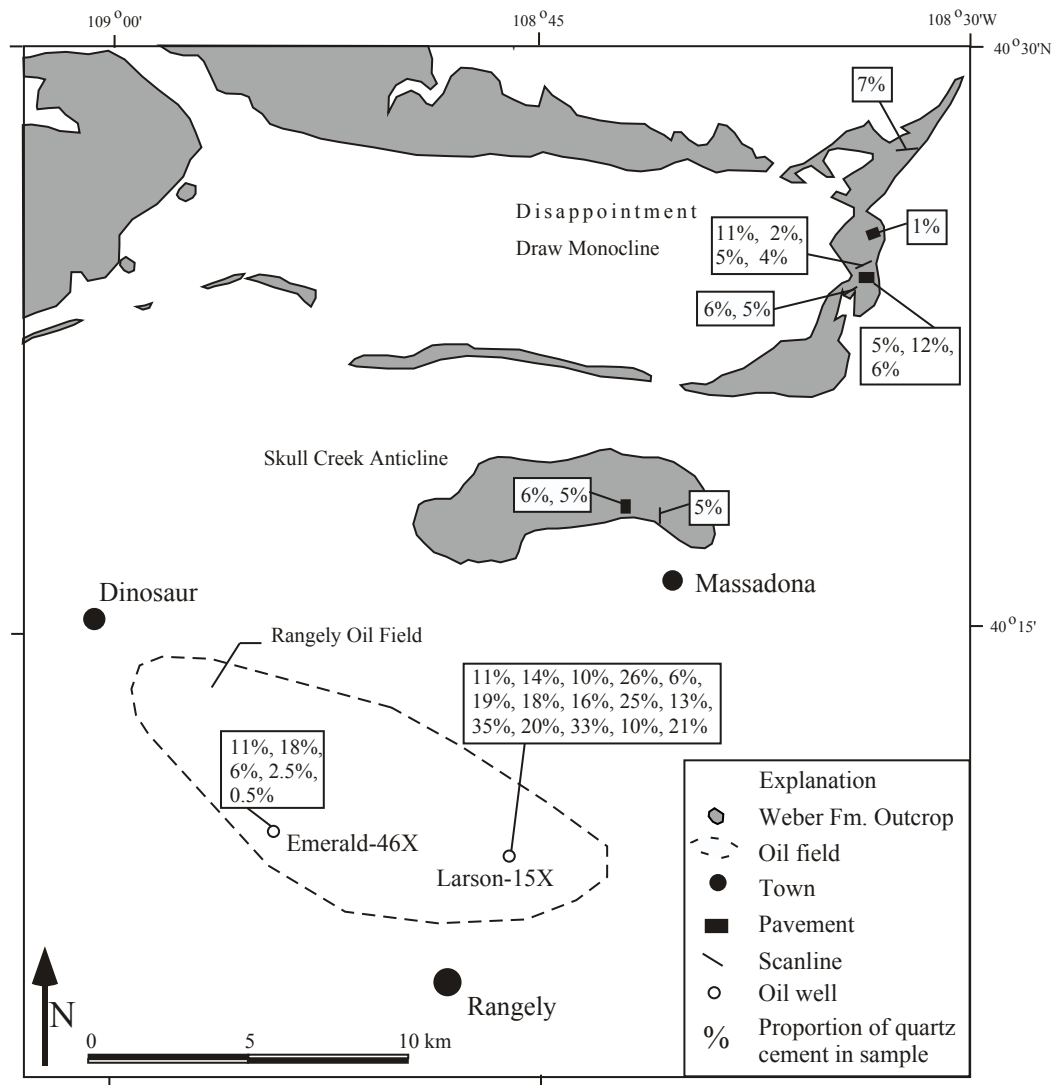


Figure 2.24. Regional distribution of quartz cement in samples of Weber Formation. Quartz cement proportion is lower in outcrops than in subsurface. Low volumes of quartz cement may indicate shallow burial or quartz cementation inhibition by the presence of other cements filling the pore space. Another possible explanation is that the surfaces of quartz grains in the outcrop area were covered with impurities or clays that prevented quartz cementation (Lander and Walderhaug, 1999).

fractures with apertures greater than 50 microns are filled with calcite, similar to macrofractures.

Quartz cement abundance increases from north to south in Rangely Field and also regionally from east to west (Koelmel, 1986). Subsurface microfractures in SEM-CL collages are filled with quartz, suggesting that related macrofractures formed during quartz precipitation (synkinematic cement, Laubach et al., 1995). Some crack-seal structures (Ramsay, 1980) in veins were diagnosed with SEM-CL photomicrographs of subsurface macrofractures. Crack-seal texture is more widely developed in subsurface fractures than in surface fractures, and patches of quartz cement forming bridges across the fracture wall are present in some SEM-CL images of macrofractures from subsurface samples. Quartz grains with large quartz overgrowths are present in these bridges, suggesting that the grains were separated from the walls and cemented with the quartz bridge.

Late carbonate cements

Stage 3 calcite cement (Fryberger and Koelmel, 1986; Table 2.4) in pores of the matrix are usually single large sparry calcite crystals filling the intergranular volume. According to Fryberger and Koelmel (1989), stage 3 calcite can also replace stage 1 calcite (early poikilotopic calcite cement), feldspars and biotite. Late calcite cement proportion of the rock volume is more important in outcrop localities than in the subsurface.

Fractures in outcrop are mostly filled with calcite. Calcite crystals in fractures show euhedral faces and prismatic habit. Calcite prisms are smaller next

to fracture walls and increase in size towards the centers of the fractures. Some macrofractures observed in the field show kinematic apertures as large as 2 m, and are filled with calcite cement with individual crystals up to 20 cm long. Preliminary microprobe analyses of outcrop fracture fill indicate that the cement is almost pure calcite with low content of iron or magnesium (K. Milliken, unpublished). Fracture-wall fragments are locally included within the vein fill. Isopachous calcite cements envelop these fragments suggesting that large pores existed locally within the fractures. Other interesting textures observed within outcrop fractures include laminated carbonate fills that resemble biogenic growths and/or speleothems (K. Milliken and R. Folk, 2002 personal communication, Fig. 2.25). Banded cements are rooted on prismatic calcite crystals of the fracture fill and are generally followed by sediment cemented with microcrystalline calcite. However, in one sample the banded carbonate structures are preceded and followed by prismatic calcite crystals (Fig. 2.25).

Other carbonate cements in Fryberger and Koelmel (1986) and Koelmel (1986) diagenetic history (Table 2.4) were primarily found in subsurface samples (Appendix 2.A; Laubach and Schwartz, 1998 unpublished; K. Milliken, 2002 personal communication). Only one outcrop sample (w-042-97) contains a small percentage of dolomite cement (1% TVR). K. Milliken (2002, personal communication) has suggested that detrital dolomite may be acting as the nucleation site for ulterior carbonate cements and that the distribution of detrital dolomite in Weber sandstones may control the proportion of carbonate cement observed.

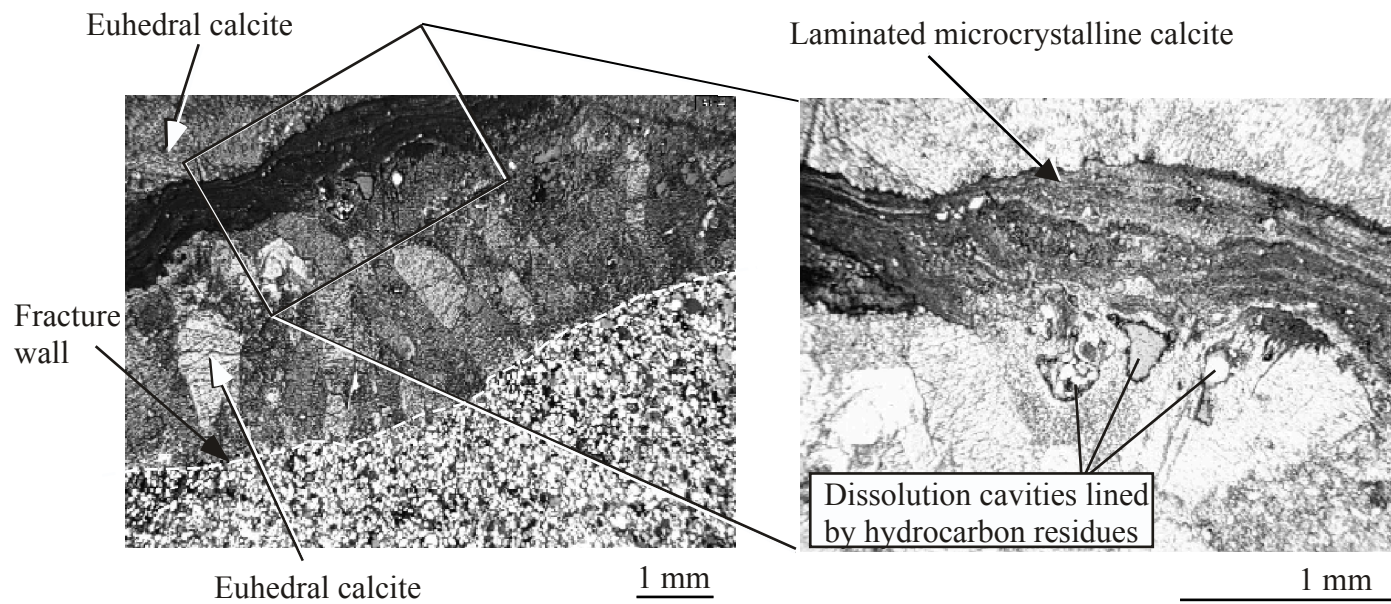


Figure 2.25. Photomicrographs of macrofractures in sample w-15 (collected by Stephen Laubach, 1998), from outcrops of Weber Formation sandstone. The vein is mainly filled with prismatic calcite crystals. A layer of banded microcrystalline calcite, associated with dissolution pores, is preceded and followed by prismatic calcite crystals. Milliken and Folk (personal communication) suggest a surface related process for the origin of these microcrystalline banded calcite features.

Ankerite fills pore space in the matrix and clogs large fractures in the subsurface (Fig. 2.26A). In subsurface fractures, quartz and ankerite are the main fracture fill components. Ankerite in subsurface fractures developed euhedral faces and shows marked zoning in SEM backscatter images (Fig 2.26B). According to Bowker and Jackson (1989) dolomite and ankerite cements are more abundant in the northwestern part of Rangely field than in the southeast. On the other hand, calcite cement is more abundant in the southeastern part of the field than in the northwest (Bowker and Jackson, 1989). Carbonate cement abundance also increases toward the base of Weber Formation in Rangely Field (Bowker and Jackson, 1989).

Hydrocarbons

Bowker and Jackson (1989) described asphaltene deposition in pores of Weber Formation sandstones at Rangely field. Remains of hydrocarbons were found in the matrix pores in outcrop and subsurface samples, suggesting that hydrocarbons migrated toward outcrops and subsurface areas. Evidence of hydrocarbon migration is also present in veins from outcrop and subsurface and suggests that the fractures propagated before hydrocarbon migration occurred. Hydrocarbon remnants are also found lining dissolution pores in the matrix and outcrop veins (Fig. 2.25), and in fractures filled with ankerite in subsurface (Fig. 2.26). Hydrocarbon migration postdated quartz precipitation as indicated by euhedral quartz surrounded by hydrocarbons in Figure 2.26.

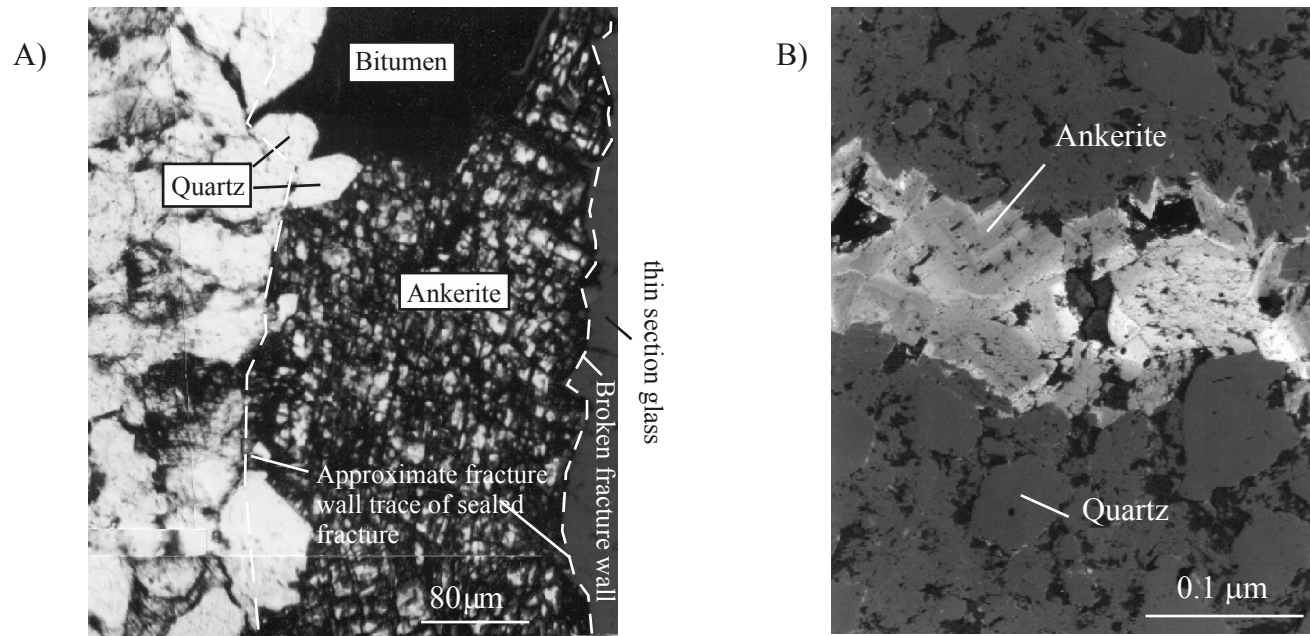


Figure 2.26. Ankerite-filled fractures in Rangely Field, Colorado. A) Euhedral quartz overgrowths lining fracture wall, bitumen postdates quartz cement. Timing relationship between ankerite and bitumen is dubious in this picture. Note rhombohedral cleavage in ankerite crystals (Emerald 46X, 1712 m depth, plane polarized light, courtesy of Stephen Laubach). B) Zoned ankerite filling subsurface fracture in Uinta Basin. Note zoning in ankerite crystals (back-scatter electron image, photomicrograph courtesy of Stephen Laubach).

A late diagenetic timing for hydrocarbon migration into the Weber Formation in the Piceance basin is proposed by Fryberger and Koelmel (1986) (Table 2.4). Waechter and Johnson (1986, and references therein) discussed the timing of oil migration into Weber Formation sandstones in the Piceance basin. Fryberger and Koelmel (1986) and Koelmel (1986) suggested that the primary phase of oil migration occurred before the Laramide-age structures formed (including Rangely Field). Hefner and Barrow (1992) suggest that generation of oil in the Phosphoria Formation probably started in the Early Jurassic based on source rock maturation modeling. Hydrocarbons were presumably trapped in a large stratigraphic trap in the Weber-Maroon transition and around paleohighs (Waechter and Johnson, 1986). Remigration of these hydrocarbons into Rangely Field presumably occurred during and/or after the deformation phase that produced the current structural configuration in the area (Koelmel, 1986).

Porosity

Porosity in outcrop samples varies from 2% to 22% (TVR, Appendix 2.A), higher than the porosity range observed in subsurface samples (0% to 12% TVR). The average porosity from outcrop samples is 11% (TVR) and from subsurface samples is approximately 3% (TVR, Appendix 2.A). The best reservoirs in Rangely Field have maximum porosity of 25% and averages of 12% (Bowker and Jackson, 1989), but the average values in marginal reservoir quality layers in the reservoir is 7% (TVR, Bowker and Jackson, 1989). The porosity is mainly primary in outcrops and subsurface locations (Appendix 2.A). A phase of

dissolution of detrital grains and cement increased the porosity, especially in outcrop localities (<5%, TVR). Koelmel (1986) estimated that up to 25% of the current porosity in Weber Formation sandstones is secondary in origin and includes dissolution of carbonate cements and unstable framework grains. It is possible that the distribution of grain coatings in the Weber sandstone stratigraphy is nevertheless the primary control on porosity preservation in these rocks.

Subsurface fracture quality results

Microfractures in outcrop and subsurface Weber Formation sandstones are filled with quartz cement and suggest that quartz precipitated during fracture propagation (synkinematic cement, Laubach et al., 1995). Synkinematic cements tend to occlude microfractures, but observational evidence (Laubach, 1999) suggests that fracture porosity preservation increases as a function of fracture aperture if only synkinematic cements fill in the fractures. In outcrop Weber sandstones, calcite cement is the dominant postkinematic cement and ankerite is the dominant postkinematic cement in the subsurface. Hydrocarbons, clays, and oxides are also postkinematic in Weber sandstones.

Degradation values quantified from thin sections at different depths in subsurface Weber sandstones describe the spatial variation of the probability of finding open fractures in the reservoir. Degradation estimates were based on point count data of samples collected from cores of the Larson 15X B well (Laubach and Schwartz, 1998 unpublished, Appendix 2.A, Fig. 2.27). Description of fracture fill proportions in macrofractures in the core allow a test of fracture

quality prediction against observations. The results of this comparison suggest that degradation is a good qualitative predictor of fracture openness in Weber sandstones. Similar results have been reported for other sandstone units (Clift et al., 1997; Laubach, 1999; Laubach et al., 2000). An analysis of the distribution of detrital dolomite, grain coatings, and feldspar abundance (original and current) in various facies of the Weber sandstone may help understand porosity, cement proportions and degradation index.

Fracture quality and sedimentary facies

Previous diagenetic studies recognized that occurrence and degree of diagenetic processes in Weber Formation sandstones are related to original sediment texture, composition, and environment of deposition (Bowker and Jackson, 1989). Fine grained, cross-stratified, quartzarenites and subarkoses, with wind-current climbing ripples and inverse-grading laminations, interpreted as eolian deposits, were least affected by pore-reduction diagenetic processes (Bowker and Jackson, 1989). Arkoses, moderately sorted, with trough cross-stratification, interpreted as fluvial, experienced abundant pore-reduction by carbonate cements (Bowker and Jackson, 1989). Subarkoses, bimodal size grain, structureless, interpreted as mixed dune-interdune sandstones, contain intermediate cement proportion between eolian and fluvial end members (Bowker and Jackson, 1989). Bioturbation, infiltrated clays, and early precipitation of calcite are pore-reducing diagenetic processes characteristic of these facies

(Bowker and Jackson, 1989). Final pore-volume reduction in structureless facies is intermediate between eolian and fluvial facies (Bowker and Jackson, 1989).

Based on Bowker and Jackson's (1989) qualitative characterization of sedimentary facies, porosity, and cement proportions in Weber Formation sandstones, it follows that there could be a relationship between fracture quality and sedimentary facies. I tested the hypothesis that sedimentary facies and fracture quality are related using a detailed description of sedimentary facies in cores of the Larson 15X B well by Fryberger (1979) and the results of fracture degradation predictions by Laubach and Schwartz (1998 unpublished) (Appendix 2.A).

The results suggest that cross-laminated facies of Weber eolian sandstones have the highest probability of containing open fractures (Fig. 2.28). Cross-laminated facies also have higher average porosity (Bowker and Jackson, 1989). Low porosity, structureless, bioturbated, and fluvial sandstones and siltstones have high degradation indexes, which predict largely filled fractures. One contorted layer sampled shows an ambiguous relationship with degradation, which may be cross-stratified facies involved in soft-sediment deformation.

MECHANICAL STRATIGRAPHY

Geldon (1986) studied the degree of stratigraphic heterogeneity within the Weber Formation in northwestern Colorado and southern Wyoming. According to Geldon (1986), shale break abundance and the number of individual beds increases to the south and east of Dinosaur, Colorado, in the same direction that

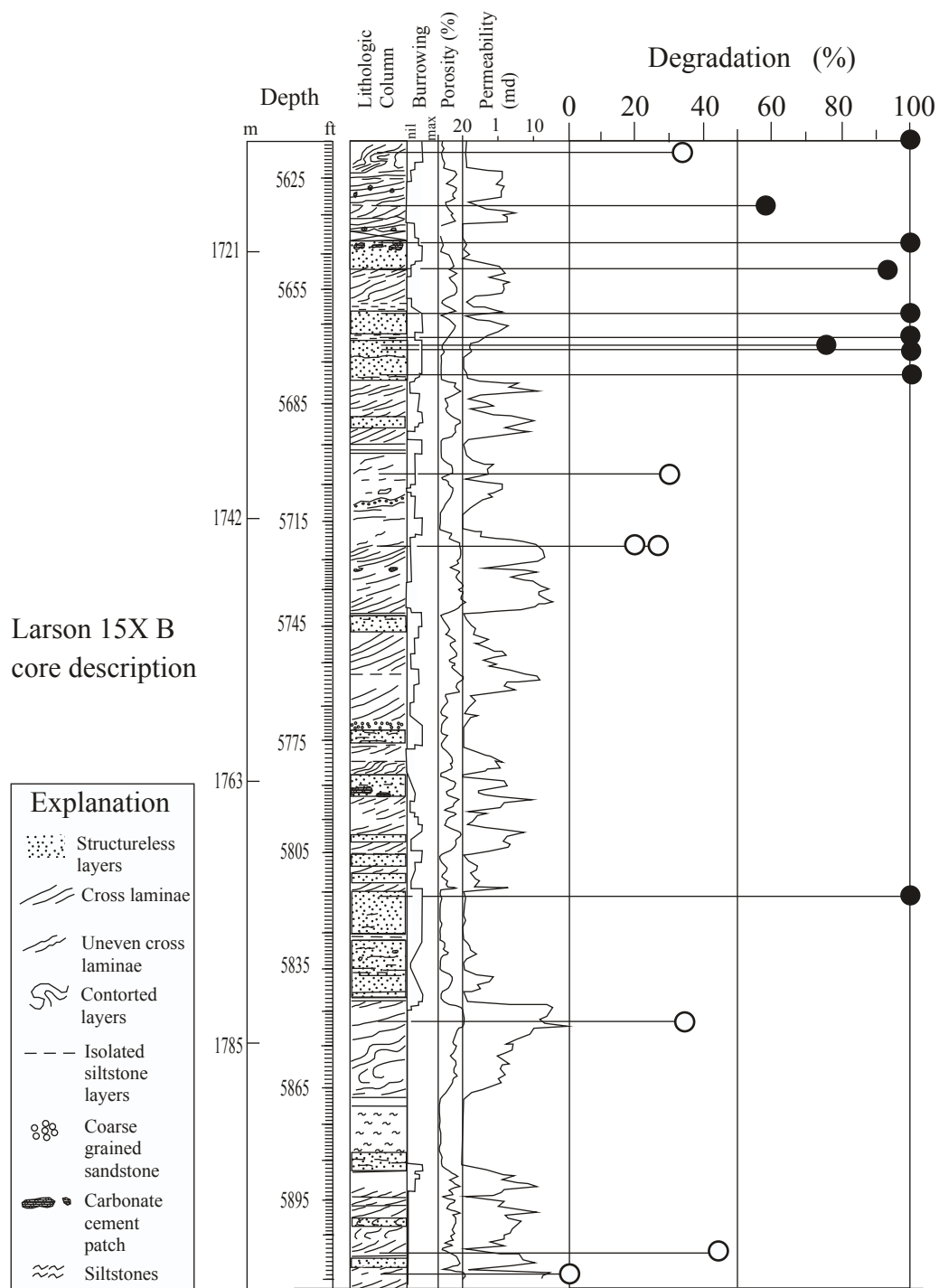


Figure 2.28. Sedimentary facies (Fryberger, 1979) and degradation values in Larson15X B well cores (Laubach and Schwartz, 1998 unpublished). Low degradation values imply high probability of open fractures, if large fractures are present.

Weber Formation thins out and changes laterally to fluvial-dominated red beds of the Maroon Formation. Consequently, shale breaks are probably more frequent in Rangely Field than in outcrop localities. Fryberger (1979) described the Weber Formation sedimentary succession along the Yampa River and showed that the middle portion of the Weber Formation at this locality is composed of thick, relatively homogeneous, structureless sandstones with few diastems. The lower and top portions of the Weber Formation are thinner than the middle part. These thinner sandstone units are separated from the thick middle unit by shale intervals and/or significant diastems. Fryberger's (1979) description of the Weber sandstone suggests that the mechanical thickness at North Disappointment scanline area is probably very thick, perhaps on the order of a hundred meters, whereas the lower portion of the Weber Formation in the Disappointment Draw area contains one or more thinner mechanical units.

A comparison of the stratigraphic column by Fryberger (1979) for the Weber Formation at Yampa Canyon, near Deerlodge Campground (Fig. 2.1), and a stratigraphic column and gamma ray log from a type well in Rangely Field (Bowker and Jackson, 1989) provide an illustration of the increase in stratigraphic heterogeneity in the Weber Formation from the outcrops studied in the north of the study area to Rangely Field in the south of the study area (Fig. 2.29). Figure 2.29 shows the intervals of eolian sandstones, interdune deposits, and fluvial facies in surface and subsurface localities, indicating the thickness of some possible mechanical layer units at these localities. The mechanical layer interpretation based on Fryberger (1979) stratigraphic column of the Weber

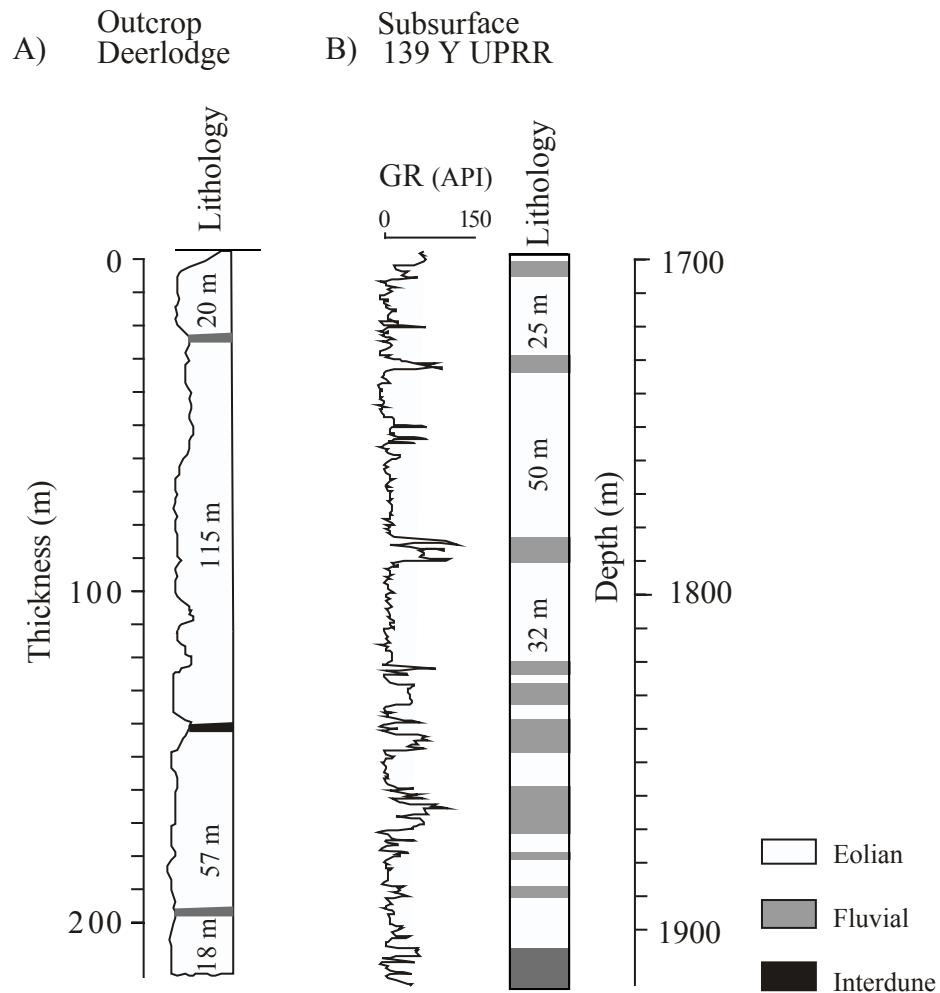


Figure 2.29. Distribution of eolian and fluvial facies in Weber Formation sections. A) Stratigraphic column at Yampa Canyon, near Deerlodge Campground (modified from Fryberger, 1979). B) Subsurface stratigraphic column from Rangely 139 Y UPRR type well (modified from Bowker and Jackson, 1989).

Formation at Deerlodge Campground can be appreciated in cliffs of the Yampa River Canyon (Fig 2.30). Fluvial facies contain mudstones that can make good mechanical stratigraphic boundaries. Interdune deposits and significant interruptions of sedimentation constitute mechanical boundaries in outcrops of Weber sandstones. Interdune deposits are associated with thin carbonate layers, mudstones, thinly laminated sandstones, and siderite nodules (Fryberber, 1979).

Observations along small canyons near South Disappointment pavement area revealed that the local mechanical layer is approximately 6 m thick where the aperture and length data from this pavement were collected. The layer exposed on top of South Disappointment pavement is a cross-stratified sandstone bed with locally contorted bedding. The base of the bed is a diastem or short interruption in sedimentation. Fractures on the pavement top terminate downward at the level of the diastem. Observations along a canyon next to Skull Creek pavement suggest a mechanical layer thickness of four meters at this other locality. The bed on which Skull Creek pavement sits is a cross-bedded sandstone with some degree of bioturbation that partly destroyed the cross-laminated structure. The mechanical layer thickness at North Disappointment pavement was not determined because the nearest canyon is more than a kilometer away from the pavement and a correlation of the beds from the pavement to the canyon was uncertain.

A north-south stratigraphic section from Bowker and Jackson (1989) illustrates a first-order mechanical stratigraphy in the Weber reservoir of Rangely Field, (Fig. 2.31). Operational fluid-flow units are vertically separated by low-permeability fluvial facies. These fluvial units can be correlated across Rangely

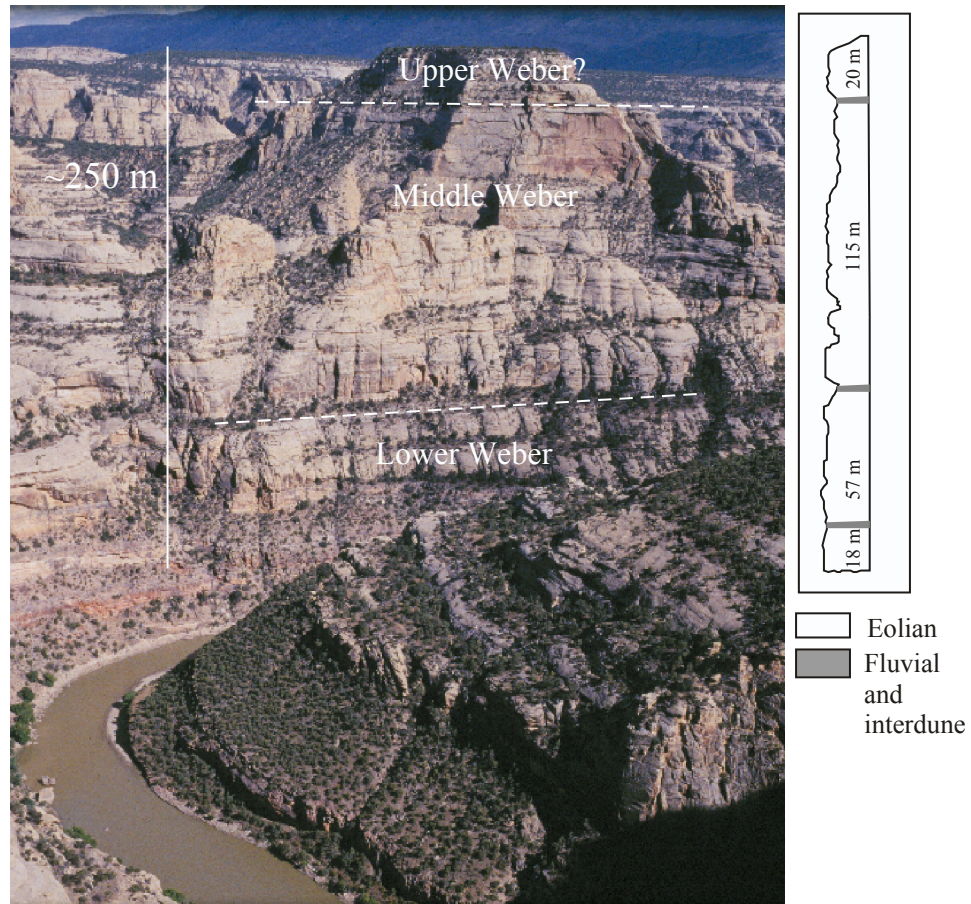


Figure 2.30. Field-based mechanical layer subdivision of Weber Sandstone in outcrops along Yampa River, Colorado and Utah. Weber Formation in this area can be subdivided into a thick middle sandstone and adjacent upper and lower thinner units. Note fracture terminations at bedding surfaces. Fracture terminations define mechanical units that control maximum fracture height. The stratigraphic column at one side of the picture is based on Fryberger's (1979) descriptions of Weber Formation sandstones along Yampa River.

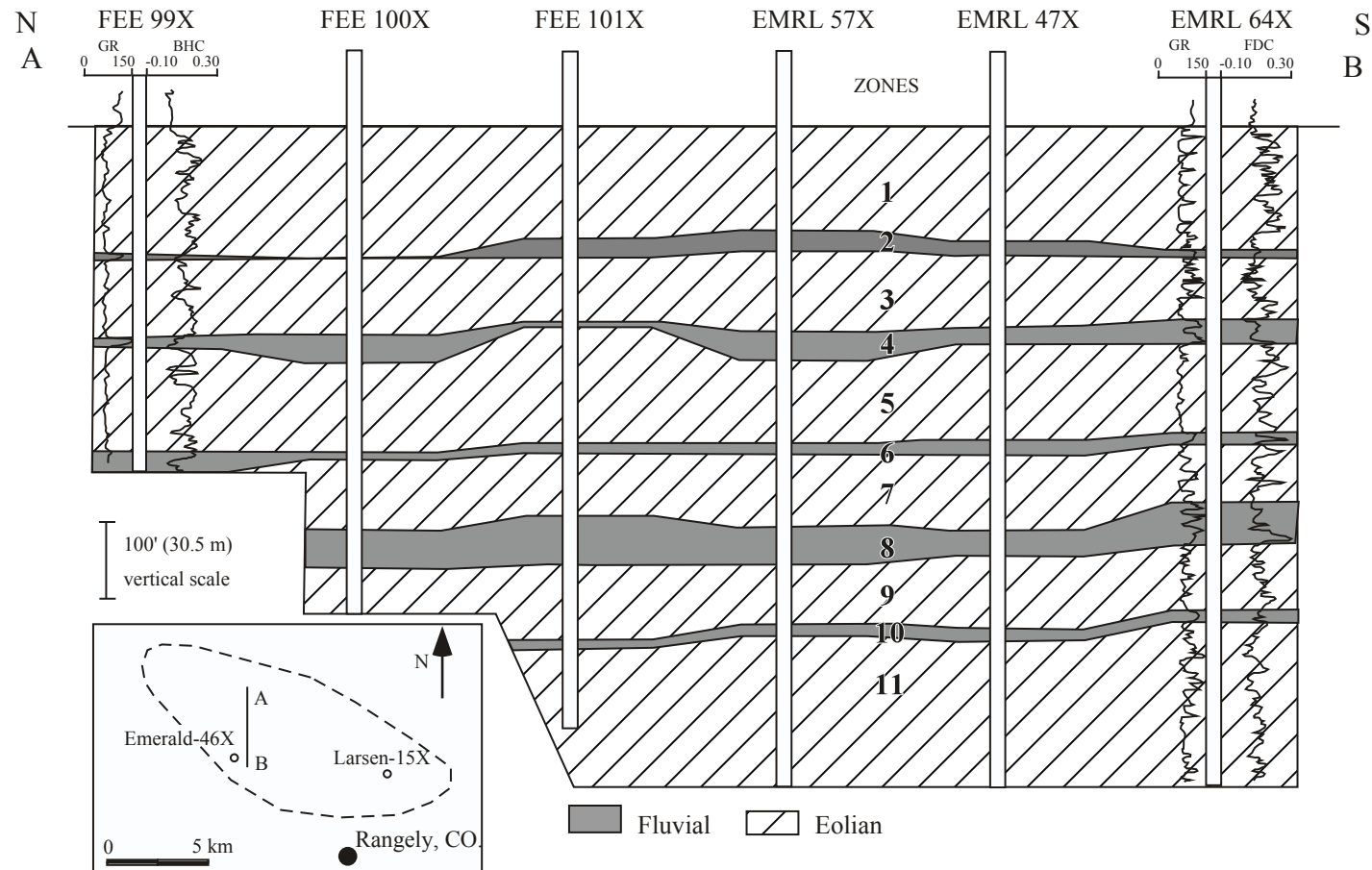


Figure 2.31. North-south stratigraphic section across Rangely Field (modified from Bowker and Jackson, 1989). Inset shows approximate location of stratigraphic cross section in Rangely Field. Logs are Gamma Ray (left) and Porosity (right), only the logs for the wells at each side of the cross section are shown for simplicity. The reservoir has been divided in 11 zones. Zones 2, 4, 6, 8 and 10 are seals for fluid flow (Bowker and Jackson, 1986). These fluvial units may also represent first-order mechanical boundaries for fracture propagation.

Field (Bowker and Jackson, 1989) separating units of eolian and mixed dune-interdune deposits, which probably represent large-scale mechanical units. Largest expected fracture sizes can be calculated for these reservoir units assuming that the boundaries of the mechanical layer limit fracture growth.

FRACTURE CONNECTIVITY

Another type of data collected from pavements was fracture connection data. Connectivity is a scale-dependent property of fracture networks (Laubach, 1992). Longer fractures have a greater probability of connection with other fractures. Connectivity also increases with fracture clustering. Fracture abundance is another important control on connectivity. The exponent of power law fracture size distributions is an indication of the proportion of small vs. large fractures in the observation domain. Large exponents indicate greater proportion of small fractures vs. large fractures. The degree of connectivity in fracture systems may be controlled in part by the proportion of large vs. small fractures in the network. The power law coefficient of the cumulative frequency distribution is a measure of the fracture intensity. Higher power law coefficients would indicate greater connectivity for similar power law exponents and similar spatial arrangements.

Connection data collected in the field consist of specifying if a fracture is isolated or has one (partly connected) or more connections (fully connected) with other fractures on the bedding surface (Ortega and Marrett, 2000). Connectivity data collected in the three pavements studied indicate that the degree of fracture connectivity in the pavements is low. Most of the fractures measured are isolated,

a few are partly connected and fractures with more than one connection are rare (Fig. 2.32). Fractures at North Disappointment pavement are the least connected and fracture networks at South Disappointment pavement show the highest proportion of connected fractures (~20% of total number of fractures). These partly connected fractures from South Disappointment pavement are well organized in swarms and extend for tens to hundreds of meters. The most common type of connection observed at South Disappointment pavement was curved (Type IIb, Ortega and Marrett, 2000) reflecting the stress perturbation interaction of fractures during growth (Olson and Pollard, 1991).

COMPUTER-GENERATED FRACTURE PATTERNS

Fracture orientation, fracture quality, mechanical layer thickness, and fracture intensity can be incorporated in realistic reservoir flow models using statistical procedures.

Documented relationships between fracture quality and other geologic parameters like sedimentary facies, stratigraphic position or structural position may guide the assignment of dual or single porosity reservoir characteristics to different portions of a reservoir. Figure 2.33 shows a preliminary subdivision of Weber reservoir sandstones in flow units, based solely on fracture quality information and the empirical sedimentary facies control found on fracture quality.

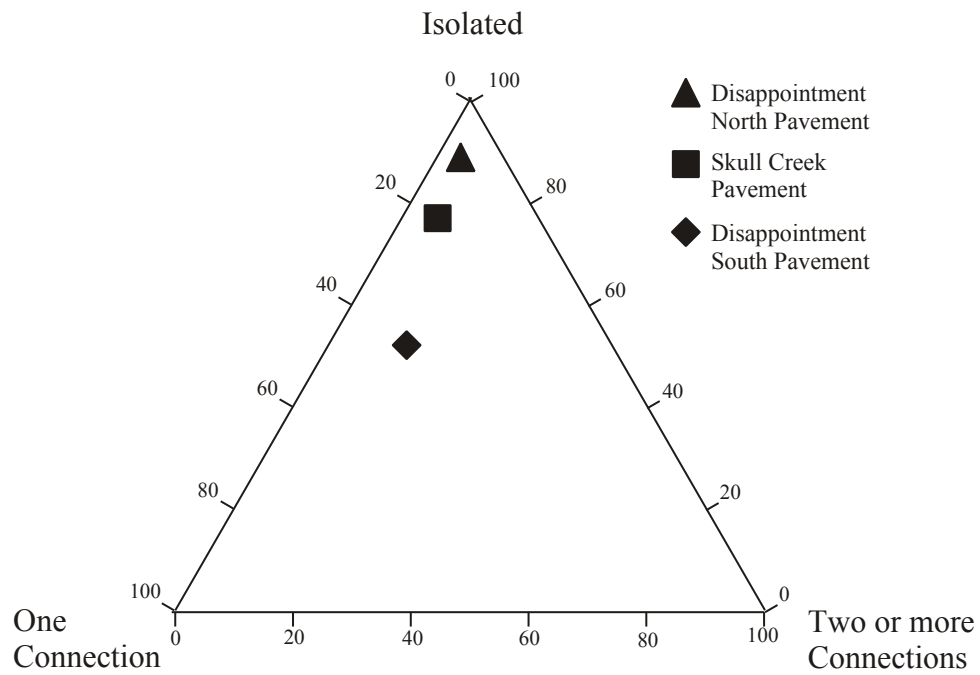


Figure 2.32. Fracture connectivity of pavements in the study area. Differences in the degree of connectivity are related in part to variations in the coefficient of the power law cumulative frequency length distribution.

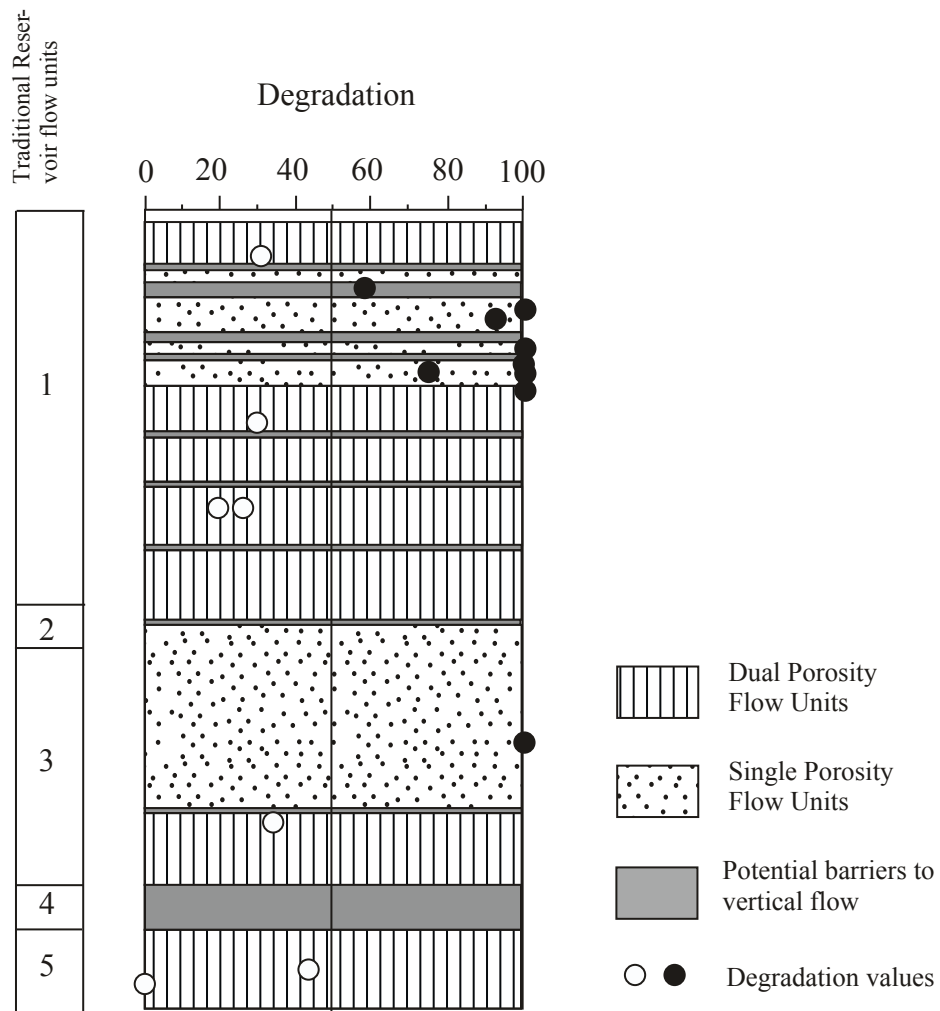


Figure 2.33. Possible fluid-flow units for Weber Sandstone reservoir based on fracture quality and sedimentary facies distribution. Potential barriers for fluid flow have been indicated. Seal layers are not all laterally continuous throughout the reservoir. (Field-wide traditional reservoir units have been indicated (Bowker and Jackson, 1989) for comparison with fracture-quality based reservoir units).

Subsurface macrofracture size predictions using microfracture data

I have used subsurface microfracture aperture and length distributions to estimate the aperture of fractures at the scale of first-order mechanical layer thickness (Table 2.5). Mechanical thickness values are based on traditional reservoir units in Rangely Field supported by field-wide correlations of fluvial mudstone intervals (Bowker and Jackson, 1989). This mechanical layer stratigraphic provides the fracture-size distribution control on the reservoir, but the fracture quality information determines how effective these fractures could be as fluid flow conduits.

To calculate the apertures of fractures that span the mechanical layer thickness I assumed that the maximum fracture height is the thickness of the reservoir unit. However, in a more general case, fractures may continue growing and connecting laterally along the bed. The frequency of fractures of height comparable to the mechanical layer thickness in areas of 10000 m² gives an approximate indication of the number of fractures that span the bed thickness in the surroundings of a given well. Using this frequency we can calculate the aperture of these fractures assuming that fracture length and apertures are related (e.g. Fig. 2.14). Maximum apertures obtained are in the order of 150 to 700 cm. Although these values seem high for fracture apertures, outcrop observations suggest that they are possible. These values indicate the kinematic aperture (distance perpendicular to fracture walls). Minerals probably occupy part of the fracture aperture and the effective fracture aperture (i.e. hydraulic aperture) is less than the kinematic aperture. Fracture quality predictions, based on matrix pore

Table 2.5. Reservoir-scale fracture size predictions based on microfracture size distribution results.

Primary set in rose diagram of microfracture strikes								
Estimates based on sample	Traditional units*	Layer thickness (m)	Length power law coefficient (mm ⁻² -e)	Length power law exponent (e)	Frequency (fractures /10000 m ²)	Aperture power law coefficient (mm ⁻² -c)	Aperture power law exponent (c)	Maximum aperture (mm)
1712	1	51	0.03064	-2.168	0.019	2.99E-06	-2.43	354
	3	31			0.056			227
	5	37.5			0.037			269
	7	30			0.060			221
	9	26			0.082			194
1738	1	51	0.106	-1.747	6.327	1.30E-04	-1.869	696
	3	31			15.097			437
	5	37.5			10.826			522
	7	30			15.987			424
	9	26			20.528			371
Secondary set in rose diagram of microfracture strikes								
Estimates based on sample	Traditional units*	Layer thickness (m)	Length power law coefficient (mm ⁻² -e)	Length power law exponent (e)	Frequency (fractures /10000 m ²)	Aperture power law coefficient (mm ⁻² -c)	Aperture power law exponent (c)	Maximum aperture (mm)
1712	1	51	0.03676	-1.578	13.70	5.40E-05	-1.85	305
	3	31			30.06			199
	5	37.5			22.26			235
	7	30			31.66			194
	9	26			39.68			172
1738	1	51	0.089	-1.742	5.61	7.30E-05	-1.885	517
	3	31			13.35			326
	5	37.5			9.58			389
	7	30			14.13			316
	9	26			18.13			277

*: Bowker and Jackson (1989)

surrogates, provide an estimate of the proportion of these large fracture porosity that may be filled with minerals. The largest fracture aperture observed along North Disappointment scanline (observation length ~208 m long) was approximately 1 m.

Fracture pattern simulations

I wrote a C⁺⁺ program (FracPattern, Appendix 4.A) to create fracture pattern realizations using the parameters of power-law fracture size distributions derived from microfracture and macrofracture maps and scanlines, mechanical stratigraphy, fracture quality, and orientation data. Fractures are located assuming a power law average spacing distribution specified by the user. The spacing distribution can be derived from the fracture aperture or fracture length distribution by obtaining the inverse of the fracture frequency distribution. The first fracture size is chosen at random from the size distribution. This first fracture of the pattern is also located at random such that it is contained within the boundaries of a simulation area. The next fracture size is chosen at random and its average fracture spacing is calculated from the spacing distribution. This spacing value is measured from the previous fracture located in the pattern to either side at random, and the center of the fracture is also located at random, making sure that the fracture is contained within the simulation area.

Aperture and length size distributions are expected inputs for the program, but if information is not available for one of them the program derives the other size distribution based on empirical aperture-length relationships (Moros, 1999),

theoretical assumptions (Marrett, 1996), and/or a minimum set of aperture-length observations.

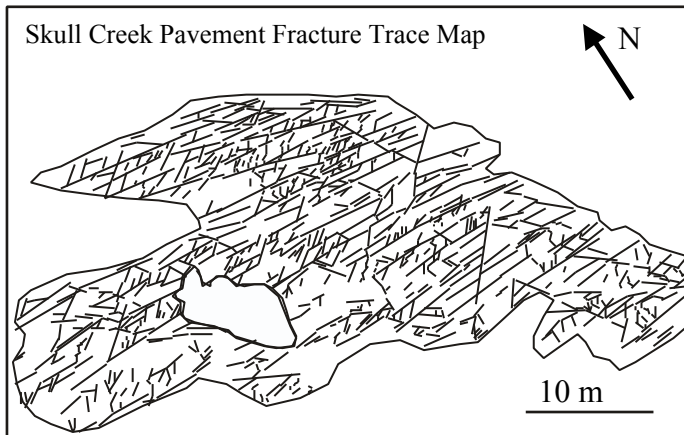
The program was first tested with information from Skull Creek pavement and the results were compared visually with interpreted aerial photos (Fig. 2.34). There is good visual agreement between observed and modeled fracture patterns, suggesting that statistical realizations can produce realistic fracture patterns if the data used for modeling are relevant. The patterns generated assume minimum fracture size preserves at least partial fracture porosity. This fracture size was chosen after inspection of thin sections made from field samples. The emergent threshold was then assumed to be 1 mm aperture.

The same procedure was applied to one of the wells studied (Larson 15X B cores) at two different depths, based on information extrapolated from microfracture analyses of SEMCL photomicrograph collages (Fig. 2.35). Results obtained for these two depths, under different assumptions of minimum fracture size preserving porosity, predict very different fracture patterns. Effective fracture connectivity (i.e., capable of conducting fluids) is predicted to be high in one of the realizations where two orthogonal fracture sets intersect and where significant fracture porosity is preserved for fractures greater than 1 mm aperture with low degradation. Effective connectivity is low for the other realization where I assumed a high degradation for this contorted bedding interval, although the analysis of one sample at 1712 m indicates low degradation. Postkinematic cement was assumed to fill fractures smaller than 5 mm aperture, only to indicate that much larger fractures than in the other realization could be filled with cement.

Skull Creek Pavement Aerial View



Skull Creek Pavement Fracture Trace Map



Skull Creek fracture pattern realization
 Strikes 50° - 65° and 80° - 110°
 Emergent threshold: 1 mm

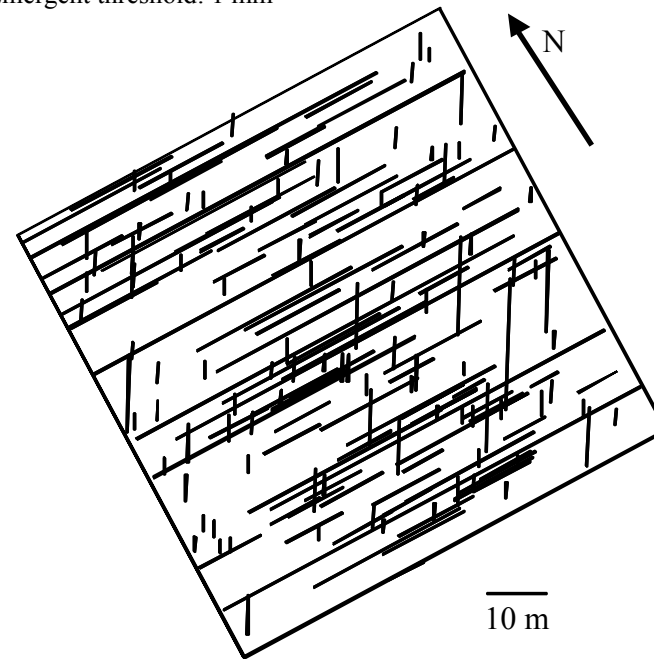


Figure 2.34. Observed and software-predicted fracture patterns for Skull Creek pavement. The software (FracPattern) generated a fracture realization based on fracture orientation, fracture length, and fracture aperture distributions from field measurements. Fracture size range displayed in the realization is based on the minimum aperture size that starts preserving fracture porosity as observed in thin sections from field samples (~ 1 mm). The pattern obtained from the model agrees visually with the fracture pattern observed in the field.

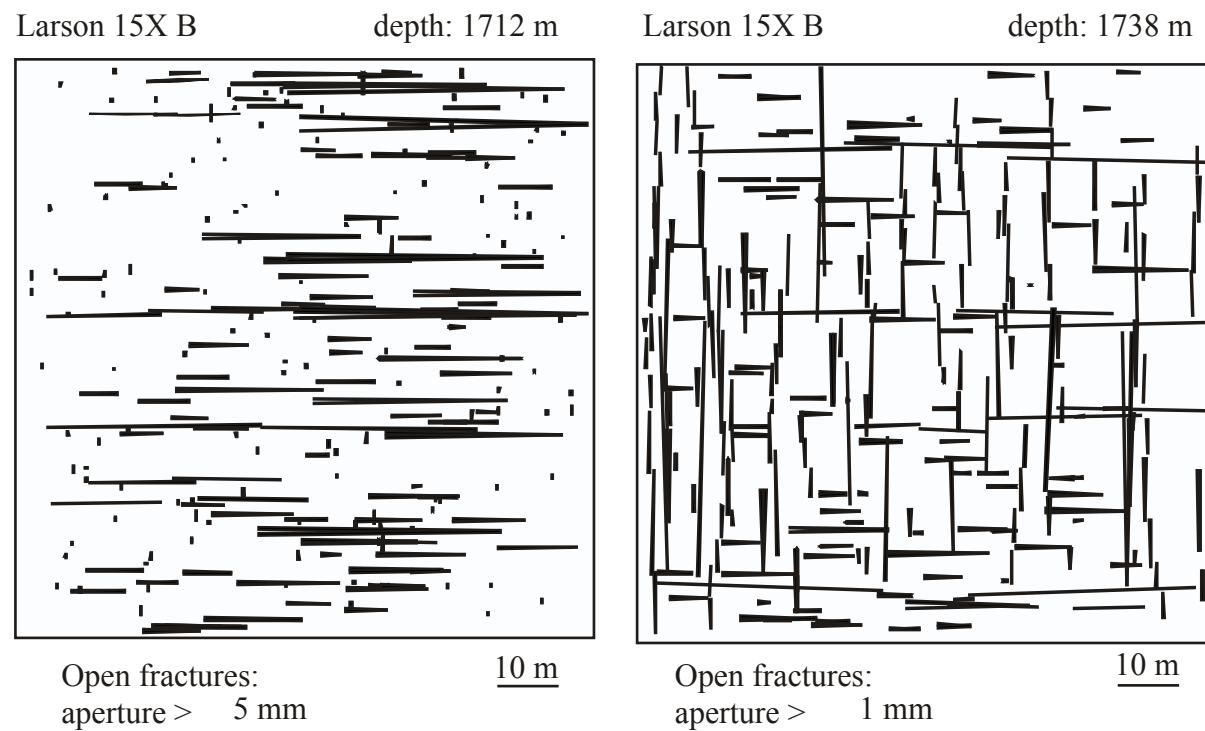


Figure 2.35. Fracture pattern realizations based on microfracture observations from thin sections at depths 1712 m and 1738 m, Larson 15X B well (Table 2.5). Connectivity of fractures potentially retaining porosity seems more favorable to fluid flow at 1738 m where two orthogonal fracture sets intersect. Fracture pattern realization from thin section at 1712 m depth suggests fracture clusters in one of the sets but lower overall connectivity. Size of open fractures is speculative for realization at 1712 m to show the impact of available fracture porosity on expected connectivity.

The realization suggests that one of the orthogonal fracture sets is almost completely sealed and does not contribute to fracture connectivity.

DISCUSSION OF RESULTS

Fracture orientations and fracture timing

Fracture strike is similar in gently dipping beds over most of the study area, and fracture strike is not systematically parallel with or perpendicular to local structures. Published fracture orientation and restoration analyses suggest that the WNW-striking fracture set predates the current structural configuration in the area (Silliphant et al., 2002; Wilkins et al., 2001). Silliphant et al. (2002) suggest that fractures at Split Mountain were sheared during fold development. However, no sheared fractures were evident in the localities studied and the great majority of fractures measured are simple opening-mode fractures. Fractures are mineralized to different degrees in all localities. The cement in some veins is prismatic calcite crystals with no evidence of shear movement along the vein walls.

Lack of genetic relationship between fractures and regional-scale structures is further supported by analysis of the spatial distribution of large fracture swarms and the structural configuration of the Disappointment Draw area. Novoa et al. (1998) interpreted the structure at Disappointment Draw as the result of monocline interference (in plan view). The northern and the southern segments of Disappointment Draw Monocline are each approximately 7 km long and are joined by a narrow monocline structure that forms a kink in the

topography near North Disappointment pavement (Fig. 2.1). Novoa et al. (1998) interpreted this kink as the interference zone between the Disappointment Draw Monocline and the Yampa River Monocline. If fracture location were associated with regional-scale structure, then I expect the occurrence of large swarms (i.e. spatial concentration of fractures) and veins near the hinges of the structure or in the narrow interference area between the two monoclines, which experienced significant strain during the formation of the current structure. Although vein swarms are present in this area, they are located away from the hinge zones and limb of the Yampa River monocline. One of the largest fracture swarms is located approximately at the center of the northern segment of Disappointment Draw Monocline. The largest fracture observed in the field, a fracture having maximum aperture of 2 m (Marrett and Laubach, 1998 personal communication), was encountered in this swarm along North Disappointment scanline. This large fracture was sampled by the North Disappointment scanline showing a local aperture of nearly 1 m at the interception with the scanline. Another fracture swarm contains veins with apertures on the order of tens of centimeters and is located between North Disappointment and South Disappointment pavements. Finally, a third fracture swarm was found in South Disappointment scanline locality in the central portion of the southern segment of Disappointment Draw Monocline.

Macrofracture strike in outcrop and in subsurface share some common characteristics (Fig. 2.7). Both in outcrop and subsurface there are two sets of fractures striking at a relatively high angle with respect to each other, one set

striking close to east and another set striking close to north. One exception is the macrofracture data from the Emerald 46X well but these fractures described as “joint-like” fractures (Narr, unpublished) strike parallel to induced fractures in the same well. Macrofracture strikes in outcrops of Skull Creek area are similar to macrofracture strike orientations in the Larson 15X B well. Fracture strikes in outcrop and subsurface are qualitatively comparable because bedding dips are relatively low in all areas and no significant vertical-axis rotations have been documented for the area. Similarities in the macrofracture strike in surface and subsurface further supports that the fracture systems studied are unrelated to the regional-scale structures in the area (Silliphant et al., 2002).

Fracture size distributions sampling effects

Mechanical layer effect on fracture length distributions

A test of the effect of mechanical layer thickness on fracture length distributions involved measuring the length of fractures in small and in large areas of South Disappointment pavement. All fractures visible with the naked eye were measured in the small area and only fractures longer than 1 m were measured in the large area. The purpose of collecting data at these two observation scales was to test whether the size distribution of large fractures is affected by topologic large-scale sampling artifacts deviating from the size distribution of smaller fractures. The estimated bed thickness for this pavement was 6 m based in observations on a nearby canyon. If topology produces a change in the power law

length distribution we expect this change to happen at a length scale approximating the mechanical layer thickness for penny-shaped fractures.

The cumulative frequency distributions for both areas show deviations from an ideal power-law distribution at the small- and large-scale ends of the size distributions (Fig. 2.12). An increase in the slope of the fracture size distribution for the largest fractures may be produced as a result of constructing a cumulative distribution from a discrete distribution in a finite observation area (Pickering et al., 1995; Bonnet et al., 2001). This effect is also called the upper-truncated power law effect (Burroughs and Tebbens, 2000). An increase in the slope of the fracture size distribution for the largest fractures can also occur by changes in sampling topology (Marrett, 1996). Censoring artifacts can also increase the slope of fracture length distributions, but this effect was avoided by choosing observation areas that enclose the total lengths of the fractures. Reliable data on the abundance of the largest fractures in the small observation area cannot be obtained because only a few of the largest fractures are present in the small observation area. The spatial architecture of the fractures can produce different effects at the large-scale end of the distribution (Ackermann and Schlische, 1997; Borgos et al., 2000).

In Figure 2.12, fracture length data from a large area of observation with a range of sizes that includes the length-scale of the mechanical layer thickness and avoids censoring and truncation artifacts shows the possible effect of mechanical layer thickness on fracture size distributions. Fracture lengths more than four times the mechanical layer thickness give sufficient control above the mechanical layer thickness to discard the possibility of an increase in slope produced by the

upper-truncated power law effect in the cumulative distribution. A bias power-law model (Marrett, 2000) adequately represents a significant portion of the fracture length distribution for fracture sizes larger than the mechanical layer thickness. Fractures smaller than the mechanical layer thickness deviate from this bias model with a shallower slope, as expected for two-dimensional sampling unaffected by topologic artifacts.

An increase in the slope of the fracture size distribution is probably present in the data from the small observation area but the effect is not clear because at most it affects only the three largest fractures. However, the three largest fractures in the small area length distribution are all longer than 6 m. Topological considerations predict that most fractures in the small observation area were two-dimensionally sampled, producing a distribution that is best model with a lower power law exponent than a three-dimensional sampling. A bias model to the small-area fracture length distribution yields a power law exponent that is lower than the power law exponent of the bias model fit to the large observation-area length distribution. These results support the idea that sampling topology artifacts must be taken into account when analyzing the size distribution of fractures that span the mechanical layer thickness. Direct application of the formulas in Marrett (1996) would probably result in incorrect predictions because other artifacts reinforce the deviation of the power law model at the large-scale end of the distribution. For example, Borgos et al. (2000) suggest that common spatial distributions of fractures would produce less-steep slopes in fracture length distributions at scales larger than the mechanical layer thickness.

The fracture length distribution obtained from Skull Creek Anticline, suggests a break in the slope of the power law distribution at the scale of approximately 3 m (Fig. 2.11). This length scale is approximately the mechanical layer thickness estimated for Skull Creek Anticline pavement, as inferred along nearby canyons (Table 2.1, Fig. 2.36).

Connectivity effect on fracture length distributions

Maps of fracture traces often show complex geometry at any given scale of observation. Rouleau and Gale (1985) proposed an index to quantify fracture connectivity. According to Rouleau and Gale (1985) the connectivity of fracture-trace maps increases with the number of fracture sets present, fracture density, and fracture orientation dispersion. Degree of connectivity can potentially affect fracture size distributions, particularly at the large-scale end of the distribution, because longer fractures have a higher probability of connecting with other fractures to form even longer fractures.

Measurement of fracture length on two-dimensional observation areas is challenging. Ortega and Marrett (2000) derived field criteria to determine fracture tips and measure fracture lengths. However, these criteria are insufficient to describe the complex geometry of interconnected fractures. Moreover, some of the most diagnostic features of interconnected fractures can be difficult to discern in outcrop (e.g., continuity of cement fill at the connection point between fractures). Interconnected fractures might actually grow as an integrated group, in which case they ought to be treated as a single structure.

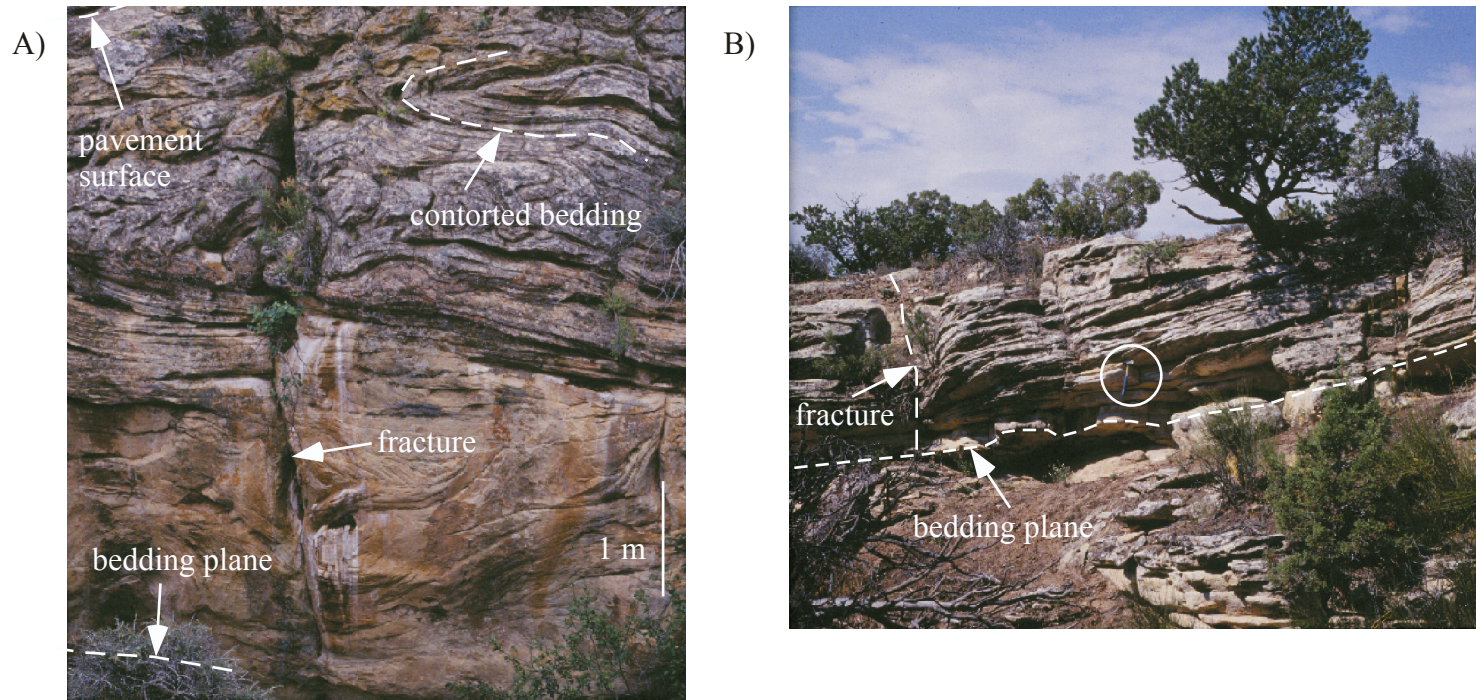


Figure 2.36. Field-based mechanical layer thickness estimation. A) Cross stratified and in part contorted layer at South Disappointment pavement (~ 6 m thick). Partly-open fracture terminates at bedding plane in A), only a small portion of the pavement surface was photographed. B) Cross stratified layer at Skull Creek pavement. Geologist hammer (~50 cm long) within circle for graphic scale . The total thickness of this layer was estimated as 4 m but weathering of the pavement top has reduced its thickness toward the Canyon. The base of the layers in A) and B) are weathering-recessive diastems.

Comparison of fracture-length distributions from fracture segments and interconnected groups in log-log plots for North Disappointment pavement (Fig. 2.15) suggests that the longest fracture segments are less heterogeneous in size than the longest interconnected fracture groups. Less variability in size at the large-scale end of the fracture-segment length distribution produces a deviation of the distribution from the underlying power law. This increase in the slope of the size distribution is probably unrelated to censoring artifacts because this sampling effect was avoided during data collection and all fractures measured are contained entirely within the observation domain. The increase in the slope of the size distribution for the fracture-segment length distribution may be produced by a change in the sampling topology of the fracture population (Marrett, 1996; Ortega and Marrett, 2000). Long fractures, spanning the thickness of the mechanical layer, will reflect three-dimensional sampling regardless of the fact that sampling was done in a two-dimensional domain. If a topologic effect produces the deviation of large fracture sizes from an ideal power law, a mechanical layer of approximately 1.3 m would be predicted for North Disappointment pavement because it is at this length scale where the length distribution departs from the underlying power law.

The fracture-length distribution for interconnected fracture clusters and isolated fractures suggests that the longest interconnected clusters follow the same length-distribution as fractures smaller than the mechanical layer thickness. This

result suggests that the increase in slope observed for the fracture-segment length distribution is in part an artifact associated with the definition of fracture length.

The definition of fracture length is not trivial (Ortega and Marrett, 2000) so criteria used for fracture length measurement should be clearly established before data collection and data sets should contain information on fracture connectivity. Connected fractures may grow together, as a single structure, and reflect the same fracture system as the smaller isolated fractures, but the geometry of connected fracture groups becomes more complex as fracture propagation progresses.

Mechanical layer effect on fracture aperture distributions

Changes in power law scaling at the large-scale end of an aperture distribution can be explained by a number of artifacts. One of these artifacts is topologic (Marrett, 1996) and occurs when fractures span the entire thickness of the layer. Fractures that do not span the entire thickness of the layer are distributed within the volume of fractured rock. Only a portion of these fractures are visible in any given two-dimensional layer-parallel exposure (e.g., bedding planes). Fractures that span the bed thickness have a better chance to be sampled by any scanline on the top of a mechanical layer than fractures distributed within the mechanical layer, some of which do not even reach the boundaries of the mechanical layer. This change in sampling probability is the topologic effect described by Marrett (1996) and its effect is to produce an increase in the slope of the size distribution. An increase in the slope of the size distribution would predict

more “small” scale fractures in the scanline sampling than the ones observed. The “small” fractures under-sampled should be within the rock volume but do not have a trace on the observation domain (typically a two-dimensional cut of the volume of rock).

The bias model for the fracture aperture distribution obtained from North Disappointment scanline (Fig 2.9) suggests that a single power law is an adequate model for the entire range of fracture sizes observed. This power law model adequately predicts the largest aperture size observed along the scanline (~1 m). The extent of the power law scaling for North Disappointment scanline also suggests that the mechanical layer thickness controlling this size distribution is very thick, possibly in the order of hundreds to a thousand meters as suggested by common fracture aspect ratios (Vermilye and Scholz, 1995; Johnston and McCaffrey 1996; Moros, 1999; Chapter 1). Fryberger (1979) estimated that the Weber Formation near Deerlodge Campground (Fig. 2.1) is 232 m thick. However, close inspection of Weber Formation cliff faces along Yampa River Canyon (Fig. 2.30) suggests that the middle-upper part of the Weber Formation is a mechanically homogeneous sandstone layer approximately 100 m thick containing no other smaller mechanical units. This portion of the Weber Formation is the best candidate for a mechanical layer thickness that explains the size of fractures observed in North Disappointment scanline area.

In contrast, the fracture aperture distribution from South Disappointment scanline shows a sharp change in the power law slope at an aperture of approximately 15 mm. If this change in the slope of the aperture distribution is

related to topologic effects then the mechanical layer should be on the order of tens of meters thick, based on the fracture aperture vs. fracture length relationship used for North Disappointment scanline. Direct observation of the mechanical layer thickness along a small canyon near South Disappointment pavement indicates a minimum mechanical thickness of 6 m. The fracture length distribution from South Disappointment pavement shows a break in the power law slope at the length-scale of the possible mechanical layer thickness (~5 m) for fracture segments in the small observation area (Fig. 2.12). The fracture length distribution of a larger observation area on this same pavement suggests that topologic artifacts produce the break in the power law exponent observed in the fracture length distribution of the small area (Fig. 2.12). A topologic effect is supported by small fractures deviating from the bias model with a shallow slope whereas the large fractures of the large observation area follow a steeper segment of the power law.

Mechanical layer control on maximum fracture size.

Fracture size data obtained in the field support the hypothesis that the mechanical layer thickness controls the maximum fracture size observed. The largest fracture in North Disappointment scanline area has a maximum kinematic aperture close to 2 m and the mechanical layer thickness estimated in this area is 100 to 120 m. Veins in South Disappointment pavement show maximum apertures of 10 to 20 cm and the mechanical layer in this area is 6 to 20 m thick. Estimated mechanical layer thickness at Rangely Field may impose a maximum

fracture size in subsurface. No fractures with cement fill in excess of 1 mm were observed in cores of Weber Sandstones from Rangely Field, which suggests thin mechanical layers (in the order of meters to tens of meters). However, microfracture aperture extrapolations predict fracture apertures as large as 70 cm for the thickest mechanical layer estimated for subsurface Weber sandstones at Rangely Field. Another explanation for the lack of large mineralized fractures in core is poor core recovery of large fractures.

Prediction of macrofracture orientation using microfracture data

Microfracture strike analyses using oriented samples from outcrops suggest that systematic measurement of high suitability microfracture strikes adequately predicts the strike of macrofractures in the same volume of rock (Figs. 2.15 and 2.16). However, microfracture strikes show greater dispersion than the macrofracture strike dispersion. Greater strike dispersion is probably associated with incorrect classification of microfractures, complex microfracture traces, and small number of microfractures measured.

A test of microfracture reproducibility in subsurface samples indicated that the dominant and secondary microfracture sets from two different areas of a thin section are reproducible (Fig. 2.21). However, the average strike and strike dispersion vary. Microfractures from collage L15-5618c(1-10) are characterized by a greater strike dispersion than microfractures from collage L15-5618c(43-54). This greater dispersion in orientation in collage L15-5618c(1-10) may be attributed to a number of effects including: incorrect classification of some

microfractures, digitization errors, and/or natural variation of fracture strike at the microscopic scale. Further comparison of the collages studied suggests that microfracture strike determination improves with the number of microfracture strike measurements and it also improves with the suitability of microfractures. The photomicrograph collage L15-5618c(43-54) contains a microfracture swarm where parallel strikes of microfractures facilitates their interpretation and classification as high-suitability microfractures. On the other hand, the photomicrograph collage L15-5618c(1-10) comes from an inter-swarm area and contains a smaller number of high suitability microfractures. The contrasting locations of these two collages within a thin section probably represents two end members of microfracture orientation results, and the differences in average strike and dispersion are possibly close to the maximum that could be found. The dominant microfracture strike may vary in a thin section because of variations in the spatial distribution of microfractures. For example, an apparent maximum microfracture strike can be found in the orientation of a secondary set if the photomicrographs are taken in a swarm of microfractures of the secondary set.

Prediction of macrofracture size distribution using microfracture data

Results of extrapolation of microfracture size distributions to the scale of macrofractures produced positive results (Fig. 2.18). This result is significant because it suggests that small, two-dimensional domains of a thin section can provide enough microfracture information to predict macrofracture size

abundance at scales that are important for fluid flow modeling and other economic purposes.

The microfracture intensity in Weber Formation sandstones is low and large areas of a thin section need to be imaged to obtain sufficient microfracture data, particularly for one-dimensional sampling. The probability of sampling fractures in one-dimensional domains is lower than the probability of sampling fractures in two-dimensional domains so fewer microfracture data can be obtained from one-dimensional sampling domains than from two-dimensional sampling domains. If only a few microfractures are present in an SEM-CL photomicrograph collage, calculation of microfracture intensity may be unreliable. In general, numerous microfractures (at least 30 and preferably over 100) probably must be imaged and sampled along a scanline to obtain a reliable estimate of microfracture intensity.

Results for Disappointment Gulch Scanline 1 (Fig 2.19) suggest that the microfracture aperture distribution may be predicted using macrofracture intensity. However, the results from North Disappointment scanline were not satisfactory. Scarce data probably produced an inadequate estimate of microfracture intensity because the area imaged from the thin section was small and the scanline length too short to provide reliable intensity values. Moreover, the microfracture intensity obtained from this sample is probably biased by the presence of a macrofracture and associated microfractures in the area where the photomicrographs were taken (e.g., microfracture spatial distribution effect).

However, for practical purposes, we are interested in using microfracture aperture distributions to predict macrofracture aperture distributions. Scarce one-dimensional data did not allow construction of reliable one-dimensional microfracture aperture distributions from the thin sections studied. The macrofracture power law distribution from North Disappointment scanline suggest that only 1 or 2 microfractures 1 micron wide or larger would be encountered by a scanline as long as a standard thin section. It consequently would have been infeasible to obtain a useful one-dimensional aperture distribution from a thin section-scale scanline for North Disappointment scanline area without more samples and an exhaustive SEM-CL imaging effort. A similar calculation of expected number of microfractures for Disappointment Gulch Scanline 1 indicates that approximately 32 microfractures 1 micron wide or larger would be found along a scanline running the length of a standard thin section. This number is not very large but might allow construction of a reliable one-dimensional aperture distribution. It follows that if fractured reservoirs in the subsurface have these levels of fracture intensity, one-dimensional aperture distributions from microfractures may not provide a useful guide for macrofracture intensity. Two dimensional aperture distributions would be needed instead and topologic conversions (2D-1D, Marrett, 1996) are necessary to estimate macrofracture abundance.

Use of subsurface microfractures for subsurface macrofracture characterization

Two-dimensionally sampled microfracture aperture distributions from SEM-CL collages of subsurface samples suggest that a power law provides an adequate model to explain their size distributions (Fig 2.22). However, microfracture size distributions are affected by sampling artifacts similar to macrofracture size distributions.

The largest apertures in the distribution of the dominant microfracture set from 1712 m depth seem to follow the power law suggested by the bias model, instead of showing the characteristic fall off. This effect might be the result of sampling microfractures in a microfracture swarm. The bias power-law model for the dominant set in the thin section from the sample collected at 1712 m depth has also a high exponent (-2.43). Exponents this high are uncommon for two-dimensional sampling of fractures (Bonnet et al., 2001). If the bias model is correct, the power law model implies that for fractures with apertures larger than ~0.01 mm this set is not the dominant set and the secondary set becomes the dominant set for larger-scale fractures.

One possible explanation for the characteristics of the microfracture size distribution from the most abundant microfracture set in the sample collected at 1712 m is that this distribution is affected by the occurrence of a microfracture swarm in the area where the SEM-CL collage was acquired. Degree of clustering in fracture networks is another parameter interpreted to affect fracture size distributions (Borgos et al., 2001; Bonnet et al., 2001), but fracture spatial organization effects on fracture size distributions are not well understood yet.

The determination of microfracture length from SEM-CL images is not trivial because many microfractures terminate at the boundaries of grains, at pores, or continue around grains, making it difficult to distinguish them from the cement that surrounds the grains.

Subsurface microfracture length distributions are adequately modeled using power law models (Fig. 2.23). Their distributions have similarities with the aperture distributions obtained for the same fracture sets in the same samples. A higher power law exponent than found for the other microfracture power law length distributions characterizes the distribution for the most abundant set in the sample collected at 1712 m depth. The bias model for the aperture and length distributions of this microfracture set are consistent and probably reflect a real underlying power law distribution or an artifact that affects both aperture and length in this microfracture set. One possible explanation for the results obtained is that the high exponents of the aperture and length distributions for this microfracture set are related to the existence of a microfracture swarm in the area where the SEM-CL collage was acquired.

The microfracture aperture distributions obtained from these subsurface samples were used as an input for making simulated macrofracture trace maps. The microfracture aperture distribution for the most abundant set in the sample collected at 1712 m was also extrapolated to reservoir scales. However, the effects of sampling a microfracture swarm can produce unreliable macrofracture predictions. A better documentation of the effects of spatial distribution on

fracture size distributions may help identify these special cases and avoid their use as representative fracture size distributions for the entire fracture system.

Fracturing and diagenesis

Conventional petrographic, SEM-CL, and probe analyses of cements in outcrop and subsurface rocks of the Weber Formation suggest important regional variations in the diagenetic history of Weber Formation sandstones (Koelmel, 1986; Fryberger and Koelmel, 1986; Bowker and Jackson, 1989; Laubach and Schwartz, unpublished, Milliken, unpublished). Important differences in the diagenesis of outcrop and subsurface rocks include: proportion of primary and secondary pores in the rock, cement phases present and proportions of these cements in the rock. Inspection of outcrop samples from Weber Formation sandstones in the study area show that outcrop sandstones have higher porosity (average 11% TVR) than subsurface equivalents (average 3% TVR) (Appendix 2.A). Quartz cement is more abundant in subsurface (average 17% TVR) than in outcrops (average 5% TVR) and the dominant carbonate fill in pores and fractures in outcrops is calcite, whereas in subsurface samples is ankerite.

Diagenetic variations have an impact in the prediction of fracture-fill, timing relationships between fracturing and cementation in the rock, and preservation of fracture porosity. Diagenesis also modifies the mechanical properties of the rock undergoing fracturing. Changes in mechanical properties of the rock have an impact on fracture growth (Olson, 1997) and may influence

fracture morphology, fracture intensity, and spatial distribution, making Weber outcrop analogues not applicable to subsurface fracture characterization.

Small volumes of quartz cement in outcrop localities suggest that Weber sandstones in these areas were not buried very deeply or that quartz grains were covered by non-quartz materials early in the burial history of these rocks (Lander and Walderhaug, 1999). In contrast, Rangely Field samples show higher proportion of quartz cement (average 17%, TVR Appendix 2.A) than outcrop localities suggesting that either these rocks were buried deeper than outcrop rocks or that quartz grains in Rangely Field had more abundant surface area available for quartz precipitation and for a longer time than outcrop rocks.

If the small proportion of quartz cement in the rocks observed in outcrops is explained by shallow burial of outcrop Weber sandstones then the differences in burial history between outcrops and subsurface localities must be important in distances of only a few tens of kilometers that separate Rangely Field from the outcrops studied. The Willow Creek Fault is an important geologic structure separating outcrop and subsurface localities. The current difference in the structural position of Paleozoic rocks (e.g., Weber Formation) at both sides of this fault is approximately a kilometer and the thickness of sedimentary units overlying Paleozoic rocks is similar at both sides of the fault (Hansen, 1986), suggesting that the burial histories of outcrop and subsurface localities are not very different. Furthermore, the current structures in the area probably formed during the Laramide orogeny, and most probably during the Paleogene time (Narr, 1991; Narr and Suppe, 1994) suggesting that there were no significant

differences in the deformation history of outcrops and subsurface localities during the entire Mesozoic time (~120 m.y.).

Another possible explanation for the small volumes of quartz cement in outcrop samples is that other cements precipitated in the pore space at relatively shallow-burial conditions and/or soon after Weber sandstone deposition reducing quartz grains surface area available for quartz cementation. Poikilotopic patches of calcite cement preserving loose packing of grains that do not have quartz overgrowths demonstrate the precipitation of early calcite cement in these rocks (Koelmel, 1986; Bowker and Jackson, 1989). However, late calcite cement also filled the pore space in outcrop samples. Inspection of outcrop samples indicates that there is considerable heterogeneity in the volumes of calcite cement in outcrop rocks (Appendix 2.A). Eight out of 14 samples contain 9% to 26% calcite cement (TVR) and calcite cement is the most important cement phase in these samples. The porosity in calcite-cemented samples ranges from 2% to 8% (TVR). However, in six out of fourteen outcrop samples calcite cement volume is negligible. In these samples porosity ranges from 7% to 19% and is generally above 10% (5 out of six samples). Clay and dust rims are present in all outcrop samples in different proportions (up to 6% TVR, Appendix 2.A). Calcite cement and clay and dust rims probably played a role preventing quartz cementation in outcrop samples by reducing the quartz surface area available for quartz precipitation.

Geohistory diagrams (Hefner and Barrow, 1992) suggest that oil generation in the Phosphoria Formation occurred by the Early Jurassic time in the

Uinta basin, west of the study area. The paleostructure in the Triassic suggests that oil was migrating from the Uinta basin in east direction through the study area during the Mesozoic time (Hefner and Barrow, 1992). Isopach maps for the Triassic also suggest that by the time of hydrocarbon migration the Weber Formation at Rangely Field and outcrop localities were covered by at least 1000 ft of sediments (Hefner and Barrow, 1992). Early oil migration into the Weber sandstones can explain the small volumes of quartz cement observed in outcrop samples because hydrocarbon migration could have prevented continuation of quartz cementation in Weber sandstones at relatively shallow burial conditions. However, early hydrocarbon migration does not explain the greater abundance of quartz cement in Rangely Field unless hydrocarbons did not migrate through the Weber sandstones at Rangely. Hydrocarbon residues cover quartz overgrowths in pores and fractures of surface and subsurface samples demonstrating that hydrocarbons migrated into these rocks after quartz cementation and probably after carbonate cementation in outcrops as indicated by dissolution features in outcrop vein fill (Fig. 2.25).

It is possible that low proportions of early carbonate cement in Weber sandstones did not prevent quartz cementation in the Rangely Field area as much as in outcrop localities. Ankerite and clay cements filled remnant porosity after quartz cementation and cementation probably stopped after oil migration toward Rangely Field. Fractures both in subsurface and surface had formed by the time of carbonate precipitation and hydrocarbon migration encountered fractures at least partly filled with quartz and carbonate cements.

Interpretation of fracture formation timing as pre-Laramide is supported by structural data (Silliphant et al., 2002; Wilkins et al, 2001) as well as diagenetic and hydrocarbon migration studies (Koelmel, 1986; Fryberger and Koelmel, 1986). Small volumes of quartz cement in the rock and fractures in outcrop suggest that calcite cement was filling fractures in outcrop areas when quartz cement continued precipitating in matrix pores and fractures in Rangely Field. Ankerite cement occurred only in Rangely field, degrading the fracture quality in the reservoir. Layers with highest primary porosity show the lowest degradation. Low degradation intervals correlate with core-based observations of fracture porosity.

Subsurface fracture quality assessment

Early diagenetic studies recognized that occurrence and degree of diagenetic processes in Weber Formation sandstones are related to original sediment texture, composition, and environment of deposition (Bowker and Jackson, 1989). A test of correlation between sedimentary facies and fracture quality in the Larson 15X B well indicated that there is an empirical relationship between these two parameters. Cross-stratified beds have the lowest degradation whereas bioturbated facies are characterized by high degradation. Only one result from contorted beds is insufficient to infer degradation in this sedimentary facies. Sediment mixing and destruction of the original sediment texture are processes that tend to reduce porosity and probably increased the degradation index. Bioturbated facies had less porosity than cross-stratified dune deposits due to the

mixing of grain sizes and introduction of clays to the sediment. Later events of cement precipitation completely filled the pores with cement, yielding high degradation values in these facies. Even if extensive dissolution of carbonate cements happened as suggested by Koelmel (1986), dissolution probably favored the facies with highest porosity, that is the cross stratified beds, further increasing their high porosity and yielding low degradation indexes.

Fracture trace pattern simulations

The statistically based fracture pattern generation program successfully simulated a fracture pattern for an outcrop in the study area based on macrofracture information obtained from the pavement. Macrofracture information used as an input for the program included: fracture orientation, mechanical layer thickness, fracture size distributions, and an estimate of the smallest fracture aperture with remnant fracture porosity.

Although selection of the minimum fracture aperture that preserves fracture porosity in Figure 2.35 simulations is not supported by quantitative data, the patterns shown illustrate the importance of incorporating fracture fill data in fracture realizations. Use of relevant fracture attributes for statistical fracture realizations can produce realistic fracture patterns similar to fracture patterns observed in nature. Moreover, these realizations are based on data collected directly from the reservoir and use assumptions that have been tested in outcrops where information about the macrofractures is abundant. Incorporating better

models of fracture spatial distributions derived from reservoir data to the realizations will potentially improve the results.

CONCLUSIONS

Inadequacies of outcrop analogs for subsurface fracture characterization oblige using local fracture information to characterize Weber sandstone reservoirs at Rangely Field. One method that can potentially characterize subsurface fracture systems using local information is to study the relationships between micro- and macrofractures. Abundant microfracture information can potentially be obtained from subsurface samples (Laubach, 1997; Ortega and Marrett, 2000) and used to predict macrofracture attributes in the same volume of rock. I used Weber Formation outcrop sandstones as a testing ground for the application of microscopic techniques for the characterization of outcrop fracture systems. The results obtained from extrapolation of microfracture length distributions to macroscopic scales in outcrops were satisfactory and suggest that this technique provides a potential solution of the subsurface macrofracture sampling problem. Macrofracture and microfracture orientation tests were also satisfactory. Successful results of orientation and fracture size distribution prediction from outcrops provided support for taking the same approach at Rangely Field.

Analyses of fracture size data suggest that the best mathematical model for fracture-size distributions obtained both from outcrops and subsurface data for microfractures and macrofractures is a power law model. Sampling artifacts produce deviations of the observations from ideal power law behavior.

Understanding and accounting for these sampling effects as well as unraveling the mathematical models that best describe them is important to obtain the underlying power law that best fits the data. But also, understanding these sampling artifacts helps identify problems in data collection, and may help recognize other attributes of the fracture system like degree of connectivity and mechanical layer effects on size distributions.

The effect of mechanical layer thickness on fracture length and aperture distributions was documented. The aperture distribution of thick mechanical layer produced a power law that spans more orders of magnitude in size than the aperture distribution of thinner mechanical layer thickness. Thick mechanical layers produce fracture size distributions where the fall off at the large-scale end of the distribution occurs at even larger scales than thin mechanical layer thickness.

Tests of the influences of fracture connectivity and fracture length measurement criteria suggest that fracture length distributions are best modeled using a power law model if the fracture length of connected fractures is obtained as the sum of the lengths of all interconnected fracture segments. Connected fracture lengths may be part of the same power law distribution of isolated fractures. Definition of fracture length as the sum of the lengths of interconnected fracture segments produced a power law distribution without the typical fall off at the large-scale end of the size distribution.

Size and orientation of subsurface macrofractures are two of the most important attributes for fluid flow modeling of subsurface fracture systems.

Fracture orientation and length influence fracture connectivity (Rouleau and Gale, 1985) and fracture aperture can limit permeability of the connected fractures (Snow, 1969, 1970; Marrett, 1996). However, fracture connectivity and degree of mineralization in the fractures are also important pieces of information for fluid flow modeling of fractured reservoirs.

Fracture quality is an empirical fracture characterization tool that addresses the likelihood of having filled or open macrofractures in sandstones on the basis of microfracture observations. Fracture quality techniques (Laubach et al., 2000) were tested in subsurface Weber Formation sandstones and the results matched observations of natural fractures from cores. An empirical relationship between fracture quality and sedimentary facies was found in the same well, and confirmation of this link between sedimentary facies and fracture quality in other wells of Rangely Field can provide a predictive tool for fracture quality prediction using conventional subsurface exploration tools. Cross-laminae facies are characterized by higher porosity than other sedimentary facies. Higher porosity decreases the degradation index for similar proportions of postkinematic cement. Microscopic information on fracture orientation, size, and degree of fracture openness was used to simulate fracture patterns where fractures were located according to simple average fracture spacing models.

Development of adequate tools for fracture spatial characterization and comparison of micro- and macrofracture spatial distributions would add significant improvement to the reservoir model but this aspect of fracture system

characterization is still unknown. However, recent advances in understanding the power law nature of fracture swarm spacing are promising (Marrett, unpublished).

CHAPTER 3: SEDIMENTARY AND STRATIGRAPHIC CONTROLS ON FRACTURE INTENSITY

Cupido Platform

INTRODUCTION

Subsurface fracture characterization is challenging mainly because of sampling problems. The first two chapters of this work tested a possible solution to the subsurface-fracture sampling problem using microstructure observations as proxies of related macrofractures in the same volume of rock. For example, microfracture orientation and frequency were used to predict the same attributes of macrofractures. The previous case studies involved siliciclastic rocks because significant advances in imaging microstructures in quartz-rich rocks allowed the collection of abundant microstructural data for macrofracture prediction from millimeter-scale areas of thin sections. Although some progress has been made recently imaging microstructures in dolostones (R. Reed, 2000 personal communication; Gomez et al., 2001) using available instrumentation carbonate rocks seem generally less suitable for systematic Scanning Electron Microscope Cathodoluminescence (SEM-CL) imaging. Consequently, we need other tools/models to predict macrofracture properties in carbonate rocks.

One way to approach subsurface fracture intensity prediction is to understand how geologic parameters control variations in fracture intensity. For example, fracture intensity models might use known stratigraphic characteristics

of sedimentary successions to predict subsurface natural fracture frequency before drilling, and may help identify/rank exploration and exploitation targets.

In this chapter, I explore the possibilities of using fundamental stratigraphic characteristics of carbonate successions to predict natural fracture frequency variations. Bed-by-bed determination of normalized fracture intensity values will be analyzed in the context of varying sedimentary facies, dolomite content, bed thickness, and position of the bed in fifth order stratigraphic cycles. The results of these analyses will answer the following questions: Which stratigraphic parameters exert the strongest control on fracture intensity distribution? What is the nature of this control? Is there a predictable pattern of fracture intensity distribution?

PREVIOUS WORK

Nelson (1985) discussed some widely accepted paradigms of geologic controls on fracture intensity. Nelson (1985) classifies these controls as 1) compositional, 2) textural (including grain size and porosity), 3) stratigraphic (bed thickness), and 4) structural.

Compositional controls on fracture intensity have been studied in laboratory experiments (e.g. Handin et al., 1963) and with systematic measurements of fracture spacings in outcrops (Das Gupta, 1978; Sinclair, 1980). Handin et al. (1963) experiments of deformation of sedimentary rocks under confining pressure suggested that fracture intensity decreases from quartzites to dolostones, to sandstones, to limestones. Handin et al. (1963) experiments also

indicated that limestones increase their ductility with burial at a greater gradient than other sedimentary rocks. Sinclair (1980) found similar results as Handin et al. (1963) measuring the fracture intensity in outcrop carbonates and suggested that fine-grained carbonates have higher fracture intensity than coarse-grained carbonates. Das Gupta (1978) in a multivariate study of fracture intensity in Mississippian carbonate rocks of southwest Alberta, Canada, concludes that higher degree of dolomitization correlates with higher fracture intensity but dolomitized beds are also thinner than limestone beds and a separation of both effects on fracture intensity is difficult.

Price (1966) found an inverse relation between rock strength and porosity, and Nelson (1985) proposed that lower porosity rocks of similar composition should have closer spaced and more numerous fractures than higher porosity rocks.

Friedman (1969) studied the abundance of microfractures in the proximity of faults and found that microfracture abundance increases with proximity to the faults and is independent of the depth of burial. Stearns and Friedman (1972) proposed a classification of fracture patterns associated with folds and proposed some genetic explanations for their occurrence. Curvature analysis has been more recently used as a predictive tool of fracture intensity distribution (e.g. Ericsson et al., 1998) based on the assumption (sometimes supported with observations) that high curvature areas of a folded layer are zones of high fracture intensity.

Bogdonov (1947) was probably the first published work on the very intuitive relationship between fracture intensity and bed thickness. After

Bogdonov (1947) numerous other authors have arrived to similar conclusions studying the average spacing of fractures in rocks of different ages, composition, grain size, porosity, and structural position (see section on bed thickness control for an extended discussion of the literature). The bed thickness/fracture spacing relationship is now one of the most widespread accepted paradigms of geologic controls on fracture intensity. However, in all empirical fracture spacing-bed thickness studies as well as other empirical investigations on geologic controls on fracture intensity, a fundamental normalization of the fracture intensity by the fracture size is lacking. In this dissertation I will reevaluate some of these paradigms using fracture intensity estimates normalized by fracture size and I will explain how the omission of the scale of observation on fracture intensity measurements produces apparent relationships between fracture intensity (or spacing) and bed thickness.

LOCATION OF STUDY AREA

The study area is located in the north-central portion of the Sierra Madre Oriental (SMO), northeastern Mexico. The SMO is a fold and thrust belt of Late Cretaceous-Early Tertiary age in central Mexico (Fig. 3.1) contemporaneous with the Paleogene-age Laramide tectonism of the rest of western North America (Marrett and Aranda-García, 1999). To the north, the SMO merges into the Chihuahua Thrust Belt, and to the south is partly covered by the Trans Mexican Volcanic Belt (TMVB). South of the TMVB, the Chiapas Belt contains folds and thrusts involving Mesozoic and younger sedimentary units.

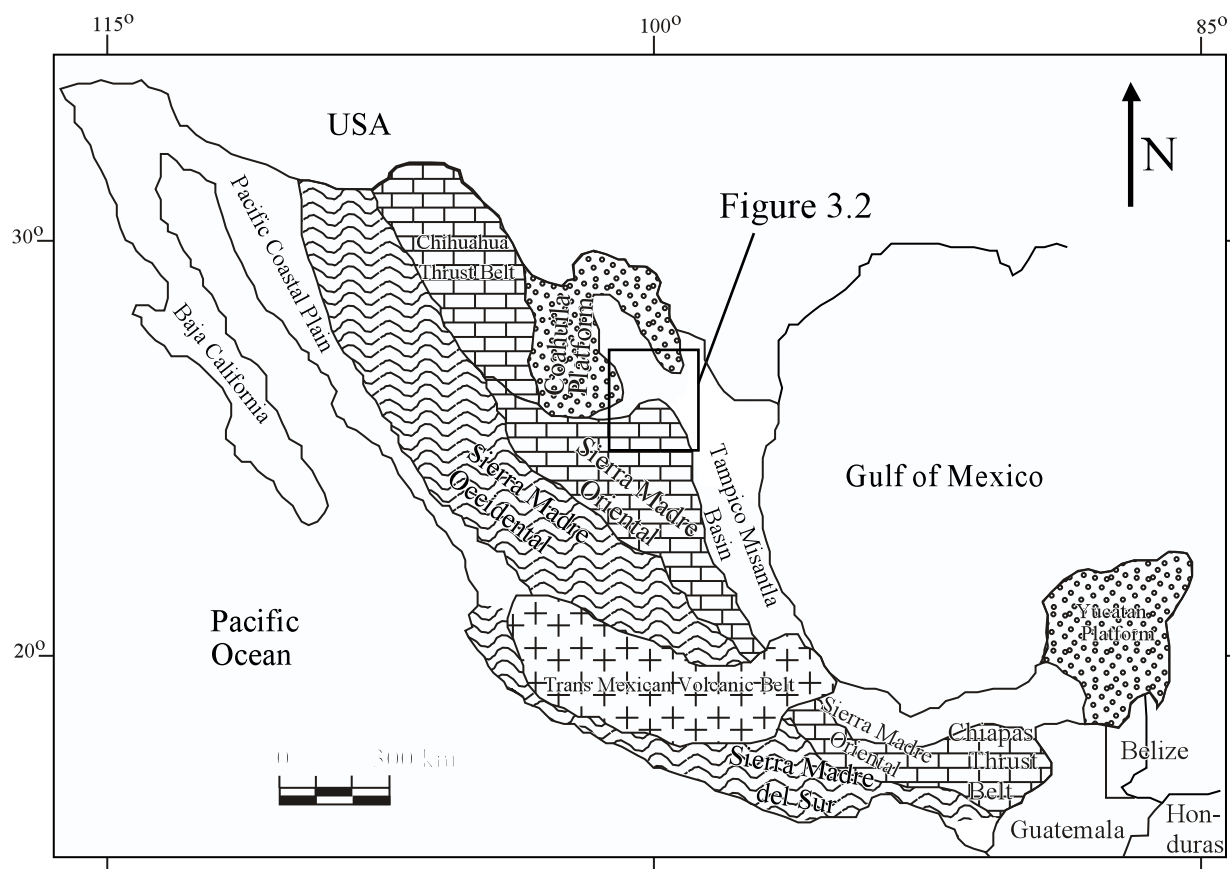


Figure 3.1. Location of study area on a map of the geologic provinces of Mexico. Basins adjacent to study area produce hydrocarbons from units equivalent to the ones exposed in the study area (Fig. 3.2) . Modified from Benavides (1956).

Excellent outcrops of the Lower Cretaceous Cupido, Tamaulipas Superior, and Tamaulipas Inferior formations near Monterrey, Mexico, provide an ideal opportunity to study sedimentary and stratigraphic controls on fracture intensity. This well-known platform-to-basin carbonate system has been the subject of a number of sedimentologic and stratigraphic studies (e.g., Goldhammer et al., 1991, and references therein). Detailed descriptions of sedimentary successions in the area are available from the literature, particularly for the most accessible localities (Wilson et al., 1984; Goldhammer et al., 1991).

Stratigraphic sections selected for study are located in the SMO, to the south of the city of Monterrey and east of Saltillo. A paleogeographic map of the Cupido carbonate platform system for Barremian-Aptian time in the area (Fig. 3.2) shows that localities selected for study are in dominantly shallow-water facies (e.g., lagoonal) of the Cupido Formation at El Chorro and La Escalera, outer-shelf transitional facies (e.g., grainstone shoals and bioherms) at Las Palmas, and open-marine, deeper-water mudstones at Iturbide.

The localities chosen allow studying an array of sedimentary facies and depositional systems in order to test several hypotheses about stratigraphic controls on fracture intensity. Despite the intense deformation experienced by these rocks during the Laramide orogeny, comparing different layers in the same structural domain of kilometer-scale folds can isolate the structural control on fracture intensity. Isolating structural variables is also possible because many of the fractures studied formed before the main phase of the Laramide orogeny (Marrett and Laubach, 2001).

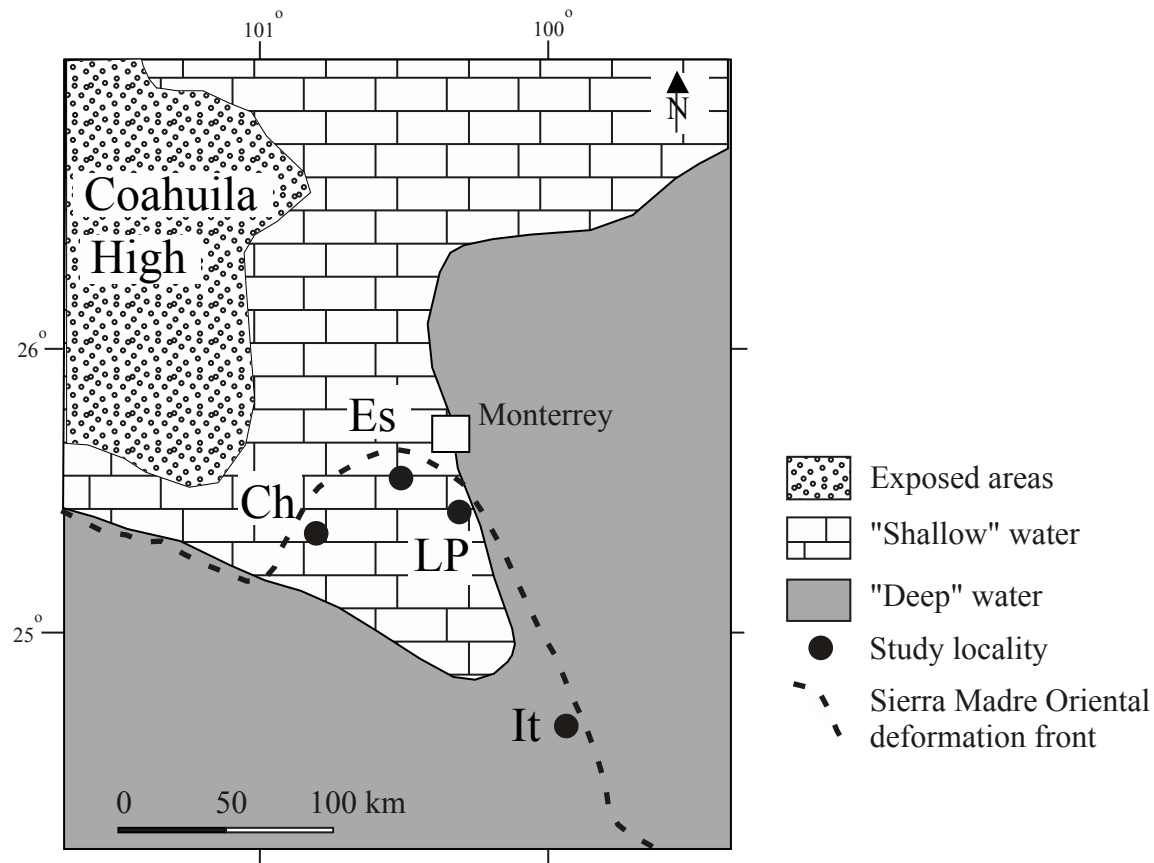


Figure 3.2. Barremian-Aptian paleogeographic map showing localities studied. Ch: El Chorro, Es: La Escalera, LP: Las Palmas, and It: Iturbide. The Cupido platform developed around the Coahuila High, a positive element at the time of Cupido Formation sedimentation. Outcrops of the Cupido Formation and equivalent deeper-water carbonates are chiefly located to the south of the dashed line. Modified from Goldhammer et al. (1991).

STRUCTURAL CONTEXT

Padilla and Sanchez (1985) mapped structural elements of the SMO in the Monterrey Salient and adjacent areas. Three of the localities selected for study are situated in the Monterrey Salient portion of the SMO (Fig. 3.3). The Monterrey Salient is an arch-shaped fold belt that extends 50 to 70 km north of the leading edge of deformation in the SMO to the west. Isoclinal detached folds bring erosionally resistant Cretaceous carbonates to the surface here. This spectacular foldbelt is composed of more than a dozen anticlines, which are 3 to 6 km wide and up to 80 km long (Fig. 3.4). The deformation style is primarily thin-skinned deformation with a lower detachment probably located in gypsum-anhydrite evaporite layers of Upper Jurassic age (Marrett and Aranda-García, 1999; Fig. 3.5).

According to Marrett and Aranda-García (1999) there is a direct relation between structural style in the SMO and presence/thickness of evaporite layers. The forelandward pinch-out of Upper Jurassic evaporite layers largely controls the leading edge of the present-day deformation front along the SMO. Where the evaporites have limited extent and pinch out (e.g., Iturbide) folds are closely spaced and frontal thrust faults are locally present at the leading edge of the

Figure 3.3. Major structural elements of the SMO near the Monterrey Salient. Study localities were selected in canyons that cut perpendicular to fold axes, Ch: Chorro, Es: Escalera, LP: Las Palmas, It: Iturbide. The area approximately covered by the Landsat image in Figure 3.4 is outlined by a grey rectangle. Structural sections in figures 3.5 (A-A') and 3.6 (B-B') are also indicated in the map. Modified from Padilla and Sanchez (1985).

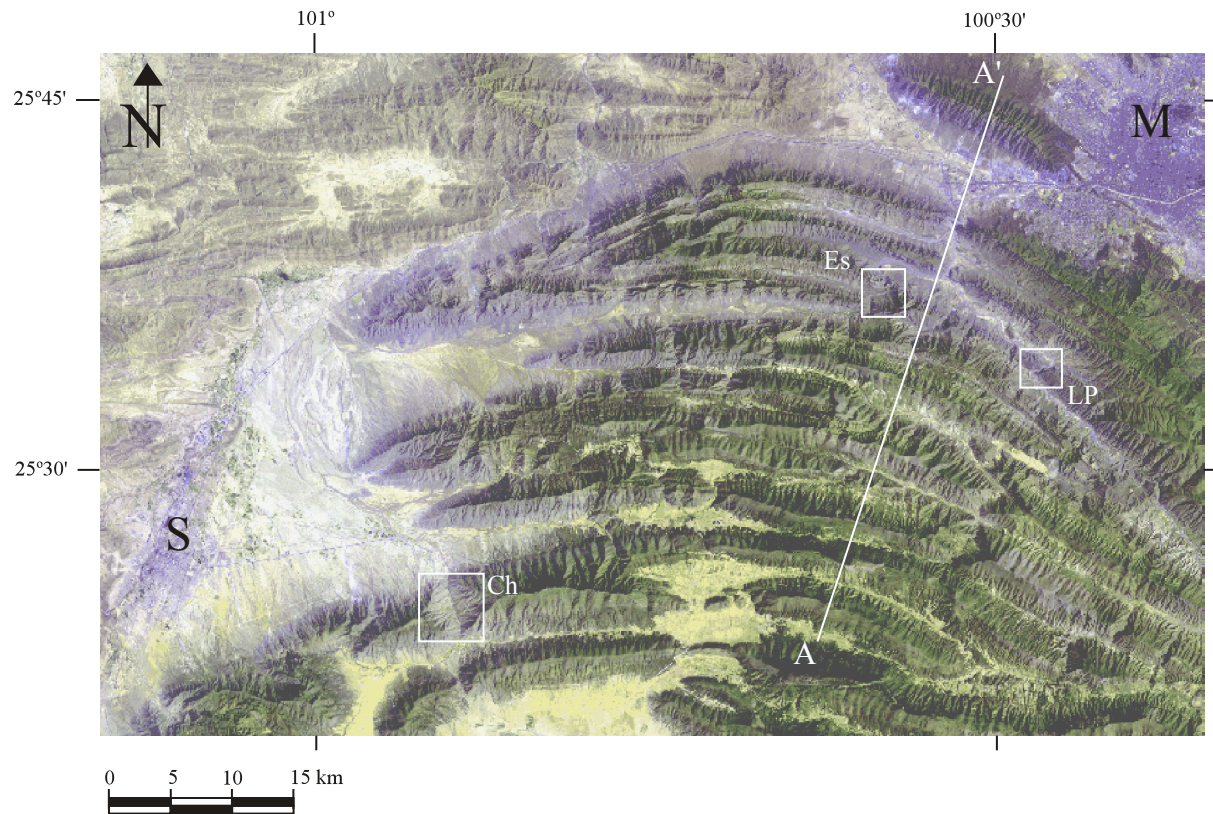


Figure 3.4. Landsat image of the Monterrey salient in the Sierra Madre Oriental showing kilometer-scale folds affecting Mesozoic rocks. Ridges are dominated by carbonate beds of Cupido and Tamaulipas Superior formations. Cross section A-A' is shown in Figure 3.5. Figure 3.3 shows approximate location of this image in a regional map with major SMO structural elements. Localities of study are along canyons that cut across anticlines in the area. Ch: El Chorro, Es: La Escalera, LP: Las Palmas, M: Monterrey, S: Saltillo.

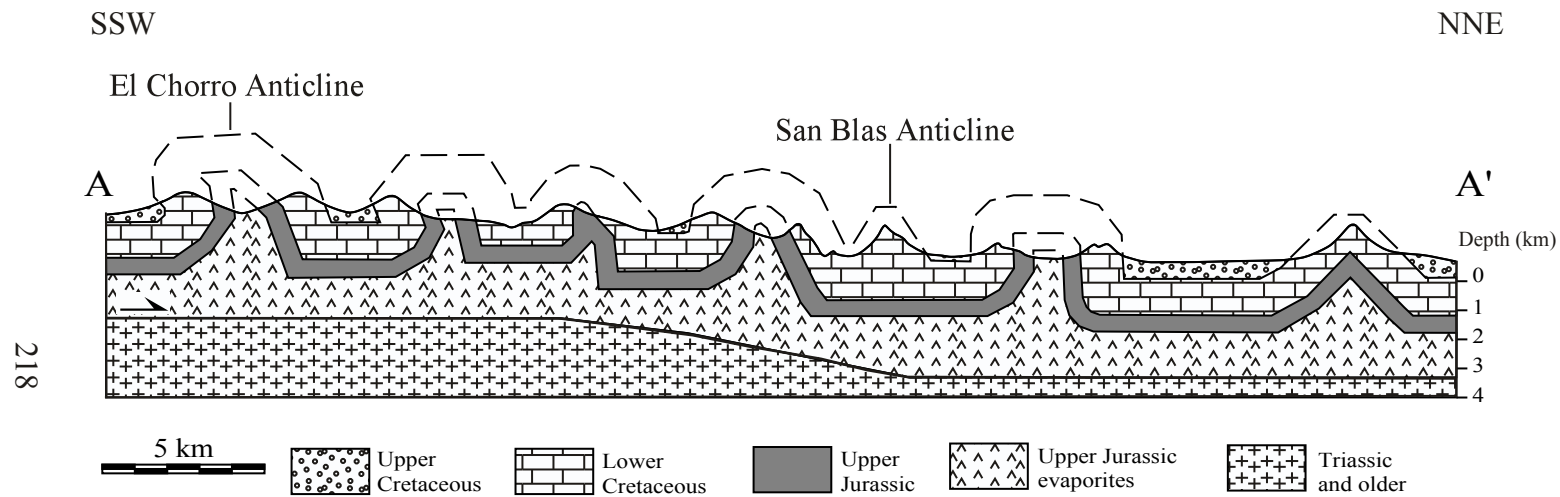


Figure 3.5. NNE-SSW cross section through Monterrey Salient illustrating structural style (see Figs. 3.3 and 3.4 for location). Folds are characterized by angular geometry only visible at a distance or air views. There is no surface evidence of faults associated with the deformation. Anticlines are upright with near-vertical limbs. Upper Jurassic evaporites crop out in some anticlinal cores and constitute the oldest rocks visible in the Monterrey Salient area. Depth and geometry of the detachment level were inferred from depth-to-basement magnetic intensity data. The southern limb of El Chorro Anticline and the northern limb of San Blas Anticline were studied in this work. Modified from Marrett and Aranda-García (1999).

deformation, whereas where the evaporites are thick and laterally extensive folds are broad, unfaulted, and widely spaced.

Folds in the Monterrey salient show curved axial traces (Figs. 3.3 and 3.4). Limited paleomagnetic measurements suggest, but do not prove, that this fold belt is an orocline (Kleist et al., 1984). However, according to Marrett (1995) and Marrett and Aranda-Garcia (1999), rock deformation on top of evaporites can produce a variety of structural trends, like the ones observed in the SMO, without requiring vertical rotation as the only mechanism explaining fold curvature. Marrett's (1995) model is interesting because it also explains the radial nature of tectonic transport in the SMO salient, and the scarcity of strike-slip faults.

The three folds selected to study sedimentary and stratigraphic controls on fracture intensity in Cupido and Tamaulipas Inferior formation carbonates were chosen primarily because they provide accessible and well-exposed successions of sedimentary facies that are representative of different portions of a carbonate platform as seen in a dip profile. Structural effects on fracture intensity were minimized by collecting data in only one limb of each fold, away from hinges, and where bedding attitude is nearly constant. Each fold limb was considered a separate structural domain with a relatively homogeneous total strain and strain history. Although mechanical stratigraphic variations in a fold limb cannot be completely discarded (Fisher and Jackson, 1999), study of two folds in the Monterrey salient suggested that most fold-related strain was accommodated by layer-parallel faults, and layer curvature from folding was only associated with

enhanced fracturing within a few meters of regional-scale hinges (Camerlo, 1998).

Two of the folds studied are located within the Monterrey Salient (El Chorro and San Blas anticlines), and one fold (Iturbide Anticline) is located to the south in the north-northwest-oriented ranges of the SMO, approximately 115 km southeast of Monterrey (Fig. 3.3). All folds display periclinal terminations in landsat images produced by slightly plunging axes (Fig. 3.6).

Camerlo (1998) studied in detail two folds of the Monterrey Salient, including one of those studied in this work (San Blas Anticline). Cupido Formation carbonates crop out in the core of San Blas Anticline, along Las Palmas Canyon. Camerlo (1998) examined a variety of deformation mechanisms in this fold and concluded that it formed by a combination of flexural slip and passive-limb rotation. Bed-parallel tectonic breccias commonly occur at La Escalera Canyon (see stratigraphic column in Appendix 3.G) suggesting that flexural slip played a role in anticline formation at this locality also. Fracture intensity distribution in a cross section of San Blas Anticline shows moderate to weak correlation with fold-related layer curvature (Camerlo, 1998). High fracture intensity zones do not always correlate with hinge position, but rather are somewhat variable along the beds and from bed to bed, in a manner difficult to explain by published models of detachment folding (Camerlo, 1998).

El Chorro Anticline is perhaps the most accessible of the folds studied. Upper Jurassic and Lower Cretaceous units crop out at both sides of Highway 57, southeast of Saltillo, along a canyon that runs perpendicular to El Chorro

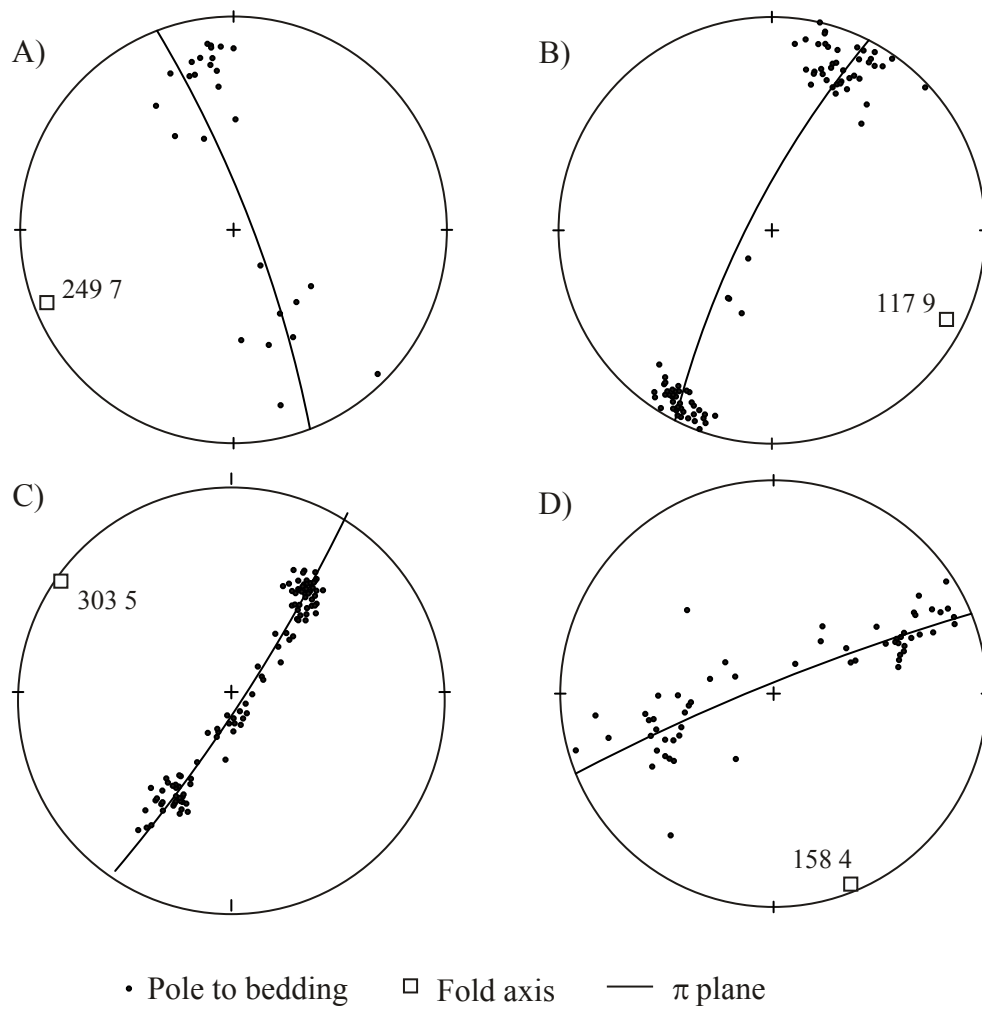


Figure 3.6. Fold axes and π planes of folds studied. A) El Chorro Anticline; B) San Blas Anticline at La Escalera; C) San Blas Anticline at Las Palmas; D) Santa Rosa Anticline near Iturbide. All folds plunge slightly. There is a saddle between La Escalera and Las Palmas localities in San Blas Anticline. Numbers represent trend and plunge of fold axes at each locality. Data provided by Randall Marrett, Rion Camerlo, Julia Gale, Bryan Pairsh, Roy Luck, Faustino Monroy and the author.

Anticline axis (Fig 3.4). El Chorro Anticline is angular when observed from a distance or in aerial views, similar to San Blas Anticline (Camerlo, 1998). At El Chorro Anticline no obvious control of fold geometry on fracture intensity was found. However, detailed studies of deformation mechanisms have not been carried out in El Chorro Anticline. Thinly bedded over to Upper Cretaceous deep-water pelagic units in the southern limb of El Chorro Anticline display parasitic folding, but Lower Cretaceous shallow-marine beds under study experienced parallel folding.

Iturbide Anticline is located approximately 115 km to the southwest of Monterrey, and west of Linares (Figs 3.3 and 3.4). Figure 3.7 shows a cross section along Santa Rosa Canyon with Iturbide Anticline at the western end of it. The town of San Pedro de Iturbide occupies the core of this overturned anticline. Two kilometers north of San Pedro de Iturbide, Iturbide Anticline branches into two anticlines: Santa María and La Muralla, with an intervening syncline (Fig. 3.3). The structural style along Santa Rosa Canyon is different from the structural style observed in the Monterrey salient. Open-marine carbonate beds of Lower and Upper Cretaceous age dominate outcrops in the forelimb of Iturbide Anticline (Fig. 3.2).

STRATIGRAPHIC CONTEXT

The stratigraphic sections studied represent laterally correlative Cupido and Tamaulipas Inferior formations of Hauterivian–Aptian age in the Sierra Madre Oriental and adjacent basins in Mexico (Fig. 3.8). The Cupido and

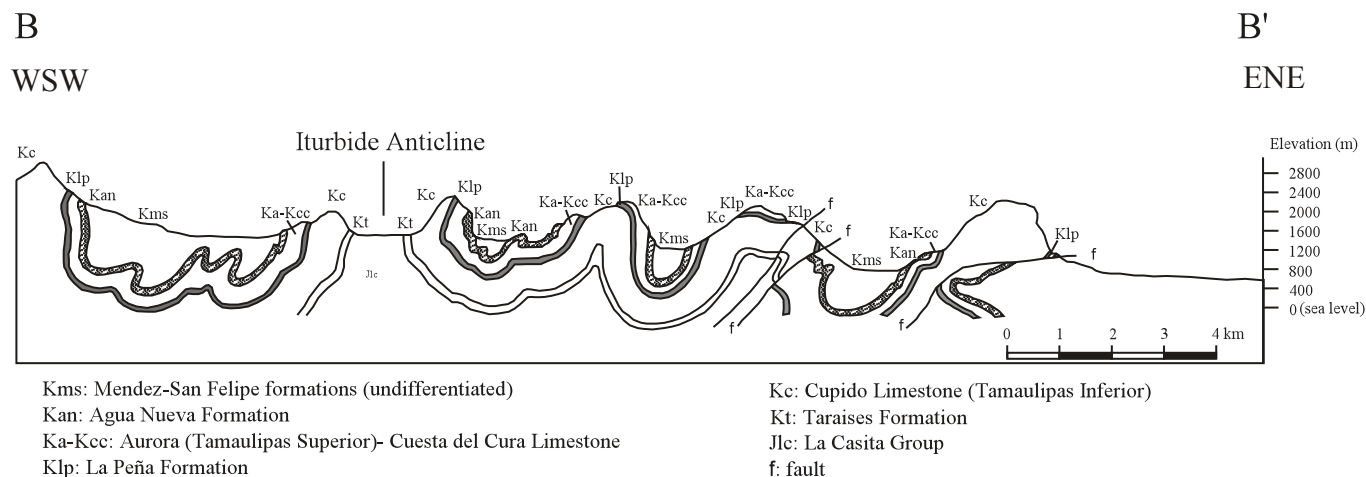


Figure 3.7. Cross section along Santa Rosa Canyon (see Fig. 3.3 for location). Modified from Diaz (1959). The northern limb of Iturbide Anticline was one of the localities selected for study. Tight folds involving Upper Jurassic to Upper Cretaceous strata suggest greater shortening in Iturbide than in the Monterrey salient area. Fold and fault vergence slightly toward the northeast, low-angle emergent faulting and recumbent folds at the deformation front differentiate this deformation style from Monterrey Salient's unfaulted broad-and-upright anticlines. Frontal and secondary thrusts suggest low-angle faulting within carbonates and clastics of Upper Jurassic-Cretaceous section. These changes in deformation style are consistent with evaporite layer pinchout from west to east (Marrett, 1995). Frontal thrust puts Lower Cretaceous open marine carbonates on top of Upper Cretaceous carbonates and clastics (break-thrust fold).

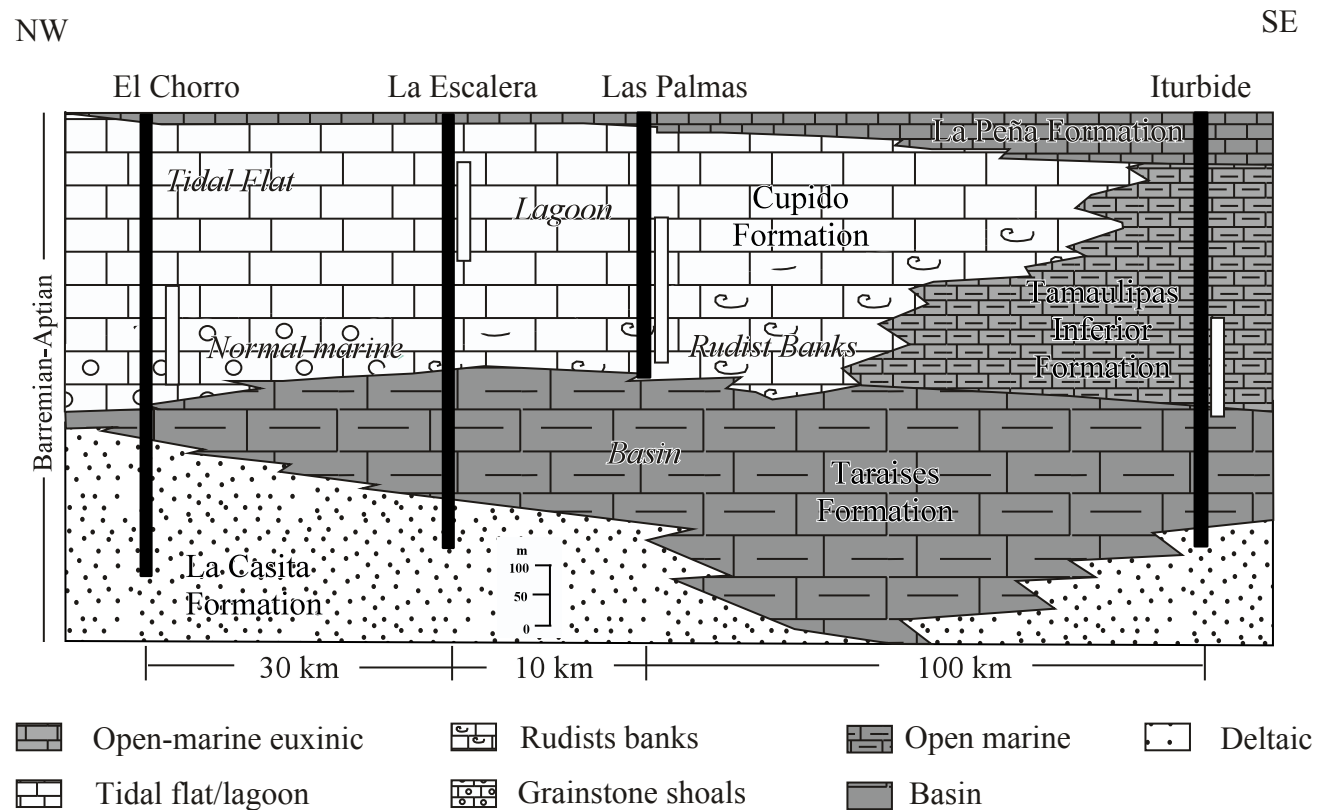


Figure 3.8. NW-SE stratigraphic section across the Cupido-Tamaulipas platform system (Modified from Wilson et al., 1984). Black columns show approximate stratigraphic interval exposed in each area. White columns indicate approximate section studied at each location. Horizontal separations between localities not at uniform scale.

Tamaulipas Inferior formations underlie the La Peña Formation, a distinct stratigraphic unit composed of black limestones and shales that commonly is recessive in outcrop. The Cupido platform prograded over open-marine carbonates of the Taraises Formation, which was deposited in deeper water conditions and overlies clastics of the La Casita and Carbonera formations near the Coahuila High (Fig 3.2). Stratigraphic and sedimentologic aspects of the Cupido carbonate platform have been studied by a number of authors (Lehmann et al., 1998, and references therein). The Sligo Formation, in the Gulf of Mexico area of the United States, is equivalent in time to the Cupido and Tamaulipas Inferior formations (Goldhammer et al., 1991; Lehmann et al., 1998).

The Cupido Formation is composed of shallow-water carbonate sediments of a prograding carbonate platform. Open marine facies of this sedimentary system are included in the Tamaulipas Inferior Formation. El Chorro and La Escalera sections are dominated by shallow-water, lagoonal and intertidal carbonate facies. Las Palmas section contains abundant bivalve bioherms and grainstone shoals of the platform's outer margin, and the section at Iturbide is mainly composed of open marine mudstones of the Tamaulipas Inferior and Taraises formations.

Sedimentary Facies in Cupido Formation

A variety of sedimentary facies are present in Cupido Formation (Conklin and Moore, 1977; Wilson et al. 1984). Figure 3.9 includes graphic examples of Cupido Formation sedimentary facies. Appendix 3.A contains a list of samples

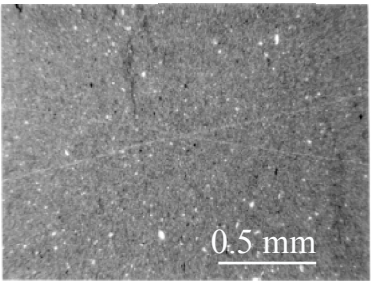
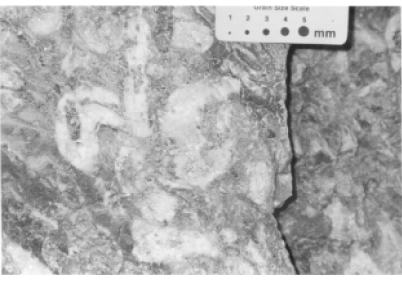
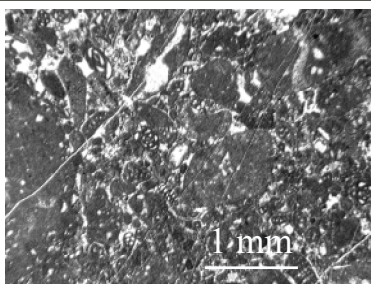
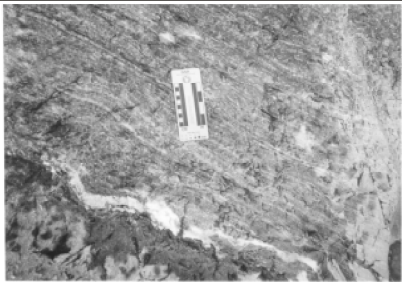
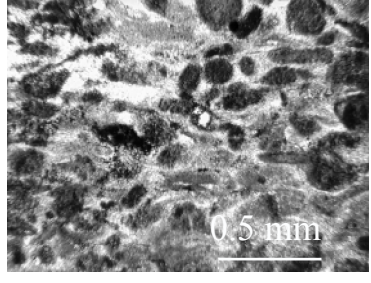
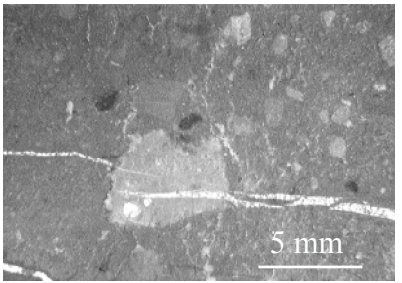
	<p>Open-marine mudstone facies. Chiefly carbonate mud. White dots are calci-spheres. Tamaulipas Inferior Formation, Santa Rosa Canyon, sample CuSr5-98-So, plane light.</p>		<p>Rudist bioherm facies. Cupido Formation, La Escalera Canyon outcrops. Large dot on scale bar has 5mm diameter.</p>
	<p>Packstone of intraclasts (large, rounded grains) and bioclasts (micritized bivalves, forams and algae). Lagoonal facies, Cupido Formation, El Chorro Canyon, sample CuLCh-2-98-So, plane light.</p>		<p>Cryptalgal laminite facies and calcite-replaced evaporites (white). Cupido Formation, La Escalera Canyon outcrops. Graduated ruler on the left side of the scale bar is 10 cm long.</p>
	<p>Grainstone of peloids (structureless, oval) and ooids (concentric layers, spherical). High-energy shoal facies, Cupido Formation, La Escalera Canyon, sample CuEsc-6-98-So, plane light.</p>		<p>Mud-supported, sedimentary breccia. Interpreted as transgressive lag remnants. Cupido Formation, La Escalera Canyon, sample CuEsc-1-98-So, plane light.</p>

Figure 3.9. Examples of typical sedimentary facies in Cupido and Tamaulipas Inferior formations. Photomicrographs are from bed-parallel thin sections.

and thin sections prepared for petrographic study and tables with the results of conventional petrographic analysis. Digital photomicrographs at a variety of scales are included in the enclosed compact disk. Detailed stratigraphic columns (Appendix 3.G) show the stratigraphic distribution of sedimentary facies in outcrops of Cupido Formation at each locality. The most abundant sedimentary facies at El Chorro and La Escalera are grainstones and lagoonal wackestone-packstones of intraclasts, ooids and bioclasts. Grainstones and bivalve banks are common at Las Palmas Canyon, whereas lagoonal facies are rare. Open marine mudstones dominate Taraises and Tamaulipas Inferior formations at Iturbide. A brief description of each sedimentary facies follows.

Open-marine mudstones

This facies is most common in Tamaulipas Inferior Formation (Iturbide locality, Santa Rosa area). Bed thickness ranges from less than 10 cm to 2 m. Open marine mudstones typically exhibit a gray-green color with a smooth to aphanitic texture in outcrop. Open marine mudstones are chiefly composed of carbonate mud (>90% micrite) and can be classified as micrite according to Folk (1962) classification or mudstones according to Dunham (1962) classification. Allochems in these rocks include thin wall globigerinids (0-3%) with spar-filled chambers, radiolarians tests and calcispheres (0-2%), and small bivalves (0-1%). Accessory components include silt-size quartz (0-3%), phosphate fragments (0-2%), and organic matter (0-5%). The presence of forams and radiolarians suggests an open-marine, outer shelf environment of deposition for these sediments.

Most mudstones show a degree of recrystallization (1-90%) from micrite-size carbonate crystals to microspar. Dolomitization also affected these rocks (0-15%). There are two kinds of dolomite crystals: late anhedral dolomite and ankerite. Ankerite is less abundant (1-5%) and is only present in some beds. Ankerite is characterized by iron-rich zoned rhombs. Anhedral dolomite was affected by recrystallization along with carbonate mud. Microspar-size crystals appear to have partly replaced dolomite crystals and affected their euhedral shape. Silicification (<1%) was a late diagenetic event and produced euhedral prismatic quartz crystals that might have nucleated in radiolarian tests, silt-size quartz grains or clay particles sometimes within stylolites.

Bioclastic-intraclastic wackestones and packstones

These facies are most abundant in shallow water successions of the Cupido Formation, representing more than 50% of the unit. In outcrop they show a variety of colors from dark gray to blue-gray, brown-gray and tan. Individual bed thickness varies from less than half a meter to three meters. These rocks are composed of micrite (15-80%) and a variety of allochems including: peloids (0-60%), intraclasts (0-30%), pellets (0-80%), ooids (0-25%), bivalve and cephalopod fragments (0-25%), miliolids (0-15%) and other benthic forams (0-5%), echinoderm fragments (0-15%), green algae (0-15%), and red algae (0-5%). The identification of allochems is sometimes challenging because of micritization (0-90%) and deformation. The presence of substantial micrite and bioturbation suggests sedimentation below the wave-base level, in subtidal conditions. Faunal

content suggests lagoonal environments, having clear water and normal salinity areas protected from wave action with an oxygenated, nutrient-rich, sedimentary bottom. Abundance of green algae and oncoids suggests shallow-water conditions close to intertidal environments. Abundant intraclasts suggest occasional storm activity, erosion and transport of indurated sediments within the carbonate platform and from nearby exposed areas.

Diagenetic processes occurring at shallow burial conditions included marine calcite cement in sheltered and intraparticle pores generating geopetal structure. Neomorphic transformations of aragonite to calcite occurred in most shell fragments. This dissolution/replacement process retained micritic envelopes in the periphery of allochems but destroyed shell internal structure. Dolomitization in bioclastic-intraclastic wackestone-packstones varies from 0 to 100%. Bulk dolomitization is important at El Chorro and La Escalera localities and is less significant at Las Palmas locality. Replacing dolomitization affects matrix and allochems. Microdolomite ($<50\ \mu$) partly preserves allochems whereas large dolomite crystals ($>50\ \mu$) generally obliterate original sedimentary textures. Large replacing dolomite complicates the recognition of original sedimentary facies in some cases.

Microdolomite is possibly associated with shallow-burial dolomitization, perhaps under the effect of hypersaline fluid circulation (Lucia and Major, 1994). Large dolomite crystals are possibly associated with deeper burial conditions and higher temperatures (Morrow, 1982). These large dolomite crystals are commonly zoned, containing cloudy cores possibly representing early microdolomite

crystals, and clear dolomite overgrowths. Recrystallization also varies widely in these rocks (0-100%). Recrystallization generated larger calcite crystals from carbonate mud (aggrading recrystallization) and locally destroyed internal allochem structures. For example, fibrous structure in bivalve shells has been replaced such that only micrite envelopes remain as evidence of the original allochem.

Oolitic-peloidal grainstones

High-energy deposits of sand-size grains are present at all localities of study in the shallow water portion of the Cupido platform (Fig. 3.2). This facies is the second most volumetrically important sedimentary facies in the portions studied of the Cupido Formation. This facies is typically grain-supported and contain little or no carbonate mud. Grainstones are often thickly bedded, ranging from 30 cm to 1 m thick in individual beds and up to 7 m for grainstone bed packages. Some beds are cross-laminated, presenting both planar and trough-cross stratification suggestive of under-water dune migration. Common allochems in grainstone facies include ooids (0-90%), peloids (0-80%), intraclasts (0-60%), pellets (0-40%), algae fragments (0-25%), bivalve fragments (0-10%), echinoderm fragments (0-10%) and forams (0-5%). Most grains show some degree of micritization (10-100%). Biologically-induced micritization obscured internal allochem structures, hindering allochem identification and generating abundant peloids in the environment of deposition.

Micritization probably occurred in lower energy environments before the grains were transported to grainstone banks. Grainstones are interpreted as high-energy deposits of limited extent, often elongated perpendicular to the main wave direction. Carbonate mud in grainstone shoals is eliminated during repeated sediment suspension produced by wave and tide action. Grainstone shoals generate cross-stratified beds by lateral migration and protect restricted lagoonal areas from wave action. According to Lehmann et al. (1998) the southern margin of the Cupido platform was fringed by high-energy grainstone shoals.

Primary porosity in grainstone facies was initially high, but was presumably occluded by cement soon after deposition. Secondary porosity is associated with selective dissolution of allochems (<5%). Isopachous marine cements are sometimes preserved around grains, followed by pore-filling sparry calcite. However, in some cases recrystallization (0-80%) has destroyed these cement textures. Dolomitization varies widely from 0 to 100% but is uncommon in this facies. Microdolomite is the most common type of dolomite found in this facies.

Bivalve banks and bioherms

Bioherms are mound-like colonial developments composed of reef-forming rudists in growth position as the dominant organism. Bivalve banks are stratiform deposits of molluscs (i.e. shell beds, Pettijohn, 1957). This facies is best developed in Las Palmas Canyon (Appendix 3.G), but it is also present at El Chorro (less conspicuous) and near the base of Cupido Formation at La Escalera

(not shown in stratigraphic column of Appendix 3.G). Bioherms can be classified as boundstones according to the Dunham (1962) classification system for carbonates. On the other hand, bivalve banks can be classified as calcirudites (Folk, 1962) or rudstones (Embry and Klovan, 1972). Individual rudist banks and bioherms at the localities studied vary in thickness from tens of centimeters to nearly 2 meters. Superposition of multiple banks and bioherms can cumulative reach 7 m of rudists-dominated limestones and dolo-limestones (e.g., Las Palmas Canyon and El Chorro Canyon). Dominant skeletal grains in this facies are rudist shells several centimeters in diameter. Rudist Bioherms and rudist banks are supported by a variety of rudists but one species often dominates the accumulation. Faunal groups include Requierids, Caprinids, Robust rudists, Chondrodonts, corals, stromatoporoids, and a variety of encrusting foraminifera and algae growths (Wilson et al., 1984; Goldhammer et al., 1991). Matrix consists of wackestones and packstones of largely micritized and dolomitized bioclasts (10-40%), ooids (5-15%), peloids (5-15%), pellets (0-10%) and forams (0-3%).

Beds of shell accumulations including whole shells, shell fragments partly transported, and ephemeral patches of colonial rudists characterize rudist banks. According to Lehmann et al. (1998) these organic structures fringed the eastern side of the Cupido platform.

Bivalve banks and bioherms show various degrees of dolomitization (0-80%) and recrystallization (0-80%). Dolomitization was not selective in all localities but mainly affected the bivalve bank matrix at Las Palmas. Cloudy microdolomite crystals are the most abundant type of dolomite in this facies

(60%-80%) but large-size dolomite crystals are also present (20-40%) and are particularly abundant in burrows. Dolomite in burrows shows some intercrystalline porosity (<3%). Dolomite impinges on allochem particles and depending on the degree of dolomitization the original texture in the rock can be altered beyond recognition. In some cases the identification of individual grains is difficult because of complete replacement by dolomite crystals. Dolomitization predated recrystallization as suggested by microspar and spar crystals corroding some dolomite crystals. Recrystallization primarily affected mud-bearing matrix in bivalve banks. Recrystallization has destroyed original fibrous structure in bivalve shells and other allochems.

Cryptalgal laminites

This facies was primarily recognized at Las Palmas and La Escalera localities where detailed columns of shallow water facies of the Cupido Formation were described (Appendix 3.G). This facies occurs at the top of upward shallowing cycles and represent multiple green algae mat growths in tidal flats (Demicco and Hardie, 1994). Algal mats are typically poor in other biological components. Mudcracks and fenestral fabrics are sometimes preserved in this facies. The water composition associated with these deposits may have reached hypersaline concentrations, explaining the association of algal mats and layers of calcite-replaced evaporite layers and evaporite nodules. Cryptalgal laminites are comprised of isopachous micrite-size layers with variable degrees of clay and detrital quartz (possibly wind-blown). Lower intertidal mudstones are

also included in this facies. Lower intertidal mudstones are largely structureless but they may preserve fenestral fabric, bioturbation and displacive calcite-replaced evaporite nodules. Cryptalgal laminites at study localities are interpreted as arid tidal flat deposits. Lehmann et al. (1998) interpreted arid and semiarid climatic conditions for this part of northeastern Mexico during the Barremian-Aptian time.

Microdolomite is the main diagenetic effect observed in cryptalgal laminites. This dolomitization is interpreted as early and is possibly related to hypersaline reflux circulation (Lucia and Major, 1994). Dolomitization can obliterate the laminated structure, making it difficult to positively identify some algal mat growths. Other shallow diagenetic effects include displacive evaporite nodules and gypsum laths, which produce different degrees of alteration of the original sedimentary texture and are common in present-day arid tidal flats (Kendall et al., 1995). Association of micrite remnants and calcite-replaced evaporite nodules help in the identification of lower intertidal mudstone facies.

Intraclastic breccias

Mud-supported and intraclast-supported breccias were identified at Las Palmas and La Escalera localities. These breccias are generally polymictic and show poor grain size sorting. Clast compositions include fragments of the underlying beds and exotic pebbles, however the most common grains are mudstone pebbles with similar composition and texture to that of the matrix of the

breccia itself. Imbricated and “edgewise” textures (Demicco and Hardie, 1994) were not found in these breccias.

Interpretations of the origin of intraclastic conglomerates and breccias vary. Possible interpretations range from pseudobreccias produced by profuse bioturbation to true breccias formed by storm processes, beach cobble deposits, mud chips in tidal flats, and transgressive lags that may or may not contain rip-up fragments from previously deposited sequences. The most common interpretation given to ancient intraclastic breccias is that they represent transgressive lag surfaces (James, 1984; Grotzinger, 1986), but alternative interpretations must be considered. Most Cupido Formation intraclastic breccias are mud-supported, suggestive of transgressive lag origin, but some imbricated grain-supported breccias of algal mat fragments overlying tidal-flat deposits possibly represent supratidal-storm breccias. Pebbles with compositions that are similar to underlying subtidal facies suggest transgressive lags. Pebbles in these breccias appear to have originated in environments of deposition similar to the matrix in which they are embedded. This observation suggests that these clasts represent rip-ups of local hardgrounds, a process occurring during storms in modern transgressive carbonate shelves (Demicco and Hardie, 1994).

Cyclicality

The cyclic character of sedimentation in the Cupido Formation is evident even from a distance (Goldhammer et al., 1999). The sawtooth skyline of the mountain ranges as seen looking along strike of the Cupido Formation is

produced by differential erosion of less resistant, subtidal limestones. Each parasequence is composed of a shallowing upward succession of sedimentary facies. Individual parasequences start with lagoonal burrowed limestones on top of hardgrounds or sedimentary breccias, sometimes followed by grainstone shoals or rudists bioherms, and capped with cryptalgal laminites and/or evidence of evaporite precipitation. Peritidal cycles typically lack of the clean grainstone shoal facies and/or bioherms. Subtidal cycles also shallow upwards and contain grainstones and/or rudists bioherms but commonly lack intertidal facies on top. Changes in thickness, composition, and number of meter-scale parasequences is complex (Lehmann et al., 1998). Lehmann et al. (1998) interpret this complexity as an effect of climatic and autogenic processes on Milankovitch-driven eustatic sea level fluctuations. Parasequence sets composed of a number of individual cycles can be grouped in packages of overall shallow-up pattern (Mitchum and Van Wagoner, 1991). These lower-frequency cycles respond to regional-scale changes in accommodation space and can be correlated across the Cupido platform (Goldhammer et al., 1991; Lehmann et al., 1998)

Wilson et al. (1984) described the cycles present at El Chorro Canyon, each lasting between 50 and 10,000 years. Parasequences at La Escalera Canyon are similar to the ones at El Chorro, except that some parasequence sets start with mud-supported, sedimentary breccias, indicative of transgressive lags. The parasequence sets at Las Palmas Canyon are more diverse. One kind of parasequence set is composed of sedimentary breccias overlain by wackestone-packstone of bioclasts, and capped by rudist banks. Some rudistid banks are up to

2 m thick at this locality. Another kind of cycle is composed of subtidal burrowed limestones that are capped by grainstones and algal laminites, similar to the ones present at El Chorro and La Escalera canyons. A few cycles are composed of grainstone shoals, peritidal facies, and collapse breccias with evidence of evaporitic sedimentation and ulterior dissolution (Appendix 3.G).

DIAGENESIS

Micritization was an important diagenetic process affecting allochems in Cupido carbonate beds. Many carbonate grains are difficult to identify as a result of micritization and need to be classified as peloids. Micritization and bioturbation occurred in the environment of deposition early after the deposition of carbonate sediments (Scholle, 1978). Ecological conditions were favorable on the Cupido platform for the proliferation of organisms, like algae and bacteria, believed to be associated with micritization (Kobluk and Risk, 1977; Smith, 1985; Reid and Macintyre, 2000).

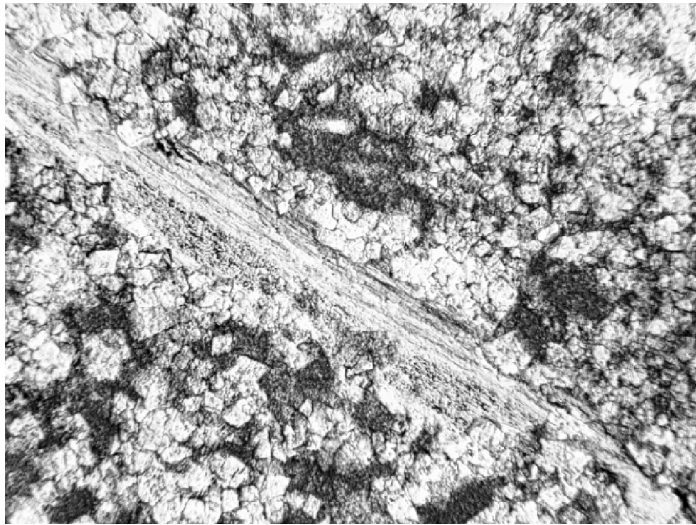
Evidence for shallow-burial compaction includes fluidized structures in fine-grain carbonates, ooid splints, broken shells impinged by other allochems, cracked flat pebbles, and flattened burrows. Early events of marine cementation and one event of dissolution were identified by Monroy et al. (2001). Early cementation of allochems in the environment of deposition explains the preservation of fragile shell fragments, spherical ooids, pellets and other soft carbonate grains throughout burial. Early cements occur in the form of isopachous aragonite or bladed calcite rims around grains, followed by mosaic calcite that

fills remnant inter-particle pores. However, later dolomitization and recrystallization have largely erased evidence of these cements.

Dolomitization was an important diagenetic process affecting Cupido Formation beds. Dolomitization was largely strata-bound, however it often affected multiple adjacent sedimentary facies-defined layers within a parasequence. Dolomitization was not controlled by sedimentary facies only because it occurred in grain-supported and mud-supported rocks, as well as boundstones and rudstones (Fig. 3.10). Dolomitized layers are often interstratified with weakly dolomitized beds or pure limestones. Interstratification of dolostones and limestones is common in other carbonate sedimentary successions (Pettijohn, 1957). In Cupido Formation, interstratification of dolostones and limestones is particularly regular where parasequences are thick or dominated by subtidal facies at the expense of peritidal facies. Pure limestones and slightly dolomitized beds are predominantly grainstones to mudstones with shell and algae fragments, intraclasts, benthic microfossils and miliolids, suggesting deposition in subtidal environments. Dolomitization primarily affected laminated and structureless mudstones of peritidal origin, with mud cracks, cryptalgal laminites, and evidence of evaporites. Dolomitization also affected some subtidal facies underlying dolomitized peritidal facies. In some cases, the dolomitization affected entire parasequences, but retained its stratiform occurrence.

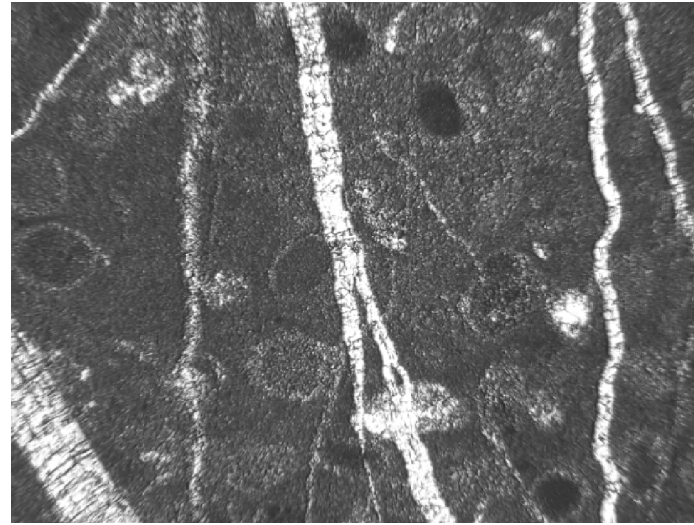
Most dolomitized layers are at or near the tops of parasequences, suggesting that shallow-water environments of deposition (e.g., tidal flat, evaporative environments) focused localized dolomitization. Similar distributions

A)



0.2 mm

B)



0.5 mm

Figure 3.10. Photomicrographs of dolomite occurrence in shallow-water facies of Cupido Formation. A) Dolomite preferentially replaced carbonate mud in the matrix of this bivalve bank. El Chorro Canyon, sample CuLCh-6-98So, plane light. B) Severe replacing dolomitization in shoal facies. Allochem ghosts allow the determination of original texture; in this case, packestone-grainstone of ooids and oolites. Note numerous fractures filled with dolomite. La Escalera Canyon, sample CuEsc-6B-98So, cross-polarized light.

of dolomitization within parasequences were described by Lehmann et al. (1998) in areas adjacent to the Monterrey Salient and in rocks of similar age. This stratigraphic organization of dolomitization suggests a relationship between dolomitization and Cupido Formation cyclicity. Lucia and Major (1994) discussed a model of hypersaline reflux-induced dolomitization in Holocene strata that explains preferential dolomitization of peritidal facies in a progradational carbonate cycle. In the Lucia and Major (1994) model, progradation of a carbonate platform leaves behind shallow water, often tidal-influenced environments where evaporation is intense, generating dense brines with high concentration of magnesium capable of dolomitizing the substrate.

Although an evaporative origin for the dolostones in the Cupido sequence is appealing in combination with Cupido Formation cyclostratigraphy, other dolomitization events also affected these rocks. Burial-related dolomitization events are supported by petrographic textures and also preliminary results of isotopic analyses in host rock and fractures (Monroy et al., 2001).

Pressure-solution due to lithostatic loading was a significant diagenetic event during burial. Bed-parallel stylolitization may have provided the necessary magnesium for dolomitization during burial (Fischer, 1988), but early dolomitization probably focused dolomitizing fluids in early dolomitized, stylolite-bound, and possibly more permeable fractured beds (Fischer, 1988). Focused burial dolomitization in early-dolomitized beds might have selectively concentrated dolomitization at the tops of parasequence cycles. This mechanism of focused dolomitization can explain how non-dolomitized bioturbated

wackestone-packstones within subtidal portions of parasequences remained largely devoid of dolomite during burial.

Monroy et al. (2001) recognized the following late diagenetic events in all localities: recrystallization, dedolomitization, and silicification. Recrystallization is a process that changes the size, orientation, or shape of carbonate components without changing their mineralogy (Folk, 1980). Recrystallization can destroy the original texture of allochems, cement, and matrix. Allochems may appear as ghosts in a groundmass of recrystallized material. Recrystallization can be aggrading or degrading, depending on whether the grain size of the recrystallized material is larger or smaller than the original size. Recrystallization effects observed in Cupido and Tamaulipas Inferior formations are chiefly aggrading and produced changes from micrite to microspar. Recrystallization postdated dolomitization as evidenced by corroded dolomite crystals, which have lost their original euhedral facets.

Silica replacement (silicification) occurred in two forms: 1) euhedral quartz crystals within fractures with large inclusions of calcite and dolomite crystals, which assures its late timing, and 2) microcrystalline quartz and chalcedony selectively replaced dolomitized allochems. However, this latter form of silicification is rare.

Dedolomitization is a diagenetic process that changes dolomite into calcite. Evidence of dedolomitization in the Cupido Formation is documented by aggressive replacement of dolomite by calcite. Monroy et al. (2001) suggested that this late diagenetic events was probably contemporaneous with exhumation in

the area. Dedolomitization in Cupido and Tamaulipas Inferior carbonates may be associated with circulation of phreatic waters, as documented by Holail et al. (1988).

FRACTURE DATA COLLECTION AND ANALYSIS

The orientation, fracture morphology, cross-cutting relationships, composition and texture of fracture fill, and the mechanical-layer thickness were recorded for each fracture set in the beds studied (Appendix 3.A, 3.B, and 3.C). The apertures of every fracture in the bed, intercepted by a fracture set-perpendicular scanline were also recorded (Appendix 3.D). Beds were chosen so that they would represent contrasting sedimentary facies, various bed thickness and degrees of dolomitization (Fig. 3.11). Mechanical bed thickness ranges from less than 10 cm to nearly 2 m. Beds studied were assigned to one of six different sedimentary facies and two diagenetic events. Sedimentary facies were classified in terms of dominant texture and allochems in the bed, and interpretations of depositional environments. However, fracture-intensity analyses were done for two broadly defined sedimentary facies. Mud-supported and grain-supported sedimentary textures comprise the two broadly defined sedimentary facies studied. Mud supported facies are associated with low energy environments whereas grain-supported facies suggest a higher energy level in the environment of deposition. At first, no distinction was made based on the environment of deposition, for example mud-supported rocks deposited in tidal, subtidal or open marine environments were all included in the same group. Separation of these

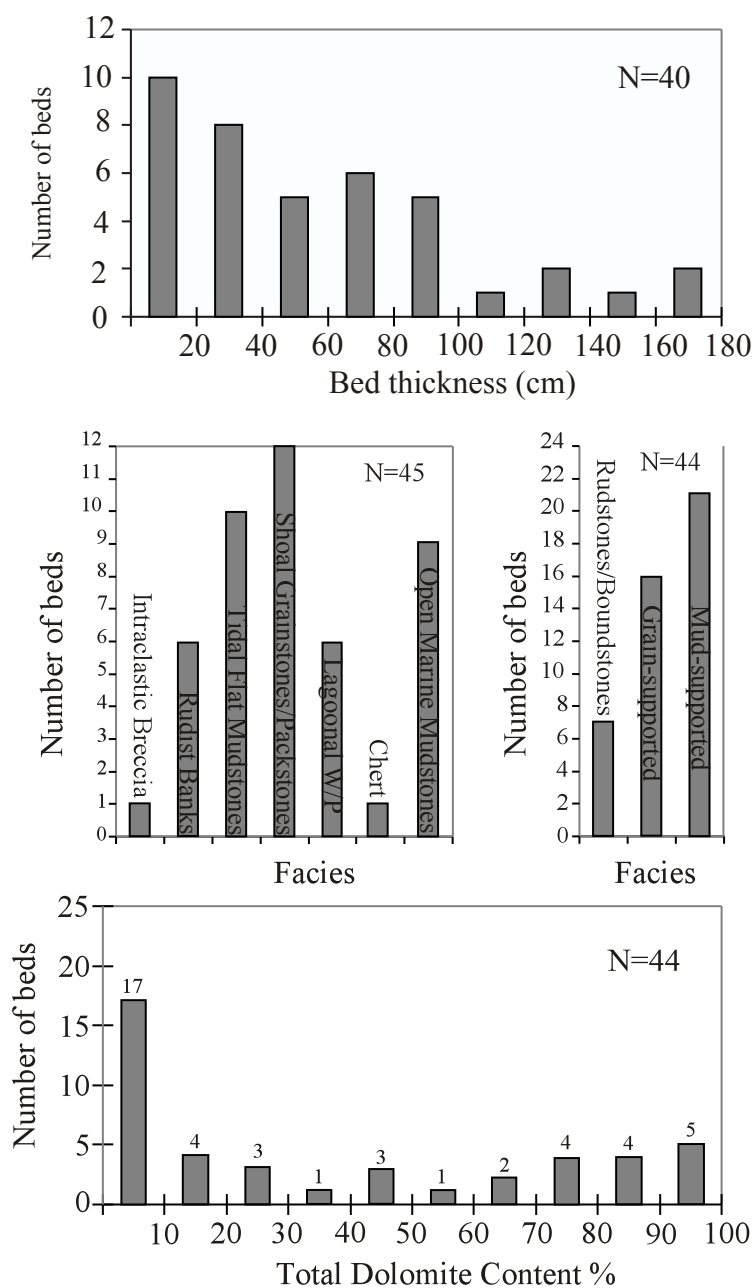


Figure 3.11. Variation of facies, bed thickness and dolomite content in data-base. Facies definition includes textural groups and depositional environment interpretations. Some histograms exclude multifacies beds and/or chert beds. Total dolomite content based on thin section point counting. Relative contribution from different dolomitization events was ignored.

broadly defined sedimentary facies in environments of deposition and their influence on fracture intensity was done in an indirect manner using maximum correlation methods (see section on sedimentary facies control on fracture intensity) and during the study of cyclostratigraphic control on fracture intensity. The diagenetic control on fracture intensity studied was dolomitization. The range of dolomite content in the rocks studied is 0 to 100%. Most beds are either highly dolomitized or not dolomitized (Fig. 3.11). The degree of dolomitization recorded for each bed represents the total dolomite content in the rock based on a quantification of the proportion of the area occupied by dolomite crystals versus calcite crystals in digital photographs of thin sections stained with alizarine red (Appendix 3.B). No attempt was made to determine relative proportions of dolomite precipitated in different dolomitization events.

Finally, an attempt was made to obtain representative fracture-intensity values for sedimentary units components of a typical carbonate fifth-order, meter-scale cycle at La Escalera and Las Palmas localities. Appendix 3.G shows the locations of the beds studied in detailed stratigraphic columns of Las Palmas, Escalera and Iturbide localities. No detailed stratigraphic column is available for El Chorro locality where fewer beds were studied. However, Appendix 3.G includes a composite stratigraphic column incorporating a description and the positions of the beds studied at El Chorro Canyon.

Fracture size data

More than 14200 fracture aperture values from 42 beds comprise the fracture size database. These data were collected along scanlines drawn perpendicular to each fracture set in bed-perpendicular exposures (Fig. 3.12). Bed-parallel exposures are very scarce in the canyons and mostly bed cross-section exposures along canyon walls were used for fracture measurement. In most cases, weakly developed fracture sets were ignored. These fracture sets do not contribute significantly to the total fracture intensity in beds having better developed fracture sets. Moreover, outcrop limitations generally prevented the collection of sufficient fracture aperture measurements for reliable determination of fracture intensity of weakly developed fracture sets (Bonnet et al., 2001). In some cases, however, an effort was made to obtain fracture intensity data from low fracture-intensity beds to document approximate fracture intensity values in these beds for purpose of comparison.

To measure the fracture apertures, a logarithmically graduated fracture-aperture comparator was used (Fig. 3.13). This tool allows collection of fracture aperture data down to $\sim 50\ \mu\text{m}$. The comparator contains lines with increasing width starting at $50\ \mu\text{m}$ and ending at 5 mm. The increments in line width are such that they represent approximately uniform multiples of each other and are thus evenly spaced when plotted on a logarithmic axis. In this way, aperture sizes were measured with consistent accuracy as viewed in a log-log graph.

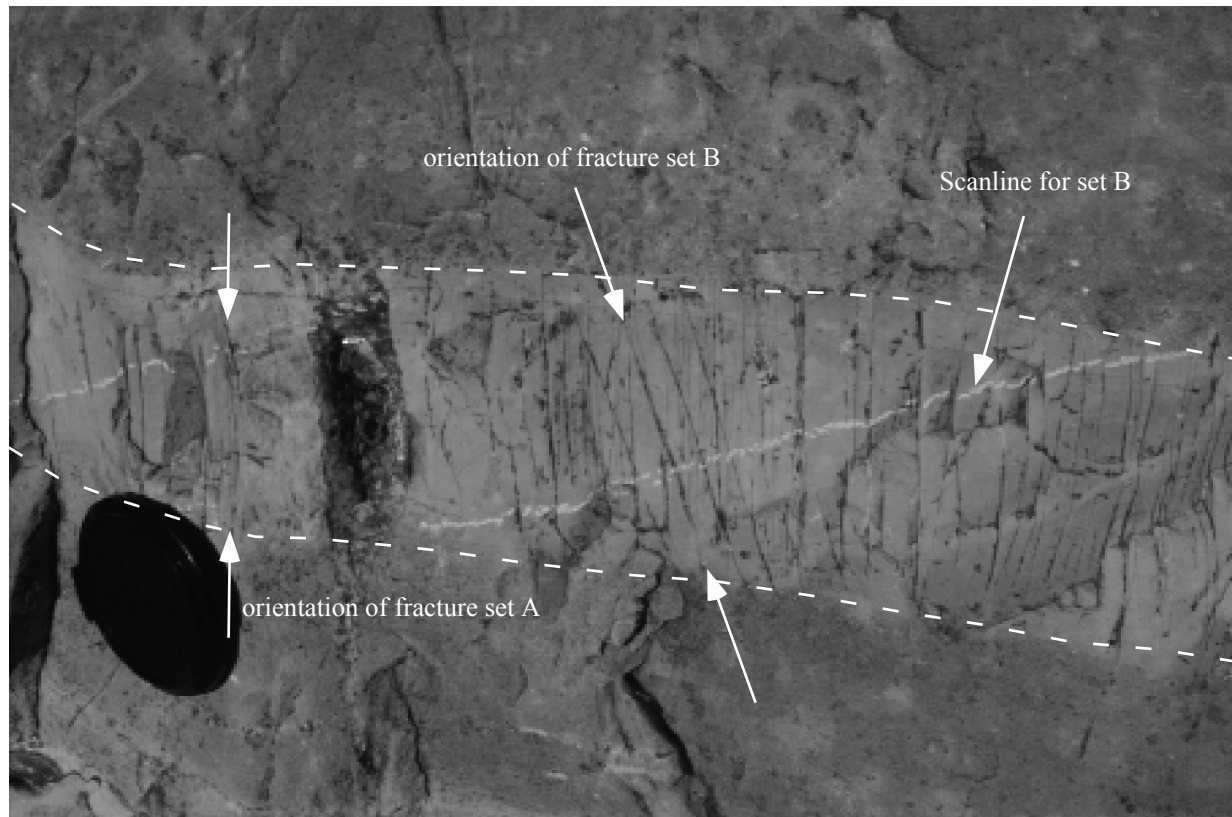


Figure 3.12. Segment of scanline for aperture-data collection in dolostone bed 3, La Escalera Canyon. Mechanical boundaries are indicated by dashed lines and correspond to systematic terminations of fractures. Two fracture sets are present in this bed. Scanline (chalk trace) is approximately orthogonal to fracture set B (inclined with respect to bed boundaries).

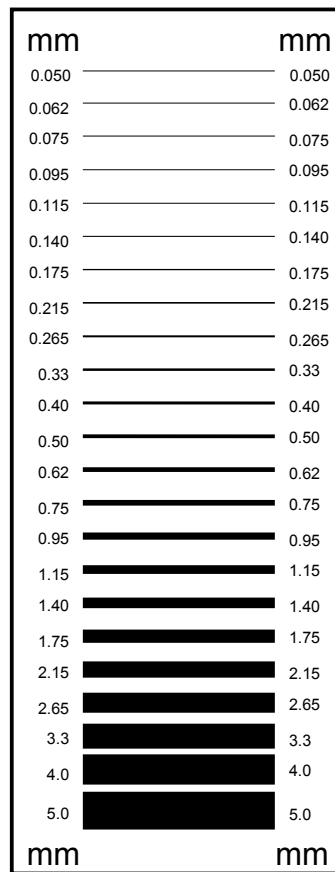


Figure 3.13. Fracture-aperture comparator. To use the comparator, fold or cut it lengthwise along its center leaving two equal sides. Cover the comparator with a plastic laminate to protect it from wear and tear in field conditions. (This version is affected by printer limitations and paper quality. Reproduction using photocopying methods will further reduce graduation quality).

Fracture timing determination

Relative fracture timing relationships are most commonly based on crosscutting relationships. Crosscutting principles suggest that a fracture set that systematically crosscuts another fracture set must postdate the fracture set that is crosscut. Although crosscutting relationships do not determine an absolute time of fracture formation, they can be used to separate groups of fractures that formed approximately synchronously and probably under similar remote stress conditions. However, crosscutting relationships can be confusing in the field and even sometimes under microscopic inspection. Reactivated fractures represent an apparent exception to crosscutting rules. These fractures suggest that fracture propagation can be prolonged during geologic time. In addition to reactivated fractures, relative timing of cement precipitation in crosscutting fractures can be difficult to interpret. Two crosscutting fractures filled with the same mineral may be impossible to date even in relative terms without special observation tools (e.g. Scanning Electron Microscope Cathodoluminescence). There is always the possibility that the same event of cement filling postdates both sets of crosscutting fractures, in which case confusion may arise from ambiguous interpretations of crosscutting relationships. Crosscutting relationships can be especially difficult to establish if fractures are open. This is commonly the case of joint patterns related to exhumation processes.

Abutting relationships are another category of observations that may be used to interpret fracture timing between different sets (e.g., Gross, 1993). Fractures that systematically abut against other fractures can be interpreted as

younger. Statistically-based abutting relationships between fracture sets have been used to support fracture timing relationships, however, numerical simulations of fracture propagation explain how orthogonal fractures may form contemporaneously under the same deformation conditions as a result of progressive fracture growth (Olson, 1997).

Fluid inclusion and isotopic analyses of fracture cement fill can provide bases for fracture timing constraints. Fractures formed under shallow burial conditions may show cement fills with isotopic signatures indicative of low temperatures at the time of cementation. Shallow-burial fractures can also show fluid inclusions indicating low-temperature homogenization. Using these methods of fracture timing requires utmost care to avoid sampling pitfalls and to assure appropriate selection of experimental standards. Certain fracture cement mineralogy might suggest deep burial cementing conditions during fracture formation. For example, ankerite cement is associated with deep burial conditions and hot deep basin brines. On the other hand, dissolution features such as dissolution-induced collapse breccias and cave formation can also provide timing brackets for fracture development.

Fracture timing can also be constrained in relation to other geologic processes occurring in the host rock including large-scale tectonic processes. For example, systematic crosscutting relationships with tectonic stylolites may help assign a tectonic or pre-tectonic origin to fractures. Similarly, if fractures systematically crosscut burial stylolites, then the fractures must have formed after considerable compaction took place in the host rock.

Patterns of fracture attributes like fracture morphology, intensity, and orientation can be used to develop working hypotheses for establishing relative timing and separating fractures into sets. Systematic orientations of fractures with respect to local or regional structures have been used as evidence for fracture origin and timing. For example, faults may be parallel to fractures and fracture swarms suggesting some genetic association. Fractures may also develop as conjugate sets in shear zones associated with large faults. Fractures can also propagate perpendicular to fold axes in response to fold axis parallel extension.

On the other hand, folds may affect pre-existing systematic fracture sets. There is ample evidence for systematic fracture sets in flat-lying beds not associated with significant deformation features. Hydrocarbon exploration activities have documented subsurface fracture systems in slightly deformed strata of numerous sedimentary basins. Recognition of pre-folding fractures in folded terrains may be difficult because fold-related fractures can also be present. Support for pre-folding fractures can be obtained by applying geometric methods of restoration. Pre-folding fracture sets show different orientations on adjacent fold limbs in the current state but equivalent orientations in both limbs after bedding is restored to horizontal. Fractures may also show direct relationship with synsedimentary features like slumps or synsedimentary faults, suggesting an early origin for the fractures. Kinematic analyses of fractures and tectonic stylolites can also help identify pre-folding fractures by recognizing orientation incompatibilities.

Data organization and analysis

The aperture data collected provided the basis for fracture intensity determinations. Fracture intensity values will be compared among beds to assess potential controls of stratigraphic characteristics on fracture intensity. The method used for fracture intensity determination is innovative and produces a less biased estimate of fracture intensity than traditional average spacing methods (e.g. Bogdanov, 1947; Ladeira and Price, 1981; Narr and Suppe, 1991; Wu and Pollard, 1995; Narr, 1996). In the next section we will see the importance of normalization of fracture intensity by fracture size, although here I will summarize a few steps taken to obtain these fracture intensity values.

The aperture data collected were organized in tables by bed and fracture set (Appendix 3.D) and their cumulative fracture-size distribution was plotted in log-log graphs (Appendix 3.E). Marrett et al. (1999) showed that the cumulative size-distribution of a variety of fracture systems in nature is adequately modeled by a single power-law spanning more than five orders of magnitude variation in fracture size. According to Marrett et al. (1999) power-law scaling results apply to carbonates, clastics and volcanic rocks and perhaps indicate that power-law scaling is a characteristic intrinsic to fracture propagation.

I have assumed that the fracture size distributions for the fracture sets studied follow power-law scaling. If the distribution follows a power law, the size distribution will plot as a line in a log-log graph. The assumption appears to be valid for most of the data sets, judging by the fracture-size distributions obtained (Appendix 3.E). However, these distributions are not perfect lines in log-log

graphs and some show significant deviations from an ideal power-law or are best modeled by two power-law segments. Deviations from power-law behavior can be explained by consideration of sampling artifacts (Ortega and Marrett, 2000). A bias-model that takes into account these artifacts and the underlying power-law distribution is the best approach to model fracture size distributions (e.g., Marrett 2000; Burroughs and Tebbens, 2001). Marrett (2000) bias model algorithms were initially applied to each distribution but in some of them the algorithm did not converge or did not produce a best estimate result after trying different combinations of initial parameter values in the range commonly observed for bias power law distributions. In many cases the algorithm failed because aperture data represented a limited range of values. However, for the majority of the distributions direct power-law regressions were adequate to model the data and yielded coefficients of determination above 0.9. A few distributions showed the influence of topologic artifacts (see section on sampling topology artifacts). Interpretation of this effect is backed up by direct field observations of aperture sizes in fractures that span the bed thickness. In these cases the distributions were separated in two segments to isolate the portion of the population unaffected by topology artifacts.

Linear weighted regressions and multivariate analysis

Stratigraphic and diagenetic controls on fracture intensity were analyzed comparing the fracture intensity of multiple beds. The number of observations together with the coefficient of determination of weighted regression analyses

provided a tool for evaluating the relative importance of stratigraphic and diagenetic controls on fracture intensity. These regressions take into account uncertainties associated with fracture intensity determinations following the methodology in Jensen et al. (1997). For a linear regression to an equation of the form $y = mx + b$, the dispersion (Δ) of N data points (x_i, y_i) that we are interested in minimizing is:

$$\Delta^2 = \sum_{i=1}^N s_i (mx_i + b - y_i)^2$$

where s is the inverse of the variance of y_i . In order to find the minimum of this function we obtain the partial derivatives of this relation with respect to m and b , and set them equal to zero. We obtain the equations:

$$\begin{aligned} m \sum_{i=1}^N s_i x_i + b \sum_{i=1}^N s_i &= \sum_{i=1}^N s_i y_i \\ m \sum_{i=1}^N s_i x_i^2 + b \sum_{i=1}^N s_i x_i &= \sum_{i=1}^N s_i x_i y_i \end{aligned}$$

that can be solved for m and b :

$$m = \frac{\sum_{i=1}^N s_i \sum_{i=1}^N s_i y_i x_i - \sum_{i=1}^N s_i x_i \sum_{i=1}^N s_i y_i}{\sum_{i=1}^N s_i \sum_{i=1}^N s_i x_i^2 - (\sum_{i=1}^N s_i x_i)^2}$$

$$b = \frac{\sum_{i=1}^N s_i y_i - m \sum_{i=1}^N s_i x_i}{\sum_{i=1}^N s_i}$$

We can calculate the coefficient of determination (r^2) as $r^2 = mm'$, where m' is the slope of the linear regression that minimizes the dispersion of points in an orientation parallel to the abscissa. The slope of this other regression (m') can be calculated using previous equations but for (y_i, x_i) data pairs.

Multivariate analysis provided a tool for linear regression in a multi-dimensional space where the individual contributions of each factor and their cross-correlations are taken into account.

FRACTURE ORIENTATIONS

Fracture sets were characterized in the field by their morphology, orientation, crosscutting relationships, and composition and texture of the mineral fill. Fracture orientation data and crosscutting relationships were recorded in tables (Appendix 3.D). In all localities, at least four fracture sets can be identified. Some fracture sets can be distinguished in the field by systematic attitude with respect to bed surfaces and systematic crosscutting relationships, but cannot be separated statistically because of the limited amount of orientation data collected and because their orientations partly overlap. Use of similar nomenclature for fracture sets at different localities indicates similarities in relative timing but does not imply that fracture sets with the same label are the same at each locality. Fracture data and analyses in this study are not sufficient to unequivocally

demonstrate that similarly labeled fracture sets are effectively the same from locality to locality. Sets A and B are the oldest sets of fractures, set C is the next youngest fracture set but scarce crosscutting relationships and changes of orientations from locality to locality suggest ambiguous timing relationships and possibly synchronous timing with A and B. Set D (if present) is the youngest at all locality.

La Escalera

La Escalera Canyon locality presents a complex array of fracture sets and stylolites in Cupido Formation beds (Fig. 3.14). Some of these sets may be present at El Chorro and Las Palmas localities because of similarities in crosscutting relationships, fracture morphology and systematic angular relationships with other fracture sets, bedding and fold axis, but not based on present-day orientations.

Burial stylolites are common at La Escalera. Diagenetic stylolites are subparallel to bedding and commonly formed along lithologic boundaries. The amplitudes of stylolite teeth vary from less than a millimeter, appreciable in thin sections, to tens of centimeters at outcrop scale. Considerable volumes of carbonate dissolution may be associated with burial stylolites but only a minimum amount can be estimated based on the cumulative teeth amplitude (Dunne and Caldanaro, 1997).

Tectonic stylolites form a high angle with bedding and the fold axis at this locality. Tectonic stylolites are bed-bound, and developed preferentially in

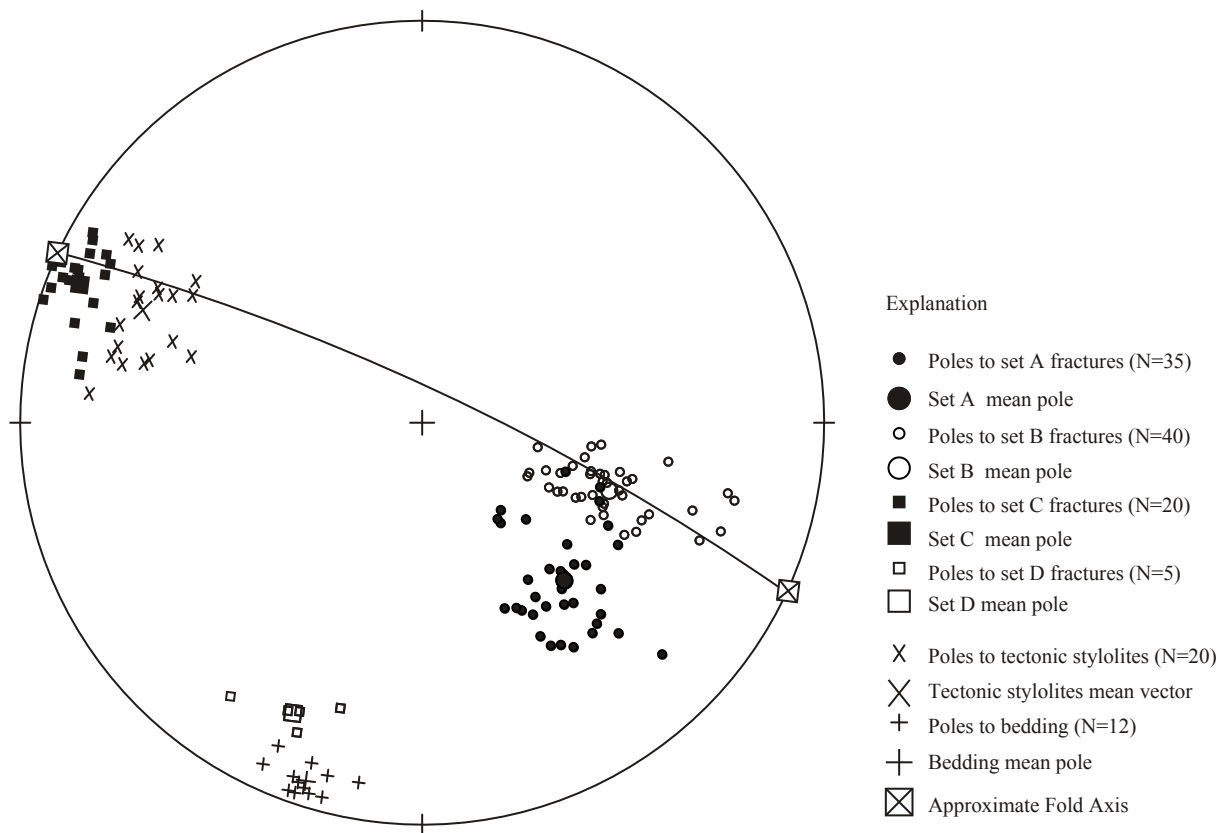


Figure 3.14. Equal area, lower hemisphere stereographic projections of fracture orientations at La Escalera locality. Fold axis plunges only a few degrees (Fig. 3.6) and was assumed horizontal at this locality. Solid line is the cyclographic trace of bedding. Fracture sets A and B are oblique to the fold axis, fracture set A is roughly perpendicular to bedding, fracture B is slightly oblique to bedding. Fracture set C forms a high angle with respect to the fold axis, and is subparallel to the tectonic stylolites. Fracture set D is subparallel to bedding.

dolostones (Beds 1, 8 and 9 in stratigraphic column, Appendix 3.G). No instances of tectonic stylolites crosscutting diagenetic stylolites were found, however a few large tectonic stylolites abut burial-stylolite surfaces (Fig. 3.15), suggesting, but not proving, that tectonic stylolites are younger than diagenetic stylolites.

Attitudes of tectonic stylolites suggest bed-parallel contraction subparallel to the fold axis (Fig. 3.14). Tectonic stylolites orientations at La Escalera are ninety degrees apart from expected orientations based on simple models of fold axis-perpendicular contraction.

Four opening mode fracture sets are present at La Escalera Canyon (Fig 3.14). Set D fractures are long, narrow, and filled with calcite cement. They are the least abundant fractures at this locality and are easier to find in non-dolomitized beds, where other fracture sets are absent or poorly developed.

Fracture set D is roughly parallel to bedding, suggesting bed-perpendicular extension and bed-parallel contraction. Bedding perpendicular fracture opening in subsurface flat-lying beds suggests that the maximum principal stress orientation associated with the formation of these fractures was not vertical, but rather parallel to bedding. Bed-parallel fractures can be produced by overpressure conditions during tectonic contraction events. Fracture set D forms a high angle with tectonic stylolites and is kinematically compatible with them, suggesting that fracture set D may be tectonic in origin. No crosscutting relationships were found for tectonic stylolites and set D fractures at La Escalera locality but tectonic stylolites crosscut other fracture sets, suggesting that other fracture sets are older.

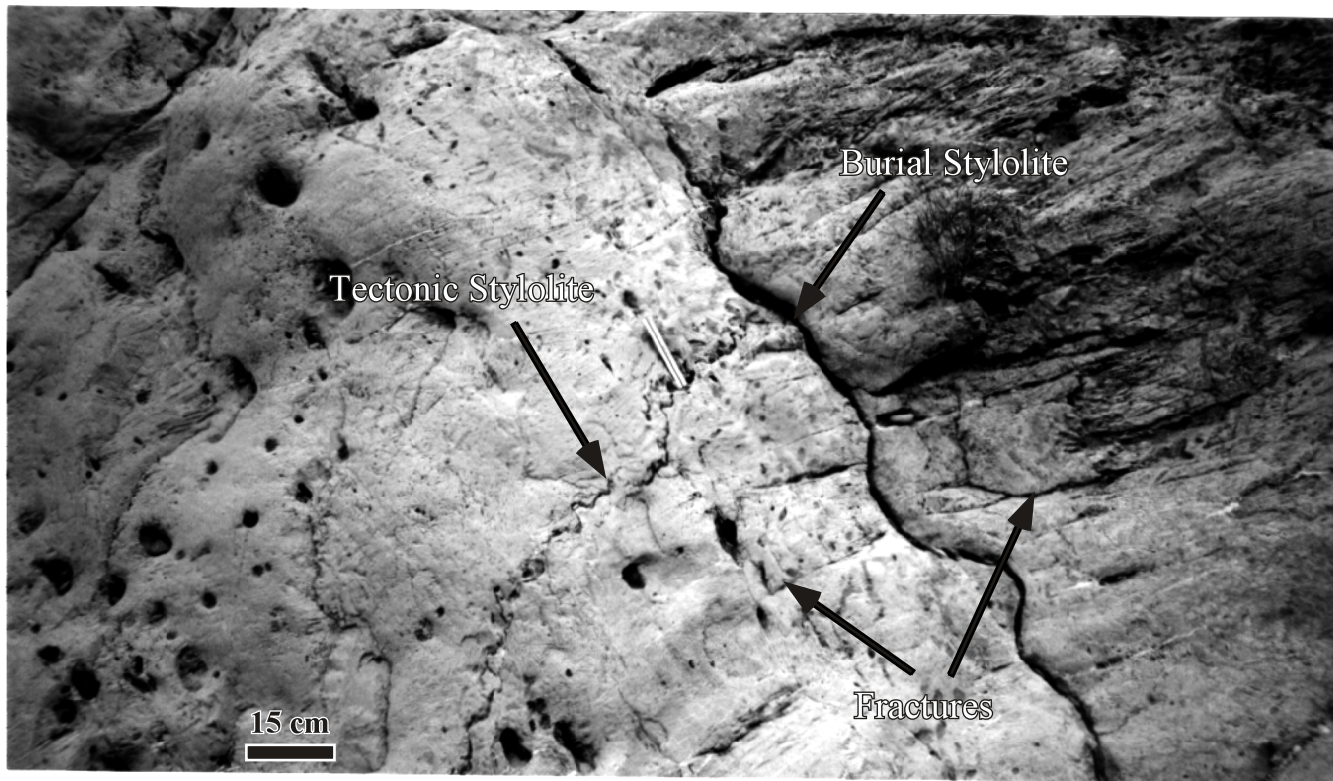


Figure 3.15. Tectonic and burial stylolites at La Escalera Canyon. Bed dips to the right of the photograph. Fractures form high angle with burial stylolite and low angle with tectonic stylolites. Amplitude of some burial stylolites suggests that appreciable amounts of rock have been dissolved. Burial stylolites preferentially developed along stratigraphic planes or at the boundaries of mechanical layers (photograph courtesy of Faustino Monroy).

If tectonic stylolites and fracture set D are contemporaneous they could have formed during fold axis-parallel contraction associated with San Blas Anticline bending into a curved axial trace (Figs. 3.3 and 3.4). Paleomagnetic data from El Chorro Anticline suggests that this structure was originally straight-trending and experienced considerable vertical-axis rotation (Kleist et al., 1984), although another possibility is that whole Monterrey salient rotated.

Fracture set C is perpendicular to the fold axis and suggests extension parallel to the fold trend. Fracture set C orientation is consistent with simple models of fold axis-perpendicular contraction and fold axis-parallel extension. Set C fractures are scarce but more abundant than set D fractures at outcrop scale. A few crosscutting relationships suggest that fracture set C is older than burial stylolites. Fracture set C is kinematically incompatible with tectonic stylolites, suggesting that these two structures formed at different times. Some tectonic stylolites nucleated along set C fracture walls suggesting that fracture set C predates tectonic stylolites and thus possibly set D as well.

Field observations indicate that fracture set C crosscuts fracture sets A and B. Based on these crosscutting relationships fracture sets A and B are the oldest fractures at La Escalera. Sets A and B can be separated in the field because A fractures are systematically oblique to bedding whereas fractures from set B are nearly perpendicular to bedding. A few mutually crosscutting relationships suggest that A and B are contemporaneous. Fracture sets A and B may constitute conjugate sets of mixed-mode veins but no significant shear offset can be identified at intersection lines in outcrop or in thin section. Fracture sets A and B

will be combined as fracture set AB but also studied separately to admit the possibility that they may represent different fracture sets. Studying fracture sets A and B separately allows independent characterization of conjugate fracture sets and the combined conjugate set. Fractures of sets A and B are the most abundant at La Escalera locality and developed preferentially in dolostone layers.

Las Palmas

Las Palmas Canyon presents an array of fracture sets as complex as La Escalera Canyon (Fig. 3.16). Separating fracture sets at Las Palmas locality is difficult because different fracture sets have similar orientation and their orientations are highly oblique to portions of the outcrop studied. Burial stylolites follow bedding plane surfaces and are not as well developed at Las Palmas as at La Escalera. Large teeth on burial stylolites at Las Palmas are most common at dolostone/limestone contacts. Fracture sets A, B, and C studied at Las Palmas abut against or are crosscut by burial stylolites, suggesting that the most recent age of pressure solution along burial stylolite surfaces is younger than or contemporaneous with the fracturing observed.

Four opening mode fracture sets were identified in Cupido Formation beds at Las Palmas Canyon (Fig 3.15). Set A and C fractures are the most abundant fractures at this locality. Fracture set B is generally less abundant. Fracture set C is oblique to the fold axis and slightly oblique with respect to bedding. Fracture set C crosscuts other fractures at Las Palmas except fracture set M.

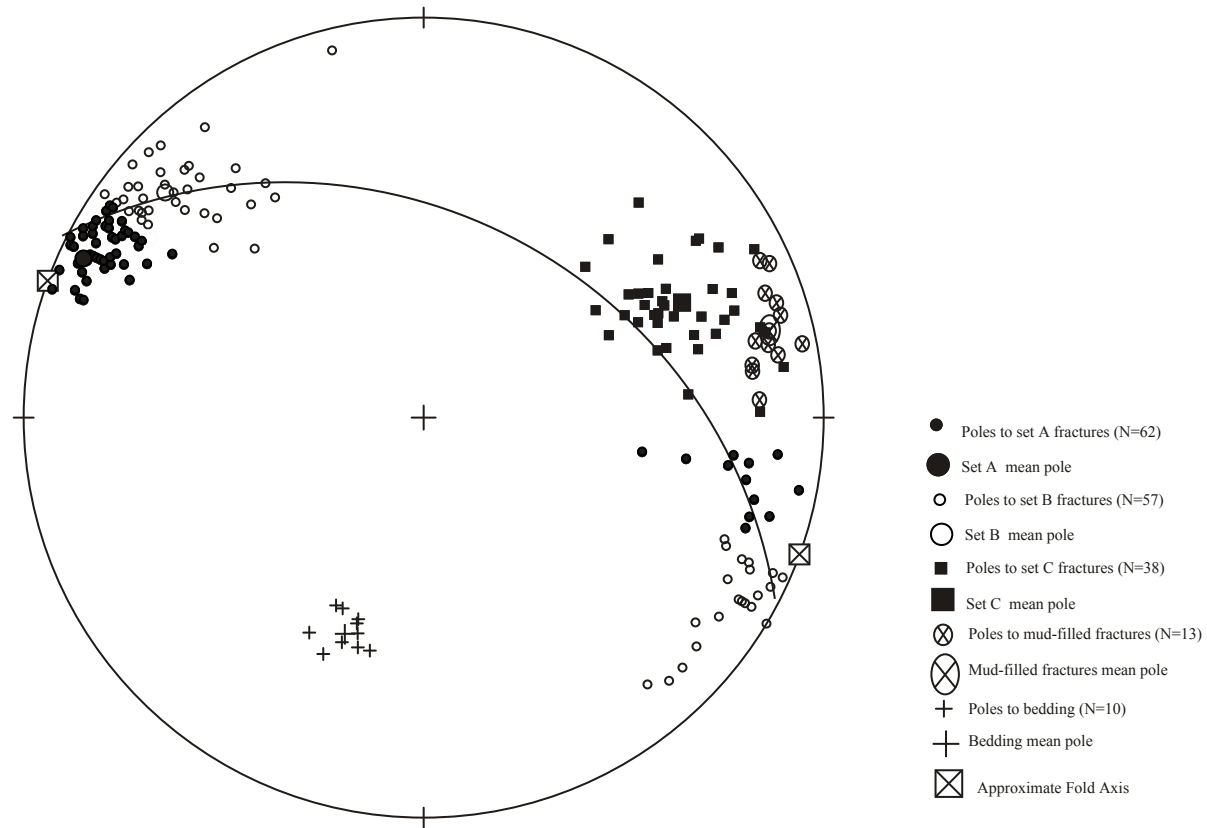


Figure 3.16. Equal area, lower hemisphere stereographic projections of fracture orientations at Las Palmas locality. Fold axis plunges only a few degrees (Fig. 3.6) and was assumed horizontal at this locality. Most fracture sets display considerable orientation dispersion and overlapping, however fracture sets are distinguishable in the field based on systematic crosscutting relationships, attitude with respect to bedding, fracture morphology and fracture fill.

Set A and B fractures have similar orientations but they can be separated in the field because fractures from set A strike more northerly than set B and because fracture set B is slightly oblique to bedding. Differentiation of sets A and B is possible on a bed-by-bed basis, but there is a significant degree of overlap in compiled orientations for all beds (Appendix 3.C). Mutually crosscutting relationships suggest that sets A and B are contemporaneous and similar to sets A and B at La Escalera locality. Fracture sets A and B at Las Palmas and La Escalera also share similar morphologic characteristics and could be conjugate sets although shear offsets were not clearly identified. Sets A and B will be considered a single set although separate analyses for sets A and B will also be carried out.

A fourth fracture set is present at Las Palmas locality. Fracture set M is characterized by calcite-lined walls and later fill by calcite mud, sometimes containing well-preserved bioclasts. Fracture set M crosscuts fracture sets A and B but its relationship to fracture set C is unclear, in part because these two sets are roughly parallel. The origin of fracture set M is problematic, but its fracture-fill characteristics suggest that muddy carbonate sediment was available and capable of migrating into this fracture system. The provenance of this fracture fill is unknown. Fracture set M is the youngest fracture set in the area and probably formed after folding occurred. Support for this latter interpretation comes from crosscutting relationships between fracture set M and bed-parallel fault surfaces and associated gauge zones (Marrett, 2001, personal communication).

El Chorro

A complex array of fracture sets is present in Cupido Formation beds at El Chorro (Fig. 3.17). Burial stylolites are not as common in the Cupido Formation at El Chorro locality as they are at La Escalera. However, isolated outcrops of dolostones down section from the section studied at El Chorro show abundant tectonic stylolites, suggesting fold-axis parallel contraction similar to San Blas Anticline at La Escalera locality.

Five fracture sets were separated at El Chorro based on systematic orientations and crosscutting relationships (Fig. 3.17). Sets D1 and D2 are vertical and show mutually crosscutting relationships among themselves but crosscut sets A, B and C. Fracture sets D1 and D2 were interpreted as a conjugate shear-vein sets. Fracture set D1 is oblique to the fold axis and forms a low angle with bedding. Fracture set D2 is parallel to bedding and to the fold axis, suggesting bed-perpendicular extension and bed-parallel contraction. Fracture set D2 is similar to fracture set D at La Escalera Canyon in morphology and geometric relationships. This similarity between fracture sets in separate folds suggests common formation mechanism and timing. Fracture set D at La Escalera was interpreted as tectonic based on its geometric relationships to bedding; fold axis, and kinematic compatibility with tectonic stylolites. Sets D1 and D2 are preliminarily interpreted as tectonic-related fractures as well, based on their late timing and geometric similarities to set D at La Escalera.

Fracture set C is perpendicular to bedding and is approximately parallel to the fold axis. Fracture set C crosscuts fracture sets A and B, suggesting that

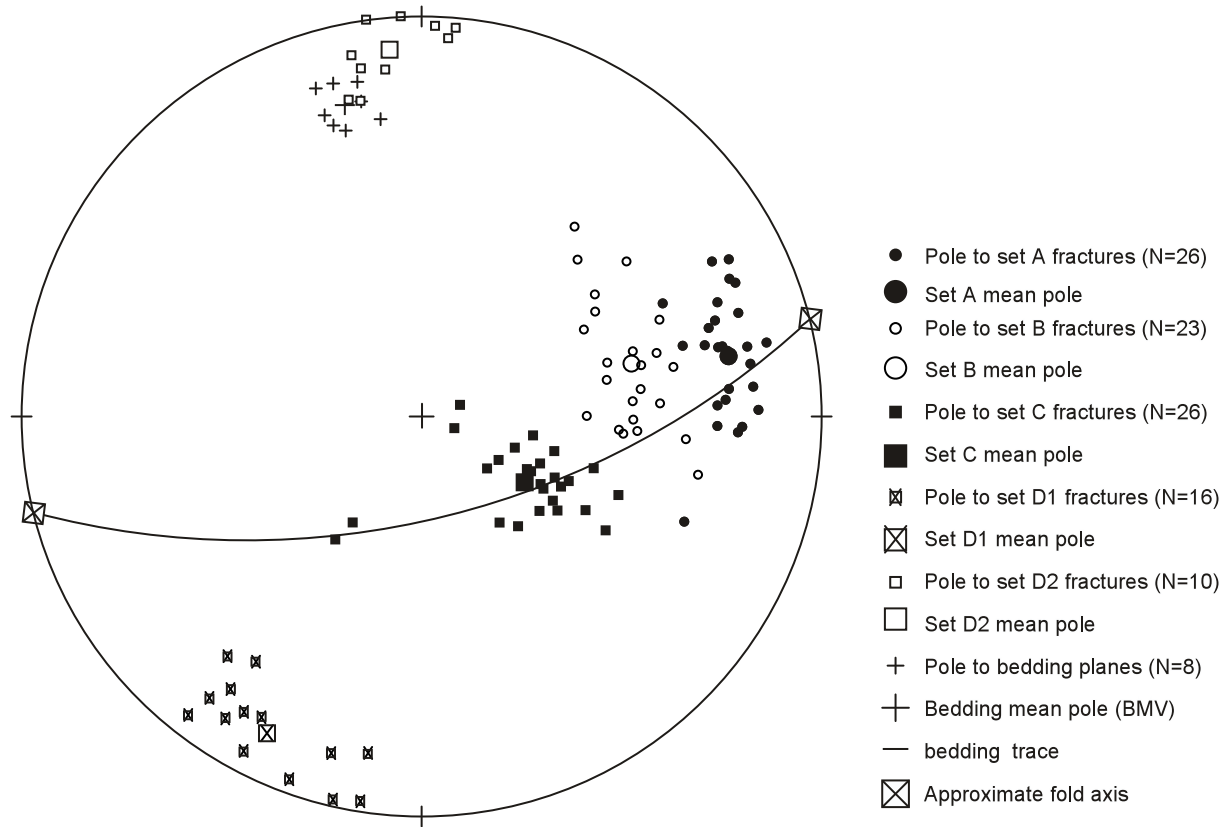


Figure 3.17. Equal area, lower hemisphere stereographic projections of fracture orientations at El Chorro locality. Fold axis plunges only a few degrees (Fig. 3.6) and was assumed horizontal at this locality. Fracture sets A, B form high angles with bedding, but are oblique to the fold axis. Set C is roughly parallel to the fold axis which plunges WSW. These sets partly overlap and show considerable orientation dispersion, but their attitudes with respect to bedding and their crosscutting relationships are systematic on a bed by bed basis. Fracture sets D1 and D2 are roughly vertical, crosscut other sets, and are interpreted as a conjugate shear-vein set.

fracture set C is younger than A and B. The orientation of fracture set C is consistent with bed-parallel extension and models of fracture formation by outer-arc extension in folds (Chamberlin, 1910).

Fracture sets A and B are the oldest fractures at El Chorro. Sets A and B can be separated in the field because fractures from set A form a higher angle with bedding than fracture set B. Set A attitude is also closer to vertical than set B. Mutually crosscutting relationships suggest that A and B are contemporaneous. Fracture sets A and B may constitute conjugate fracture sets. However, no shear offsets across sets A and B were identified in the field.

Iturbide

Fractures studied at Iturbide Anticline are located in Tamaulipas Inferior Formation, which primarily contains carbonate mudstones and chert nodules. Iturbide beds present a complex array of fracture sets and stylolites with considerable orientation dispersion. All fracture sets and tectonic stylolites at Iturbide form high angles with bedding (Fig. 3.18).

Burial stylolites are common at the boundaries of Iturbide mudstones, however some bed surfaces also show evidence of bed-parallel slip in the form of slickolites. The amplitudes of stylolite teeth in Iturbide beds are smaller than for bed-parallel stylolites in other localities and range from less than a millimeter to a couple of centimeters. Burial stylolite surfaces show large wavelength amplitude ratio producing a wavy bedding plane surface characterized by broad basins and ridges that could be mistaken as current ripples.

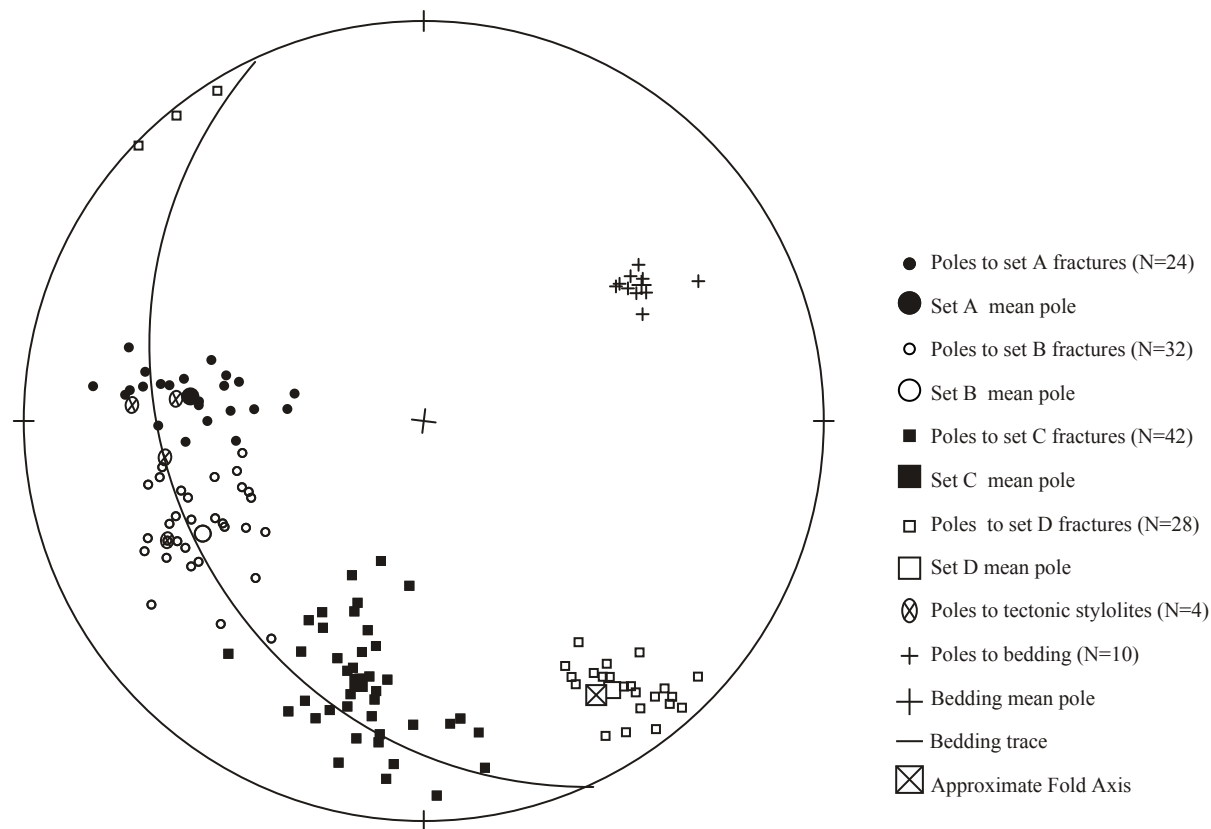


Figure 3.18. Equal area, lower hemisphere stereographic projections of fracture orientations at Iturbide locality. All fracture sets form high angles with respect to bedding. Fracture sets A, and B are slightly oblique to the fold axis. Fracture set C is oblique to the fold axis. Fracture set D is roughly perpendicular to the fold axis. Tectonic stylolites are parallel to fracture sets A and B.

Tectonic stylolites are also present at Iturbide, but they are less abundant than at La Escalera locality. Tectonic stylolites form a high angle with bedding and are slightly oblique to the fold axis at this location. Tectonic stylolites are bed-bound and developed preferentially in some mudstone layers for a reason still unclear. Perhaps organic matter content and/or abundance of allochems and accessories in some mudstones played an important role in the development of stylolites in certain beds (e.g., Bed #7). No instances of tectonic stylolites crosscutting burial stylolites were found. Attitudes of tectonic stylolites suggest bed-parallel contraction at high angle with the fold trend. Tectonic stylolite and fold geometry are consistent with a contemporaneous origin by fold-axis perpendicular contraction.

Four fracture sets are present at Iturbide Anticline (Fig 3.18). Fracture morphology in all sets is similar. Fractures are generally long and narrow, but fractures that reach bed boundaries have apertures that locally increase toward the boundary and abruptly terminate there. Fractures are arranged in swarms with common en echelon geometry.

Fracture set D is orthogonal to bedding and to the fold axis, suggesting bed-parallel extension and fold axis-perpendicular contraction. Fracture set D also forms a high angle with tectonic stylolites, and consequently is kinematically compatible with them and folding. No crosscutting relationships were found between tectonic stylolites and set D fractures at Iturbide, but tectonic stylolites crosscut other fracture sets suggesting that other fracture sets are older and perhaps unrelated to tectonic events. Similar kinematic relationships were

described by Lu (2000) in other folds in the area. Figure 3.19 shows an example of veins and stylolites in mudstone beds in one of these folds, demonstrating that synchronous structures indicative of bed-parallel contraction or extension are present in this area.

Fracture set C is oblique to the fold axis. Crosscutting relationships suggest that fracture set C is older than burial stylolites. Fracture set C crosscuts sets A and B, as observed on several beds in the field and in thin sections. Development of tectonic stylolites along fracture set C walls suggests that fracture set C predates tectonic stylolites and possibly fracture set D as well. Fractures with large aperture in set C were preferentially affected by tectonic stylolites. Development of tectonic stylolites along fractures has been also documented for carbonates in the Cumberland Plateau, in southern Tennessee (Railsback, and Andrews, 1995). Perhaps mechanical contrast between matrix and fracture cement favors tectonic stylolite nucleation along fracture walls that form a high angle with the axis of maximum contraction.

Fracture sets A and B are the oldest fractures at Iturbide. Fracture sets A and B crosscut each other, suggesting synchronous timing and possibly conjugate origin. The conjugate brittle origin of sets A and B is also supported by systematic small offsets. Shear offsets on fracture sets A and B are small compared with the fracture apertures, suggesting dominantly opening-mode movement. Considerable overlap in orientation exists for fracture sets A and B when fracture orientations from all beds are plotted in the same stereographic projection (Fig. 3.18). Both sets A and B are slightly oblique to the fold axis at Iturbide. Crosscutting

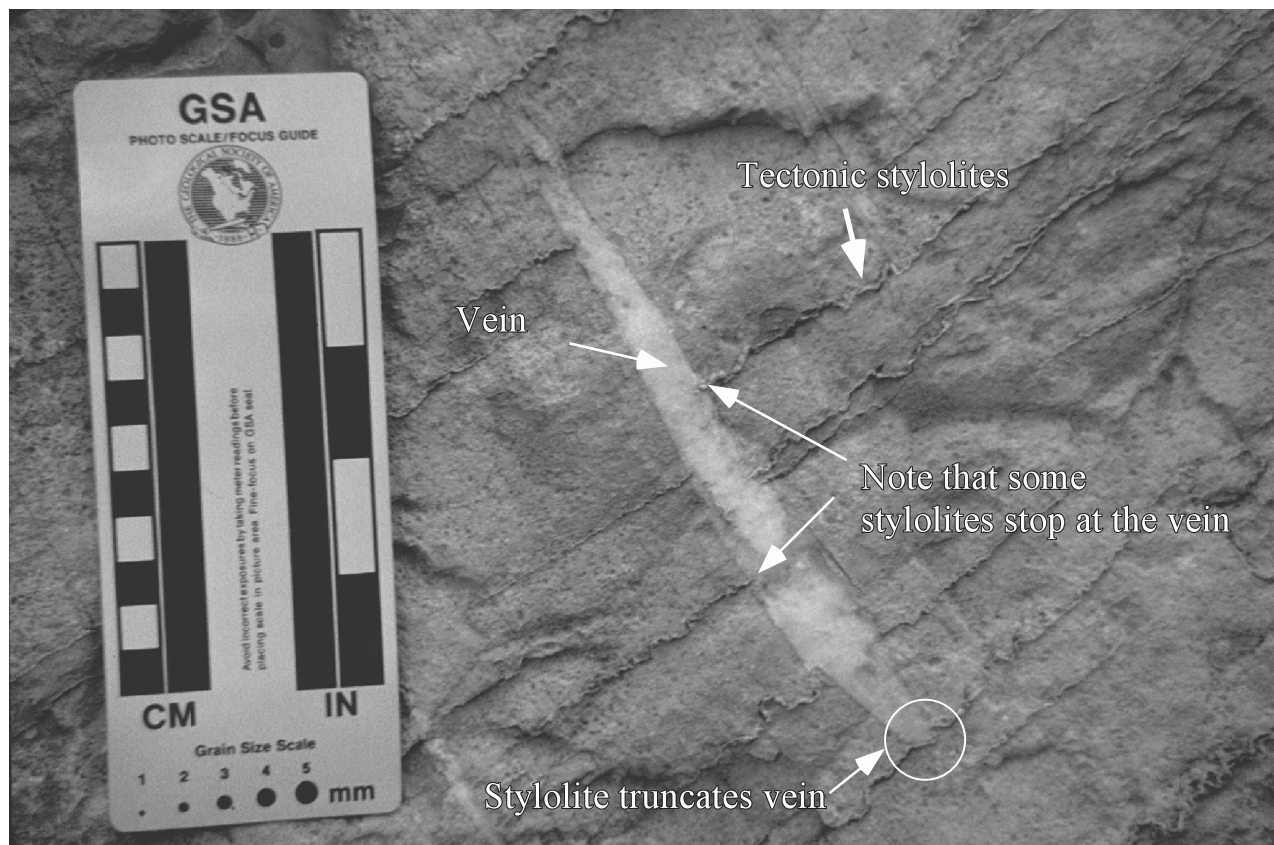


Figure 3.19. View of the base of a carbonate mudstone bed showing transform veins and stylolites in Tamaulipas Inferior Formation, El Mural, Santa Rosa Canyon, near Iturbide. Mutually cross-cutting relations between the vein and stylolites include stylolites that stop at the vein walls or a few millimeters inside the vein and do not have a continuation on the other side of the vein, and a stylolite that truncates one tip of the vein (circle).

relationships with tectonic stylolites discussed above suggest that fold formation and fracture sets A and B are unrelated. The walls of fracture sets A and B are parallel to the tectonic stylolites and kinematically incompatible. Development of tectonic stylolites along the walls of fracture sets A and B confirms that sets A and B are older than tectonic stylolites. Based on relationships between tectonic stylolites and fracture set D discussed above, fractures A and B are also older than set D fractures. A few crosscutting relationships between sets A and D support older timing for sets A, B. Fracture sets A and B are studied together as a combined fracture set AB and also separately as in other localities.

FRACTURE TIMING

Fracture timing is often difficult to characterize. Crosscutting relationships are used as evidence of relative fracture timing, but absolute timing of fracture formation and distinction between tectonic-induced versus burial-related and exhumation-related fractures has been a long lasting controversial topic among geologists. The most frequent association found in the literature is that of fracturing as a smaller scale expression of larger scale features like faults and folds, but in many cases alternative possibilities could not be ruled out or were not considered.

Fracture timing in the SMO

Crosscutting relationships and kinematic considerations were used to assign relative timing to fracture sets at the localities studied. Fracture timing hypotheses were also proposed in terms of the burial and deformation history of Cupido and Tamaulipas Inferior formations. However, restoration tools were not discussed previously to support these timing relationships and to relate fracture sets from different localities. For example, unfolding bedding at La Escalera and Las Palmas brings sets A, B and C close to the primitive circle of the stereographic projection (Fig 3.20) suggesting a pre-fold timing for these fracture sets but few people would conclude pre-fold timing from these results. Fracture sets A and B from Las Palmas locality and Fracture set C from La Escalera show similar attitudes before and after folding. Similarly, fracture sets A and B from La Escalera show similar attitudes to fracture set C from Las Palmas Canyon. Fracture set C is scarce at La Escalera locality but abundant at Las Palmas locality. Field observations indicate that fracture set C crosscuts fracture sets A and B at both localities, however similar orientations of these fracture sets at different locations in San Blas Anticline forelimb suggest a common origin and timing for all these fracture sets based solely on orientation similarities. Poles to fracture set D at La Escalera cluster in a nearly vertical direction, suggesting a tectonic origin. Fracture set D is kinematically compatible with tectonic stylolites that show a roughly vertical attitude in the unfolded state. Tectonic stylolites and fracture set D may have formed during late fold axis-parallel contraction and are

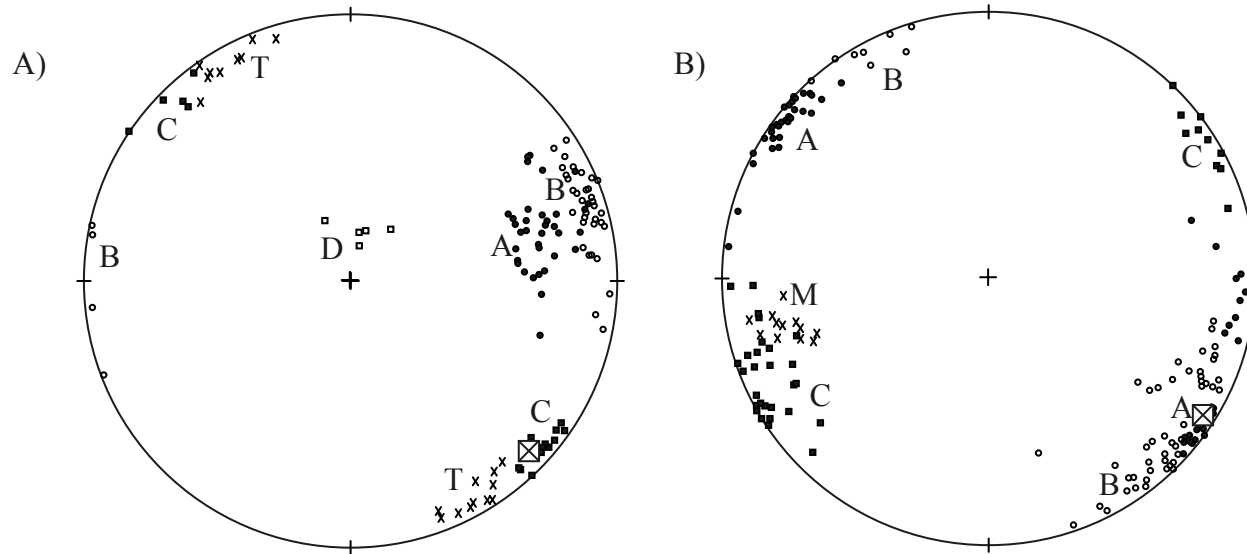


Figure 3.20. Unfolded fracture orientation data, San Blas Anticline, A) La Escalera, B) Las Palmas (explanation of symbols in Figs. 3.13 and 3.15). Simple rotations around fold axis restoring bedding to horizontal. Fold axis is indicated by a crossed large square before restoration. Restoration reveals two dominant fracture sets approximately 60-70 degrees apart. Crosscutting relationships between sets A and B are mutual suggesting that these sets are synchronous. Field data indicate that set C crosscuts sets A and B at both localities but a synchronous timing among all three sets is possible. Set C at La Escalera is parallel to sets A and B at Las Palmas and only a few crosscutting relationships between set C and sets A and B were found at La Escalera. Set D restores to a horizontal attitude suggesting the association of this set to tectonic stylolites and folding. T are poles to tectonic stylolites and M are poles to late, mud-filled fractures.

incompatible with simple fold axis-perpendicular contraction models of fold formation.

Unfolding of El Chorro anticline brings fracture sets A, B and C close to vertical, suggesting that these fractures formed at high angle with bedding (Fig. 3.21). After restoring bedding to horizontal at El Chorro, the poles of fracture sets A, B and C cluster with northwest-southeast trends and coincide with the orientations of sets A and B at Las Palmas and set C at La Escalera. However, at El Chorro, no fracture poles show northeast-southwest trends. Paleomagnetic data suggest that El Chorro Anticline experienced a counter-clockwise rotation of approximately 38° (Kleist et al., 1984). Restoring this vertical-axis rotation to unfolded El Chorro fracture data brings most of fracture set C into the northeast-southwest quadrants and retains sets A and B in the northwest-southeast quadrants. However, the acute angle between sets AB and set C at El Chorro faces a very different direction than the one shown by these sets in San Blas Anticline. Fracture set C at El Chorro crosscuts sets A and B indicating that set C is younger than sets A and B at this locality. Fracture set C at El Chorro is roughly parallel to the fold axis and might be associated with the formation of the fold. Unfolding of fracture sets D1 and D2 brings them to subhorizontal to moderate dips, suggesting that these sets are similar to set D at La Escalera Canyon. Fracture sets D1 and D2 are the youngest sets at El Chorro, coinciding with interpreted timing for fracture set D at La Escalera and suggesting that these fractures may have formed during the same event at both localities.

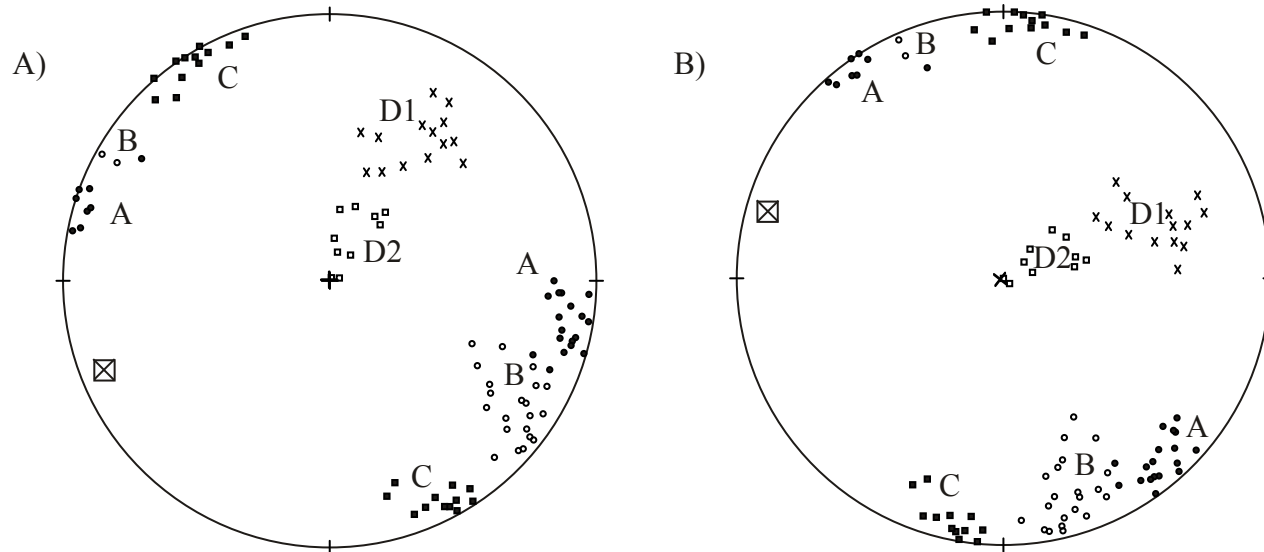


Figure 3.21. Unfolded fracture orientation data, El Chorro Anticline (symbols are explained in Fig 3.16). A) Simple rotation around fold axis restoring stratification to horizontal. The unfolding rotation is assumed to be about a horizontal axis however the fold axis plunges a few degrees to the southwest. B) Rotation of unfolded data 38° around a vertical axis as suggested by paleomagnetic data (Kleist et al., 1984). Fracture sets D1 and D2 are the youngest and are probably associated with the formation of the fold. Fracture sets A, B and C probably formed when bedding was horizontal. Fracture set C is younger than sets A and B and forms a low angle with the fold axis suggesting possible association with the contraction event that produced the fold.

Unfolding fractures from Iturbide Anticline (Fig 3.22) produced results comparable with the ones obtained from localities in shallow-water facies of Cupido Formation. Clusters of poles to fractures appear in all quadrants close to the primitive circle. Poles to fracture sets A and B trend northeast-southwest and poles of fracture set C trend west-northwest-east-southeast. Dispersion in fracture orientation is high but sets A and B form an acute angle of approximately 45° with set C fractures. Sets A and B are roughly parallel to the fold axis and tectonic stylolites. Tectonic stylolites here are kinematically compatible with set D, which shows a high angle with the fold axis. Tectonic stylolites and set D fractures are consistent with bed-parallel contraction roughly perpendicular to the fold axis. The magnitude of the plunge of Iturbide Anticline fold axis is unknown. Lu (2000) compiled fold axes orientations for other anticlines in Santa Rosa Canyon indicating plunges of less than five degrees. Two restorations were carried out to cover a range of reasonable plunges for Iturbide fold axis, from horizontal to 20 degrees southeast. The restorations do not produce significant differences in the results discussed above. However, a plunging anticline restores fractures to orientations closer to vertical suggesting that a plunging model for the restoration may be more accurate.

As mentioned before, direct association of fold deformation and fracturing is a common and perhaps valid assumption in many areas. A reasonable hypothesis for most structural geologists working in the SMO would be to relate the fracturing observed to the tight folds present in the area. Shortening estimates for the Monterrey Salient area (e.g. 30% according to Marrett and Aranda-García,

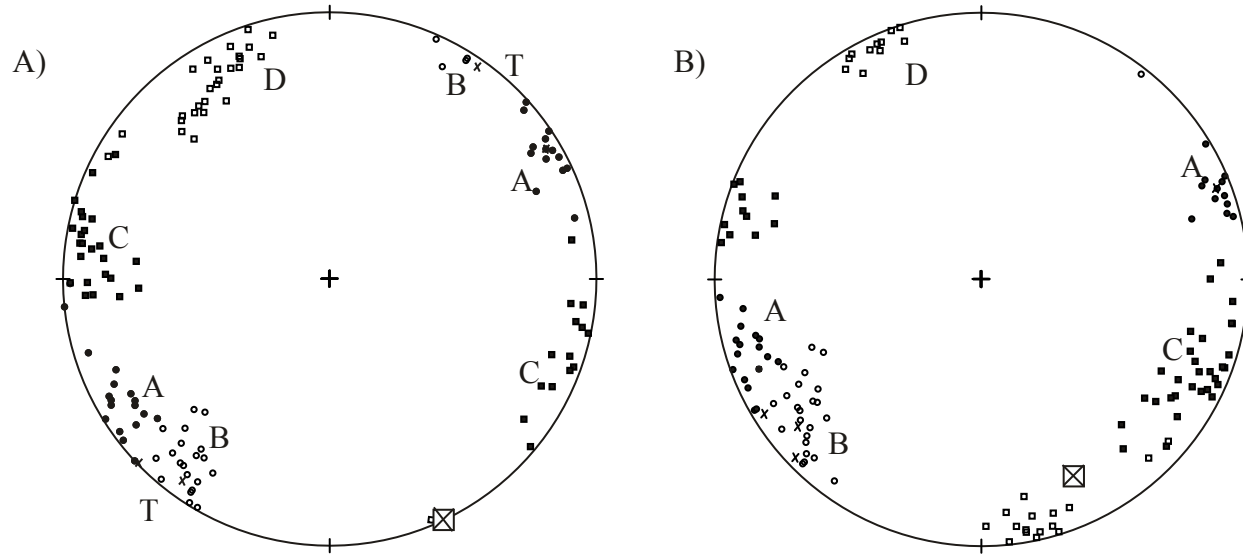


Figure 3.22. Unfolded fracture orientation data, Iturbide Anticline (symbols are explained in Fig 3.17). A) Simple rotation around fold axis restoring stratification to horizontal and assuming bed-strike parallel horizontal fold axis; B) rotation around fold axis restoring stratification to horizontal and assuming a bed-parallel 20° southeast plunging fold axis. Fracture set D is the youngest and is probably associated with tectonic stylolites (T) and folding. Fracture sets A, B and C probably formed when layers were horizontal based on cross cutting relationships with set D and tectonic stylolites as well as contradictory kinematics. Fracture set C is younger than A and B. Sets A and B show mutually crosscutting relationships and small shear offsets and are interpreted as shear-veins. Sets A, B and C orientations resemble the orientations of similarly labeled sets in other localities. A plunging anticline is probably a better model for the restoration judging by a more regular distribution of fracture poles.

1999) suggest that some fractures are probably structural in origin. However, in Cupido Formation beds in the Monterrey Salient area, fracture-crosscutting relationships with respect to synsedimentary or early burial processes suggest that a priori associations of fracturing and the Laramide-age deformation observed are inappropriate (Marrett and Laubach, 2001).

Fractures with an orientation, morphology and mineralogy similar to those of sets A and B are present in rotated blocks in collapse breccias at Las Palmas Canyon (Fig. 3.23). This crosscutting relationship poses an important timing constrain on these fracture sets if the timing for the collapse can be established. The collapse breccia at Las Palmas locality contains blocks of multiple sizes and angularity. Some blocks are as large as 1 m in diameter including intact portions of the ceiling of the collapse cavity, and can be visually restored back to their original position before collapse. Blocks in the breccia can be correlated with adjacent undisturbed layers, suggesting a local provenance. The collapse affects several parasequences including dolomitized peritidal facies, and non-dolomitized subtidal packstones and wackestones. Large blocks of calcite-replaced evaporites were also involved in the collapse. At the base of the collapse breccia at Las Palmas Canyon there is a layer of laminated evaporite replaced by calcite that pinches out laterally. This layer of evaporite and entire blocks of calcified anhydrite in the breccia suggest that the large collapse at Las Palmas Canyon is similar to smaller scale collapse features described in the literature (Goldhammer et al., 1991), and others found at La Escalera (Fig. 3.24). Collapse breccias in Cupido Formation have been previously associated with fluctuations of sea level

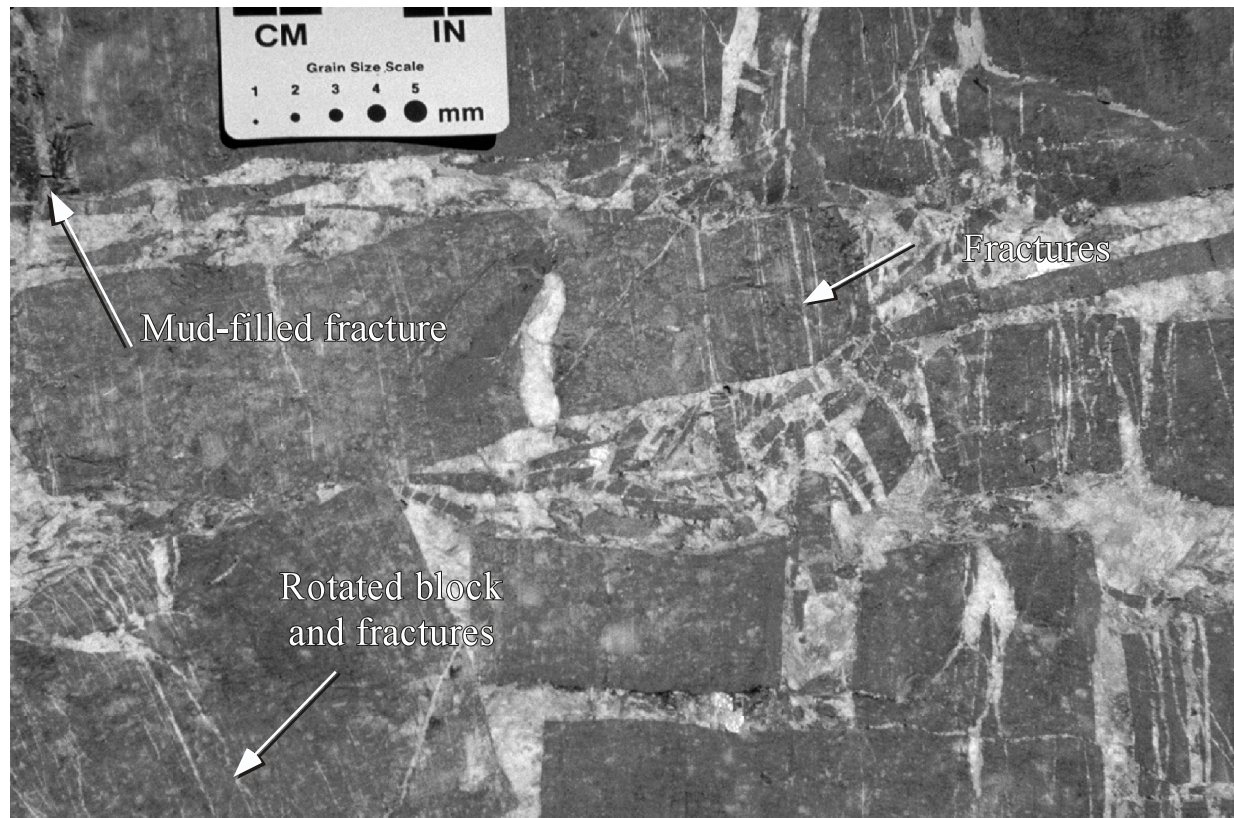


Figure 3.23. Collapse breccia at Las Palmas Canyon. Rotated blocks, containing rotated fractures that are truncated at block boundaries, prove that fractures formed before the collapse. Collapse breccias are associated with gravitationally-driven fall of bed pieces into cavities left by dissolved evaporites. Dissolution of evaporites and collapse has been associated with variations in sea level during Cupido Formation sedimentation (Goldhammer et al., 1991). Large dot on scale is 5 mm in diameter (photo courtesy of Randall Marrett).

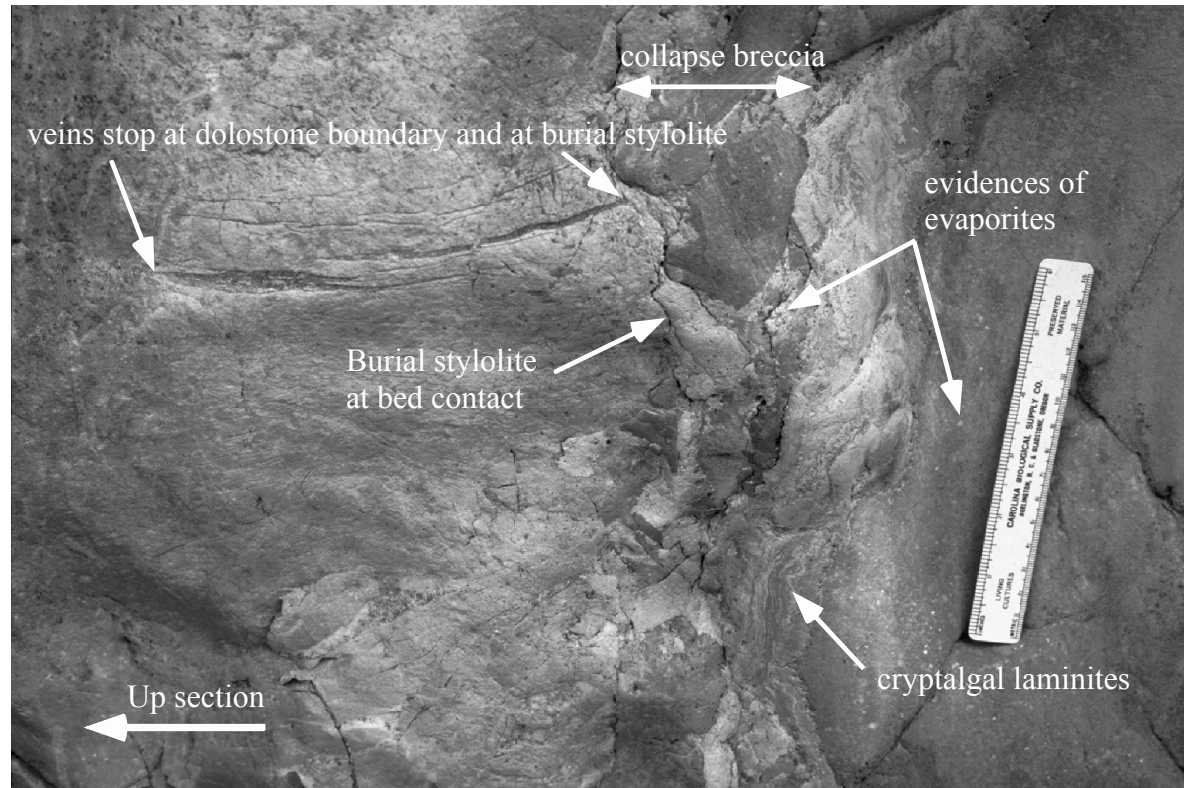


Figure 3.24. Collapse breccia at La Escalera Canyon. Underlying the collapse breccia are cryptalgal laminites 5 to 10 cm thick, suggesting deposition in tidal flat environment where evaporite precipitation is common (note calcite-replaced nodules and evaporite layer remnants). Overlying the collapse breccia is a fractured, dolomitized layer. Note that fractures in the dolostone layer did not propagate through the collapse breccia. Note also that burial stylolite postdates fractures and collapse breccia.

during the sedimentation of this unit (Goldhammer et al., 1991). It is then possible that these pre-folding fractures in Cupido Formation breccias formed under shallow-burial conditions, during the time-span of the Cupido Formation sedimentation, probably during the first tens of meters of burial. Carbon and Oxygen isotope analyses of cement around collapsed blocks in Las Palmas Canyon breccia may provide quantitative evidence to further restrict fracture timing in these beds by constraining temperature of cement precipitation (Monroy et al., 2001).

Collapse breccias are generally strata-bound, although sometimes collapse features extend up-section several meters (e.g., Las Palmas Canyon, Appendix 3.G), thus suggesting the existence of an interconnected dissolution-induced cave-system. Another line of evidence for the early origin of collapse breccias is that the breccias clearly occurred before burial stylolites. Burial stylolites are often found at collapse breccia boundaries (Fig. 3.24), and are absent in blocks within the breccia itself. Further support for the early origin of collapse breccias comes from the development of sedimentary fill deposits leveling the topography created by the collapse (Fig. 3.25). Goldhammer et al. (1991) describes similar stratigraphic pinch outs in collapse breccia outcrops in localities to the north of the study area (e.g., Potrero Garcia).

FRACTURING AND DIAGENESIS

Petrographic analyses of samples from the 43 carbonate beds in which fractures were studied allow a preliminary assessment of the diagenetic history

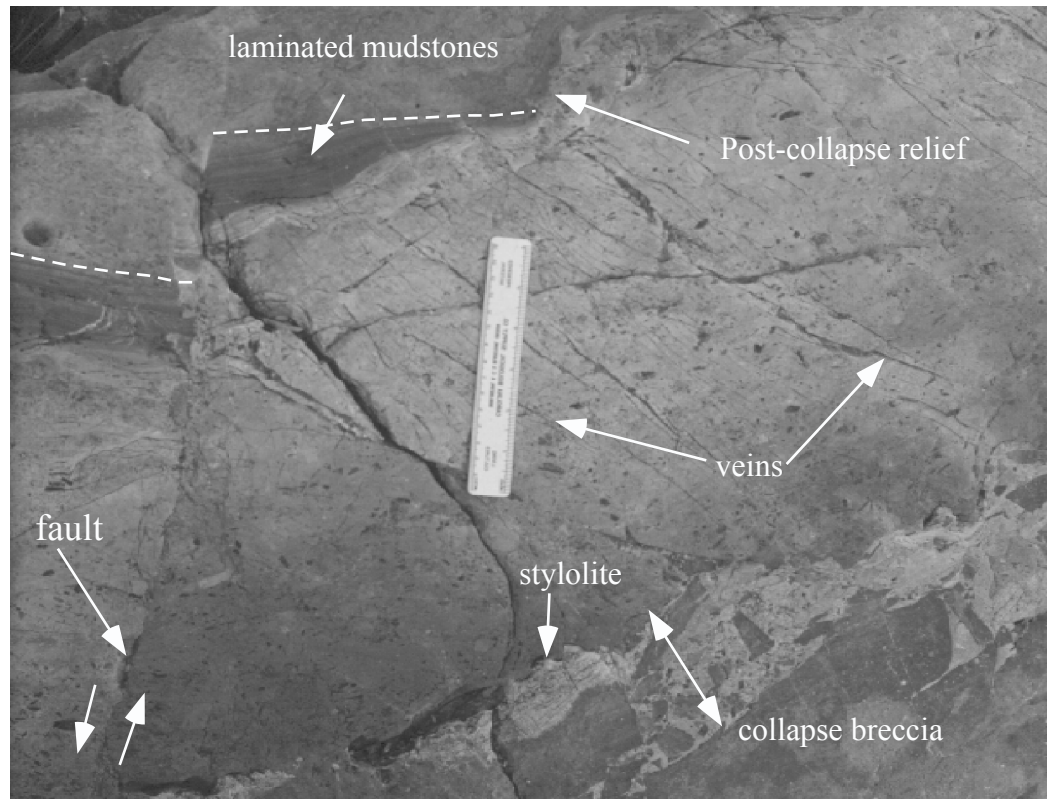


Figure 3.25. Collapse breccia at La Escalera Canyon. Note overlying fractured dolostone layer and irregular top surface generated after the collapse. Normal faulting possibly associated with continuation of collapse in underlying evaporite layers. Topographic irregularities after collapse were leveled by laminated mudstones, which pinch out toward local topographic highs. Graduated ruler is approximately 15 cm long.

and its relation with fracturing (Fig. 3.26; Monroy et al., 2001). Fracture-fill cements include calcite, dolomite, and quartz. Fractures in dolostones are lined by euhedral dolomite crystals and contain dolomite bridges from wall to wall suggesting that dolomite was the first mineral phase filling these fractures. Multiple dolomite bridges adjacent to each other give a fibrous texture to the fracture fill, with saw-tooth contacts between the fibers and “brisket-like” internal texture. Ramsay (1980) described similar fibrous veins and interpreted them as indicative of cementation synchronous with fracture opening. Cupido fracturing contemporaneous with dolomite cementation is shown by crack-seal textures in dolomite-filled fractures. Dolomite cement is then synkinematic, using Laubach’s classification of cement timing with respect to fracture timing (Laubach et al., 1995; Laubach, 1996; Laubach, 1997). Dolomitized layers in shallow water facies of Cupido Formation generally show higher fracture intensity than limestone layers, at least visually. Blocks of fractured dolostones and limestones in collapse breccias suggest that dolomitization and early fracturing occurred before dissolution collapse (Fig. 3.23).

Calcite cement precipitated after dolomite precipitated, filling the remaining pore space in fractures (Fig. 3.27). Calcite is then postkinematic according to Laubach’s classification. Alternating dolomite bridges and postkinematic calcite cement produced a mottled texture in some fractures similar to the zebra dolomite texture of intensely altered dolomites (Fischer, 1988; Fig. 3.28).

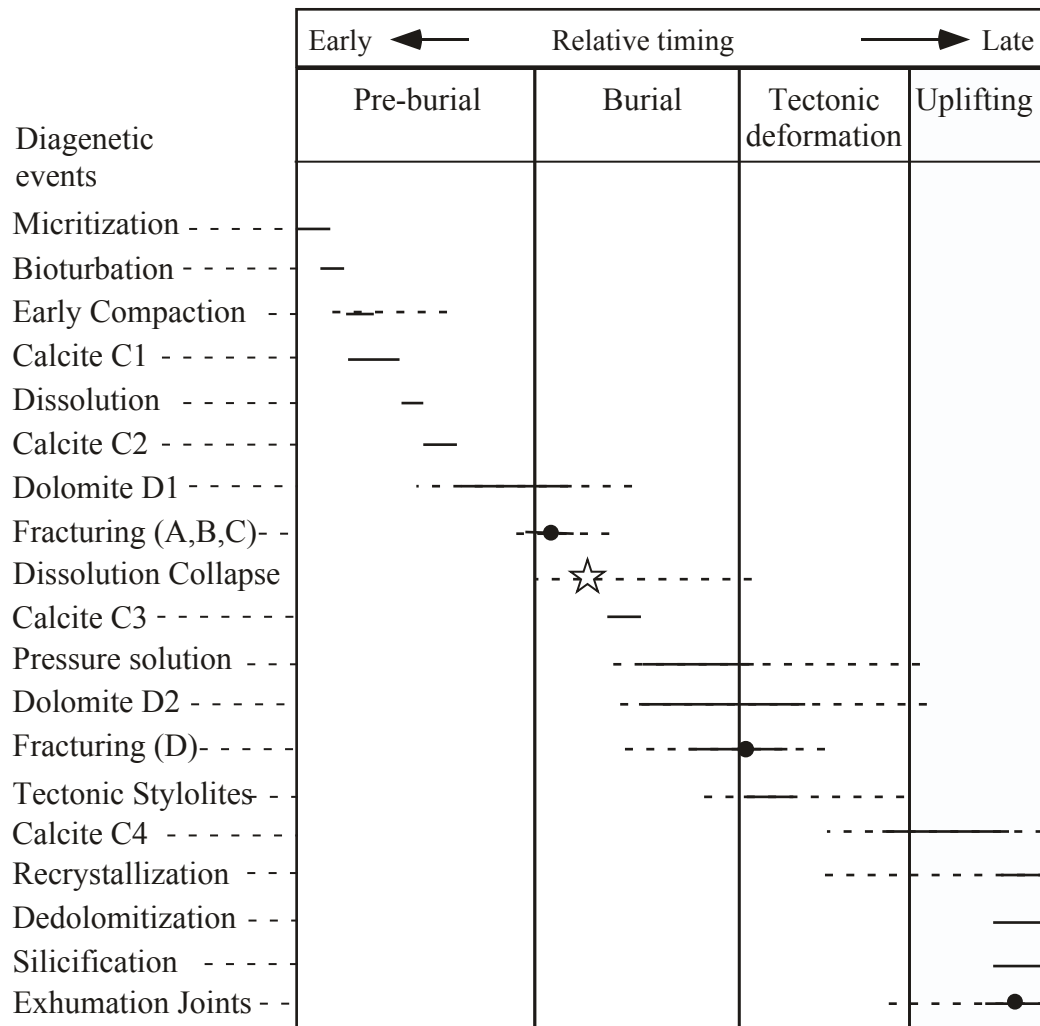


Figure 3.26. Paragenetic sequence for shallow water facies Cupido Formation. El Chorro, La Escalera and Las Palmas localities. Fracturing events in the diagenetic history of the Cupido Formation (modified from Monroy et al., 2001). Most probable timing for breccia collapse indicated by a star. Interpreted timing for fracturing events indicated by black dots. Dashed line suggests possible extent of event. Solid line represent probable timing based on combined field observations, petrography and kinematic analyses.

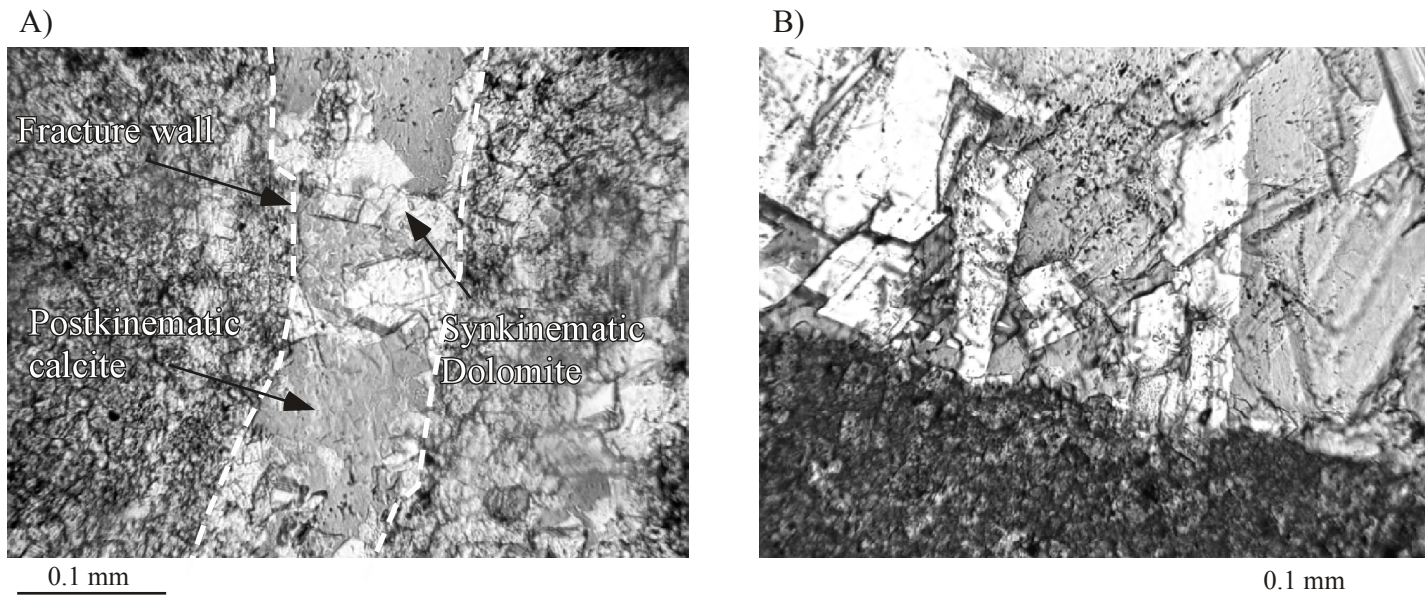


Figure 3.27. Photomicrographs of cement-fill in fractures of Cupido Formation. A) Vein lined with synkinematic dolomite, which also formed bridges of euhedral crystals joining fracture walls. Postkinematic calcite filled remaining fracture porosity. Las Palmas Canyon, sample CuLPa-9-98p, cross-polarized light. B) Detail of euhedral dolomite bridges (white) and overlapping?/replacing? postkinematic calcite (light grey). Dolomite bridges are rooted on matrix-dolomite crystals exposed at the fracture walls. Las Palmas Canyon, sample CuLpa-3-98So, plane light.

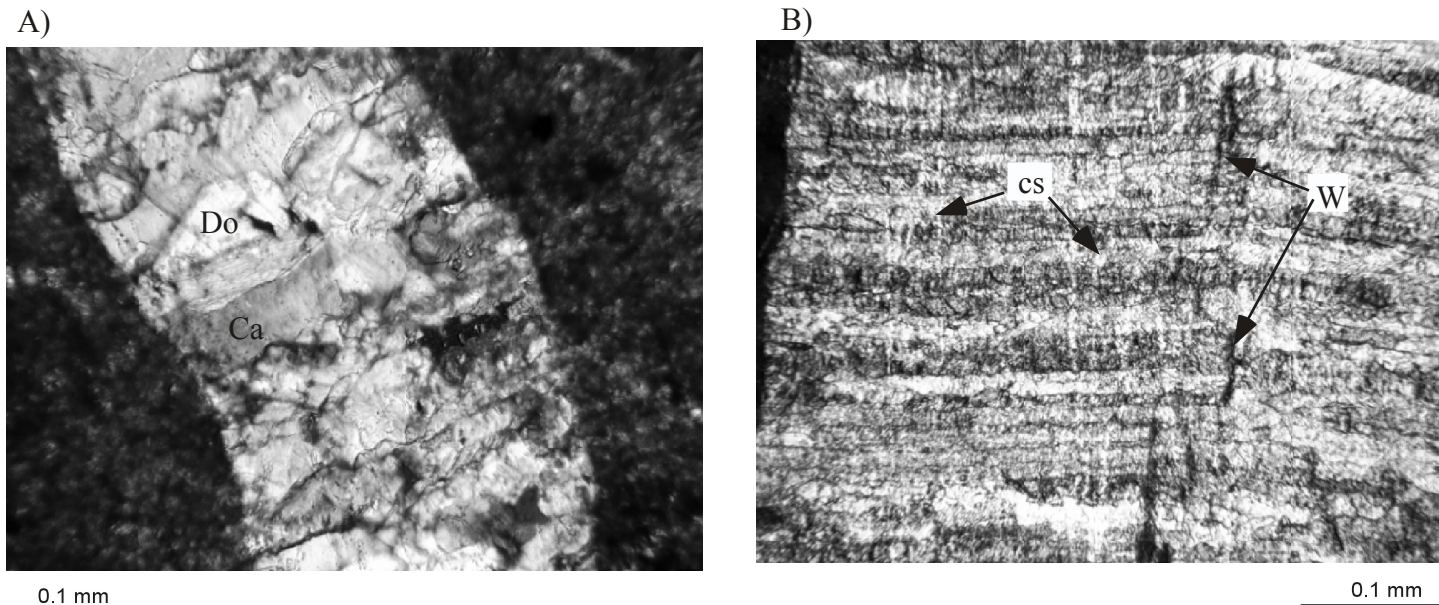


Figure 3.28. Photomicrographs of cement-fill textures in fractures of the Cupido Formation at La Escalera Canyon. A) "Zebra-stripe" texture of alternating fibrous dolomite bridges (Do, light gray) and postkinematic calcite (Ca, darker gray). Postkinematic calcite partly replaces/covers dolomite rhombs, but "ghosts" of dolomite crystals can still be recognized. Sample CuEsc-6B-98-So, cross-polarized light. B) Dolomite-filled vein showing crack-seal texture. Pieces of fracture wall (W) are included within the vein during repeated opening events. Thin, clear dolomite-filled fractures orthogonal to fibrous crystals (cs) are additional evidence of repeated crack-sealing process. Sample CuEsc-2-98So, plane light.

Recrystallization did not occur in all limestone beds, but where present it blurred the contrast between mineral fill in older fractures and matrix and obscured fractures having apertures smaller than the average grain size of recrystallization. Fractures with apertures smaller than 5 microns are difficult to distinguish from matrix in these rocks. Only a few grainstones and boundstones recrystallized to sparry calcite. In these cases, fractures with apertures less than a tenth of a millimeter can be indistinguishable from matrix.

Dedolomitization and silicification are late-diagenesis effects on fracture fill (Fig. 3.29; Monroy et al., 2001), affecting dolomite and calcite cements in fractures and matrix. Crosscutting relationships and petrographic textures suggest that dedolomitization and silicification occurred after fracturing. Dedolomitization passively converted dolomite back to calcite by removing magnesium from dolomite. Silicification was volumetrically small (approximately 1% of rock volume) and most petrographic observations suggest silicification by replacement of calcite in fractures. Absence of quartz-lined fractures or quartz crack seal textures suggests that fracture propagation had stopped at the time silicification was happening.

NORMALIZED FRACTURE INTENSITY

Fracture intensity, fracture density, and fracture frequency all describe fracture abundance in rocks. Fracture frequency is a general term that includes fracture intensity and fracture density. Fracture intensity is a quotient having units of inverse length between the number of fractures, sum of fracture lengths, or sum of fracture surface area, and the length, area, or volume of observation (Mouldon

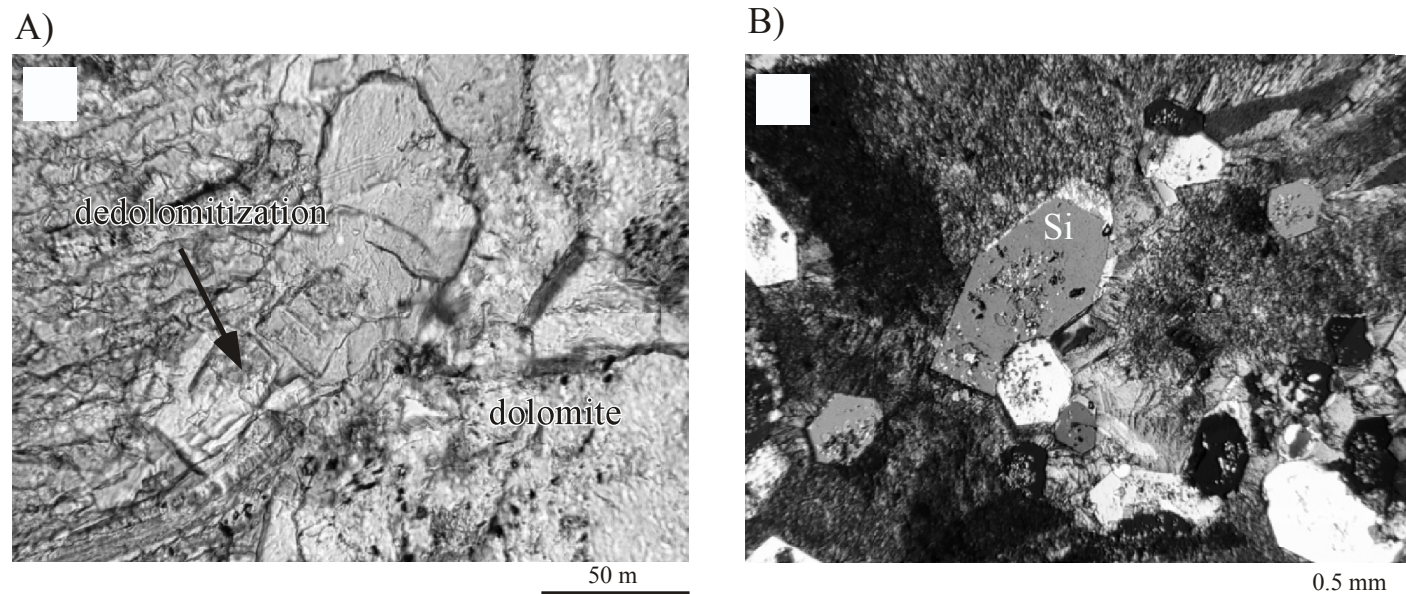


Figure 3.29. Photomicrographs of late diagenetic events affecting vein cement. A) Dedolomitization is shown by "corroded" dolomite crystals, partly replaced by calcite. Some calcite rhombs (darker gray) might have been dolomite crystals now completely replaced by calcite during dedolomitization. Las Palmas Canyon, sample CuLPa-1-00So, plane light. B) Replacement of calcite cement by silica (Si). Note sparse euhedral quartz crystals in vein material. Quartz crystals typically contain numerous carbonate inclusions. La Escalera Canyon, sample CuEsc-7-98So, cross-polarized light.

et al., 2001). The literature contains numerous examples of fracture intensity determinations, most commonly from outcrops (e.g., Corbett et al., 1987; Huang and Angelier, 1989; Narr and Suppe, 1991; Gross, 1993), but also from subsurface (Corbett et al., 1987; Lorenz and Hill, 1991; Narr, 1996), and laboratory tests (Rives et al., 1992; 1994, Wu and Pollard, 1992, 1995; Mandal et al., 1994). Fracture intensity (F) is usually determined from one-dimensional observation domains (i.e., scanlines) by dividing the number of fractures (N) by the total length (L) of scanline:

$$F = \frac{N}{L}$$

However, the most common indication of fracture abundance reported in the literature is the average spacing (S) between fractures counted along a scanline (Huang and Angelier, 1989; Narr, 1991; Gross, 1993; Ji and Saruwatari, 1998). This value is exactly the inverse of the fracture intensity.

$$S = \frac{1}{F}$$

Frequency distributions of fracture spacing can be modeled by negative exponential (Priest and Hudson, 1976; Pineau, 1985), log normal (Sen and Kazi, 1984; Narr and Suppe, 1991; Rives et al., 1992; Becker and Gross, 1996; Pascal et al., 1997), Gamma (e.g., Huang and Angelier, 1989; Gross, 1993; Castaing et al., 1996), or even normal distributions (Ji and Saruwatari, 1998). Using analytical methods we can obtain the expected spacing value (i.e., mean spacing) assuming that spacing follows one of these distributions (Larsen and Marx, 1985). Sampling

bias could also explain variations in the best mathematical model for published fracture spacing distributions, although Rives et al. (1992) and Ji and Surawati (1998) suggest alternative explanations for this variability.

There are a number of mechanical models that explain the apparently regular fracture spacing observed in some layered rocks (Lachenbruch, 1961; Price, 1966; Hobbs, 1967; Sowers, 1972; Pollard and Segall, 1987; Narr and Suppe, 1991; Gross, 1993). However, in determining average fracture spacing from model results none of these models accounts for the fact that different size fractures are required to cross beds of different thickness. Likewise, data in support of relationships between bed-thickness and fracture intensity or spacing are unclear about the size of fractures used for spacing determinations. Authors typically have not specified if the fractures counted were all that he or she could see with a naked eye, or perhaps only those that reached the boundaries of the mechanical layer (Huang and Angelier, 1989; Lorenz and Hill, 1991; Castaing et al., 1996). Moreover, the size of fractures visible on an outcrop varies according to exposure quality and fracture-fill characteristics, which typically have not been accounted for. Furthermore, if we changed the scale of observation, for example from outcrop scale to microscopic scale, our estimates of fracture intensity or spacing would be different. This lack of rigor potentially introduces bias in the calculation of fracture intensity or spacing.

Calculation of normalized fracture intensity

The use of cumulative-frequency fracture-size distributions addresses the scale problems inherent to average fracture spacing determinations. Cumulative-frequency fracture-size distribution plots yield a measure of the abundance of fractures that explicitly varies according to their size. This method effectively quantifies fracture intensity for detection thresholds corresponding to all fracture sizes considered. It has the advantage of facilitating direct comparison between data sets collected at different scales of observation or levels of resolution. The following example will illustrate the advantages of using cumulative-frequency fracture-size distributions over the traditional method to measure and compare fracture abundance.

Figure 3.30 shows a cross section of a fractured bed in which fracture abundance is to be determined along a one-meter long scanline at two different scales of observation. This example represents real aperture data collected along a scanline along a dolostone bed approximately 8 cm thick at La Escalera Canyon. The fractures have been randomly located in the cross section because for the following analysis the actual location of the fractures is not important. First, only fractures with apertures greater than 0.5 mm have been plotted (Fig 3.30A). Fracture size spans an order of magnitude, from 0.5 to 5 mm in aperture size measurable with a 0.5 mm graduated ruler. After calculating the average spacing at this scale of observation (24 fractures in 1000 mm) we find that the fracture intensity in this bed is approximately 24 fractures/m (Fig. 3.26A). However, if we included all the fractures with apertures down to 50 microns (28 fractures in 200

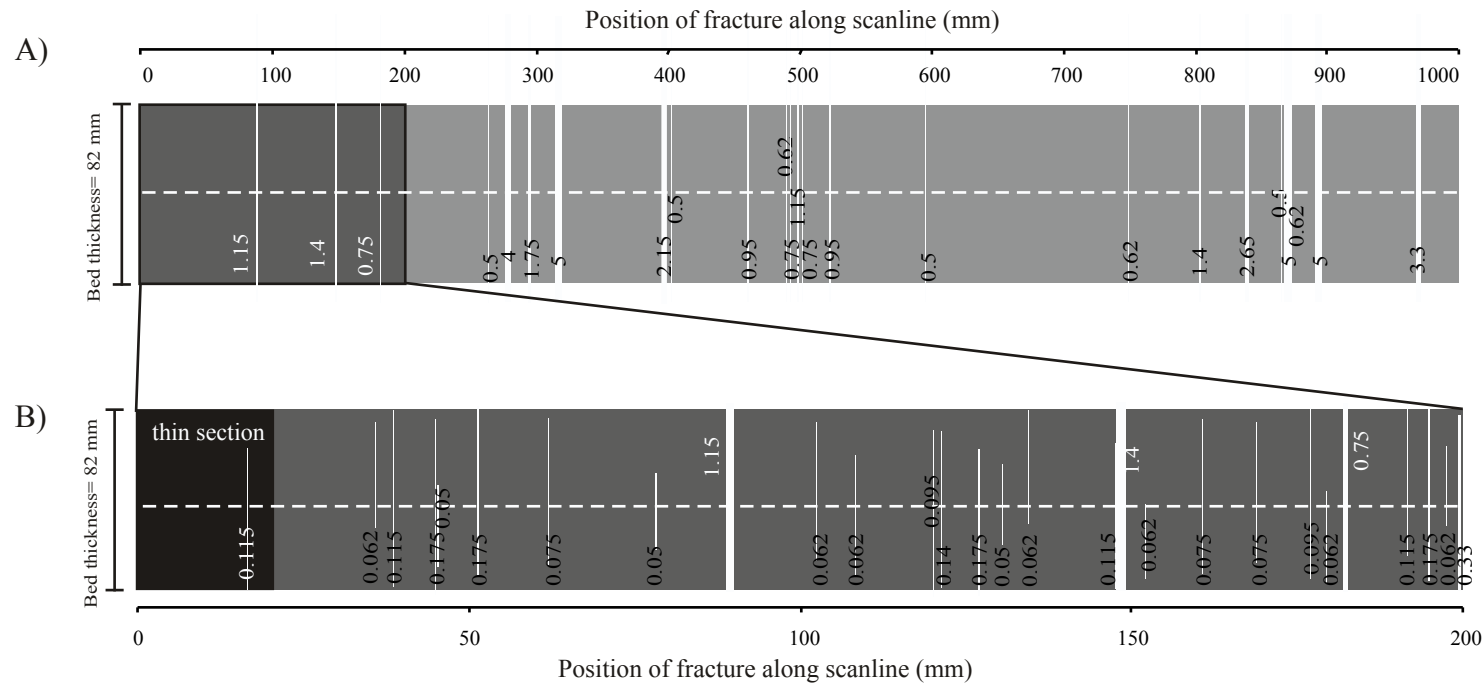


Figure 3.30. Cross section of bed #3 La Escalera Canyon. Fractures of set A are solid white lines, fracture aperture is the number next to each fracture. The scanline is represented by a dashed line running perpendicular to the fractures. A) All fractures with apertures greater than 0.5 mm are shown, these fractures typically span the mechanical layer. The average spacing between fractures is 40 mm; B) First 20% of the bed (dark area in A)) showing fractures with apertures greater than 50 microns. The average fracture spacing at this scale of observation is 7 mm. Area in black represents approximate width of a thin section. Calculation of fracture intensity from a thin section using traditional methods yields an average fracture spacing of less than 1 mm. All fractures in the thin section are invisible at outcrop scale with the exception of one fracture 0.115 mm wide.

mm), measurable with a hand lens and the aperture comparator (Fig 3.13), the fracture intensity is 140 fractures/m (Fig. 3.26B), nearly an order of magnitude higher than the one previously calculated. Furthermore, microfracture aperture data from a thin section of this bed indicate the fracture intensity of fractures larger than 5 microns wide (10 fractures in 12 mm) is yet an order of magnitude higher, namely over 1000 fractures/m (figure 3.26C). This illustrates that fracture intensity depends on scale of observation and that fracture size must be taken into account in order to calculate meaningful fracture intensities.

The cumulative fracture intensity derived from the fracture-size distribution provides a measure of fracture intensity that explicitly accounts for fracture size and permits comparison of data collected at different observation scales. This normalized fracture intensity allows direct comparison of data sets for any aperture size. To make a cumulative frequency fracture-size distribution plot we followed these steps:

- 1) List all the fracture apertures from the largest to the smallest.
- 2) Number the fractures such that the largest one will be number one and the other fractures will receive higher numbers as the aperture size decreases (i.e., generate a list of cumulative numbers).
- 3) Simplify the list by eliminating all fractures with a the same aperture size except for the one with the largest cumulative number.
- 4) Normalize the cumulative numbers by the length of the scanline. This will generate values of cumulative fracture intensity (i.e., number of fractures of a certain aperture or larger per unit length of scanline).

This parameter is a measure of the fracture intensity in the rock at a given scale of observation and can be used to compare and contrast fracture intensities from different beds.

- 5) Make a plot of cumulative fracture intensity versus aperture size to display the distribution in graphic form. A number of fracture size distributions can be adequately modeled using simple mathematical laws. Power-law distributions plot as lines in a log-log plot. Exponential fracture-size distributions plot as a line in a log-linear graph.
- 6) Obtain the parameters of the best model for the distribution observed.

An example of a normalized cumulative fracture size distribution plot is shown in Figure 3.31 for fracture set A in bed 3, La Escalera Canyon. These data are adequately modeled by a power law function defined by a coefficient and a power-law exponent. The power-law function predicts the abundance of fractures of a certain size or larger per unit length of scanline. The coefficient represents the value of the power-law function for a fracture size of 1. The exponent of the power law represents the slope of the power-law line in a log-log plot. This exponent is always negative because the cumulative frequency of small fractures is greater than or equal to the cumulative frequency of larger fractures.

Obtaining the normalized fracture intensity for a given fracture size or larger is simple. From the cumulative-frequency fracture-size distribution plot (Fig. 3.31) we read the corresponding frequency (number of fractures per unit

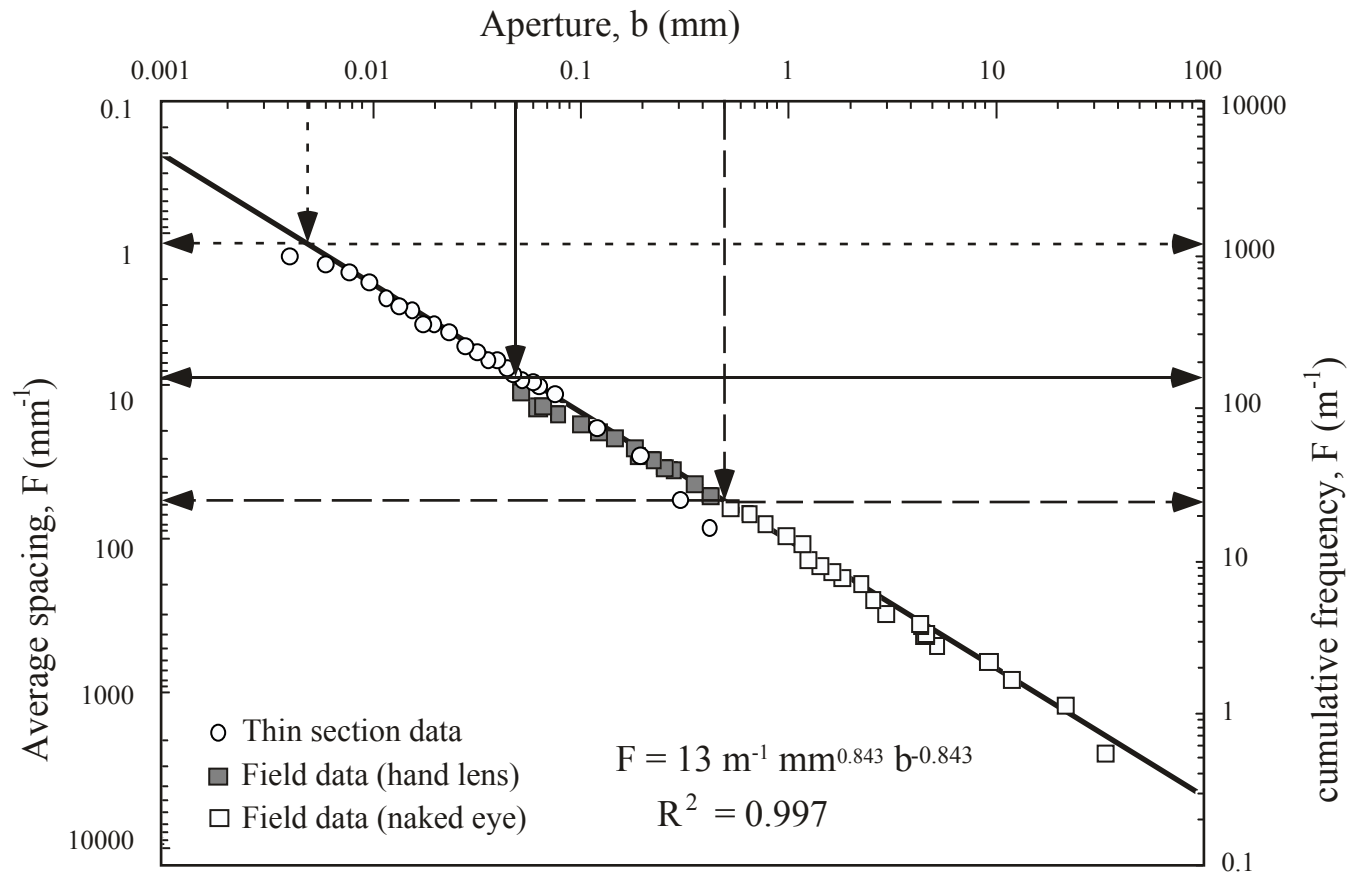


Figure 3.31. Normalized fracture intensity from cumulative fracture size frequency distribution. Set A (230 38), dolostone bed#3, 8.2 cm thick, La Escalera Canyon. Fracture abundance can be characterized as intensity (cumulative frequency) or average spacing (inverse of cumulative frequency).

length of observation) for a given fracture size using the power-law distribution model as a guide. We can also obtain an average spacing value using the power-law, referring to an ordinate axis graduated with inverse frequency values (i.e., spacing). For the exercise discussed previously, we can now obtain the fracture abundance and average spacing for any scale of observation.

The arrows in Figure 3.31 indicate the scale dependence of fracture abundance. Figure 3.28 illustrates graphically the simpler approach based on counting fractures without accounting for their sizes. This approach generates a simple estimate of average spacing and intensity that is valid, but only for some unknown threshold of fracture aperture. Consequently, spacing/intensity values cannot be compared confidently with measurements from other scanlines because aperture thresholds might differ due to variable outcrop quality, different fracture morphologies, or different size of fractures required to span a layer. Additionally, there is no information about sampling bias possibly affecting the data. Fracture intensity (or spacing) values are similar to the cumulative frequency for the example case because I specified a range of fracture sizes for the calculation. However, in most examples in the literature there are no specified limits for fracture size in the calculation. Patterned areas in Figure 3.32 suggest ranges of fracture intensity at different observation scales.

Sampling and topology artifacts

Fault scaling studies have dominated the literature on fracture scaling (Bonnet et al., 2001, and references therein; Marrett et al., 1999, Ackerman et al.,

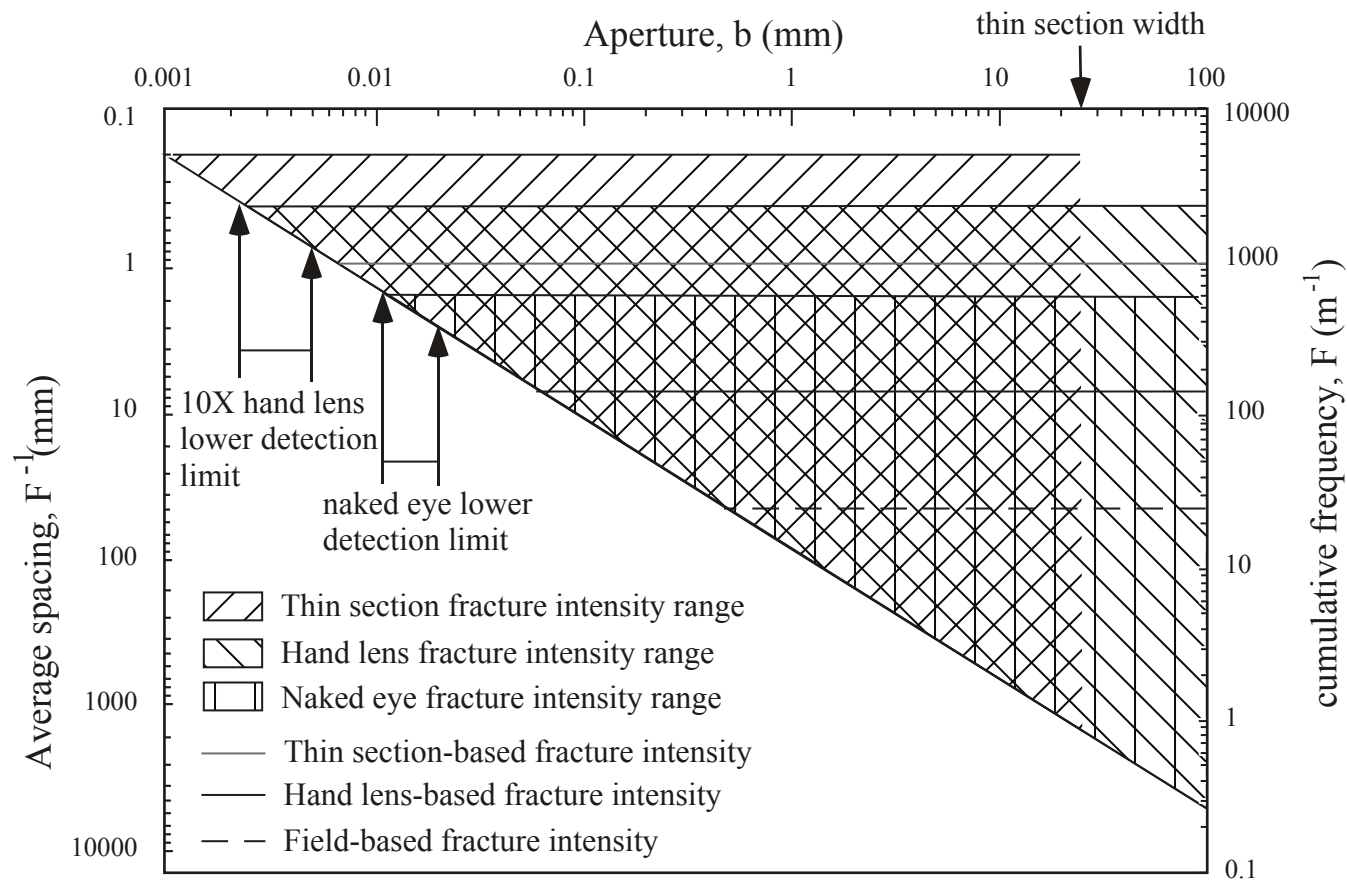


Figure 3.32. Representation of the fracture-counting method for fracture intensity calculation in a log-log graph. Thick lines represent example explained in text and lower detection ranges are approximate for Cupido Formation. The counting method is fraught with errors introduced by inconsistent limits of minimum fracture size counted for the calculation. Patterned areas are determined by approximate minimum size detectable at various observation scales. Note range of possible fracture intensities and overlapping areas.

2001). Much less abundant is the literature on opening-mode fracture scaling. However, there is now general agreement about the power-law nature of open-mode fracture-size distributions (Gudmundsson, 1987; Wong et al., 1989; Heffer and Bevan, 1990; Barton and Zoback, 1992; Gillespie et al., 1993; Hatton et al., 1994; Sanderson et al., 1994; Belfield and Sovich, 1995; Clark et al., 1995; Gross and Engelder, 1995; Johnston and McCaffrey, 1996; Marrett, 1997; Marrett et al., 1999; Ortega and Marrett, 2000; Bonnet et al., 2001). Most work on this aspect of fracture population statistics has been done for fracture length. However, fracture length determinations are prone to subjective interpretations of fracture tips. These non-unique fracture length measurements arise from the difficulties of clearly defining what is a through-going fracture when fractures branch or intersect (Ortega and Marrett, 2000). Studies of fracture-aperture distributions are less common in the literature, perhaps because of the lack of appropriate tools for effective fracture-aperture measurement in the field. However, considerable progress has been made in recent years using new methods for accurate fracture aperture measurements, which have generated some very well constrained fracture aperture-size distributions (Ortega et al., 1998; Marrett et al., 1999).

Marrett et al. (1999) showed examples of opening-mode fracture and fault size distributions that follow consistent power laws across three to five orders of magnitude in size. Some of these distributions included microscopic scale aperture data from sandstones and carbonates. However, fracture size distributions commonly show deviations from an ideal power law in the small and

large fracture size portions of the distribution. Sampling, topology and statistical artifacts produce these deviations.

Truncation artifacts: Deviations of small fractures from the scaling shown by larger fractures of a size distribution have been long recognized in the literature as truncation artifacts (Baecher and Lanney, 1978; Barton and Zoback, 1992; Pickering et al., 1995). Truncation artifacts can be explained by variable sampling completeness for fracture sizes near the limits of resolution of the observation tool (e.g., smallest fracture size accurately measurable with the naked eye varies from place to place in outcrop exposures). However, a mathematical description of truncation artifacts has not been proposed yet. In a log-log plot the portion of the size distribution affected by truncation artifacts typically show a convex-upwards curved shape that decreases in slope with decrease in fracture size. I tried to avoid truncation artifacts by artificially imposing a lower cut off to the sizes of fracture apertures collected, even though smaller fractures commonly were visible. The cut off value corresponds to the smallest graduation size in the comparator. Fracture apertures smaller than this cut off value are still distinguishable even with a naked eye, but those fractures were ignored because they could not be reliably measured.

Censoring artifacts: Censoring artifacts have been best described for fracture length distributions obtained from two-dimensional domains (i.e., maps). Censoring occurs when a fracture continues beyond the limits of the observation

domain and its true size cannot be determined. Inclusion of these fractures in the distribution acknowledges their presence but degrades accuracy of the length distribution. The censoring effect produces an apparent homogeneity of large fracture sizes compared with the wider range of sizes for non-censored fractures. Censoring disproportionately affects data from the largest fractures because the probability that a fracture continues beyond the limits of the observation area is proportional to fracture size. Censoring effects on a fracture-size distribution produces an increase in the slope (exponent of the power-law) for the largest fractures.

Censoring artifacts affecting aperture size distributions have not been appropriately documented. Two-dimensional sampling of fracture apertures is not intuitive and has largely been avoided in fracture-size distribution studies. Aperture censoring can be an indirect consequence of fracture length censoring because the largest aperture of censored fractures cannot be determined unequivocally. Aperture size distributions have more commonly been obtained for one-dimensional sampling domains (i.e., scanlines). Censoring artifacts in one-dimensional domains are not expected for apertures with the exception of the trivial cases of a scanline that stops in the middle of a fracture before reaching the other fracture wall, or exposure limitations that prevent complete sampling of large-aperture fractures.

Topologic artifacts. Topologic artifacts are best illustrated by referring to a specific example. Assume a number of layer-perpendicular fractures randomly

distributed in a layer of rock. Imagine that these fracture sizes follow a power law distribution. The volume of rock will contain some fractures that span the thickness of the layer and other fractures that are partly or totally embedded in the layer. In any two-dimensional slice of this volume parallel to the layer the probability of sampling a fracture that does not reach both boundaries depends on the fracture height but a complete sampling of fractures that span the layer thickness will be obtained. This means that we effectively obtained a three-dimensional sampling of these fractures from a two-dimensional observation domain. However, fractures that do not span the layer thickness will show lower apparent abundance than their true abundance in three-dimensions. The cumulative size distribution will reflect this change in apparent abundance as a decrease in the slope of the power-law distribution for non-spanning fractures, which typically are most abundant (Marrett, 1996).

Similar reasoning can be extended to one-dimensional sampling domains. A scanline perpendicular to the fractures in the layer will sample a subset of all fractures in the volume. The probability of sampling a fracture with this scanline is proportional to the fracture area. In this case, not only fracture height but also fracture length and the geometry of the fracture surface will determine the sampling probability. Fractures that span the layer thickness and the limits of the study volume will reflect a three-dimensional abundance. Only those fractures that do not reach the bed boundaries or the lateral boundaries of the study area will reflect a one-dimensional sampling.

Mechanical boundary effect: The effect of mechanical thickness on fracture height distribution is trivial and can be explained using topologic arguments. However, the effects of mechanical layer boundaries on fracture length and aperture distributions are poorly documented. Ortega and Marrett (2000) showed that uncensored fractures in fracture-length distributions deviate from an ideal power-law distribution with an exponent that cannot be explained by topologic artifacts. It is possible that fracture-propagation limits affect the relationships between aperture and length scaling, however no systematic study of fracture aperture/fracture length scaling variations below and above the length scale of the mechanical layer have been done. If length and/or aperture growth rates are perturbed when fractures reach the bed boundaries we expect non-topologic effects that would be difficult to distinguish from topologic ones.

Under-sampling of large fractures: Power-law scaling predicts that large fractures are the least common in a fractured volume of rock. Consequently, most size distributions are poorly controlled at the large-scale side of the distribution. Also, spatial distribution of fractures will affect the probabilities of sampling. For example, if fractures are highly clustered and the observation domain intercepts a swarm of fractures then the size distribution may show an anomalously high number of fractures for the size of the observation domain. Fracture clusters often (but not always) include large fractures. Mechanical modeling of en echelon fracture arrangements suggests that fracture growth and clustering of large fractures is favored in this type of fracture spatial distribution (Olson and Pollard,

1991). More typically, scanlines shorter than clusters half-spacing will under-sample large fractures. Consequently, spatial distribution of fractures affects estimates of large-fracture intensity. Calculation of small-scale fracture sizes is more reliable, particularly if long scanlines and large amounts of data are collected.

A bias model for a size distribution (e.g. Burroughs and Tebbens, 2001) takes into account small-scale and large-scale artifacts and allows us to obtain the underlying power law that best fits the data. Marrett (2000) proposed a methodology to obtain the underlying power law distribution from a fracture size distribution affected by deviations of fractures below the underlying power law model. This bias model was applied to each fracture size distribution in the data set but in most cases, a limited range of data values or significant sampling and topologic artifacts did not allow the extraction of a power law for these distributions. In these cases, a power-law regression was applied to the distribution trying to separate a priori one-dimensional from two-dimensional sampling effects. Selection of a portion of the fracture size distribution least affected by sampling artifacts facilitates comparison of fracture intensity between beds. Inspection of the beds studied and the fracture aperture distributions obtained from these beds show that fractures with an aperture of 0.2 mm are generally in the one-dimensionally sampled portion of the size distribution (Appendix 3.E). Following Johnston and McCaffrey (1996) and Moros (1999), fractures 0.2 mm in aperture are expected to have lengths in the order of 2 to 20 cm in carbonate rocks suggesting that fractures with apertures of 0.2 mm do not

span both boundaries of the majority of beds studied (Appendix 3.A). Apertures of 0.2 mm are also readily visible with the naked eye in the majority of beds suggesting that truncation artifacts do not severely affect sampling of these fractures.

Calculation of normalized fracture-intensity uncertainties

Assigning fracture intensity values to a volume of rock is challenging. In the previous sections I discussed how scale of observation and fracture size are important parameters in fracture intensity calculations. Use of fracture size distributions promises a solution to the influence of fracture size on fracture intensity by choosing a common fracture size as the basis of fracture intensity comparisons. However, sampling, topology, number of observations, and spatial architecture of fracture arrays can prevent us from accurately obtaining the underlying size distribution for a given fracture system. For example, we expect to obtain a progressively more reliable approximation of the normalized fracture intensity when we collect progressively more fracture data as we extend an observation scanline. Extending the scanline reduces possible fracture spatial distribution effects on fracture size distributions and improves the probability of adequately sampling the largest fractures. Fracture systems tend to cluster in swarms at a hierarchy of scales of observation (Nelson, 1985; Marrett, 2001). This non-regular spatial distribution of fractures has potential impact on the normalized intensity determination because the number of fractures observed at a

given scale varies according to the position of the scanline with respect to the spatial distribution of fracture clusters.

One estimate of the uncertainty in the normalized fracture intensity determinations is the variance of fracture intensity values as the collection of data progresses along a scanline. To calculate this uncertainty, the normalized fracture intensity is calculated for progressively larger portions of the complete scanline. The standard deviation of the normalized fracture intensity values are then calculated for every new fracture 0.2 mm aperture or larger encountered along the scanline using all the fracture intensity values obtained for 0.2 mm aperture or larger previously encountered along the scanline. The normalized fracture intensity value and its uncertainty are then plotted in a graph of the normalized fracture frequency versus fracture number along the scanline (Appendix 3.F). From analysis of the graphs we learn that when a fracture of the threshold size or larger (e.g., 0.2 mm aperture or larger) is found along an observation scanline its normalized abundance increases. Whereas, when only smaller size fractures are found, the fracture intensity decreases due to a local increase in the observation scanline length. The standard deviation of the successive normalized fracture intensities provides a measure of the variability of fracture intensity. One standard deviation around the expected fracture intensity value encompasses approximately 68% of the normalized intensity values determined up to a given spot along the scanline (Koch and Link, 1971).

In the calculations of normalized intensity uncertainties, the first 20 fracture intensity estimates were ignored because the normalized fracture intensity

is very unstable when small numbers of data are used. It was assumed that the normalized fracture intensity up to a given point in the scanline is independent of previous determinations, and thus the expected value is the last normalized intensity obtained. We justify the use of this method because we expect a progressively more representative fracture intensity determination as the scanline progresses, whereas a mean fracture intensity determination is a worse approximation. The estimation of uncertainty (i.e., dispersion) using one standard deviation around the expected value is conservative.

The calculation of the total fracture intensity in a bed requires an integration of the fracture intensities of all sets of fractures present in the bed. An estimation of the propagation of errors of the addition of normalized fracture intensities must be obtained. If Q is the sum of normalized fracture intensities for all sets (e.g., A, B, C,...), we can obtain the approximate uncertainty associated with Q as:

$$\sigma_Q = \sqrt{\sum_{i=1}^N \sigma_i^2} \quad (1)$$

(Young, 1962), where σ is the standard deviation and I represents each of the N fracture sets present in the bed. Another way of estimating the combined uncertainty of the sum of fracture intensities (σ_{all}) is by weighting the fracture intensities (I_i) by the inverse of the uncertainties associated with each of these estimates ($1/\sigma_i$). This method of weighting aims to decrease the impact of the least confident estimates, often associated with problematic size distributions or

limited data, and provides a better approximation to the uncertainty of fracture intensity in the bed. The formula used to calculate this dispersion is:

$$\sigma_{all} = \frac{\sum_{i=1}^n I_i}{\sum_{i=1}^n \frac{I_i}{\sigma_i}} \quad (2)$$

Uncertainty estimates using equations 1 and 2 proved to be similar in most cases but with consistently higher estimates when equation 1 was used. The uncertainties reported below were obtained using equation (2).

Normalized fracture intensity results

Fracture aperture data were collected using a hand lens and the fracture-aperture comparator (Fig. 3.13) on fracture-perpendicular scanlines (Fig. 3.12). A separate scanline-based data set was recorded for each fracture set present in a bed. Approximately two hundred fractures per set were measured where possible. Outcrop limitations forced collection of fewer fractures in some cases (Table 3.1). An effort was made to collect data from low-intensity fracture sets and beds having low fracture intensity in order to document geologic controls on fracture intensity and to obtain a representative range of fracture intensities in the rocks.

For each bed and each fracture set, a calculation of the normalized abundance of fractures greater than 0.2 mm was obtained. Appendix 3.D contains tables with the aperture data collected in the field. Graphs of fracture intensity vs. aperture size were used to analyze the fracture size distribution of each fracture

Table 3.1. Summary of number of fracture data collected and scanline lengths in beds studied.

Locality	Bed Number	Apertures measured				Scanline length (mm)			
		Set A	Set B	Set C	Set D	Set A	Set B	Set C	Set D
Escalera	1	202	148			705	1511		
	2	233	219			1024	1568		
	3	229	241			1689	959		
	4		206				1537		
	5B			62				8331	
	6A	8		9		2007		2667	
	6B	200	240			1422	2311		
	7	210	205			1918	1372		
	8	218	213			927	851		
	9	204	224			1664	1588		
	10		84				13183		
	11		202				12370		
	12	206	197			876	921		
Iturbide	1	215			61	3721			6223
	2	189		86		2400		5169	
	3			166	204			4267	7734
	4			163	194			6566	5283
	5	182				2261			
	6			210				2921	
	7			389				3810	
	8				411				2394
	9			220	200			4559	5207
	10	233		220	210	3683		7988	5639
Palmas	1	21	217			2276	2578		
	2	223	30			5639	5146		
	3		59	248			3602	3975	
	4	121		19		6807		1532	
	5	93		72		5194		2438	
	6	219		33		2032		1077	
	7	109		112		5458		9068	
	8	204		24		1702		2921	
	9	206		115		1727		2096	
	10	222		206		1715		3073	
Chorro	1		213		23		4547		5004
	2			225	210		1219		2515
	3	219	207			3239	3315		
	4	65	215			1278	1524		
	5	212	57	70		2718	2616	2616	
	6	203	51	49		5499	6248	5258	
	7	213		48		1511		3302	
	8	200		43		5067		4389	

set and to obtain the normalized fracture intensity (Appendix 3.E). The uncertainty values associated with the normalized fracture intensity distributions are also summarized in graphs and tables (Appendix 3.F).

La Escalera

La Escalera is an excellent locality for fracture intensity studies. The forelimb of San Blas anticline exposes multitude of shallow-water Cupido Formation beds with sub-vertical attitude. Dolostones and limestones dominate the succession at La Escalera. At this locality, thirteen beds were selected for study based on field determinations of sedimentary facies. Petrographic analyses verified the composition and sedimentary textures determined in the field (Appendix 3.B). Beds were selected not only to assure sedimentary facies variability but also to sample a variety of bed thicknesses and degrees of dolomitization.

The methodology for normalized fracture intensity determination was explained in a previous section. In most beds two different fracture sets were measured, and the best power-law model was found for each set for fractures reaching the bed boundaries and within the bed (Table 3.2). Fracture sets A and B are best developed in La Escalera beds, particularly in dolomitized or partly dolomitized beds. Fracture set C was studied in two slightly dolomitized beds only. Fracture intensity in La Escalera beds varies through approximately 2.3 orders of magnitude (Table 3.3). Most fracture-aperture distributions from this locality can be analyzed using a bias-regression model (15 out of 22; Marrett,

Table 3.2. Power law parameters, La Escalera Canyon.

Bed Number	1D-Power-law Exponent			1D-Power-law Coefficient		
	Set A	Set B	Set C	Set A	Set B	Set C
1	-0.644	-0.455		0.027	0.027	
2	-0.729	-0.949		0.025	0.007	
3	-0.685	-0.610		0.017	0.040	
4		-0.756			0.012	
5B			-0.953&			0.0004&
6A	-0.334&		-1.277&	0.001&		0.00007&
6B	-0.707	-0.771		0.011	0.008	
7	-0.935	-0.805		0.004	0.010	
8	-0.843	-1.095		0.015	0.006	
9	-0.912	-0.821		0.008	0.010	
10		-0.293&			0.003&	
11		-0.967			0.004	
12	-1.374*	-1.407*		0.003*	0.003*	

*: suspect data (recrystallized limestone)

&: less than 100 fractures measured

Table 3.3. Normalized fracture intensity, La Escalera Canyon.

Bed Number	1D-Normalized Fracture intensity (number of fractures >0.2 mm wide/ mm)									
	Set A	±	Set B	±	A+B	±	Set C	±	All	±
1	0.076	0.011	0.055	0.010	0.131	0.010			0.131	0.010
2	0.080	0.035	0.032	0.008	0.112	0.018			0.112	0.018
3	0.051	0.007	0.106	0.017	0.157	0.011			0.157	0.011
4			0.041	0.001	0.041	0.001			0.041	0.001
5B							0.002&	0.001	0.002	0.001
6A	0.002&	0.002			0.002	0.002	0.001&	0.001	0.003	0.002
6B	0.034	0.015	0.027	0.010	0.060	0.012			0.060	0.012
7	0.017	0.004	0.038	0.011	0.055	0.007			0.055	0.007
8	0.057	0.022	0.034	0.012	0.091	0.017			0.091	0.017
9	0.034	0.011	0.038	0.012	0.072	0.012			0.072	0.012
10			0.005& #	0.001	0.005	0.001			0.005	0.001
11			0.017 #	0.002	0.017	0.002			0.017	0.002
12	0.031	0.009	0.031*	0.020	0.062	0.012			0.062	0.012

*

&: less than 100 fractures measured

#: truncation artifacts

*: suspect results (recrystallized limestone)

2000). The majority of the distributions show linear segments in log-log plots spanning from one to nearly three orders of magnitude in aperture size. These results suggest that a power law is the best model for these distributions (Bonnet et al., 2001).

Outcrops in the study area have exceptionally good quality and fractures as thin as 50 microns can be readily detected in most cases. Truncation is not a significant artifact in most distributions studied. However, truncation artifacts are important for fracture set B in bed 10. Bed 10 is a non-dolomitized, clean, cross-stratified grainstone. Fractures filled with clear calcite in this bed are difficult to see in the field, particularly fractures thinner than the average grain size in the rock (~0.5 mm). Truncation bias appears to be present in fracture aperture distributions obtained from set B in bed 11 (Table 3.3; Appendix 3.E).

Aperture distributions from small fractures of sets A and B in bed 1 show a significant deviation from the power law model suggested by bias model algorithms. In this bed, fractures with apertures larger than 0.5 mm in size typically span the bed thickness and fractures thinner than this threshold have at least one tip embedded in the layer. The bias model algorithm attempts to fit a single power-law to these data and does not separate fractures that span the bed thickness and smaller fractures. However, in this case it is clear that the power-law indicated by the bias model includes fractures that do and do not span the bed thickness. Fractures that span the bed thickness are typically organized in steeper power laws, which reflect sampling in higher dimensional domains (Marrett, 1996; Wojtal 1996). Furthermore, the bias power law exponent in these one-

dimensional distributions is high, suggesting a mix of size distributions with a low exponent (one-dimensional) and distributions with a high exponent (two-dimensional). An alternative model was obtained for most distributions acknowledging the distinction between fractures that do and do not span the bed thickness (Appendix 3.E). These alternative size-distribution models eliminated or reduced truncation artifacts apparent in the bias model regression.

Departures from an ideal power-law model also occur for large apertures. A possible explanation for these departures is sampling topology artifacts (Marrett, 1996), but some of these departures can also be produced by under-sampling of large fracture sizes. Some fracture aperture distributions in La Escalera probably reflect a pseudo two-dimensional sampling because the majority of the fractures in the fracture size distribution span the bed thickness.

Beds 5 and 6 have considerably lower fracture intensity than other beds studied at La Escalera locality. Only a few aperture measurements were recorded from these beds (62 and 17 respectively) because of a combination of very low fracture intensity and outcrop limitations. Fracture-aperture distributions obtained from these beds provide only an approximate indication of fracture intensity.

Las Palmas

Las Palmas Canyon is located in San Blas anticline forelimb, the same structure and limb where La Escalera beds were studied approximately 15 km away. Exposures at Las Palmas include the upper portion of Cupido Formation

and a complete exposure of the (informal) Cupidito Member (Goldhammer et al., 1991). Las Palmas Canyon outcrops offer the widest variation of sedimentary facies and degrees of dolomitization for fracture intensity studies. However, outcrop limitations restrict opportunities of studying bed thickness effects on fracture intensity for any given sedimentary facies or degree of dolomitization. Ten beds were selected for fracture intensity determinations at Las Palmas Canyon, mainly with a focus on trying to unravel degree of dolomitization control on fracture intensity. Although degree of dolomitization was estimated in the field, subsequent petrographic analyses were used to assess degree of dolomitization in these rocks for the analyses below.

Three fracture sets can be separated at this locality based on their systematic orientations and crosscutting relationships. In most beds two different fracture sets were measured for fracture intensity determinations. The predominant fracture sets at Las Palmas are subparallel to the average orientation of outcrop. Care is necessary to take advantage of the irregularities in the outcrop to determine fracture intensity in these beds. A series of scanlines segments comprise the observation domains for fracture aperture measurements in seven out of ten beds studied at this locality. Scanlines were maintained in an orientation perpendicular to the fractures, avoiding outcrop exposures nearly parallel to the set and taking advantage of local ledges and irregularities. Accurate aperture measurements are also difficult when fractures are subparallel to the outcrop. A visual estimate of the aperture size was necessary. Holding the fracture aperture comparator perpendicular to the fracture and visually matching a line in the

comparator with a projection of the fracture aperture in a fracture-perpendicular plane accomplished this. The intensity of fracture set A was measured in nine out of ten beds at Las Palmas. The scanline lengths of some secondary fracture sets are based on projection of the scanline to a fracture-perpendicular orientation (set C, in four out of eight beds). Fracture set B was measured in only three beds with more than 20 of these fractures.

Table 3.4 shows a summary of the power law exponents and coefficients obtained from the aperture size distributions obtained. The variation of normalized fracture intensity for fractures with apertures larger than 0.2 mm in Las Palmas span about an order of magnitude (Table 3.5). The majority of the distributions (14 out of 21) show two linear segments in log-log plots (Appendix 3.E) and power-law regressions to these segments produce high coefficients of determination. The segment with the lowest power-law exponent typically includes fractures that do not span the bed thickness and the steeper segment includes fractures that reach the bed boundaries. These changes in power-law scaling were chiefly interpreted as topologic effects. Topologic effects make large fractures show abundance that corresponds to higher dimension observation domains. One-dimensional sampling of fractures that span the observation domain yield the same fracture abundance obtained when sampling of these fractures is performed in layer-perpendicular two-dimensional sampling domains (Marrett, 1996), because fractures that span the observation domain (e.g., fracture height equal to bed thickness in cross-section exposures) have the same probability of being sampled in one-dimensional (i.e., scanlines) as in two-dimensional

Table 3.4. Power law parameters, Las Palmas Canyon.

Bed Number	1D-Power-law Exponent			1D-Power-law Coefficient		
	Set A	Set B	Set C	Set A	Set B	Set C
1	-0.279&	-0.622		0.0043	0.0131	
2	-1.265	-1.600&		0.0009	0.0000	
3		-0.189	-0.558		0.0096	0.0105
4	-0.947		-0.391&	0.0010		0.0035
5	-0.731		-0.946	0.0017		0.0013
6	-1.852		-2.450&	0.0004		0.00005
7	-0.559		-0.445	0.0036		0.0032
8	-0.749		-0.836&	0.0097		0.0013
9	-0.467		-0.576	0.0181		0.0134
10	-0.606		-0.847	0.0067		0.0025

&: less than 50 fractures measured

Table 3.5. Normalized fracture intensity, Las Palmas Canyon.

Bed Number	1D-Normalized Fracture Intensity (number of fractures >0.2 mm wide/mm)									
	Set A	±	Set B	±	A+B	±	Set C	±	All	±
1	0.0067&	0.0015	0.0356	0.0126	0.0424	0.0058			0.0424	0.0058
2	0.0069	0.0017	0.0007&	0.0002	0.0076	0.0010			0.0076	0.0010
3			0.0130	0.0010	0.0130	0.0010	0.0258	0.0052	0.0388	0.0022
4	0.0046	0.0011			0.0046	0.0011	0.0066&	0.0023	0.0112	0.0016
5	0.0055	0.0018			0.0055	0.0018	0.0060	0.0024	0.0115	0.0021
6	0.0079	0.0059			0.0079	0.0059	0.0010&	0.0007	0.0089	0.0032
7	0.0089	0.0022			0.0089	0.0022	0.0065	0.0015	0.0154	0.0018
8	0.0324	0.0104			0.0324	0.0104	0.0050&	0.0019	0.0374	0.0065
9	0.0384	0.0077			0.0384	0.0077	0.0339	0.0111	0.0722	0.0090
10	0.0178	0.0055			0.0178	0.0055	0.0098	0.0026	0.0275	0.0039

±: standard deviation

&: less than 50 fractures measured

domains. In contrast, fractures smaller than the bed thickness will have a probability of being sampled proportional to their heights in bed-parallel exposures, and proportional to their lengths in cross sectional exposures.

Bias power law algorithms failed to provide power-law models for most distributions at Las Palmas. Failure of the algorithms is due in part to limited range of fracture aperture data in the distributions, sharp changes of slope in log-log plots produced by sampling topology effects, and absence of a clearly rectilinear middle segments in the distributions.

El Chorro

Eight beds were selected for fracture intensity determinations at El Chorro Canyon. Beds selected at El Chorro are non-dolomitized and dolomitized grainstones and dolomitized wackestones. Four out of eight beds have no dolomite and the other four beds have dolomite contents over 50% in volume. Most beds studied at El Chorro (six out of eight) are grain-supported facies, primarily grainstones, and only two beds are wackestones. Five fracture sets can be separated at El Chorro based on systematic orientations and crosscutting relationships. In most cases, only two fracture sets in a given bed show sufficient abundance to allow fracture intensity determination. Three fracture sets were measured in beds 5 and 6. More than 200 fracture aperture measurements were collected from the primary fracture set in each bed and between 40 and 100 fracture aperture measurements from secondary sets (Table 3.1).

Table 3.6 contains a summary of power law exponents and coefficients for the distributions obtained at El Chorro and the size distributions themselves are included in Appendix 3.E. Fracture intensity of fractures with aperture larger than 0.2 mm at El Chorro spans less than one orders of magnitude (Table 3.7), similar to the degree of fracture intensity variation observed at Las Palmas locality. The majority of the distributions (14 out of 18) show linear segments in log-log plots that can be modeled by power-laws (Appendix 3.E). Power-law regressions to these data produce coefficients of determination typically better than 0.9 (16 out of 18 distributions). The segment with the lowest power-law exponent typically includes small-aperture fractures that do not span the bed thickness and the steeper segment includes fractures that reach the bed boundaries. Power law regressions were obtained separately for each segment using as a guide field-based aperture observations of fractures that reach the bed boundaries. In most cases this size is close to the change in slope in the fracture aperture distribution.

Bias sampling algorithms failed to provide power-law models for most distributions at El Chorro. Failure of the algorithms can be explained using the same arguments proposed above for distributions from Las Palmas locality.

Iturbide

Iturbide outcrops offer an opportunity to study bed thickness effects on fracture intensity. Sedimentary facies and degree of dolomitization are similar in all beds of Tamaulipas Inferior and Taraises formations cropping out at this locality. Open-marine mudstones are the dominant beds exposed at Iturbide. The

Table 3.6. Power law parameters, El Chorro Canyon.

Bed Number	1D-Power-law Exponent				1D-Power-law Coefficient			
	Set A	Set B	Set C	Set D	Set A	Set B	Set C	Set D
1		-0.529		-0.445&		0.0091		0.0024
2			-1.926	-1.213			0.0005	0.0015
3	-0.852	-0.925			0.0038	0.0034		
4	-0.548	-0.991			0.0035	0.0026		
5	-0.863	-0.665	-0.992		0.0059	0.0032	0.0014	
6	-0.851	-1.377	-0.563&		0.0015	0.0001	0.0012	
7	-0.636		-0.533&		0.0176		0.0038	
8	-1.116		-0.776&		0.0011		0.0010	

&: less than 50 fractures measured

Table 3.7. Normalized fracture intensity, El Chorro Canyon.

Bed Number	1D-Normalized Fracture Intensity (number of fractures >0.2 mm wide/mm)											
	Set A	±	Set B	±	A+B	±	Set C	±	Set D	±	All	±
1			0.0213	0.0050	0.0213	0.0050			0.0049&	0.0067	0.0262	0.0052
2							0.0111	0.0055	0.0106	0.0091	0.0787	0.0069
3	0.0150	0.0043	0.0151	0.0031	0.0300	0.0036					0.0300	0.0036
4	0.0085	0.0079	0.0128	0.0042	0.0213	0.0052					0.0213	0.0052
5	0.0237	0.0037	0.0093	0.0041	0.0330	0.0038	0.0069	0.0019			0.0399	0.0032
6	0.0059	0.0012	0.0009	0.0006	0.0068	0.0011	0.0030&	0.0012			0.0098	0.0011
7	0.0490	0.0156			0.0490	0.0156	0.0090&	0.0019			0.0579	0.0074
8	0.0066	0.0013			0.0066	0.0013	0.0035&	0.0013			0.0101	0.0013

&: less than 50 fractures measured
±: standard deviation

degree of dolomitization in these beds is under 15%. Outcrops are moderately good quality, providing both bed plane exposures (bed basal surfaces) and cross-section views for fracture study. Ten beds were selected for fracture intensity determination. Nine out of ten beds are mudstones and one bed is a nodular chert layer. All beds studied are located in the same structural domain of Iturbide Anticline to isolate structural controls on fracture intensity.

Up to four sets of fractures can be identified in Iturbide beds based on systematic orientations and crosscutting relationships. All fractures are filled with calcite so fracture fill cannot be used to discriminate fracture sets. Fracture set B is not well developed and was ignored for fracture intensity determinations. Fracture set B is possibly conjugate with fracture set A based on mutually cross-cutting shear offsets between fractures A and B. In all beds one primary (i.e., most abundant) fracture set was studied and commonly an additional secondary set was also considered for fracture intensity determination. Three fracture sets were analyzed in bed 10.

Aperture measurements were collected along fracture-perpendicular scanlines on bedding plane exposures. Cross sectional views of the beds allowed convenient determination of the minimum aperture size of fractures reaching the bed boundaries. Perhaps the most significant problem with fractures in Iturbide beds is that tectonic stylolites developed after vein filling and have orientations subparallel to fracture sets A, B and C. These stylolites sometimes nucleated along fracture walls, locally prohibiting accurate determination of the fracture aperture before pressure solution occurred. Tectonic stylolites did not affect

fracture set D, which is kinematically compatible and contemporaneous. Fracture set D is present in five out of ten beds studied. Fracture set C is the most commonly present in the beds studied (seven beds) and fracture set A was studied in only four beds.

The majority of aperture distributions in Iturbide beds show linear segments in log-log plots (Appendix 3.E) and single power-law regressions to these segments produce high coefficients of determination ($r^2 > 0.9$). Table 3.8 contains a summary of the power law exponents and coefficients obtained from Iturbide beds fracture size distributions and Appendix 3.E shows the distributions, power law models, and comments on the size distributions characteristics. The variation of fracture intensity at Iturbide spans nearly an order of magnitude (Table 3.9). Most fracture aperture distributions were not suitable for bias-regression analysis (Marrett, 2000) because most fracture aperture distributions are affected by sampling topology effects or have fewer data than the minimum required by the algorithms. Observed departures from an ideal power law in the large aperture portions of the distributions have been related to topologic effects produced by fractures that span the bed thickness, as indicated by field observations.

The following sections analyze what role sedimentary and diagenetic factors played on fracture intensity observed in rocks studied. The problem is clearly a multivariate one but I start by investigating simple correlations of each one of the variables considered and fracture intensity (Koch and Link, 1971).

Table 3.8. Power law parameters, Iturbide Anticline. Underlined parameters were calculated using topologic conversions of two-dimensional distributions to one-dimensional distributions according to Marrett (1996), and assuming an approximately linear relationship between aperture and length (Moros, 1999).

Bed Number	1D-Power-law Exponent			1D-Power-law Coefficient		
	Set A	Set C	Set D	Set A	Set C	Set D
1	-0.677		-1.045*	0.0077		0.0004*
2	-1.123	-1.889*		0.0026	0.00006*	
3		-1.310	-0.781		0.0023	0.0023
4		-0.771	-1.078		0.0031	0.0013
5	-0.853			0.0049		
6		-1.101			0.0019	
7		-0.999			0.0022	
8			<u>-0.354</u>			<u>0.0284</u>
9		-1.481	-1.973		0.0005	0.0001
10	-0.558	-1.845	-1.522	0.0110	0.0001	0.0004

*: less than 100 fractures measured

Table 3.9. Normalized fracture intensity, Iturbide Anticline. Underlined values were obtained from theoretical one-dimensional distributions derived from two-dimensional distributions using Marrett (1996) equations, and assuming a linear relationship between aperture and length (Moros, 1999).

Bed Number	1D-Normalized Fracture Intensity (number of fractures >0.2 mm wide/mm)							
	Set A	±	Set C	±	Set D	±	All	±
1	0.0229	0.0066			0.0022*	0.0006	0.0250	0.0036
2	0.0158	0.0030	<u>0.0013</u>	0.0010			0.0171	0.0026
3			0.0189	0.0033	0.0081	0.0017	0.0270	0.0026
4			0.0107	0.0027	0.0074	0.0013	0.0181	0.0019
5	0.0193	0.0055					0.0193	0.0055
6			0.0112	0.0023			0.0112	0.0023
7			0.0110	0.0059			0.0110	0.0059
8					<u>0.0502</u>	0.0017	0.0502	0.0017
9			0.0054	0.0022	<u>0.0024</u>	0.0023	0.0078	0.0022
10	0.0270	0.0053	0.0016	0.0004	0.0046	0.0017	0.0331	0.0014

*: less than 100 fractures measured

±: standard deviation

SEDIMENTARY FACIES CONTROL ON FRACTURE INTENSITY

Sedimentary controls on fracture intensity were analyzed by taking into account the following sedimentologic attributes of the rocks studied 1) energy conditions in the environment of deposition as suggested by the Dunham (1962) classification of carbonate textures; 2) carbonate mud content in the rock, and 3) interpreted environment of deposition.

Sedimentary facies are difficult to characterize quantitatively because a variety of physical, chemical, and biological attributes are used for sedimentary facies determinations. For example, no attempt was made to assign numeric values to the combination of attributes such as interpreted energy level in the environment of deposition, paleobathymetry, biologic content or bioturbation. Instead, rocks were separated into mud-supported (mudstones and wackestones; Dunham, 1962) and grain-supported (packstones and grainstones; Dunham, 1962) textures, suggestive of contrasting energy conditions during sedimentation. Mud-supported sediments are generally deposited in two kinds of low-energy conditions: 1) below the reach of fair-weather wave action in subtidal environments, and 2) under intertidal conditions in tidal flat environments. Grain supported facies suggest a high level of energy in the environment of deposition. Grainstones are deposited in wave-agitated areas of the sea floor where mud particles are suspended and washed away. These sedimentary conditions are typical of platform shoals. Packstones are more difficult to characterize in a depositional energy fashion. Allochems are the framework support in packstones,

suggesting but not assuring a relatively high energy level in the environment of deposition.

The presence of mud in packstones can be explained in multiple ways: 1) carbonate mud was present in the environment and allochems were added to originally mud-supported sediments (e.g., bivalve packstones with dominant whole shells); 2) soft pellets were deposited along with less compliant grains but pellets were disintegrated during compaction (analogous effect to pseudomatrix formation in sandstones); 3) mud was introduced into the sediment after framework deposition via mechanical sieving or bioturbation; 4) unstable energy level in the environment of deposition allowed preservation of carbonate mud and grains; and 5) turbidity, high-viscosity currents transported grains and mud together under special flow regime conditions. Most packstones studied are chiefly composed of transported grains and show evidence of bioturbation. These packstones are interpreted to have been deposited under moderately high energy conditions, perhaps in the fringes of grainstone shoals or bivalve banks, or represent occasional storm deposits. Carbonate mud in these packstones found its way through the pores during low-energy conditions at the bottom of the water column, was introduced by bioturbation, and/or represents disintegrated soft pellets after compaction. Mud content was estimated using petrographic microscope (Appendix 3.B). Mud percent volume of rock was determined using visual percentage estimation charts (Terry and Chilingar, 1955). Percentage error in estimation of mud content probably ranges between 5 and 10%.

Environment of deposition for each bed studied was interpreted from rock composition, texture, biologic content, energy level during deposition, and position of the bed within stratigraphic cycles. Sedimentary environments were classified into typical sedimentary realms in an arid-climate, carbonate platform ramp including tidal flat environment, low energy subtidal environment (e.g., protected areas behind grainstone shoals), and high-energy subtidal environment (e.g., grainstone shoals). Bivalve banks are a special category and were classified as low energy or high energy subtidal depending on the matrix texture of the bank. Bivalve banks are most abundant and best developed at Las Palmas Canyon but are also present at El Chorro locality.

Various plots test sedimentary facies controls on fracture intensity. Permutations of normalized fracture intensity and sedimentary facies include: 1) contrast of normalized fracture intensity for each fracture set, combinations of sets and all sets in grain-supported and mud-supported rocks; 2) analysis of correlation between fracture intensity and mud content; 3) analysis of sedimentary environment and fracture intensity.

El Chorro

At El Chorro locality eight beds were analyzed. Six beds selected at this locality are grainstones and only two beds were classified as mud-supported facies. One of these mud-supported layers is best classified as a wackestone-matrix bivalve bank, and the other bed is a pelletoidal wackestone probably deposited in a low-energy lagoonal setting.

A grainstone bed shows the highest fracture intensity for set A, however, the uncertainty associated with the fracture intensity in this grainstone bed is high (Fig. 3.33). The next highest fracture intensity for set A is in a mud-supported bed. Fracture set A intensity in other mud- and grain-supported beds are lower and comparable to one another. Similarly, two grainstone beds show the highest fracture intensity for set B (Fig. 3.33), followed closely by the fracture intensity in two mud-supported beds. These beds have, in turn, higher fracture intensity than a third grainstone bed. Fracture intensity of combined sets A and B is highest in one of the grainstone beds (Fig. 3.33), but the second highest fracture intensity is present in a mud-supported bed. Combined sets A and B intensities in other grain- or mud-supported beds is comparable. Set C intensity is also slightly highest in one grain-supported bed (Fig. 3.33), but the second highest intensity value is in mud-supported facies. The fracture intensities of set C in other mud- and grain-supported facies are comparable. The overall pattern observed in Figure 3.33 is, however, of considerable overlap in the fracture intensity in grain-supported and mud-supported beds, with a few grainstone beds having slightly higher intensities but also with significant fracture intensity uncertainties.

Plots of normalized fracture intensity versus mud content at El Chorro show considerable scatter (Fig. 3.34). Weighted linear regressions lines were obtained for each set, combination of sets A and B, and total fracture intensity in each bed.

Weighted regressions to plots of normalized fracture intensity and mud content indicate poor correlation between these two parameters (Fig. 3.34). The

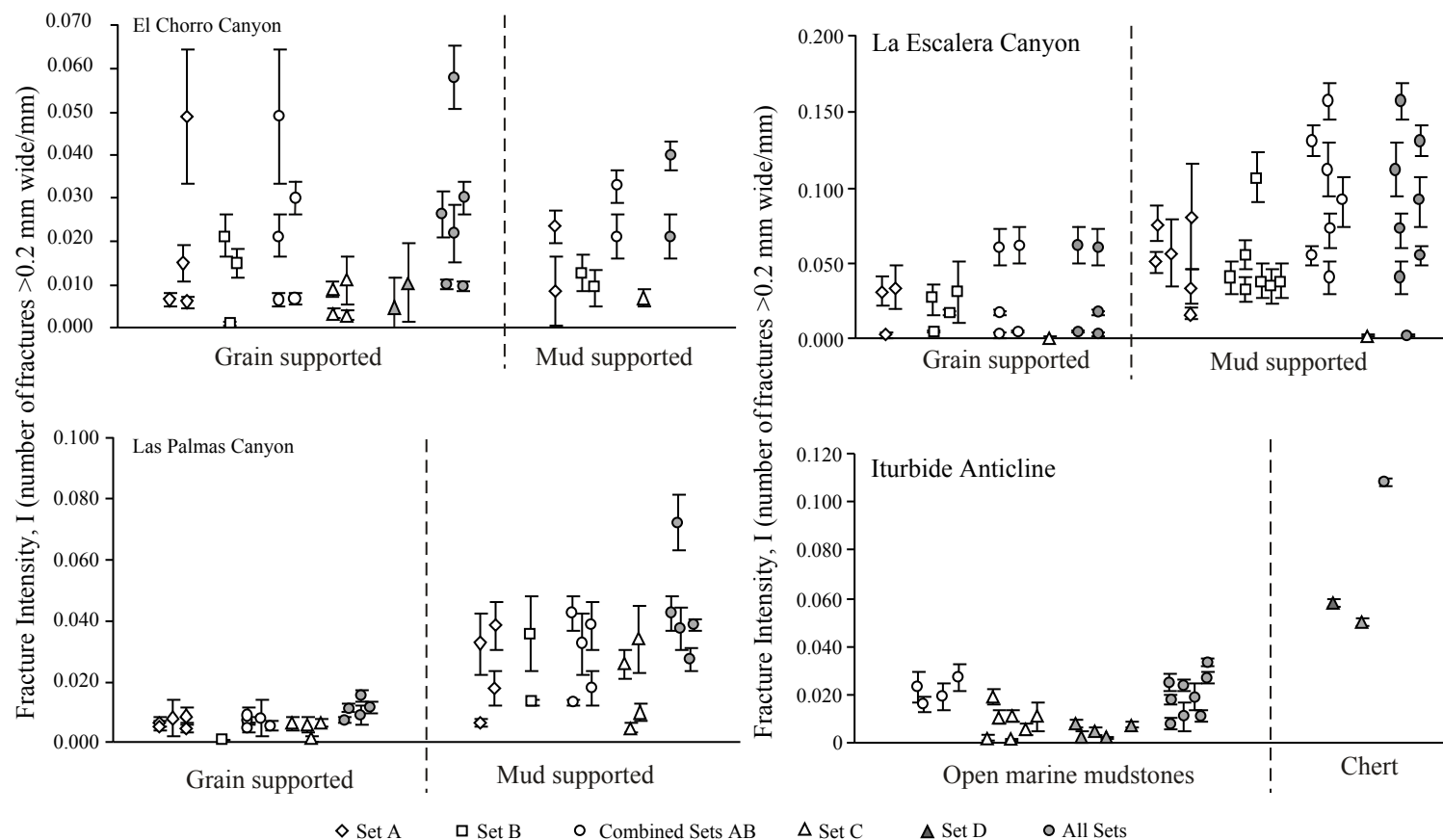


Figure 3.33. Sedimentary facies control on fracture intensity. Overlapping fracture intensity ranges for individual fracture sets suggest that sedimentary facies is not the primary control on fracture intensity. Fracture intensity tends to be higher in mud-supported rocks than in grain-supported rocks. Fracture intensity in one nodular chert bed at Iturbide Anticline is higher than in adjacent mudstones.

El Chorro Canyon

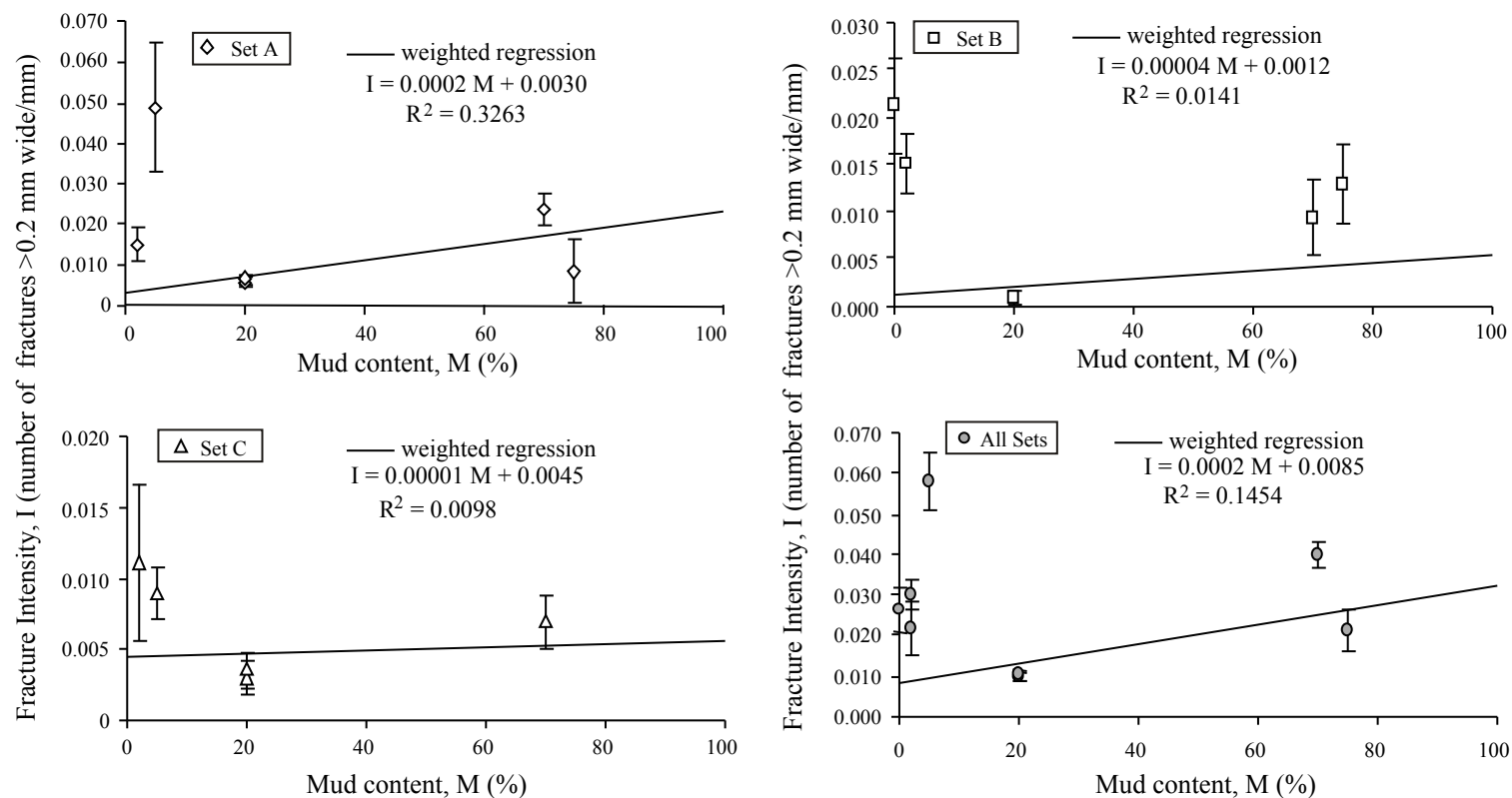


Figure 3.34. Normalized fracture intensity and mud content El Chorro Canyon. Scatter in the data is high and coefficients of determination are low. However, weighted regressions indicate that fracture intensity apparently increases with increase in carbonate mud content in the rock. Some grainstone beds have high fracture intensity but the uncertainties associated with these fracture determinations are also high. Only two layers with more than 50% mud were studied at this locality.

regressions suggest that fracture intensity of each set weakly increases with an increase in mud content in the rock. Most beds studied are grain-supported and only two mud-supported layers have more than 50% mud content. A single layer with low mud-content and high fracture intensity has little effect on the weighted regressions because of its large uncertainty in fracture intensity. Regressions yield low coefficients of determinations, suggesting at best a weak correlation between mud content and fracture intensity at this locality. There is more than 10% probability of obtaining similar coefficients of determination between two uncorrelated variables (Young, 1962), however the consistency in the relationship obtained for various combinations of individual and combined sets intensity supports a weak correlation between mud content and fracture intensity at El Chorro. It is possible that a nonlinear relationship is a better model for the relationship between mud content and fracture intensity. This nonlinear model should explain relatively high fracture intensity for low and high mud content but low intensity for moderate mud content.

La Escalera

At La Escalera locality 13 beds were analyzed. A dolomitized wackestone layer shows the highest fracture intensity for set A (Fig. 3.33). Three mud-supported beds show the next highest fracture intensities for set A at La Escalera, but remaining mud-supported beds show fracture intensities comparable to the ones observed in grain-supported beds for set A. Fracture set B intensity is highest in a dolomitized mudstone bed (Fig. 3.33). Fracture intensities of set B in the

other five mud-supported beds at La Escalera are greater than fracture set B intensity in grain-supported beds. The combined fracture intensity for sets A and B is highest in a mud-supported dolomitized bed (Fig. 3.33). Four mud-supported beds have the next highest combined fracture sets A and B intensities, but the two next highest fracture intensity are associated with two grain-supported beds. Fracture intensities for combined sets A and B in other mud-supported beds is higher than the fracture intensities in the other two remaining grain-supported beds. Fracture set C is not well developed at La Escalera, but fracture set C intensity calculated in one mud-supported bed is higher than the intensity of this set in a grainstone bed (Fig. 3.33). Total fracture intensity shows a similar behavior as the fracture intensity for combined sets A and B, being highest for a dolomitized mudstone and another four mud-supported dolomitized layers.

Weighted regressions to normalized fracture intensity and mud content for Sets A, B, and combined sets A and B suggest that these two parameters have a modest positive, correlation (Fig. 3.35). The coefficients of determination for these regressions vary from $r^2=0.5351$ for set B to $r^2=0.7664$ for combined sets AB, suggesting that there is less than a 2% chance that these variables are uncorrelated (Young, 1962). The slope of the regression lines suggests that mud content can produce a variation of normalized fracture intensity ranging from 0.04 to 0.12 fractures /mm, in fractures with aperture greater than 0.2 mm. Fracture set C intensity was measured in only two beds with low fracture intensity, one of them is a grain-supported bed and the other is a mud-supported subtidal facies layer.

La Escalera Canyon

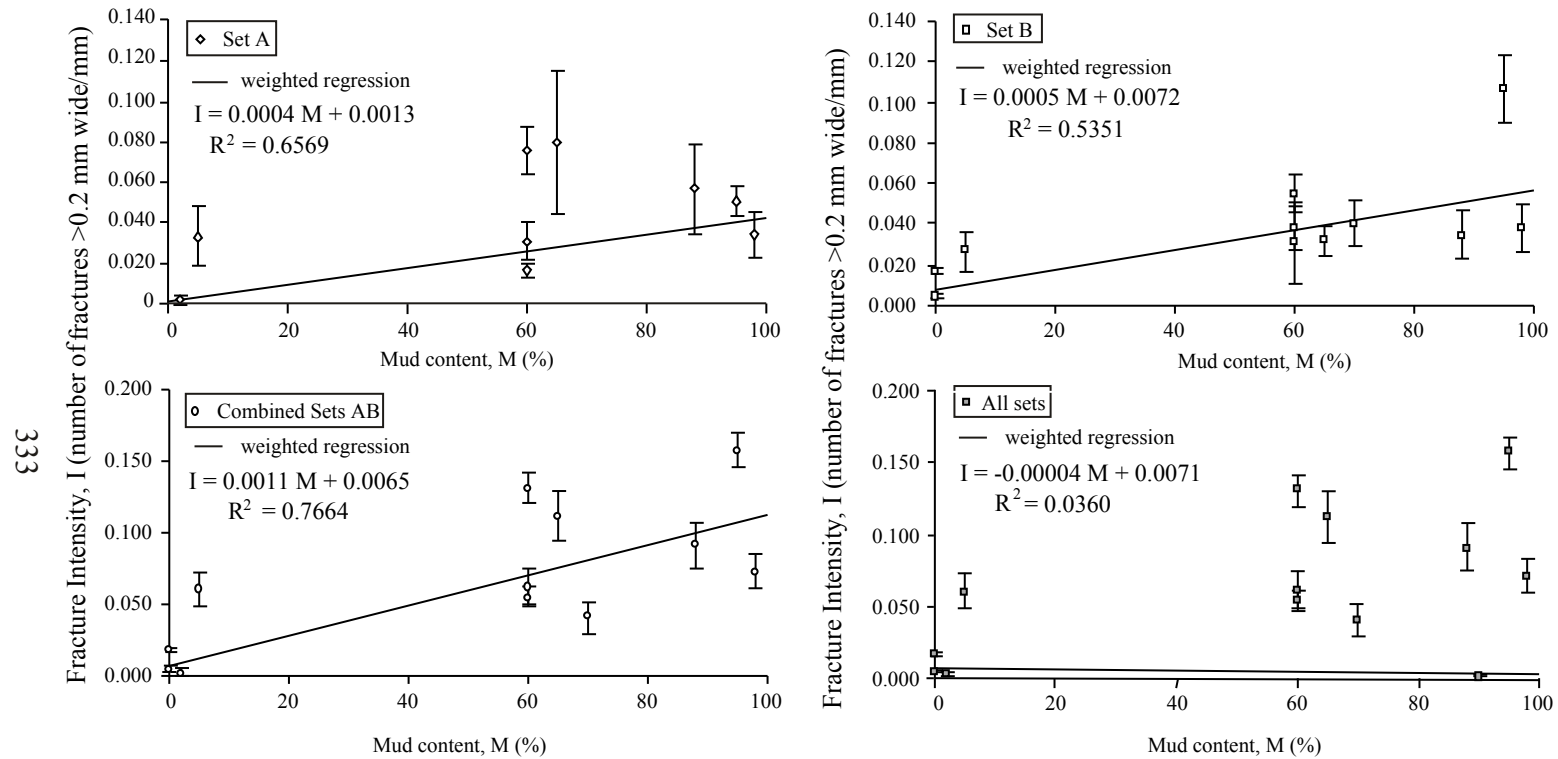


Figure 3.35. Normalized fracture intensity and mud content La Escalera Canyon. Fracture intensity increases with mud content for sets A and B and combined sets AB. All mud-supported beds in which sets A and B were analyzed show a degree of dolomitization greater than 70% in volume. Fracture set C intensity was analyzed in only two beds with very low fracture intensity, one grainstone and one lagoonal mudstone with 20% dolomite. The results for set C are included in the plot for all sets. Weighted regression to all sets intensity suggests no correlation between mud content and fracture intensity.

The results of fracture set C intensity determinations are included in the plot for combined intensity of all sets in Figure 3.35. Weighted regressions to all sets suggest that there is no correlation between mud content and fracture intensity. The inclusion of a low fracture intensity wackestone has changed the results obtained for sets A, B and combined sets AB from other mud-supported beds, suggesting that mud-content is not the only geologic control on fracture intensity. All other mud-supported beds are dolomitized in proportions greater than 70% and are associated with tidal-flat environments of deposition.

Las Palmas

Results of normalized fracture intensity determinations in various sedimentary facies at Las Palmas Canyon locality show similar behavior to that observed for La Escalera. At Las Palmas locality mud-supported beds show inconsistent but generally higher fracture intensities than grain-supported beds (Fig. 3.33). The total fracture intensity (all sets) at Las Palmas in each mud-supported beds is higher than the highest total fracture intensity obtained for grain-supported layers. Combined fracture sets A and B intensity are also higher than combined A and B fracture intensities in grain-supported beds. Although fracture intensity of individual sets A, B and C show some degree of overlapping, highest fracture intensity for individual sets is also found in mud-supported beds.

Linear regressions of fracture intensity vs. mud content indicate a positive correlation between these two parameters, consistent with results from El Chorro and La Escalera (Fig 3.36). The coefficients of determination for these weighted

Las Palmas Canyon

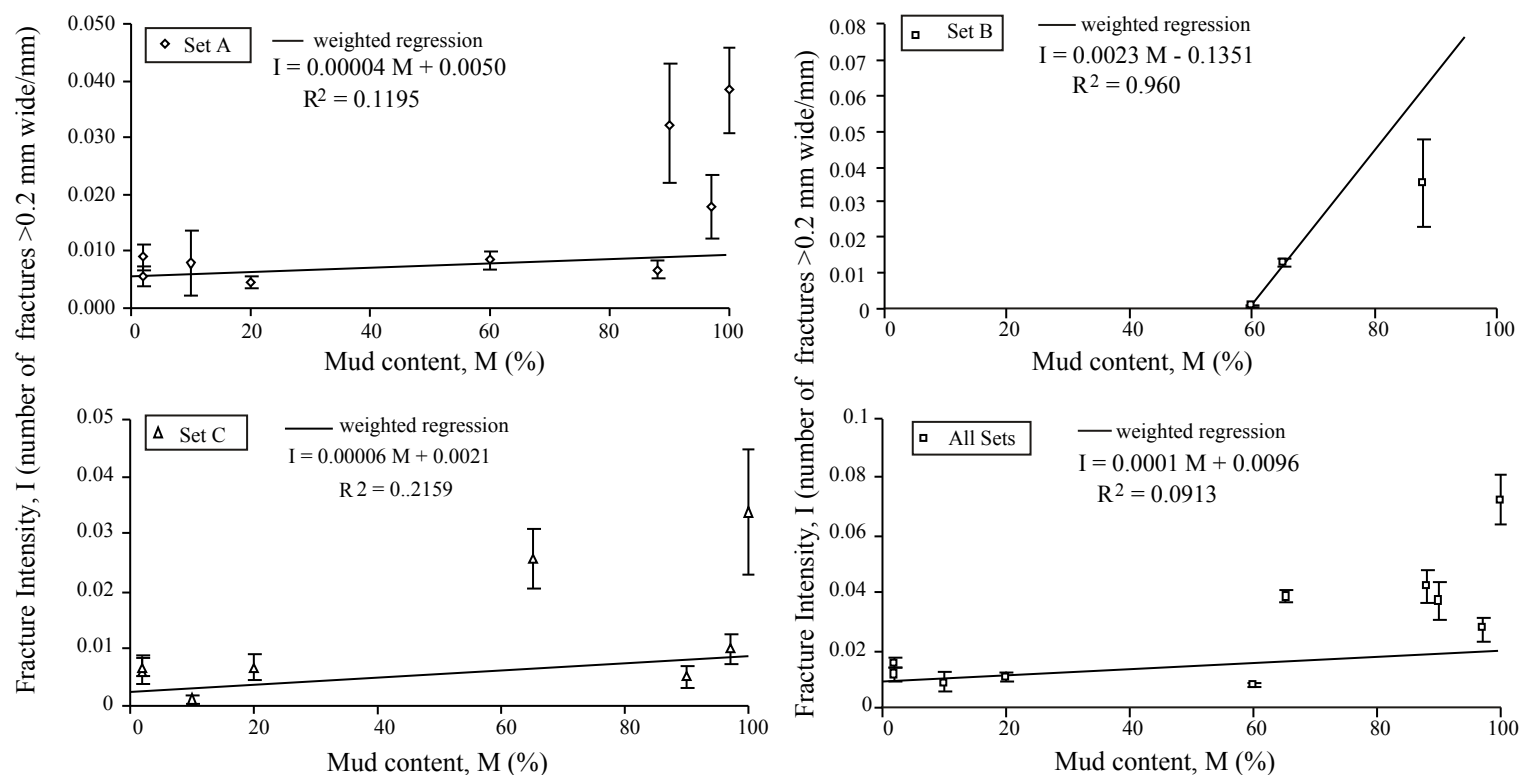


Figure 3.36. Normalized fracture intensity and mud content, Las Palmas Canyon. Fracture intensity increases with increase in carbonate mud content at this locality. Moderate to low coefficients of determination suggest that other geologic parameters in addition to mud content probably affect fracture intensity in these rocks.

regressions are $R^2=0.1195$ for set A, $R^2=0.2159$ for set C, $R^2=0.0913$ for all sets combined. This range of variation in the coefficient of determination is consistent with the scatter of the data and suggests that more data are necessary to establish a more reliable relationship between mud-content and fracture intensity. There is more than a 10% probability that two unrelated variables show similar coefficients of determination (Young, 1962). The highest coefficient of determination corresponds to set B, studied in only three layers, which implies this determination is statistically unreliable (Young, 1962). The highest fracture intensity values observed at Las Palmas are associated with three dolomitized tidal flat mud-supported layers and one mud-supported partly dolomitized rudist bank.

Iturbide

No grain-supported facies were studied at Iturbide. All beds studied at this locality are open-marine mudstones, with the exception of a layer with abundant bed-parallel elongated chert nodules. Total normalized fracture intensity in chert nodules is up to twice the normalized fracture intensity in mudstone beds (Fig. 3.33). An analysis of other sedimentary facies effects on fracture intensity at this locality is not possible, but comparisons of the fracture intensity at Iturbide and other localities may be useful to understand sedimentary controls on fracture intensity across a carbonate ramp. These comparisons must be regarded as qualitative because fractures studied at Iturbide may not be directly comparable to fractures in beds 100 km away in terms of timing, origin, and remote

stresses/fluid pressures. However, comparison of fracture intensities in beds from different localities is valid because the fracture systems compared formed before folding occurred.

Normalized fracture intensities for individual sets in Iturbide mudstones are, on average, lower than fracture intensities observed in shallow water mud-supported rocks of the Cupido Formation. The highest fracture intensities were observed in dolomitized mud-supported rocks at La Escalera Canyon. Some beds at La Escalera have fracture intensities twice as high as the highest fracture intensities obtained at other localities. However, there is considerable similarity in the highest values of fracture intensity and fracture intensity variability in all localities. Some anomalously high fracture intensities in grain-supported layers were found at La Escalera and El Chorro. These differences in fracture intensity for similar sedimentary facies suggest that other geologic processes in addition to sedimentary facies control fracture intensity in Cupido Formation rocks.

Sedimentary environment of deposition and fracture intensity

Sedimentary facies are the result of chemical, physical and biological conditions in the environment of deposition. When sedimentary facies are defined in detail they can be correlated to a given sedimentary environment (Walker, 1979). In the previous section I analyzed differences in fracture intensity between two broad classes of sedimentary facies (i.e., grain supported and mud supported), but no attempt was made to separate these facies into more environment-specific facies. This differentiation was not practical for the previous analysis because of

the large variability of sedimentary environments in a carbonate ramp and the limited number of beds studied.

Because quantification of sedimentary environments is challenging, I will plot the interpreted environments of deposition for the beds studied on an abscissa in such a way as to maximize correlation and determine an upper bound on depositional environment control of fracture intensity. To obtain the maximum correlation relationship I sort the normalized total fracture intensity from the lowest to the highest and number the beds progressively such that the bed with the lowest fracture intensity is bed number one and the bed with the highest fracture intensity receives the highest number. A regression line to the crossplot of fracture intensity vs. bed number represents the upper limit of correlation for the population (Fig. 3.37). Labeling the data points with the interpreted environment of deposition provides a tool to assess the significance of sedimentary environment controls on fracture intensity.

At Las Palmas locality, the bed with the highest fracture intensity is a mudstone interpreted as a deposit in intertidal environment (Fig. 3.33). The bed with the second largest fracture intensity is interpreted as deposited in a low-energy subtidal environment. Other subtidal low-energy and two intertidal rocks are the next highest fracture intensity beds. Lower fracture intensity is associated with high-energy subtidal environments, typically grainstones, packstones and rudist banks with grain-supported matrix.

Similar results were obtained for La Escalera Canyon, although exceptions are also present. At La Escalera locality, the highest fracture intensity is

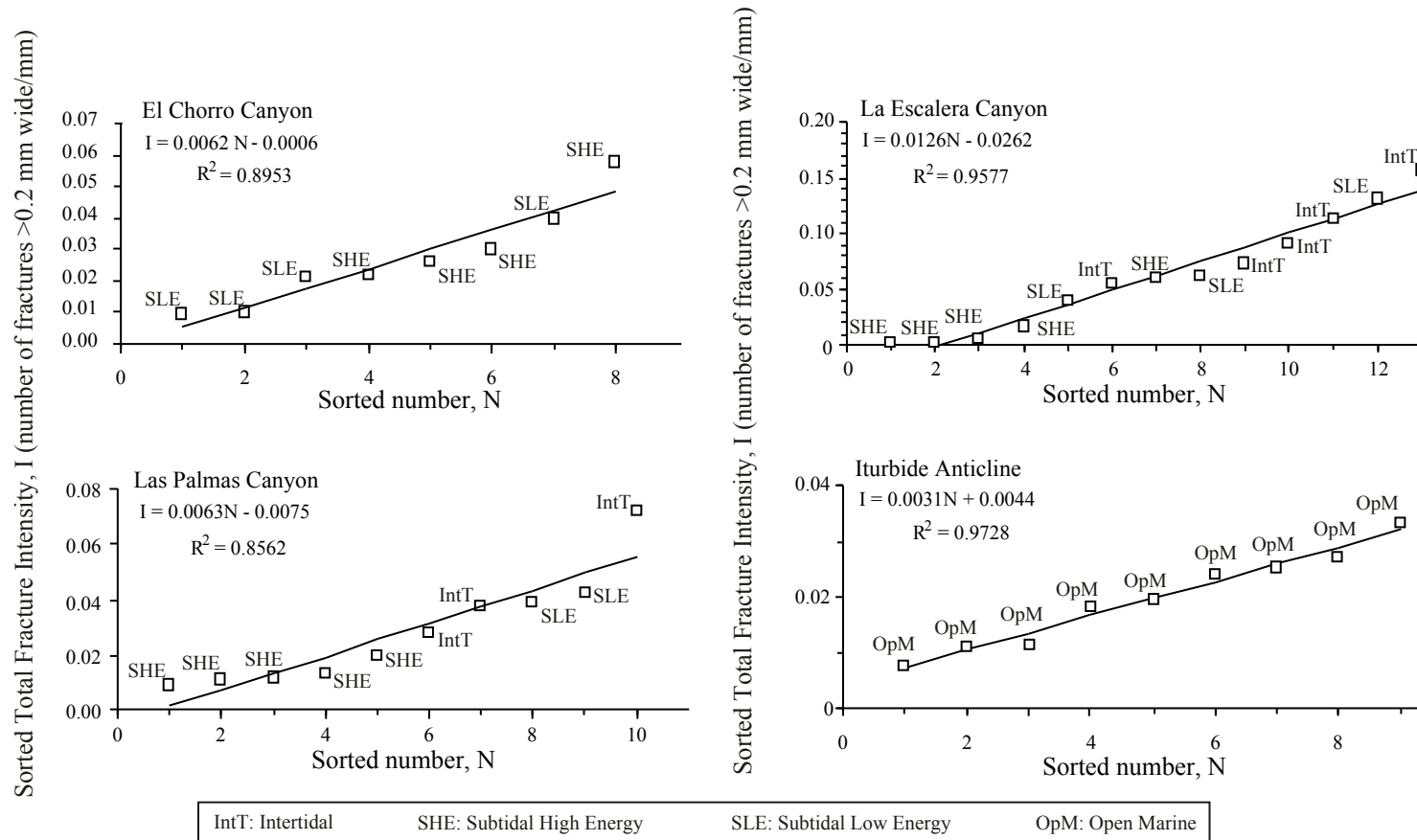


Figure 3.37. Total normalized fracture intensity and interpreted sedimentary environment of deposition. Fracture intensity was sorted from lowest to highest and beds were numbered progressively. High fracture intensity is commonly associated with intertidal mud-supported facies. Low fracture intensity is often associated with subtidal facies, particularly high energy facies. Exceptions suggest that fracture intensity depends on additional geologic variables.

associated with a mudstone bed of intertidal environment (Fig. 3.33). The next highest fracture intensity corresponds to a layer deposited in a low-energy subtidal environment. The following three highest fracture intensity values are associated with intertidal environments and the next one is again a layer deposited in subtidal low-energy conditions. The next highest fracture intensity is associated with a dolomitized grainstone of ooids, interpreted as a shoal deposit in a high-energy subtidal environment. This grainstone layer represents an exception to the pattern observed at Las Palmas Canyon at La Escalera, because this bed has higher fracture intensity than one additional intertidal wackestone and one subtidal low-energy packstone. The lowest fracture intensities occur in grainstones of subtidal environments, similar to Las Palmas results.

At El Chorro the highest fracture intensities are associated with four high-energy layers and a subtidal low-energy wackestone (Fig. 3.33). The lowest fracture intensities occur in partly dolomitized subtidal low-energy packstones. This pattern breaks dominant pattern at Las Palmas and La Escalera.

The upper limit of correlation for beds at Iturbide is the highest obtained in all localities. The range of variation of fracture intensity in Iturbide mudstones is small suggesting that all mudstone beds had similar resistance to brittle failure. Sedimentary environment considerations at Iturbide are trivial because all beds studied were deposited in open-marine ramp carbonate environment of deposition.

BED THICKNESS CONTROL ON FRACTURE INTENSITY

A common statement among structural geologists is that fracture spacing is proportional to bed thickness, all other variables unchanged (Bogdanov, 1947; McQuillan, 1973; Ladeira and Price, 1981; Nelson, 1985; Huang and Angelier, 1989; Lerche and Narr, 1986; Narr and Suppe, 1991; Wu and Pollard, 1995; Ji and Saruwatari, 1998; Bai et al., 2000; Bai and Pollard, 2000 and references therein). The earliest work establishing a systematic variation of fracture intensity with bed thickness is that of Bogdanov (1947), who published a drawing of an outcrop where systematic orthogonal joints are more closely spaced in thinner beds than in thicker beds. After this initial work, a number of authors arrived at similar results (Price, 1966; McQuillan, 1973; Ladeira and Price, 1981; Nelson 1985, Angelier et al. 1989, Huang and Angelier 1989, Aydan and Kawamoto 1990, Narr and Suppe, 1991; Mandal et al. 1994, Gross et al., 1995). The hypothesis is also cited in several structural geology textbooks (e.g., Suppe, 1985, Price and Cosgrove, 1990), indicating ample acceptance of this geologic concept.

Some authors supported a linear relationship between fracture spacing and bed thickness (Bogdanov, 1947; Huang and Angelier, 1989; Narr and Suppe, 1991), whereas others argued for a non-linear relationship at certain scales (McQuillan, 1973; Ladeira and Price, 1981; Lerche and Narr, 1986; Mandal et al., 1994). However, a common characteristic in all empirical investigations on the topic is that fracture size was not taken into account to determine fracture spacing. Theoretical predictions of fracture spacing also must confront this issue unless fractures are assumed to have the same size. Presumably the postulated bed

thickness/fracture spacing relationships are based on some minimum fracture size counted in a census in which smaller fractures are ignored. For example, it is reasonable to assume that only those fractures that reach the boundaries of a mechanical layer commonly have been counted for average spacing determination (e.g., Narr and Suppe, 1991). The use of this criterion is explicit in some studies (Laubach and Tremain, 1991). Illustrations in most papers cited above show fractures that span the mechanical layer thickness. Consequently, if spacing is determined for fractures with heights tied to bed thickness, then it follows that the spacing/bed thickness concept reflects a relationship between average fracture spacing and fractures having different heights in different layers. Most size distributions for natural fracture populations show a spectrum of fracture sizes. Where this is true, reducing the threshold size for counting fractures in a census for any specific layer results in counting a greater number of fractures and leads to a decrease in average spacing. Therefore, average fracture spacing is inherently dependent on the size threshold for fracture counting in any one layer, and the criterion probably varied from layer to layer in previous work. What, then, does the classic relationship between average fracture spacing and bed thickness mean?

Systematic change of fracture spacing with bed thickness raises strain incompatibility issues if we assume fractures have the same size (e.g. aperture) in adjacent beds. This problem is not new to structural geologists. Explanations for differences in strain between adjacent beds with different average spacing include different deformation mechanisms for each bed, and development of bed-parallel slip surfaces (Price, 1966; Hobbs, 1967; Narr and Suppe, 1991; Fisher et al.,

1995; Zhao and Ji, 1997; Ji and Saruwatari, 1998). Another explanation is that average fracture spacing is not a diagnostic strain indicator because the size of fractures must be known for strain determination. Lorenz and Hill (1991) expressed skepticism on the classic bed thickness fracture spacing relationship after a detailed study of slant/horizontal and vertical cores in the gas-producing sandstones of the Piceance Basin. To avoid potential influence of variable fracture size on apparent spacing I will use the normalized fracture intensity in each bed. Systematic variations of fracture intensity with variation in mechanical bed thickness will be explored.

Mechanical bed thickness

Mechanical bed boundary identification is a non-trivial problem in sedimentary successions, particularly for fracture studies in carbonate sediments which may not develop definite stratification planes between contrasting sedimentary facies. Mechanical bed thickness is defined here as the dimension perpendicular to depositional surfaces in a volume of sedimentary rock with a distinct fracture intensity. Limiting surfaces for mechanical bed thickness determination are recognized by systematic fracture terminations at a certain level within the sedimentary succession. This definition encompasses equivalent definitions of mechanical layer by Corbett et al. (1987), Narr and Suppe (1991), Gross, 1993; Gross and Engelder, 1995; Becker and Gross, 1996). Bed thickness is often delimited by a discrete stratification plane or a pressure-solution surface and generally includes a volume of sediments with similar textural and

compositional characteristics. Systematic termination of fractures at a certain level in a sedimentary pile often coincides with a combination of changes in lithology, sedimentary facies or porosity and reflects changes in mechanical properties of layered rocks at the time of fracturing.

Normalized fracture intensity and mechanical bed thickness

Normalized fracture-intensity provides a method, unbiased by the scale of observation, to investigate the possible effect of bed thickness on fracture intensity in Cupido and Tamaulipas Inferior formations. Normalized fracture intensity is a more robust parameter than average spacing for fracture intensity comparisons between different beds. Ideally, we must compare fracture intensities in beds with different thickness, in the same locality, and with similar mechanical properties at the time of fracturing. Although we studied the fracture intensity in more than 40 beds from Cupido and Tamaulipas Inferior formations, it is difficult to find a representative subset of beds that meets the requirements previously specified. At Iturbide beds selected for analysis are all open-marine mudstones ranging in thickness from 7 to 122 cm. Most beds studied from La Escalera Canyon are dolostones containing more than 50% dolomite and eight out of nine have more than 80% dolomite as determined by point counting. Dolostone beds at La Escalera Canyon range in thickness from 8 to 178 cm, providing more than an order of magnitude variation in bed thickness for the analysis. The degree of dolomitization in most beds studied at Las Palmas is lower than 50% (seven out of 10 beds studied). Given that sedimentary facies does not have a first order

control on fracture intensity, we analyzed bed thickness vs. fracture intensity relationships in all limestone beds from Las Palmas as a group, and the remaining three dolostones as a separate group. At El Chorro, all grainstone beds are limestones and were analyzed as a group, whereas the other four beds studied at El Chorro are dolostones and comprise another group for bed thickness/fracture intensity analysis.

La Escalera

Weighted regression results for La Escalera Canyon dolostones suggest that there is little to no correlation between bed thickness and fracture intensity at La Escalera Canyon (Fig. 3.38). The coefficient of determination for least-squares regression to total fracture intensity is close to zero, showing that variations in thickness cannot account for observed differences in fracture intensity. Weighted regression lines for individual fracture sets also yield low coefficients of determination. The coefficient of determination for set A, based on data from 8 beds, is $r^2=0.0226$, and the coefficient of determination for set B, based on 9 beds, is $r^2=0.0088$. The coefficient of determination to the combination of sets A and B is also very close to zero ($r^2=0.0114$). Results for set C are not shown because this set is sufficiently developed in only two limestone beds and regression to only two points is trivial.

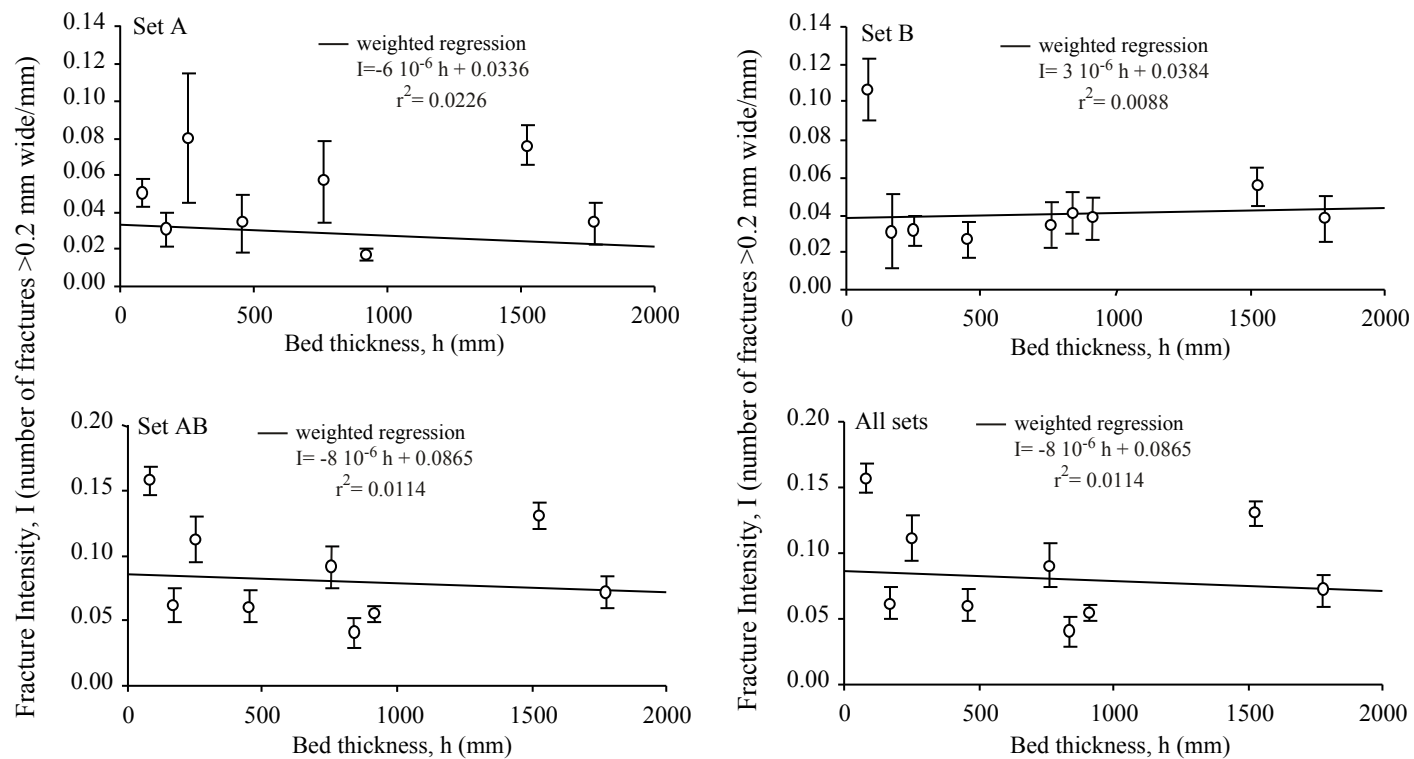


Figure 3.38. Bed thickness control on fracture intensity, dolostone beds ($>50\%$ dolomite content), La Escalera Canyon. Weighted regressions suggest that bed thickness does not correlate with fracture intensity for individual sets or total fracture intensity across nearly an order of magnitude variation of bed thickness. Fracture set C was not included because it was studied exclusively in limestone beds.

Iturbide

Total fracture intensity at Iturbide shows inconsistent correlation behavior with bed thickness (Fig. 3.39). Weighted linear regression to combined set AB yields $r^2=0.4548$ based on four data points. However, the probability of obtaining a coefficient of determination $r^2=0.4548$ by chance with four data points from unrelated variables is more than 10% (Young, 1962). Weighted regression to set D yields $r^2=0.9689$, based on five data points and can be considered a reliable correlation. However, despite the degree of reliability of the correlation between bed thickness and fracture intensity in these beds, both weighted regressions suggest an increase of fracture intensity (decrease in average spacing) with an increase in bed thickness, opposite to the expected behavior according to the literature (Nelson, 1985; and references therein). Note, however, that these results are based on few observations (4 beds for set AB and 5 beds for set D), and might not be statistically significant. The coefficient of determination for fracture set C is close to zero ($r^2=1.9 \cdot 10^{-6}$), suggesting no correlation between bed thickness and fracture intensity based on data from these six mudstone beds.

One potential problem with fracture intensity estimates from Iturbide is that aperture data from fracture sets A, B, and C are suspect. Locally, tectonic stylolites developed along fracture walls, reducing the apertures of some fractures and making measurement of the original fracture apertures impossible. Results from fracture set D, unaffected by tectonic stylolites, produce the strongest correlation between fracture intensity and bed thickness but the correlation is

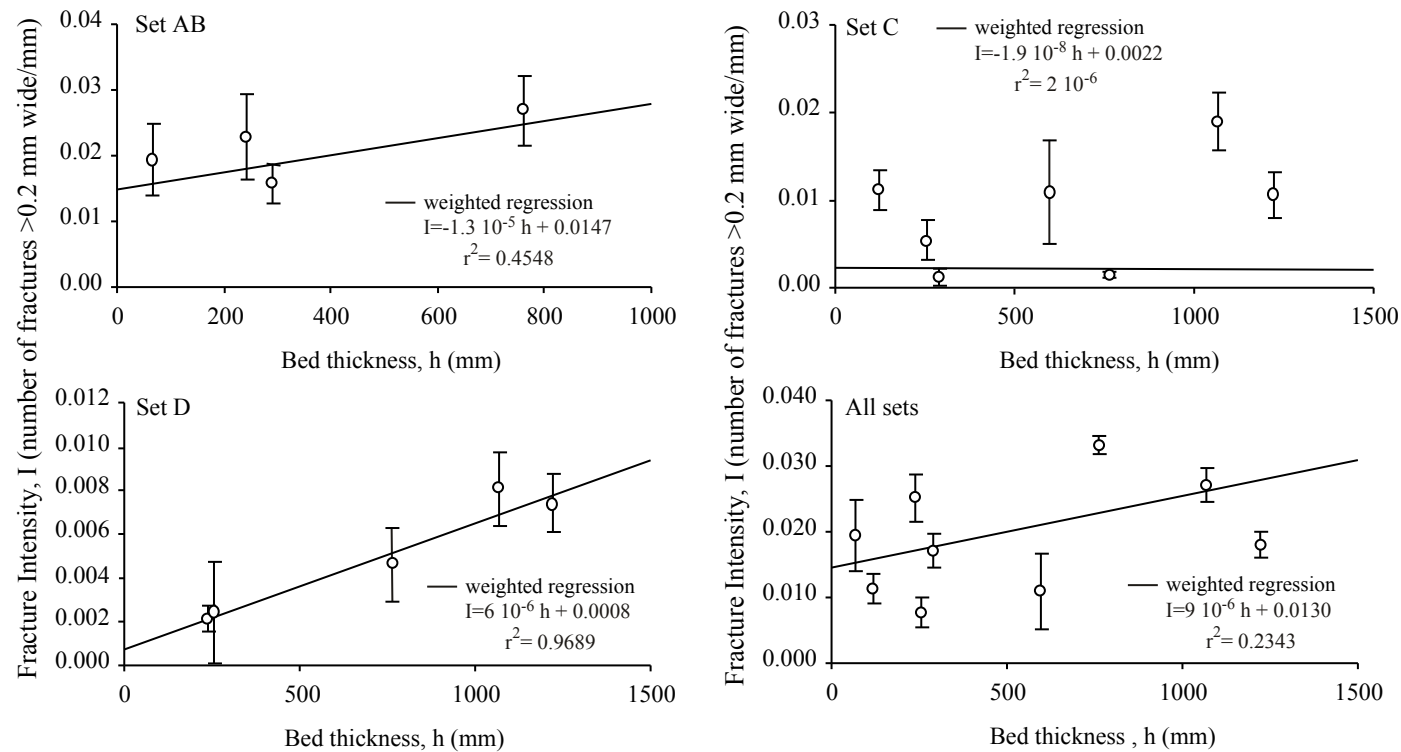


Figure 3.39. Bed thickness control on fracture intensity, open marine mudstones, Iturbide Anticline. Bed thickness and fracture intensity relationships are contradictory for different fracture sets. Weighted regression lines suggest no correlation or the opposite fracture intensity vs. bed thickness relationship expected from previous work (Nelson, 1985; and references therein). Analyses from sets AB and D are based on five or less measurements and should be regarded as statistically dubious. High data dispersion suggests that more analyses are necessary before reaching reliable conclusions.

opposite to the one expected from the literature. Weighted regression to total fracture intensity in the beds yields a low coefficient of determination ($r^2=0.2343$) suggesting that fracture intensity increases with bed thickness, similar to the relationship obtained for fracture sets AB and D, although there is more than 10% probability of obtaining this degree of correlation for similar number of data points between uncorrelated variables. In conclusion, more data are necessary to clarify the results from Iturbide mudstones, but the data available suggest that there is at best a weak relationship between bed thickness and fracture intensity. Furthermore, the most reliable relationship suggests the opposite proportionality from the one reported in the literature.

Las Palmas

Plots of bed thickness vs. fracture intensity for Las Palmas locality limestone beds are inconsistent (Fig. 3.40), similar to results from Iturbide Anticline mudstones. Weighted regression to set A suggests that fracture intensity (i.e. inverse of average spacing) decreases with an increase in bed thickness as suggested in the literature (Nelson, 1985; and references therein). However, the degree of correlation is low for the number of data points analyzed ($r^2=0.07$ for 6 beds), suggesting no correlation between the variables studied. Plots of normalized fracture intensity for sets AB and C suggest no correlation between bed thickness and fracture intensity, or at best a correlation opposite from the one expected based on the literature. Weighted regression to total intensity data (all

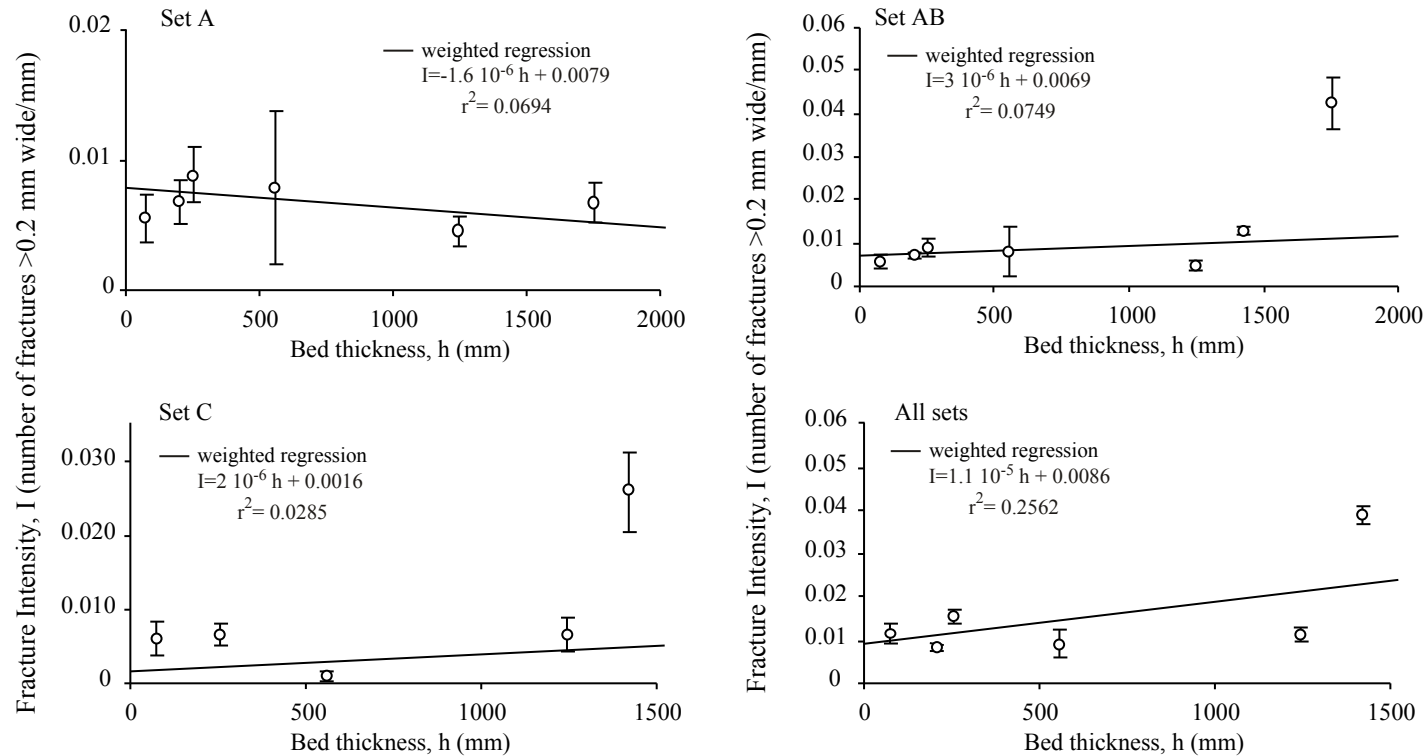


Figure 3.40. Normalized fracture intensity and bed thickness, limestones ($<50\%$ dolomite content), Las Palmas Canyon. Relationships between bed thickness and fracture intensity based on weighted regressions are non-systematic. Fracture intensity for set A show a relationship as described in the literature. However, the variation of fracture intensity expected is small across over an order of magnitude variation in bed thickness. Regressions to set AB, set C data and all sets suggest a relationship opposite to the paradigm in the literature or no relationship at all. Coefficients of determination are very low given the number of data points, indicating that this degree of correlation can happen by chance between two uncorrelated variables (Young, 1962).

sets) produces similar results, with a better coefficient of determination, but still too low to indicate a reliable correlation.

Only three dolostone beds were studied at Las Palmas but their fracture intensity/bed thickness characteristics were also compared (Fig. 3.41). Regressions to three data points require coefficients of determination very close to one to indicate any reliable correlation. Weighted linear regressions to sets A, C and combined sets AC (all sets) suggest no correlation between bed thickness and fracture intensity. Coefficients of determination are low and the slopes of the regression lines are almost parallel to the abscissas, suggesting that little change in fracture intensity is expected from variations of bed thickness of nearly an order of magnitude. A nonlinear regression (e.g., hyperbolic) could produce a good model for the fracture intensity versus bed thickness data in Figure 3.41, particularly for set C. A hyperbolic relationship between fracture intensity and bed thickness would be expected from an inverse relationship between fracture spacing and bed thickness (Ladeira and Price, 1981).

El Chorro

At El Chorro locality beds can be separated in dolostones and limestones. Limestones studied are all high-energy (shoal) grainstones whereas dolostones are all mud-bearing carbonates. Normalized fracture intensity of sets A, B, C and D were collected in limestone beds but only a couple of data points are available for analysis because not all sets are present in all beds studied (Fig. 3.42). Data from fracture sets A, B and C in grainstones suggest the opposite bed thickness/fracture

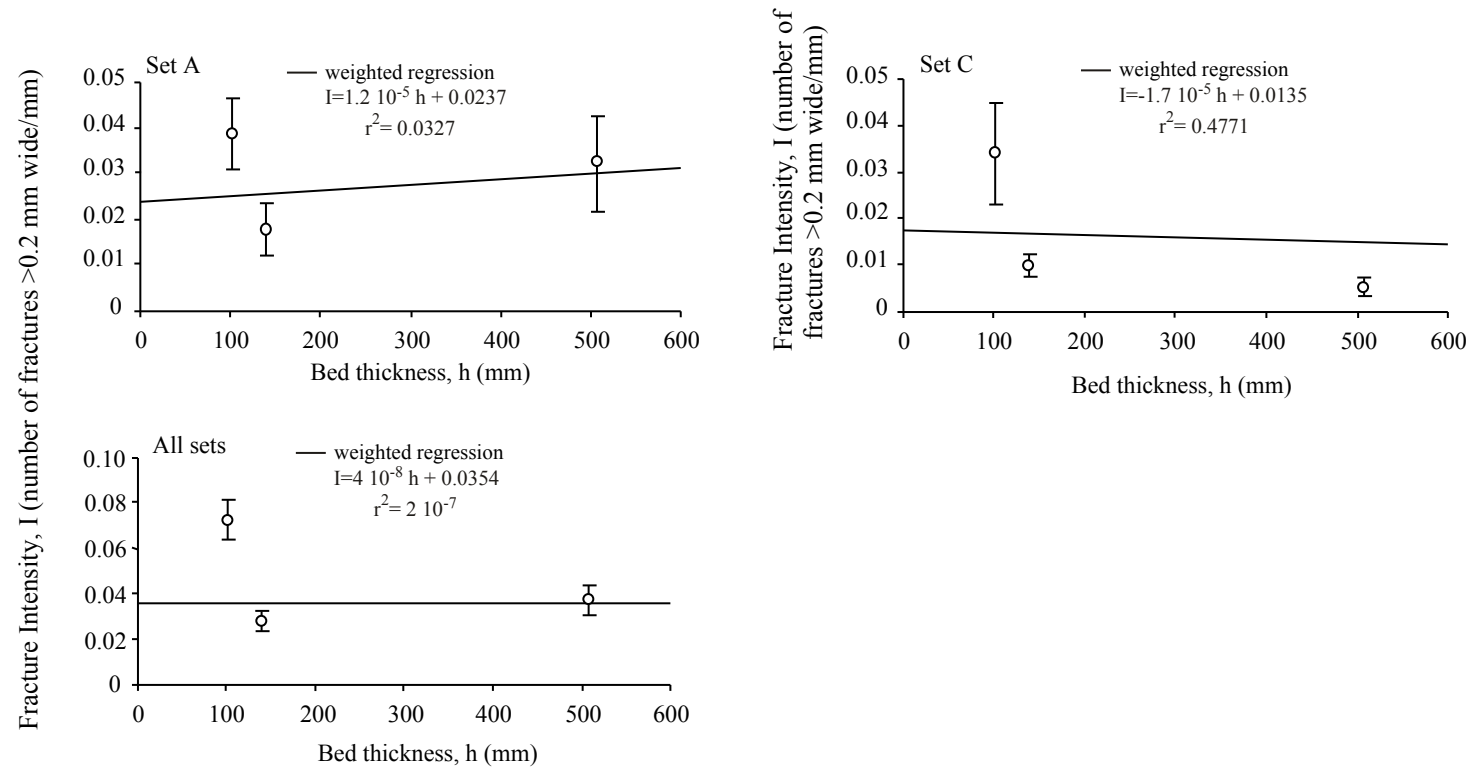


Figure 3.41. Normalized fracture intensity and bed thickness, dolostones ($>50\%$ dolomite content), Las Palmas Canyon. Relationships between bed thickness and fracture intensity based on weighted regressions in dolostones suggest that normalized fracture intensity and bed thickness are uncorrelated. Changes in bed thickness do not reflect significant changes in normalized fracture intensity. Results are based on only three beds and may not be statistically significant. However, results obtained are consistent with results obtained from limestones at this locality and other localities as well.

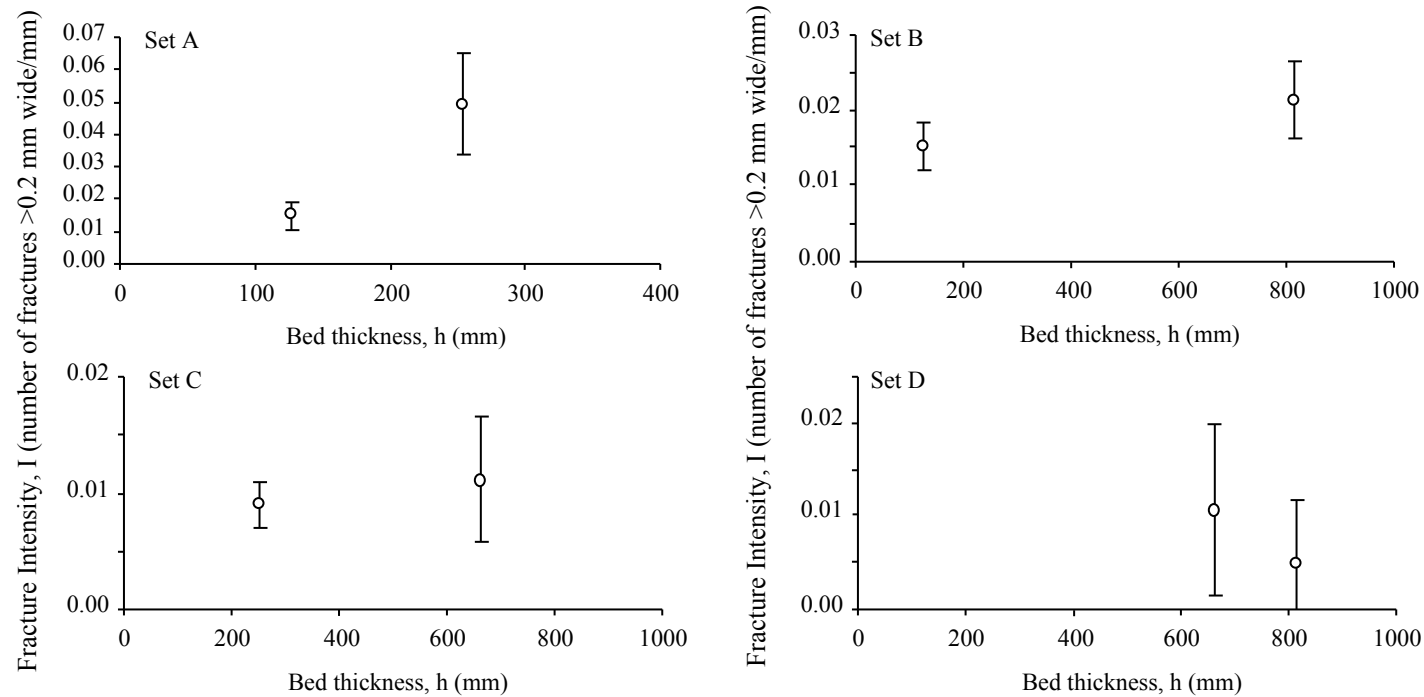


Figure 3.42. Normalized fracture intensity and bed thickness, grainstones, El Chorro Canyon. Individual fracture set intensities can be analyzed in groups of two out of four grainstone beds studied. Regressions to these data are trivial, but scatter plots for sets A, B and C suggest that fracture intensity does not augment with decreasing bed thickness. An exception is represented by set D, where the fracture intensity decreases with an increase in bed thickness. However, there is considerable uncertainty in the determination of the fracture intensity for set D in each of these two beds.

intensity relationships as suggested in the literature (Nelson 1985, and references therein). The data available for set D suggest a decrease in fracture intensity with an increase in bed thickness as proposed in the literature. However, normalized fracture intensity determinations show considerable uncertainty. Weighted regression to all sets in non-dolomitized grainstones (Fig. 3.43) suggests that as bed thickness increases fracture intensity decreases, as proposed in the literature. Three beds comprise the data set for all sets weighted regression and the coefficient of determination obtained is low ($r^2=0.138$) which suggest that there is a high probability that the variables analyzed do not correlate.

Weighted regressions to sets in dolomitized beds suggest the opposite relationship between fracture intensity and bed thickness as expected from the literature. Weighted regressions to combined sets AB, set C and all sets suggest a relationship between bed thickness and fracture intensity opposite to the one expected according to the literature. However, coefficients of determination are low, suggesting no correlation between bed thickness and fracture intensity.

In conclusion, the majority (and most reliable) of fracture intensity data associated with carbonates of Cupido and Tamaulipas Inferior formations suggests no relationship between bed thickness and fracture intensity. The second most common relationship found is opposite to the one predicted in the literature (e.g., Nelson, 1987, and references therein). The least common relationship found is a direct proportionality between average fracture spacing (calculated as the inverse of fracture intensity) and bed thickness as proposed in the literature, although in these cases as well as most of the other analyses the number of

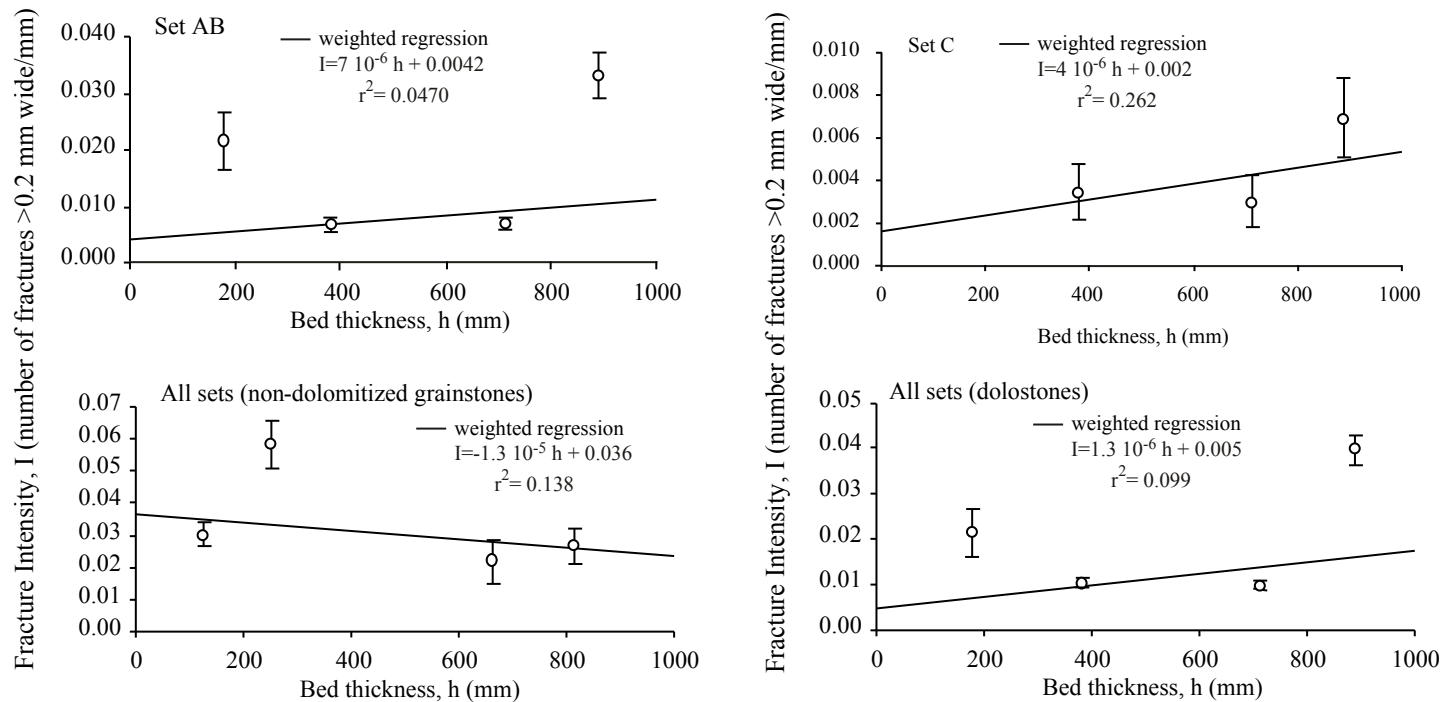


Figure 3.43. Normalized fracture intensity and bed thickness in dolostones (>70% dolomite content), El Chorro Canyon. Weighted regression for sets AB and set C suggest that fracture intensity increases with bed thickness, opposite to relationship expected from the literature. Regression to total intensity in dolostones also suggest the relationship previously described. Weighted regression to all sets in non-dolomitized grainstones shows that an increase in bed thickness correlates with a decrease in fracture intensity as expected from an increase in average spacing as described in the literature. However, for regressions with four data points only coefficients of determination greater than 0.8 assure that probability of correlation by chance is less than 10% (Young, 1962).

observations are limited. Use of normalization of fracture intensity to study bed thickness control on fracture intensity yields a different result from most common conclusions from study of this issue. Because normalized fracture intensity provides an unbiased determination of fracture intensity that takes into account fracture size, it is possible that previous work on fracture intensity relationships with bed thickness was adversely affected by fracture size bias. Although in most published cases it is unclear which fracture sizes were counted or not for fracture spacing determination, the use of average spacing of fractures that span the bed thickness would be biased by the variable sizes of fractures measured. Larger fractures are less abundant than smaller fractures, and consequently thicker beds will show apparently wider spacing even if fracture abundance is constant.

A POSSIBLE EXPLANATION FOR THE APPARENT BED THICKNESS/FRACTURE INTENSITY RELATION

Increase of fracture intensity in inverse proportion to bed thickness is implied by numerous publications on relationships between bed thickness and fracture spacing (e.g., Bai and Pollard, 2000, and references therein). It is daunting to challenge an idea supported by more than 50 years of observations. However, inspired by Mandelbrot (1982), work on the statistics of fracture sizes during the last 20 years has led to the belief that in many cases fractures have a fractal geometry (Gudmundsson, 1987; Wong et al., 1989; Heffer and Bevan, 1990; Barton and Zoback, 1992; Gillespie et al., 1993; Hatton et al., 1994; Sanderson et al., 1994; Belfield and Sovich, 1995; Clark et al., 1995; Gross and

Engelder, 1995; Johnston and McCaffrey, 1996; Marrett, 1997; Ortega et al., 1998; Marrett et al., 1999; Ortega and Marrett, 2000). Fractures exist at different scales of observation from the microscopic scale (Bonham, 1957; Onasch, 1990; Laubach, 1997) to the macroscopic scale. Furthermore, Marrett et al. (1999) showed examples of inverse power-law scaling of opening mode fracture apertures and fault displacements that span up to five orders of magnitude in size and represent rocks with various lithologies. Inverse power-law scaling implies a greater abundance of small fractures than large fractures. Although this abundance relationship for small and large fractures is also intuitive, it has been consistently neglected in the literature of bed thickness and fracture intensity/spacing relationships. Although it is typically difficult to determine retroactively which fracture sizes were counted for average fracture spacing analysis in most published work, it is reasonable to assume that the fractures chosen in many cases were those that reach the boundaries of the mechanical layer (e.g., Narr and Suppe, 1991; Gross, 1993).

The size of fractures required to reach the boundaries of the mechanical layer changes with the thickness of the mechanical layer itself. If we assume an inverse power-law size distribution for these fractures (fractal geometry), then a variation in fracture abundance with fracture size will occur even in the absence of differences in fracture abundance as measured by normalized fracture intensity. Thicker beds will require larger (less abundant, so more widely spaced on average) fractures to span the bed (Fig. 3.44 A). Thinner beds will require smaller (more abundant, more closely spaced) fractures to meet the same criteria (Fig.

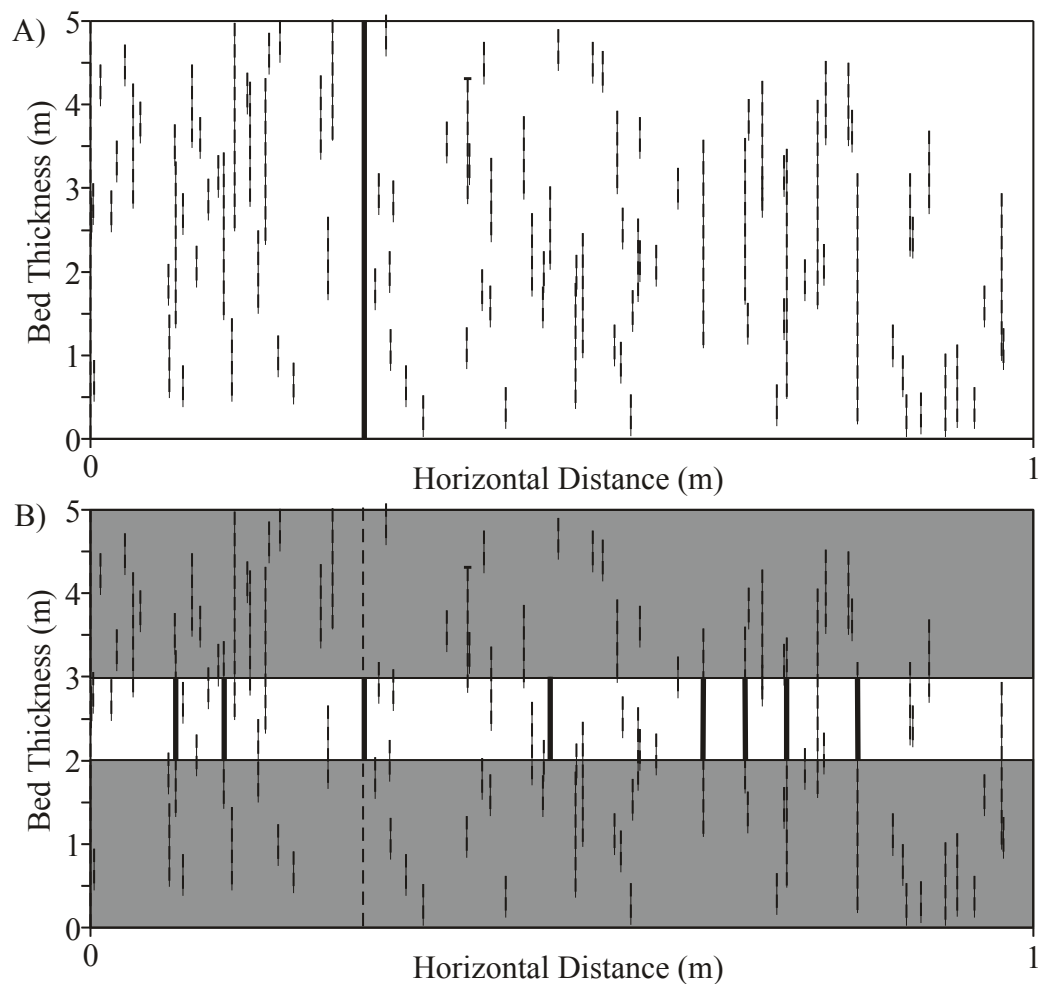


Figure 3.44. Apparent increase of fracture intensity with decrease in fracture height considered. The diagrams shown represent cross sections of beds. Fracture heights were generated such that their sizes follow a power-law distribution. Fracture height is limited by the boundaries of the mechanical layer in which they propagate. Diagram A suggests a wider average spacing than diagram B even though fractures in both cases have the same fracture size distribution. Namely, if the criteria used to count fractures for fracture spacing calculation is that fractures must reach the boundaries of the mechanical layer to be counted, then fewer fractures reach the boundaries of the thicker bed, and more (and smaller) fractures span the bed thickness in thinner beds, even if the beds have the same distributions of normalized fracture intensity. This example as well as the example in Figure 3.26 motivates the use of normalized fracture intensity with reference to a specific fracture size as a tool for fracture intensity comparisons among beds with different attributes.

3.44 B). Consequently, the average spacing of fractures that reach the boundaries of the mechanical layer in thinner beds will be smaller than the average spacing of fractures that reach the boundaries of the mechanical layer in thicker beds, even if fracture abundance is constant. Figure 3.44 C shows another example of the fracture scale effect on apparent fracture spacing in two beds with different thickness and the same fracture length distribution. Figure 3.44 D shows the results of selecting different bed thickness layers from Figure 3.44 A, illustrating how a power-law-distributed fracture height distribution can generate the traditional relationship between bed thickness and average fracture spacing reported in the literature.

Average fracture intensity of fractures that span the bed thickness

Deep water carbonate mudstones from Iturbide locality were selected for a comparison of fracture intensity bed thickness relations using normalized fracture intensity and the traditional method of counting the number of fractures that span the bed thickness divided by the scanline length. The beds from this locality were chosen because the most significant difference among these beds is their bed thickness. All beds are carbonate mudstones composed mostly of carbonate mud (micrite), less than 6% allochems, and less than 10% (TVR) dolomite content. The fracture sets analyzed correspond to a combination of fracture sets A, B and C at this locality, all of which are interpreted as pre-folding fractures that are older than fracture set D, possibly folding-related. The intensity of each fracture

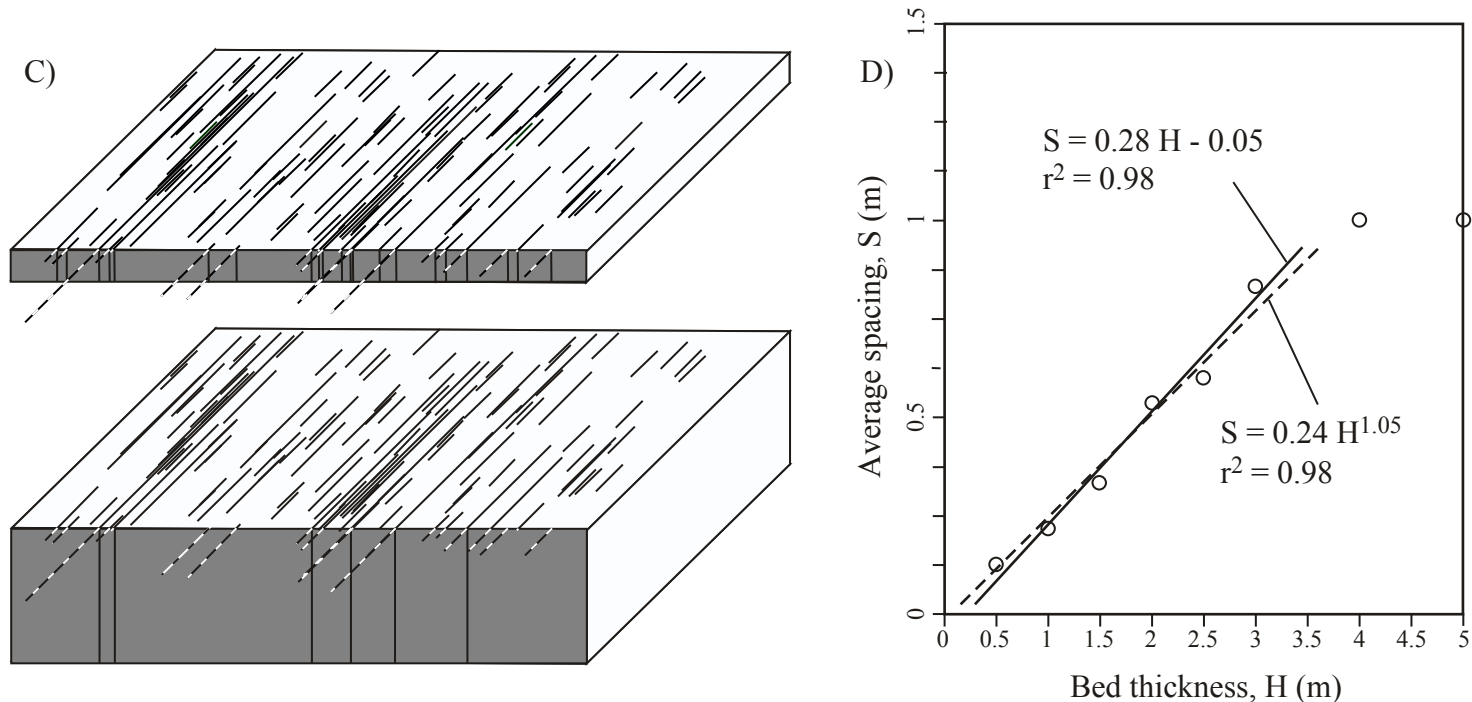


Figure 3.44 continued. C) Another example of the non-normalized fracture size effect on bed thickness/spacing relationship. In this case two layers with different mechanical thickness but same fracture length distribution and fracture spatial organization as seen on bed parallel exposures have apparently different fracture intensity in cross section. If we assume a square geometry for the fractures and count only the fractures that span mechanical layer, then shorter and thinner fractures span the mechanical layer thickness in the thin bed than in the thicker bed. D) Plot of bed thickness and average spacing for fractures that span the bed in diagram A). Bed thickness varies from 0.5 to 5 m and average spacing includes different positions in diagram A). A linear regression is an adequate model for bed thickness below 3 m (as reported in the literature), however a power law regression is also an adequate model for this limited range of bed thickness variation. Average spacing for beds thicker than 3 m is constant because of finite size of model considered, although similar large-scale behavior was reported by McQuillan (1973) and Ladeira and Price (1981) in natural examples.

set was calculated separately and then added to obtain the fracture intensity of the combined sets ABC.

Figures 3.44 E and F show results of applying both methods of fracture intensity determination to Iturbide beds. The normalized fracture intensity was determined for fractures with aperture greater than 0.2 mm (Fig. 3.44 E). Errors were calculated using formula (4) and a weighted regression line has been fit to the data. The weighted regression line is characterized by a low slope and a small coefficient of determination $r^2=0.070$. The coefficient of determination suggests that there is no significant correlation between bed thickness and fracture intensity, and the slope of the line suggests that no significant changes of fracture intensity occur across 1.5 orders of magnitude variation in bed thickness. Moreover, if there is any correlation, the slope of the weighted regression line suggests that fracture intensity increases with an increase in bed thickness, which is opposite to the relationship expected for an increase in fracture spacing with an increase in bed thickness as proposed in the literature.

Fracture intensity was also estimated using the traditional method in which only fractures that span the bed thickness are counted (Fig. 3.44 F). The solid curve represents a power law regression to the fracture intensity data, which is adequately modeled by a power law yielding a coefficient of determination $r^2=0.90$ and suggests that intensity of fractures that span the bed increases with decreasing bed thickness. The dashed line represents a linear regression to the average spacing of fractures that span the bed thickness, simply obtained as the inverse of the fracture intensity of the most abundant fracture set. A linear

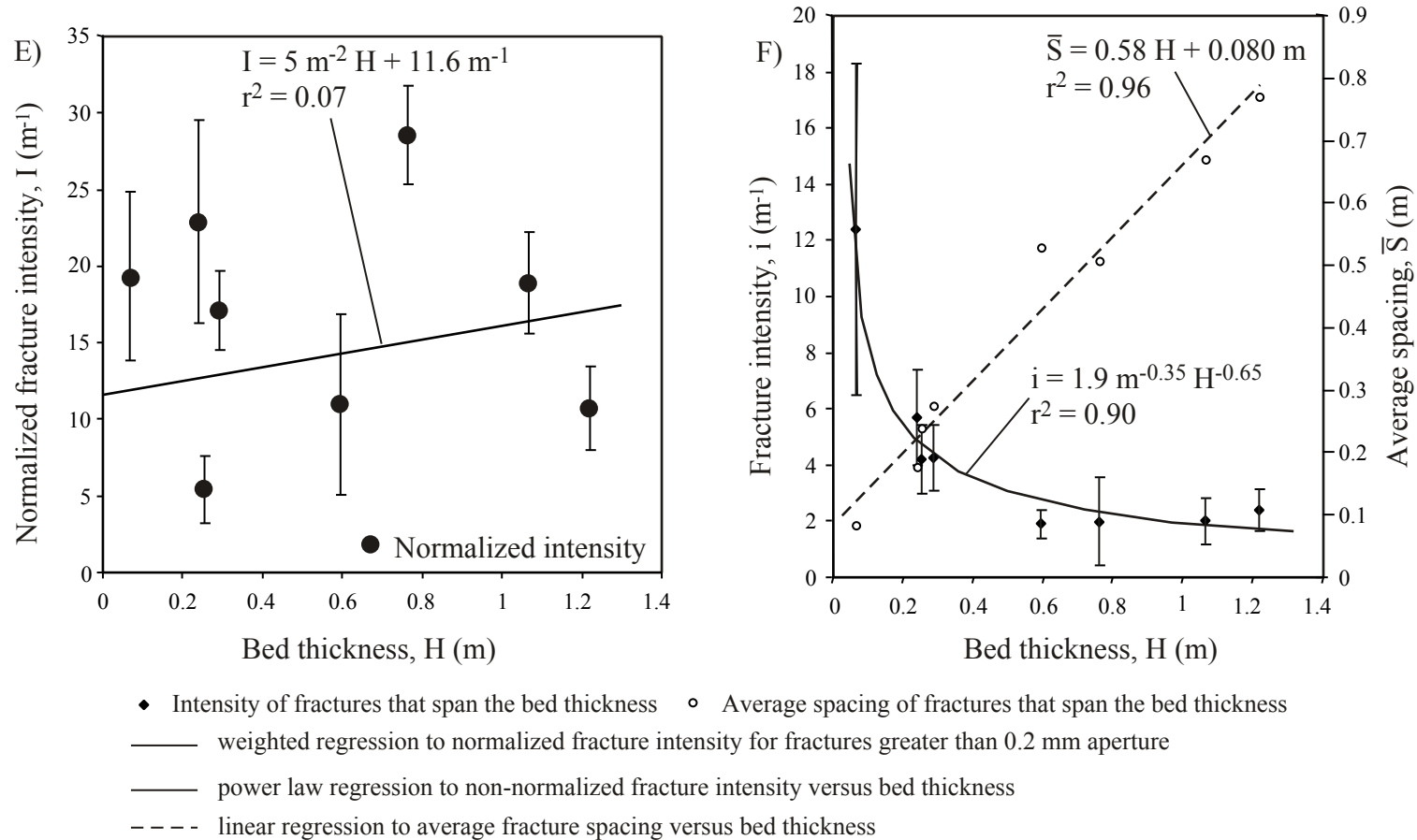


Figure 3.44 continued. Comparison of normalized and non-normalized fracture intensity for Iturbide mudstones. E) Normalized fracture intensity shows lack of correlation with bed thickness. F) In contrast, non-normalized fracture intensity produces an apparent correlation with bed thickness and consequently produces a spurious correlation of average fracture spacing with bed thickness.

regression to these data adequately explains the variation of average spacing of fractures that reach both bed boundaries, and is similar to results reported in the literature for other stratified rocks of different lithology, age, and tectonic setting (e.g., McQuillan, 1973; Ladeira and Price, 1981; Huang and Angelier, 1989; Narr and Suppe, 1991; Gross 1993). Because fracture height for fractures that reach the bed boundaries changes from bed to bed, fractures of smaller height are included in the census for a thin bed than for a thick bed, where fractures have to be larger (and usually are more scarce) to reach the bed boundaries.

Although this exercise includes data from only one locality in the study area, it nevertheless illustrates an issue of potentially wider applicability. The results of this exercise depend on purely geometrical and statistical attributes of three-dimensional fractures having a variety of sizes, smaller fractures being generally more abundant than large fractures (an observation commonly reported for natural fracture systems, including both joint and vein arrays). Indeed, for randomly located fractures that follow a power law distribution of heights, average spacing can be written as:

$$\bar{S}_{1D} = \frac{1}{F_{1D}} = \frac{1}{kH^{-j}} = \frac{H^j}{k}$$

where \bar{S} is the average spacing of fractures that reach the bed boundaries, F_{1D} is the one-dimensionally sampled fracture intensity, H is mechanical layer thickness, and k and j are the coefficient and exponent of the fracture height distribution. Consequently, average spacing can be approximated by a linear relationship with bed thickness if j is about one. The analogous exponent for fracture aperture

distributions commonly is observed to be about one in nature as shown in this dissertation and reported in the literature (Barton and Hsieh, 1989; Barton and Zoback, 1990; McCaffrey et al., 1994; Sanderson et al., 1994; Clark et al., 1995; Belfield and Sovich, 1995; Gross and Engelder, 1995; Marrett, 1997; Marrett and Laubach, 1997; Laubach et al., 1998; Ortega et al., 1998; Belfield, 1998; Marrett et al., 1999).

Perhaps, the fracture intensity vs. bed thickness concept has been reinforced through time by the use of a biased methodology for fracture intensity calculation (Fig. 3.44). In this chapter, the use of normalized fracture intensity, which explicitly accounts for fracture size and scale of observation, has shown that bed thickness does not represent a major control on fracture intensity in Cupido and Tamaulipas Inferior formation carbonates. It is possible that this example from Mexico is unusual. However, the fact that a methodology modeled after the traditional approach yields an outcome typical of the classic result suggests otherwise.

A mechanical explanation for this non-intuitive result is beyond the scope of this dissertation. However, it is possible that mechanical principles control the spatial organization (spacing distribution) of fractures in a volume of rock (Hobbs 1967; Narr and Suppe, 1991; Olson 1993; Wu and Pollard, 1995; Olson 1997) but that average spacing is a poor statistic of spatial organization. Empirical studies as well as mechanical modeling may have arrived at the same conclusions about bed thickness/spacing relationships because the same systematic flaws in the methodology of fracture spacing calculation affect them both. This

methodological flaw may have obscured more interesting and perhaps more useful interpretations of bed thickness effects on fracture attributes (e.g., fracture clustering).

DOLOMITIZATION CONTROL ON FRACTURE INTENSITY

The effect of dolomitization on fracture intensity was the only diagenetic effect studied. A number of authors have indicated that lithologic composition of layered rocks affects fracture abundance (Harris et al., 1960; Nelson, 1985; Narr, 1991; Nelson and Serra, 1995). Dolomitization is a process that changes the mineralogy of limestones after sediments have been deposited. Petrographic observations suggest that dolomite precipitation and replacement occurred, at least in part, before tectonic folding of shallow water facies of Cupido Formation (Monroy et al., 2001; Fig. 3.26). Dolomitization is only a minor diagenetic process in open-marine mudstones of Iturbide at Santa Rosa Canyon so these data were not considered in this part of the study. Recrystallization is another important diagenetic event affecting these rocks but occurred after pre-folding fractures formed so no relationship between degree of recrystallization and pre-folding fracturing is expected (Monroy et al., 2001; Fig. 3.26).

Dolomite precipitation most probably occurred at successive stages starting very early in the burial history of these rocks (Monroy et al., 2001; Fig 3.26). A model for early dolomite replacement is that of hypersaline water circulation from evaporative environments (King, 1947; Adams and Rhodes,

1960; Lucia and Major, 1994). Dolomitization associated with hypersaline flux occurs at shallow burial depths and early in the diagenetic history of the rocks. In the Lucia and Major (1994) dolomitization model, hypersaline reflux characterized by high concentration of magnesium promotes the dolomitization of beds immediately below the evaporative environments. This model has potential application to shallow-water facies of Cupido Formation characterized by cyclic occurrence of dolostone and limestone layers and absence of shales. Dolostones are frequently found at the top of parasequence cycles, associated with calcite-replaced evaporite nodules, and intertidal and supratidal deposits. This early dolomite probably became the focus of subsequent dolomite precipitation (Morrow, 1982), which may have been concentrated in these early fractured beds due to their relative higher permeability.

Original sedimentary facies of highly dolomitized beds can often be recognized by the presence of ghost allochems. However, in the following analysis sedimentary facies and bed thickness will be ignored. As demonstrated in previous sections, sedimentary facies has a modest influence on fracture intensity and bed thickness has no significant control on the fracture intensity observed in these rocks. All the dolomite in the beds was assumed to have formed before or synchronously with fracturing and consequently assumed to have had a potential effect on fracture intensity. Petrographic observations of dolomite-bridged crack-seal textures (Ramsay and Huber, 1987) in veins support the assumption that dolomite had an effect on the mechanical properties of the beds studied at the time

of fracturing. Dolomite content in Cupido Formation rocks was measured using point counting of thin sections stained with alizarine-red.

Only data from La Escalera Canyon, Las Palmas Canyon, and El Chorro Canyon were considered for this analysis because beds at Iturbide experienced degrees of dolomitization that range only from 0 to 15%. Only beds with more than 10% dolomite content were studied. Some of these beds also show evidence of dedolomitization (Folk, 2001, personal communication). Dedolomitization replaces dolomite with calcite, potentially complicating determination of the original dolomite content in the rock.

Las Palmas

There is a positive correlation between normalized fracture intensity and dolomite content at Las Palmas (Fig. 3.45). The coefficient of determination for a linear weighted regression to total fracture intensity per bed is high ($r^2 = 0.72$), suggesting that there is less than 1% probability of obtaining this degree of correlation from spurious data. Linear regressions for individual set A, combined sets AB and set C at Las Palmas Canyon also suggest a positive correlation between fracture intensity and dolomite content. Fracture set B intensity was obtained for only three beds at Las Palmas locality because it is poorly developed in all other beds (not shown in Figure 3.44), but weighted regression to these three points shows similar behavior as results from other fracture sets.

The coefficient of determination for set A based on data from seven beds ($r^2 = 0.69$) suggests that there is only a 2% probability of obtaining this degree of

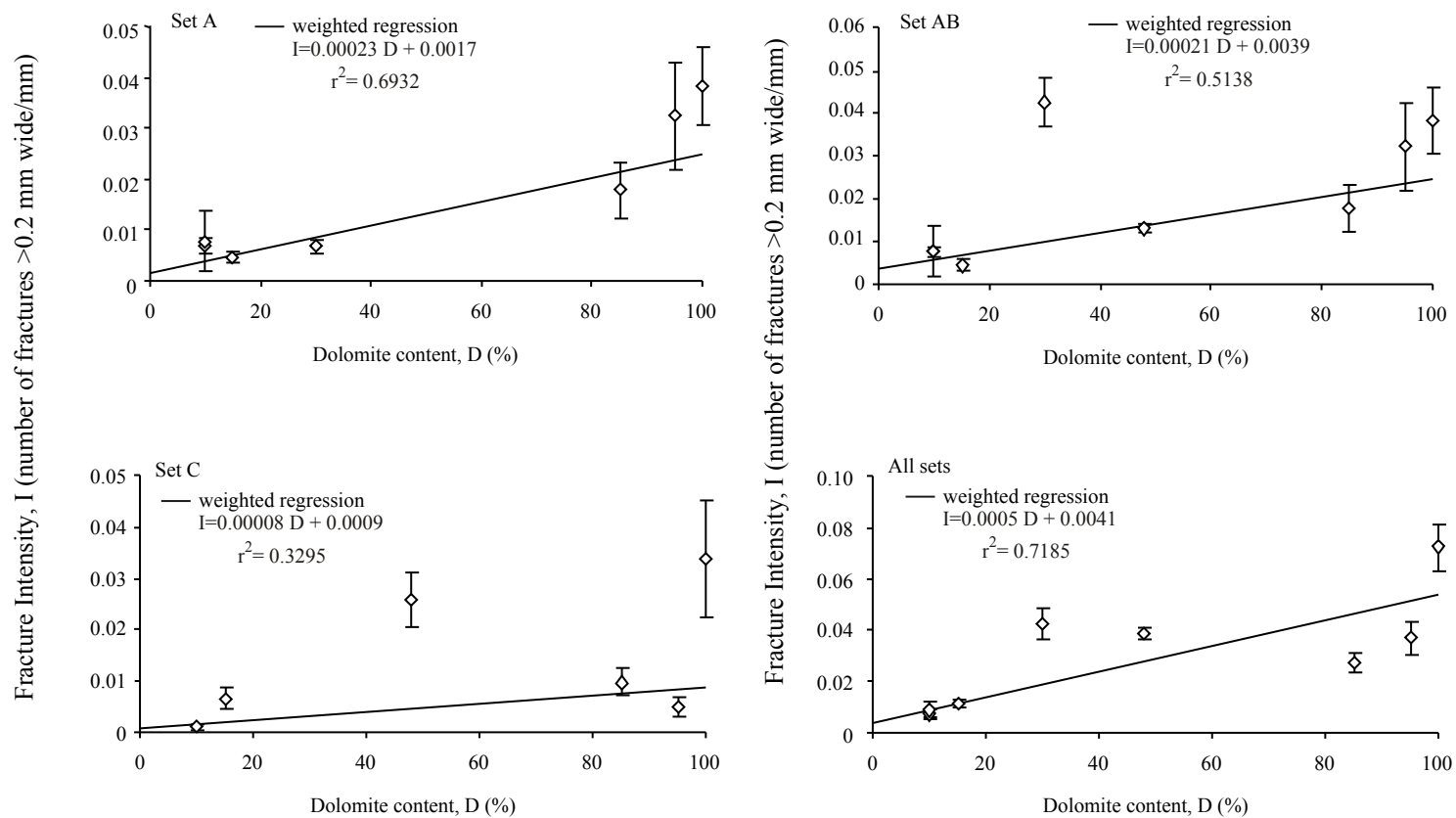


Figure 3.45. Control of dolomite content on fracture intensity, Las Palmas Canyon. Weighted Linear regressions to total and individual set fracture intensities suggest a positive correlation between dolomite content and fracture intensity.

correlation from the same number of data points representing unrelated variables (Young, 1962). Linear regression to combined sets A and B yields a positive correlation between fracture intensity and dolomite content and a coefficient of determination ($r^2=0.51$), based on seven beds that suggests a similar degree of correlation as set A alone. A positive correlation between fracture intensity and dolomite content was also found for set C. The coefficient of determination for set C is weak ($r^2=0.33$) based on fracture intensity determinations in 7 beds. There is approximately a 10% probability of obtaining this coefficient of determination from seven data points of unrelated variables (Young, 1962).

La Escalera

La Escalera data also suggest a positive correlation between fracture intensity and dolomite content (Fig. 3.46). Coefficients of determinations from data at La Escalera are similar to those from Las Palmas. Different degrees of dolomitization are present at Las Palmas Canyon, but at La Escalera most beds are highly dolomitized and there is only sparse control for weakly dolomitized beds. Petrographic work in La Escalera and Las Palmas samples suggests that the assumption that all dolomite predates or is synchronous with fracturing might be incorrect and may explain the scatter of the data in both localities. The coefficient of determination for independent sets A and B at La Escalera are $r^2=0.4586$ and $r^2=0.7404$ respectively, determined in nine and eleven beds respectively. There is less than a 5% probability of obtaining the degree of correlation found for set A from uncorrelated variables, and the probability is less than a fraction of a percent

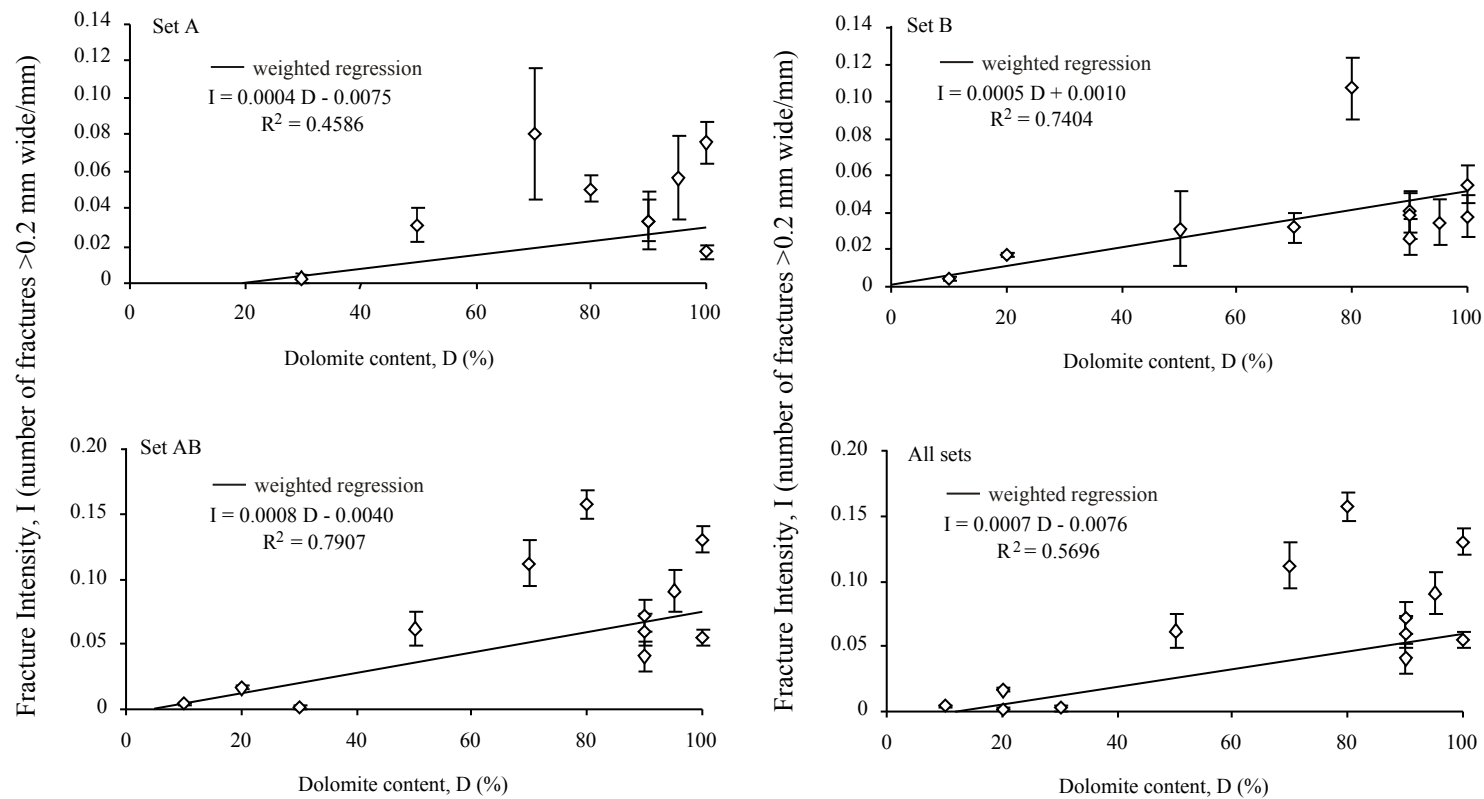


Figure 3.46. Control of dolomite content on fracture intensity, La Escalera Canyon. Weighted linear regressions suggest a positive correlation between dolomite content and fracture intensity. Most beds studied at La Escalera contain more than 50% of dolomite.

for set B. The coefficients of determination for combined sets A and B and all sets are also high ($r^2=0.7907$ and $r^2=0.5696$, respectively), suggesting a definite and consistent correlation between fracture intensity and degree of dolomitization.

El Chorro

Dolomite content at El Chorro locality is greater than 30% in four beds studied and is very low in the other four beds, some of which show indications of dedolomitization in cathodoluminescence images and etched thin sections (Folk, 2002, personal communication). Dolomite content vs fracture intensity analyses of four dolomitized beds are consistent with the results obtained in Las Palmas and La Escalera, suggesting a positive correlation between fracture intensity and dolomite content (Fig. 3.47). The coefficient of determination is moderately high and similar for set A ($r^2=0.5032$), combined sets AB ($r^2=0.5495$), and total intensity combining all sets ($r^2=0.5290$). These coefficients of determination do not allow high confidence in the correlation of the variables studied (Young, 1962), but their consistent behavior, similar to Las Palmas and La Escalera results, improves the degree of confidence for a correlation between dolomite content and fracture intensity. Weighted regression to only three points from set C yields a very high coefficient of determination ($r^2=0.9276$), however this value is not high enough to indicate less than a 10% probability of correlation by chance. The coefficient of determination for a weighted regression to set B is also high (not shown in Figure 3.47) and the regression suggests the same relationship between dolomite content and fracture intensity indicated by other fracture sets at

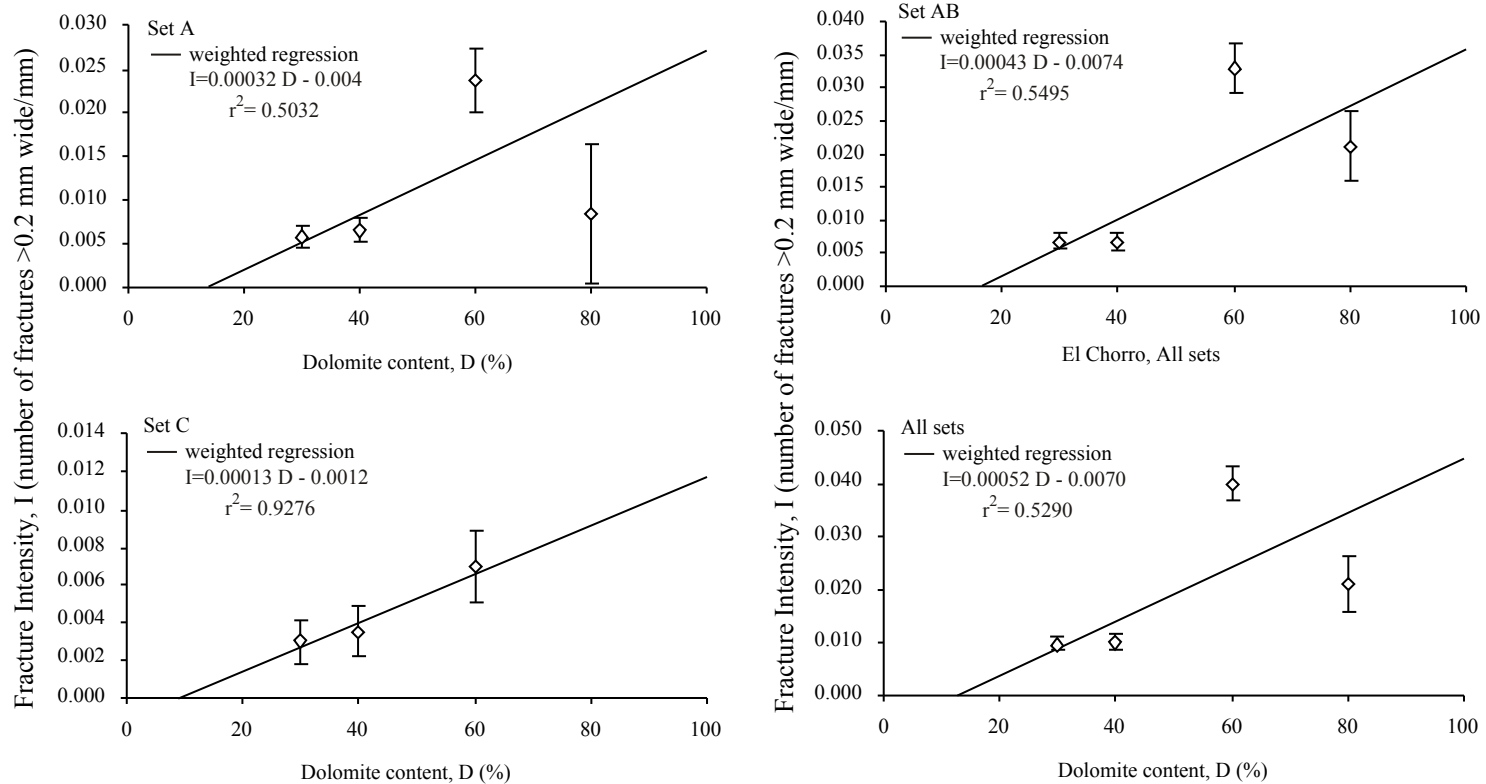


Figure 3.47. Control of dolomite content on fracture intensity, El Chorro Canyon. Weighted linear regressions to limited data points suggests increase of fracture intensity with increase of dolomite content.

this and other localities, but only three data points are available for this regression and the result is probably not statistically significant.

Consistency in the relationship between dolomite content and fracture intensity and moderately high to high coefficients of determination suggests that dolomite content and fracture intensity are systematically related. This relationship and the presence of synkinematic dolomite in the fractures suggest that fracturing and dolomitization are linked processes, indicating that one causes the other or one is a prerequisite for the other to occur.

CYCLOSTRATIGRAPHIC CONTROL ON FRACTURE INTENSITY

The stratigraphic sections studied were subdivided in fifth order sedimentary cycles (parasequences) following the methodology illustrated by Goldhammer et al. (1991) in his section at Potrero Garcia, to the north of the study area. Most parasequences are composed of subtidal facies at the base and peritidal facies on top. Subtidal cycles are generally devoid of peritidal sedimentary facies.

Fracture intensity in beds generally increases toward the top of the parasequences (Figs. 3.48 and 3.49). The degree of dolomitization increases upward in a similar fashion within the parasequences (Figs. 3.48 and 3.49). Moldovanyi and Lohman (1984) described similar distributions of dolomite content in the United States for Sligo Formation sequences that are lateral correlatives of Cupido Formation. In most cases, cycles that do not show this

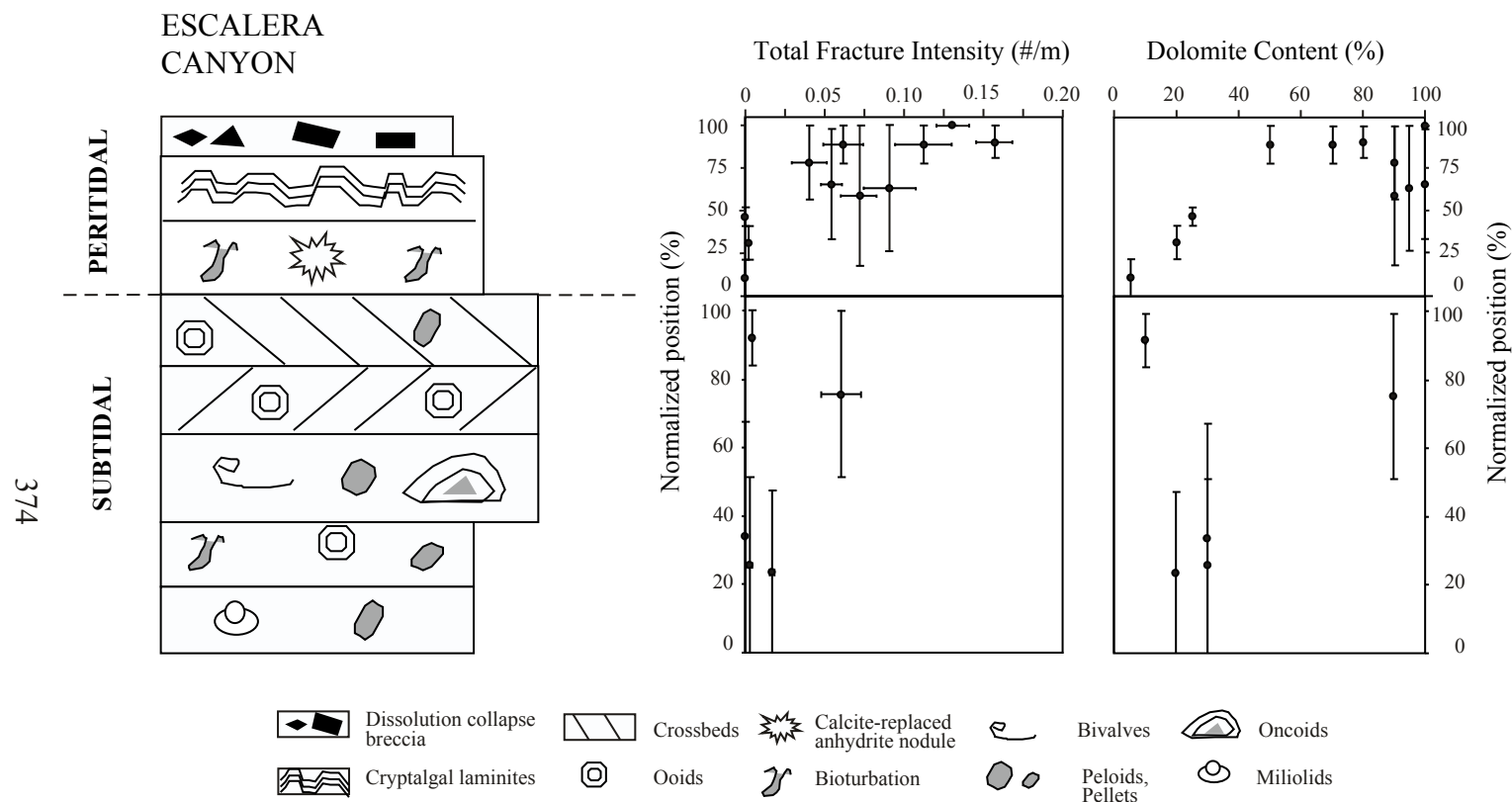


Figure 3.48. Schematic distribution of fracture intensity and degree of dolomitization in peritidal and subtidal parasequences at La Escalera Canyon. For most parasequences an increase in dolomitization toward the top of the parasequence is accompanied by an increase in fracture intensity. Some cycles do not show this behavior, however, and in many of these anomalous cycles peritidal facies are absent at the parasequence top. Type cycles after Goldhammer et al. (1991). Fracture intensity was calculated as the total number of fractures with aperture larger than 0.2 mm per meter of scanline.

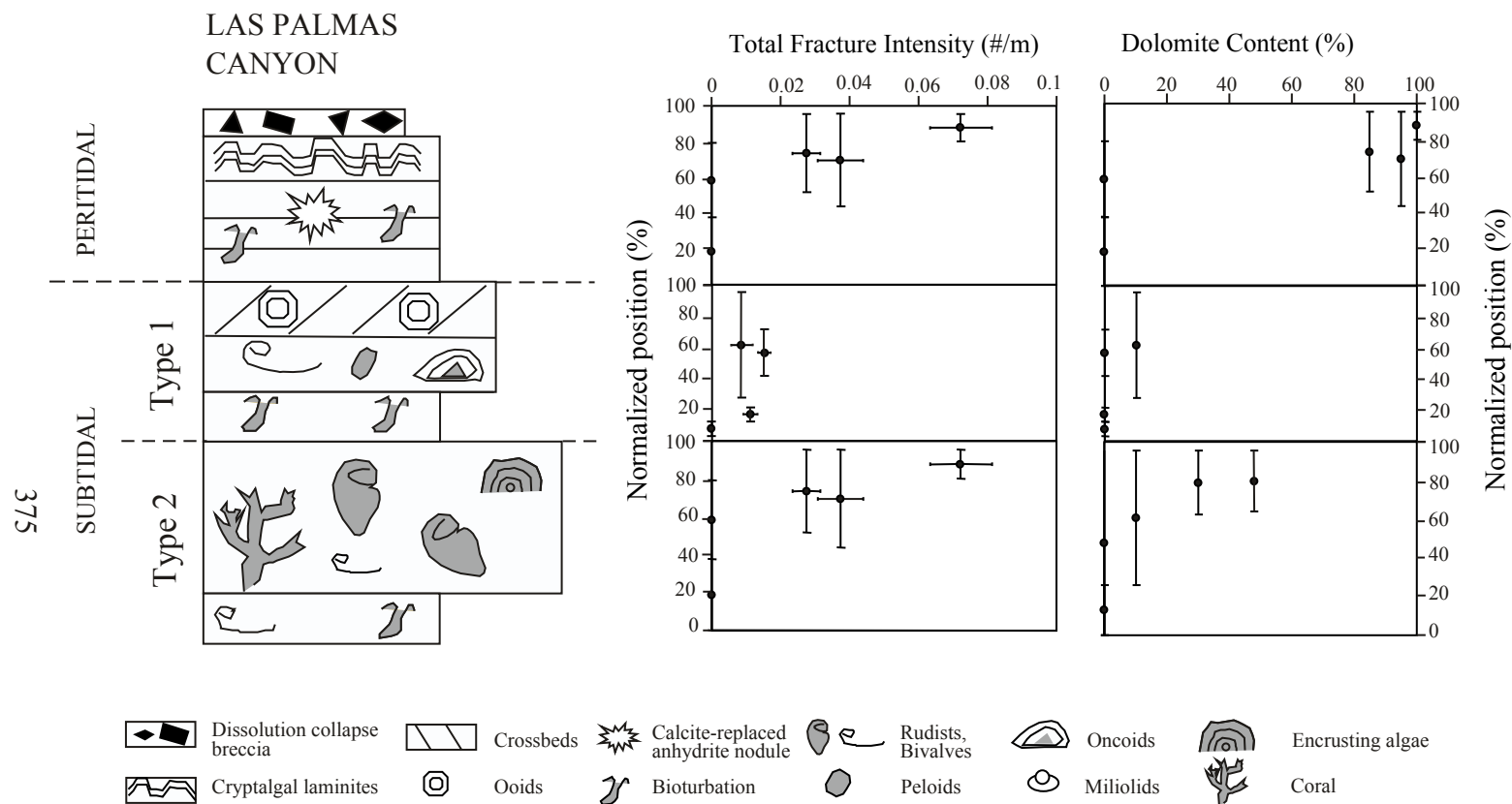


Figure 3.49. Fracture intensity and dolomite distribution in peritidal and subtidal parasequences at Las Palmas Canyon. Two kinds of subtidal cycles are present at Las Palmas locality: subtidal cycles capped by grainstone shoal deposits, and subtidal cycles capped by bioherms or bivalve banks. Fracture intensity increases toward the top of cycles and correlates with an augment of dolomitization. Under-sampling explains why subtidal cycles capped by grainstones do not show observed fracture intensity pattern in these graphs. Type cycles after Goldhammer et al. (1991). Fracture intensity was calculated as the total number of fractures with aperture larger than 0.2 mm per meter of scanline.

pattern of fracture intensity lack peritidal facies on top. Consequently, peritidal cycles (as defined by Goldhammer et al., 1991) have higher probability of showing fractures than subtidal cycles. Some subtidal cycles capped by grainstone shoals or bivalve banks do not show an increase of fracture intensity toward the top of the parasequence. Subtidal cycles with no fractured layers lack dolostone caps. Organization of fifth order cycles in fourth and third order cycles also suggest that parasequences lacking dolomitized caps occur in transgressive system tracks. An example of this cyclic hierarchy can be interpreted for the middle part of Las Palmas locality (Appendix 3.G), composed by a succession of subtidal cycles capped by grainstone shoals and/or rudist bioherms and mostly barren of fractures.

These observations can be integrated in a fracture-diagenetic-cyclostratigraphic model. During deposition of a typical parasequence cycle, the top of the parasequence was deposited in an evaporative environment with hypersaline waters. Reflux of marine waters and concentration of magnesium in pore space at the top of the parasequence led to early dolomitization. Peritidal facies are favored by dolomitization but the dolomitization front sometimes extended to include subtidal facies below (Morrow, 1982), particularly in thin parasequences. This may explain why there is no absolute correlation between fracture intensity and sedimentary facies or mud content. Similarly, bed thickness does not seem to play a dominant role on fracture intensity when topologic artifacts are taken into account.

On the other hand, mechanical layer thickness is probably determined by a combination of variables that includes sedimentary facies, porosity, permeability and the thickness of the dolomitized zone. Degree of dolomitization probably dominated the mechanical properties of the layer and determined first-order degree of fracturing. However, analyses of fracture intensity and bed thickness in dolostones from La Escalera, Las Palmas and El Chorro suggest that bed thickness exerts very poor (if any) effect on observed fracture intensity.

Early dolomitization probably made parasequence tops more brittle than the surrounding mud-supported subtidal facies and possibly unconsolidated grainstones. Adjacent non-dolomitized beds could deform ductily by distributed grain boundary sliding, whereas dolomitized layers were more cemented and deformed brittly. After early dolomitization at the top of the parasequence, subsequent dolomitization events at greater burial conditions may have focused on these beds containing previously formed dolomite crystals. Partly open fractures in early dolomitized beds also may have constituted high permeability conduits necessary for circulation of large volumes of dolomitizing fluids. Focused dolomitization probably continued throughout most of the burial history of these early-dolomitized layers. Other dolomitization models like the water-mixing model (Morrow, 1982) may explain continued growth of dolomite crystals in early-dolomitized layers. Isotopic analysis (Monroy et al., 2001) probably reflects a continued process of dolomitization throughout the burial history of Cupido Formation (Morrow, 1982).

Correlation between stratigraphic variables

Previous sections evaluated the control of stratigraphic variables on fracture intensity in limestones and dolostones of Cupido and Tamaulipas Inferior formations. Those analyses assumed that fracture intensity is the dependent variable whereas dolomite content, sedimentary facies, normalized position of the bed in the stratigraphic cycle, and bed thickness are the independent variables. Results of separate bivariate analyses of one independent and the dependent variables suggested some degree of correlation between some these stratigraphic variables and fracture intensity. The degree of correlation was not very high in most situations and an important degree of data dispersion was obtained for most scatter plots. Data scatter and marginal coefficients of determination may be a result of multiple sources such as insufficient number of beds studied, insufficient number of fracture measurements for some beds and some fracture sets, influence of unknown variables, and combined influence of different (correlated or not) stratigraphic variables. In this section the degree of correlation between the “independent” variables (i.e., stratigraphic controls) is analyzed.

Dolomite content, normalized position in the parasequence, and mud content show a significant degree of correlation among themselves (Fig. 3.50). This degree of correlation can be explained by early dolomitization initially controlled by hypersaline reflux, affecting primarily intertidal mudstones and shallow subtidal facies close to the intertidal areas. Some beds of subtidal origin were affected by dolomitization but some are not. This inconsistent relationship between degree of dolomitization and environment of deposition explains in part

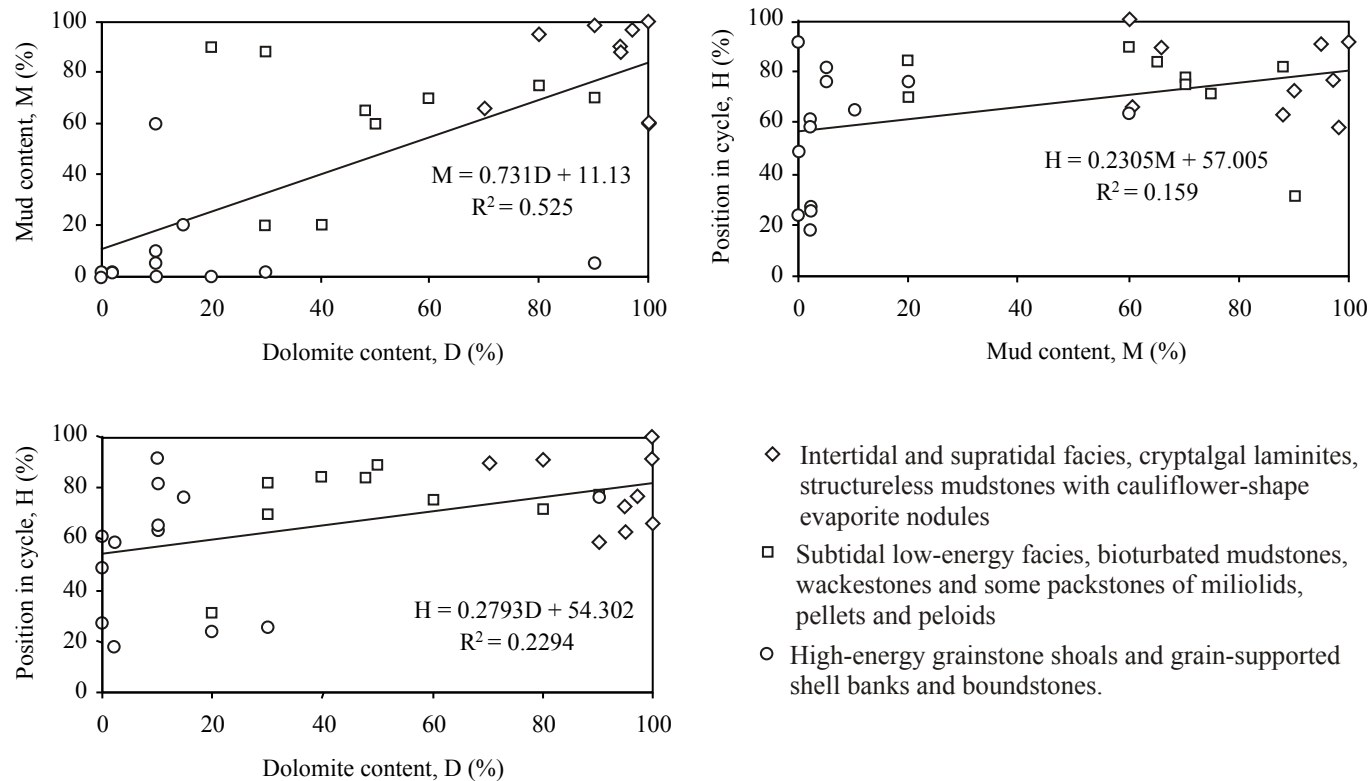


Figure 3.50. Correlation analysis between stratigraphic variables. Regressions suggest a positive correlation between dolomite content, mud content and stratigraphic position. All coefficients of determination imply statistically significant correlation between these variables. Intertidal mudstones are preferentially dolomitized and also found at the top of parasequences. Subtidal mud-bearing rocks have less tendency to dolomitization, and subtidal grainstones and rudist shoals are characterized by even lower dolomite content.

the dispersion in the data. Figure 3.45 also shows the interpreted environment of deposition for the beds studied. Inspection of these graphs suggests that there is also a correlation between the environment of deposition, degree of dolomitization, mud content and position of the bed in the parasequence. Intertidal mudstones at the top of parasequence cycles are commonly dolomitized and have high probability of displaying high fracture intensity.

Correlation of bed thickness and the previous three variables is poor (Fig 3.51). This result was expected from the results obtained by bivariate analysis of bed thickness and fracture intensity.

MULTIVARIATE ANALYSIS

Virtually all geological data are inherently multivariate in nature. For example, multiple variables are necessary for a complete description of the most simple geological objects. In many situations, however, we can justify our focus on bivariate analyses of relevant variables. In previous sections I studied the effects of individual stratigraphic controls (i.e., independent variables) on fracture intensity (i.e., dependent variable), and the dispersion of the data around weighted regression lines was evaluated using scatter diagrams. Results of these analyses indicated strong positive correlation of fracture intensity with dolomite content and normalized position of the bed in fifth order stratigraphic cycles. Moderate-to-good positive correlation was found between fracture intensity and mud content in some cases. The previous section explored the degree of correlation among pairs of stratigraphic variables, indicating that dolomite content, mud

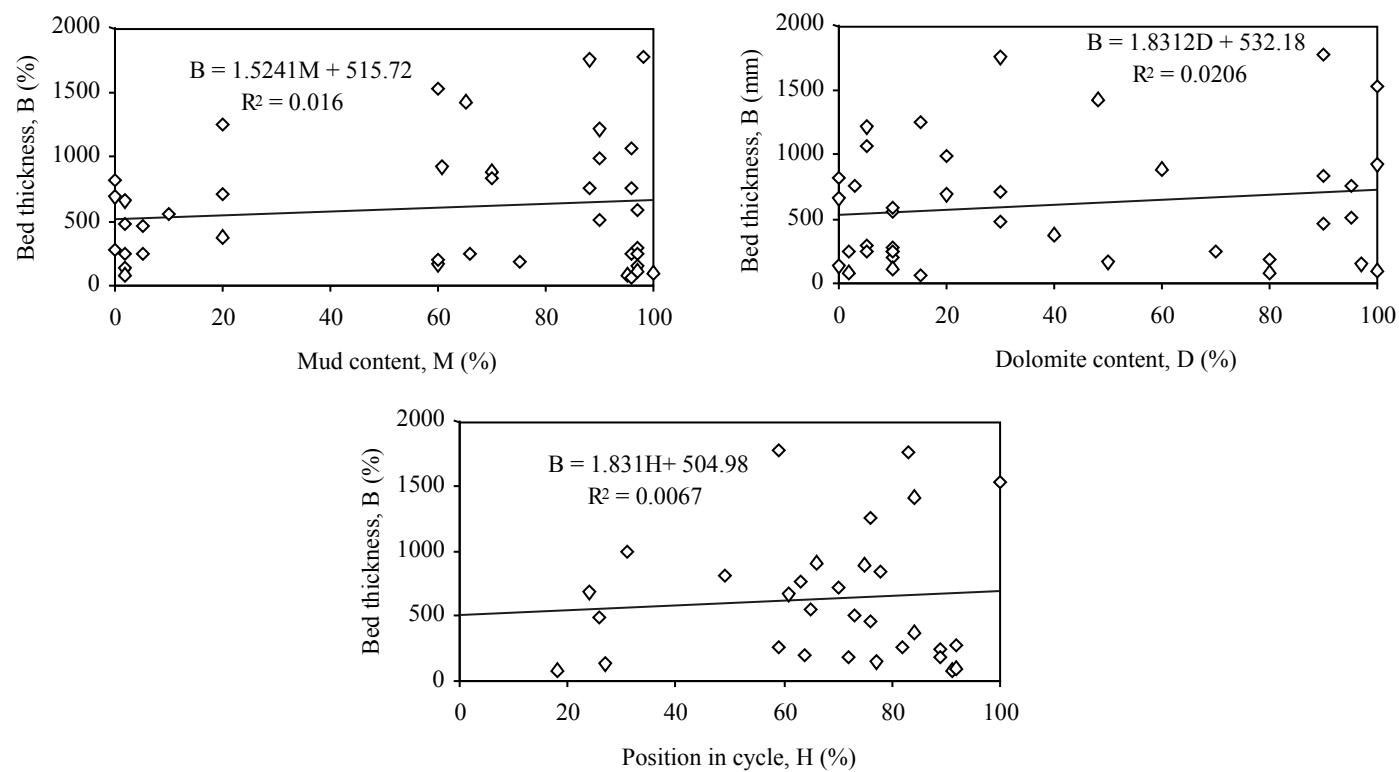


Figure 3.51. Correlation test between bed thickness and other stratigraphic variables. No significant correlation was found between bed thickness and other stratigraphic variables studied.

content and position of the bed within a stratigraphic cycle are correlated to certain degree. Bed thickness, however, does not show a statistically significant correlation with other stratigraphic variables. Correlation among “independent” variables is an indication of the need for multivariate techniques to study the data (Swan and Sandilands, 1995). Multivariate analysis was used to simultaneously evaluate the effects of stratigraphic controls on fracture intensity in Cupido and Tamaulipas Inferior formations. Most results are shown and discussed in numerical form because graphical representation of multidimensional data and graphical display of multivariate results are challenging.

Two multivariate techniques were found amenable to the objectives of this investigation: multiple regression and principal component and factor analysis (Swan and Sandilands, 1995). The goal of multiple regression analysis is to find and test the best fit equation that describes the relationship between a dependent variable (i.e., fracture intensity) and a number of independent variables (e.g., bed thickness). Principal component analysis explores the directions of maximum variance in the data and evaluates the degree of influence of a number of variables on the data. Multiple linear regression was chosen because of its easy implementation. The model used for the regression is:

$$Y = \beta_0 + \sum_{i=1}^I \beta_i X^{(i)} + \varepsilon$$

where $X^{(i)}$ is a set of independent variables, Y is the dependent variable and I is the total number of variables considered. The linear coefficients (β) of these equations can be found solving the I set of equations:

$$\begin{bmatrix} \text{Cov}(\mathbf{X}^{(1)}, \mathbf{X}^{(1)}) & \dots & \text{Cov}(\mathbf{X}^{(1)}, \mathbf{X}^{(I)}) \\ \vdots & \ddots & \vdots \\ \text{Cov}(\mathbf{X}^{(I)}, \mathbf{X}^{(1)}) & \dots & \text{Cov}(\mathbf{X}^{(I)}, \mathbf{X}^{(I)}) \end{bmatrix} \begin{bmatrix} \beta_1 \\ \vdots \\ \beta_I \end{bmatrix} = \begin{bmatrix} \text{Cov}(\mathbf{X}^{(1)}, \mathbf{Y}) \\ \vdots \\ \text{Cov}(\mathbf{X}^{(I)}, \mathbf{Y}) \end{bmatrix}$$

I assumed that the independent variables are independent of each other to simplify the calculations. This method can be justified because our interest is to investigate the effect of stratigraphic variables on fracture intensity and not to make predictions of the fracture intensity from specific values of stratigraphic variables. Positive dependence among independent variables will likely favor their effect on the independent variable. If the influence of a variable can be found by considering it independent of the others, then we will find better grounds to demonstrate its influence on the dependent variable. The *Regression* function in Microsoft Excel[®] was used to generate statistics and linear coefficients of the multiple regression.

Multiple linear regression

Multiple regression analysis to 40 beds yields results similar to those obtained from bivariate analyses, and reinforce some of the preliminary conclusions derived from the limited number of data. Small numbers of beds were usually available for bivariate regressions because I isolated not only the structural and locality variables, but also each variable was analyzed maintaining other variables approximately constant. Four variables were included in the multivariate analysis: dolomite content, mud content, position of the bed in the

stratigraphic cycle and bed thickness. In multiple linear regression analysis it is recommended to exclude variables that are known to have little effect on fracture intensity, for example bed thickness in this case. However, the bed thickness effect on fracture intensity is an important paradigm so this variable was included in the analysis also.

Table 3.10 contains the results of multiple regression analysis on total fracture intensity. The coefficient of determination of this multiple regression is $r^2=0.4660$ for the total fracture intensity in 40 beds. The F-test (Swan and Sandilands, 1995) suggests a reliable correlation between independent and dependent variables. There is less than a 1% probability of obtaining this coefficient of determination in a multiple regression between the same numbers of unrelated variables. Independent variable coefficients suggest that dolomite content is the most significant control on fracture intensity. Results of T-test (Swan and Sandilands, 1995) for dolomite content ($T=2.86$) suggest less than a 1% probability of casting doubts on the reliability of this coefficient determination. Normalized position of a bed in a stratigraphic cycle is similar in importance to dolomite content for determining fracture intensity in the bed. This degree of control on fracture intensity by normalized position of the bed in a cycle reflects the correlation observed between dolomite content and normalized position. T-test on normalized position yields $T=2.78$, suggesting that the determination of the coefficient of determination is reliable. Mud content is marginally important in the determination of total fracture intensity. T-test on mud content ($T=1.61$) suggests more than a 10% probability of spurious

Table 3.10. Summary output of multiple linear regression analysis for total fracture intensity and stratigraphic variables. F value allows rejection of the null hypothesis, assuring a statistically significant relationship between the independent variables and the dependent variable, fracture intensity. T-tests suggest that there is a statistically significant correlation between fracture intensity, dolomite content, position of bed in cycle and mud content with less than 0.5% probability of correlation by chance between unrelated variables. Bed thickness influence in fracture intensity is negligible.

Regression Statistics	
Multiple R	0.682644663
R Square	0.466003736
Adjusted R Square	0.404975591
Standard Error	0.027759922
Observations	40

ANOVA					
	df	SS	MS	F	Significance F
Regression	4	0.02353725	0.005884	7.635882	0.000156164
Residual	35	0.026971465	0.000771		
Total	39	0.050508714			

	Coefficients	Standard Error	t Stat	P-value	Lower 95%	Upper 95%
Intercept	-0.02881704	0.015525799	-1.85607	0.071878	-0.060336131	0.002702
Dolomite	0.000382674	0.000133816	2.859702	0.007102	0.000111013	0.000654
Mud	0.000183544	0.000113896	1.611499	0.116054	-4.76784E -05	0.000415
Position	0.000653642	0.000235163	2.779525	0.008699	0.000176235	0.001131
Thickness	-3.6505E -06	9.60945E -06	-0.37988	0.706328	-2.31587E -05	1.59E -05

significance of this multiple regression coefficient. The linear regression coefficient for bed thickness suggests negligible effect of bed thickness on fracture intensity ($\beta_B = -3.6 \times 10^{-6}$). Dispersion in the fracture intensity versus bed thickness space is probably high, as suggested by the T-test value ($T = -0.38$).

Multivariate analysis to total fracture intensity includes results from fracture set D, which in some localities is interpreted as related to fold formation. Including this set in the multivariate analysis is possibly inappropriate because the structural variable was not quantified. Fracture sets A, B and C possibly formed before folding during shallow to deep burial of the sedimentary pile. Results of fracture intensity in these sets can be reliably studied as a group, although they are associated with different localities and structural positions. Total fracture intensity for the combination of these sets is possibly a better indication of reliable stratigraphic controls on fracture intensity. Results of multivariate analysis of the combined sets A, B and C are shown in Table 3.11.

Multiple linear regression coefficients of determination suggest a reliable correlation between the variables considered and fracture intensity. F-test suggests high confidence in the coefficient of determination with negligible (i.e., less than 0.1%) probability of similar degree of correlation by chance. Dolomite content is the most important factor influencing fracture intensity and contributes nearly 60% of the effect on fracture intensity. T-test on dolomite content suggests that there is more than 99% confidence in the determination of this coefficient. Normalized position in the stratigraphic cycle is also an important parameter determining fracture intensity. T-test suggests a confidence level of 93%. Mud

Table 3.11. Summary output of multiple linear regression analysis for combined sets A, B and C fracture intensity and stratigraphic variables. Fracture sets A, B, and C most probably formed before folding. F value allows rejection of the null hypothesis (i.e., no correlation) with less than 1% probability of obtaining these coefficients of determination by chance. T-tests suggest that there is a statistically significant correlation between fracture intensity, dolomite content, and position of bed in cycle with more than 95% reliability in the coefficients of determination. Mud content and bed thickness T-test statistics suggest poor and negligible correlation with fracture intensity, respectively.

Regression Statistics	
Multiple R	0.706575302
R Square	0.499248657
Adjusted R Square	0.442019932
Standard Error	0.026881915
Observations	40

ANOVA					
	df	SS	MS	F	Significance F
Regression	4	0.025216408	0.006304	8.723742	5.39269E -05
Residual	35	0.025292306	0.000723		
Total	39	0.050508714			

	Coefficients	Standard Error	t Stat	P-value	Lower 95%	Upper 95%
Intercept	-0.015247584	0.015889148	-0.95962	0.343828	-0.047504309	0.017009141
Dolomite	0.000482164	0.000145085	3.323323	0.002093	0.000187626	0.000776703
Mud	4.80423E -05	0.000114394	0.419973	0.677073	-0.00018419	0.000280275
Position	0.000466252	0.000249756	1.866828	0.070321	-4.07809E -05	0.000973285
Thickness	-1.68959E -07	9.12855E -06	-0.01851	0.985338	-1.87009E -05	1.8363E -05

content is poorly correlated with fracture intensity of combined sets ABC. There is more than 35% probability of unreliable determination of this coefficient as suggested by the T-test, also suggesting high dispersion of the data in the fracture intensity-mud content space. Bed thickness does not have an important effect on the intensity observed and the determination of the coefficient is unreliable, with more than 98% probability of obtaining a similar coefficient from uncorrelated variables.

Multiple regression analysis was also carried out on combined sets AB and set C separately (Tables 3.12 and 3.13) as well as for total fracture intensity at La Escalera Canyon (Table 3.14). La Escalera Canyon was selected because a greater number of beds were studied at this locality than at other localities. Results are similar to the ones reported in Tables 3.10 and 3.11 but the degree of correlation is lower and the coefficients are less reliable. Results using data from other localities yielded contradictory and unreliable results and they are not shown here. Scarce data is the most probable explanation for inconsistent results from other localities except for La Escalera Canyon. Multivariate regression with more abundant data from all localities for total, sets ABC, AB, and C, showed consistent results, indicating the same relative importance of stratigraphic controls on the fracture intensity observed.

CONCLUSIONS

Fracture intensity values vary with observation scale. Comparison of fracture intensities among volumes of rock requires a normalization of fracture

Table 3.12. Summary output of multiple linear regression analysis for combined sets AB intensity and stratigraphic variables. Fracture sets A and B are most probably conjugate sets that formed before folding. Analysis of these sets as a population is justified based on fracture timing at La Escalera, Las Palmas and El Chorro. F value allows rejection of the null hypothesis (i.e., no correlation) with less than 2.4% probability of obtaining these coefficients of determination by chance. T-tests suggest that there is a statistically significant correlation between fracture intensity and dolomite content with more than 90% reliability in the determination of this coefficient of multiple linear regression. Regression coefficients suggest that position in cycle is the second most important control on fracture intensity. Mud content and bed thickness T-test statistics suggest poor and negligible correlation with fracture intensity, respectively.

Regression Statistics	
Multiple R	0.684446617
R Square	0.468467172
Adjusted R Square	0.40403895
Standard Error	0.029950927
Observations	38

ANOVA					
	df	SS	MS	F	Significance F
Regression	4	0.026090568	0.006523	7.271149	0.000258372
Residual	33	0.029602914	0.000897		
Total	37	0.055693482			

	Coefficients	Standard Error	t Stat	P-value	Lower 95%	Upper 95%
Intercept	-0.012149566	0.013205215	-0.92006	0.364219	-0.039015799	0.014716667
Dolomite	0.000526475	0.000186909	2.81675	0.008128	0.000146206	0.000906743
Mud	-9.54841E -06	0.00016944	-0.05635	0.955401	-0.000354278	0.000335181
Position	0.000349837	0.000224895	1.555557	0.129353	-0.000107715	0.000807388
Thickness	1.32545E -06	1.07904E -05	0.122835	0.902982	-2.06279E -05	2.32788E -05

Table 3.13. Summary output of multiple linear regression analysis for set C intensity and stratigraphic variables. Fracture set C F value does not allow rejection of the null hypothesis (i.e., no correlation) with more than 30% probability of obtaining these coefficients of determination by chance. T-tests suggest poor reliability in the determination of coefficient of multiple linear regression for dolomite, mud content and bed thickness. T test for normalized position suggests that this parameter exerts the greatest control on fracture intensity distribution observed at this locality. Some grainstone beds show evidences of dedolomitization which may explain in part a lack of correlation of fracture intensity and dolomite content.

Regression Statistics	
Multiple R	0.59813175
R Square	0.35776159
Adjusted R Square	0.100866226
Standard Error	0.008769615
Observations	15

ANOVA					
	df	SS	MS	F	Significance F
Regression	4	0.000428409	0.000107	1.392635	0.304719317
Residual	10	0.000769061	7.69E -05		
Total	14	0.00119747			

	Coefficients	Standard Error	t Stat	P-value	Lower 95%	Upper 95%
Intercept	-0.00462508	0.007582293	-0.60998	0.55548	-0.02151948	0.01226933
Dolomite	-3.4839E -05	0.00016058	-0.21696	0.832605	-0.000392634	0.000322956
Mud	9.69374E -05	0.000128331	0.755372	0.467444	-0.000189001	0.000382876
Position	0.000186275	0.000128501	1.449605	0.177795	-0.000100042	0.000472592
Thickness	-2.2757E -06	6.83288E -06	-0.33305	0.745976	-1.75003E -05	1.29489E -05

Table 3.14. Summary output of multiple linear regression analysis for total fracture intensity and stratigraphic variables, La Escalera Canyon. F-test allows rejection of the null hypothesis and suggests that there is correlation between the variables indicated and fracture intensity. T-tests for individual variables suggest that there is moderate to good correlation between fracture intensity, dolomite content, position of bed in cycle and mud content (0.5% probability of degree of correlation by chance between unrelated variables for this degree of freedom is 1.78). Bed thickness influence in fracture intensity is negligible.

Regression Statistics	
Multiple R	0.836379865
R Square	0.699531279
Adjusted R Square	0.549296918
Standard Error	0.033663776
Observations	13

ANOVA					
	df	SS	MS	F	Significance F
Regression	4	0.021106854	0.005277	4.656267	0.0309575
Residual	8	0.009065999	0.001133		
Total	12	0.030172853			

	Coefficients	Standard Error	t Stat	P-value	Lower 95%	Upper 95%
Intercept	-0.031943797	0.032652351	-0.9783	0.356579	-0.1072403	0.043353
Dolomite	0.000681577	0.000400271	1.702788	0.127016	-0.0002415	0.001605
Mud	0.000403448	0.000301941	1.33618	0.218247	-0.0002928	0.0011
Position	0.00062178	0.000464777	1.337801	0.217742	-0.00045	0.001694
Thickness	-1.99132E -05	2.32744E -05	-0.85558	0.417115	-7.358E -05	3.38E -05

intensity values specifying a fracture size.

A study of normalized fracture intensity variations with facies, bed thickness and degree of dolomitization in Cupido and Tamaulipas formations suggests that only the degree of dolomitization is an important predictor of fracture intensity distribution. Degree of dolomitization is closely related to stratigraphic position of beds within fifth-order sequence stratigraphic cycle. These relationships were documented for individual and combined fracture sets in four different localities separated kilometers in between using bivariate weighted regressions and multivariate methods.

Normalized fracture intensity data allows rejection of the classic bed thickness-fracture spacing hypothesis, a long-standing paradigm in structural geology, at least for carbonates of the Sierra Madre Oriental. Commonly observed natural fracture scaling and topology principles suggest that results obtained from carbonates in the SMO have a more general application to fracture spacing/bed thickness relationships. A possible explanation of consistent bed thickness-fracture spacing results reported in the literature is given revealing a possible flaw in the traditional method of average fracture spacing determination.

Analyses of fracture textures support the hypothesis that dolomite precipitation and fracturing occurred, at least in part, synchronously in these rocks. Early dolomitization possibly controlled fracture initiation under shallow burial conditions. Fracturing possibly continued at greater depth as suggested by crack-seal textures and synkinematic dolomite precipitation. Preferential fracturing occurred in dolomitized beds at the top of fifth-order cycles. This

sequence-stratigraphic-diagenetic-fracturing model has potential use for fracture-system prediction in similar carbonate successions of other regions.

Appendices

Paper copies of this dissertation are kept at the Perry Castañeda Library, The University of Texas at Austin, and the Geology Library, Department of Geological Sciences, The University of Texas at Austin. These paper copies contain a CD with the appendices data in digital form. All appendices in this CD are in Portable Digital Format (PDF) viewable with Acrobat Reader, which is available for free at: <http://www.adobe.com>. Additional copies of the appendices in paper and digital form are kept by Dr. Randall Marrett (Supervisor, Department of Geological Sciences), archives of the Fracture Research and Application Consortium, Bureau of Economic Geology, The University of Texas at Austin, Dr. Stephen Laubach (Senior Research Scientist, Bureau of Economic Geology), and the author.

APPENDIX 1.A: OPENING MODE FRACTURE SCALING LITERATURE REVIEW

List of significant papers where opening mode scaling of fracture apertures and/or length are included. The table contains the author(s) and year of publication, the type of fracture studied, the fracture attributes measured or analyzed and fracture scaling results associated, aperture-length relationships (if available), and the mathematical model interpreted for the fracture size distribution, including the interpretation of changes in fracture scaling parameters

with observation scale. Some papers are based on data collected by other authors and in those cases the paper with the original data used has been indicated.

Fracture aperture and length distributions require collection of data from all the fractures observed in a two-dimensional or one-dimensional domain (e.g. scanline). Cumulative Number vs a fracture attribute is the most common representation of fracture size distribution found in the literature. Another type of size distribution representation used in early publications is frequency histograms. Fracture aperture/length relationships do not require systematic collection of data from all the fractures in the observation domain but rather selected fracture aperture/fracture length pairs that are then plotted in a log-log graph. The most common kind of size distribution interpreted for opening mode fracture attribute data is a power law model. Power law models interpreted from observations include a single power law for the entire range of observations and varying power law parameters with changes in observation scale. Some joint length studies produce size distributions best modeled by exponential or lognormal distributions.

APPENDIX 1.B: OBK-1 SAMPLES AND PETROGRAPHY

Summarizes the thin sections used in this case study, point count results, and percentages of major framework, matrix, and cement components. Also included is a triangle with Folk (1980) classification of sandstones.

APPENDIX 1.C: OBK-1 FRACTURE ORIENTATION DATA

Contain macrofracture (vein and fault) as well as stylolite orientation data collected from Ozona Blakeney Kruger No 1 well cores. Veins and stylolites orientations are described by their strike and dip, and faults orientation and kinematics are indicated by strike and dip of the fault surface, and the trend, plunge and sense of fault plane kinematic indicators.

APPENDIX 1.D: OBK-1 FRACTURE SIZE DATA

Contains microfracture and macrofracture data collected from SEM-CL photocollages and core samples from the Ozona Blakeney Kruger No 1 well. Each table contains a header that explains the unit where the data were collected, location, macro- or microfracture, core or SEM-CL, sample ID, orientation, notches, and size of the observation domain.

APPENDIX 2.A: WEBER SAMPLES AND PETROGRAPHY

Information about the samples collected in the field and from cores for the Weber Formation case study. Included in the tables is a list of thin sections used for petrographic and SEM-CL imaging. Also included are point count results (Laubach and Schwartz, unpublished, Fracture Research and Applications Consortium, The University of Texas at Austin).

APPENDIX 2.B: WEBER FRACTURE DATA

These tables contain microfracture data collected from SEM-CL photocollages from surface and subsurface samples, and. macrofracture data from outcrops. Each table contains a header that explains the unit where the data were collected, location, macro- or microfracture, core, outcrop or SEM-CL, sample ID, orientation, notches, and size of the observation domain.

APPENDIX 3.A: CUPIDO/TAMAULIPAS BEDS STUDIED AND SAMPLES

Summarizes field-based data from the beds selected for fracture intensity determinations as well as the samples and thin sections obtained from them. Beds were numbered and labeled in the field and this nomenclature has been retained throughout the study. Dolomite content corresponds to field based estimates from rock reaction to HCl. Dolomite values in the tables were callibrated using laboratory-based analyses and incorporating other sedimentary and stratigraphic information. Bed orientation is given following the right hand rule.

Samples were oriented in the field marking by north and the orientation of planar surfaces on the samples. Parallel- and perpendicular-to-bedding thin sections were cut prepared from some samples, although the majority of thin sections are parallel to bedding to facilitate observation and measurement of opening mode fractures at high angle to bedding.

APPENDIX 3.B.:CUPIDO/TAMAULIPAS PETROGRAPHIC DESCRIPTIONS

This appendix contains a table that summarizes petrographic observations of thin sections prepared from outcrop samples collected from Cupido and Tamaulipas Inferior formations in various study localities in the Sierra Madre Oriental. Only major grain groups are included. Marine cements are described as isopachous (grain coating), and blocky (pore filling) when recognizable. Dolomite percentages include all dolomite present in the sample with no timing distinction.

APPENDIX 3.C.: CUPIDO/TAMAULIPAS FRACTURE ORIENTATION DATA

The orientations of representative fractures belonging to fracture sets and subsets present in beds studied as well as other beds in study localities are contained in this appendix. Fracture orientations are given according to the right hand rule. In the right hand rule format the orientation of a planar surface is specified using a strike azimuth and the dip of the plane. Strike azimuth is such that dip is to the right of the strike azimuth when facing strike direction. Fracture set nomenclature is as follows: 1) the two first letters identify the locality: LP: Las Palmas Canyon, CH: El Chorro Canyon, ES: La Escalera Canyon, and IT: Iturbide; 2) the following letters identify the fracture set as interpreted in the field. Some fracture sets show overlapping orientations when plotted on a stereographic projection but are readily distinguished in the field based on crosscutting

relationships, fracture fill, fracture morphology, and systematic orientation with respect to bedding.

Information about bed number, crosscutting relationships with other fracture sets, and fracture fill are also included in the tables.

APPENDIX 3.D.: CUPIDO/TAMAULIPAS FRACTURE SIZE DATA

These tables contain the fracture aperture data collected along scanlines drawn perpendicular to the main fracture sets in beds selected for study. The fracture number indicates the position of the fracture along the scanline. Fracture apertures are given in mm and correspond to the kinematic aperture of fractures (opening displacement of fracture walls). Fractures were measured with a fracture width comparator and the help of a hand lens (see Chapter 3, Methodology). Every table is preceded by data pertaining to the fracture set studied, including formation, bed number, fracture set, samples associated with it, thin sections cut, orientation of sample relative to bedding, orientation of sample notch relative to north, and scanline length.

APPENDIX 3.E.: CUPIDO/TAMAULIPAS FRACTURE APERTURE DISTRIBUTIONS

Compilation of fracture aperture size distributions discussed in Chapter 3. All graphs are log-log plots of cumulative fracture frequency versus fracture aperture. The cumulative frequency represents the number of fractures with a

given aperture or larger in a mm length of rock perpendicular to a fracture set, calculated as the observed cumulative number divided by the length of the scanline. Apertures are expressed in millimeters. Plots show least-squares power-law regressions to the distributions in graphic and algebraic form. Power-law models were derived from bias models following Marrett (2000) when possible. There are alternative models for observed one-dimensionally sampled aperture, but only preferred interpretations are included. An arrow indicates normalized fracture intensities for fracture apertures greater than 0.2 mm. These normalized intensity values, and their corresponding standard deviations (Appendix 3.F) are the basis of the correlation procedures and multivariate analysis discussed in Chapter 3.

APPENDIX 3.F.: CUPIDO/TAMAULIPAS NORMALIZED FRACTURE INTENSITY ERROR ANALYSIS

These graphs present the variation of normalized intensity for fractures with an aperture of 0.2 mm or larger, calculated as the cumulative number of fractures of that size or larger divided by the scanline length as the collection of fractures progresses along the scanline. Note that the normalized fracture intensity is plotted against the fracture number along the scanline and not the distance along the scanline. Fracture number one is the first fracture measured along the scanline. Fractures are consecutively numbered up to the last one measured at the end of the scanline. The axis of the abscissas can also be thought of as average spacing times the number of fractures observed.

The graphs also include the standard deviation of the normalized fracture intensity estimate as new fractures larger than 0.2 mm aperture are encountered along the scanline. The standard deviation is the square root of the variance of the fracture intensity estimates obtained up to a given fracture larger than 0.2 mm along the scanline. The right-end values of the graph represent the final estimates. Circles indicate the frequency estimated by fitting a power-law distribution model to selected one-dimensionally sampled fractures (Appendix 3.E).

Variations in the standard error of normalized fracture intensity along the scanline provide information about the reliability of fracture intensity estimates. The behavior of the fracture frequency (fracture intensity) curve also suggests clustering or anticlustering of fractures with apertures larger than 0.2 mm in aperture size. For example, if fracture intensity goes up consistently this might indicate spatial concentration of fractures in this portion of the scanline. If fracture intensity remains stable it probably indicates lack of spatial concentration (i.e. anticlustering). Reduction of the standard deviation at the end of the scanline would suggest higher reliability in the fracture intensity determination (i.e. closer to background or true normalized intensity). An augment of the standard deviation as scanline progresses suggests low reliability of the final fracture intensity determination and suggests that spatial fracture distribution is affecting fracture intensity determination. In most cases the first twenty fractures have been ignored in the error calculations because of common unstable behavior of normalized fracture intensity when only a small number of fractures are available.

APPENDIX 3.G.: CUPIDO/TAMAULIPAS STRATIGRAPHIC COLUMNS

This appendix contains the stratigraphic columns of the localities studied in Chapter 3. The stratigraphic columns contain information about the stratigraphic unit(s) studied, thickness scale, graphic lithologic description of each bed in the sequence, type of contact with adjacent beds, a sedimentary facies interpretation based on Dunham (1962), principal framework components, presence of natural fractures and abundance, fifth order stratigraphic cycle boundaries, beds studied and samples collected, and lower hemisphere stereographic projections of fracture and stylolite orientation for each bed.

References

- Ackermann, R. V., and R. W. Schlische, 1997. Anticlustering of Small Normal Faults Around Larger Faults. *Geology*, 25(12), pp. 1127-1130.
- Ackermann, R. V., R. W. Schlische, and M. Withjack, 2001. The Geometric and Statistical Evolution of Normal Fault Systems: An Experimental Study of the Effects of Mechanical Layer Thickness on Scaling Laws. *Journal of Structural Geology*, 23, pp. 1803-1819.
- Adams, J. E., and M. G. Rhodes, 1960. Dolomitization by Seepage Refluxion. *American Association of Petroleum Geologists*, Bulletin, 44(12), pp. 1912-1920.
- Aguilera, R., 1980. Naturally Fractured Reservoirs. *Petroleum Publishing Company*, Tulsa, 703 p.
- Atkinson, B. K., and P. G. Meredith, 1987. The Theory of Subcritical Crack Growth with Applications to Minerals and Rocks. In: Fracture Mechanics of Rock. Atkinson B. K. (ed.). *Academic Press*, San Diego, California.
- Aydan, O., and T. Kawamoto, 1990. Discontinuities and Their Effect on Rock Mass. In: Rock Joints. N. Barton and O. Stephansson (eds.), *Balkema*, Rotterdam, pp. 149-156.
- Baecher, G. B., 1980. Progressively Censored Sampling of Rock Joint Traces. *Mathematical Geology*, 12, pp. 33-40.
- Baecher, G. B., N. A. Lanney, and H. H. Einstein, 1977. Statistical Description of Rock Properties and Sampling. *US Symposium on Rock Mechanics*, 18th, pp. 5C1.1-5C1.8.
- Baecher, G. B., and N. Lanney, 1978. Trace Length Biases in Joint Surveys. *Symposium on Rock Mechanics*, Proceedings, 19th (1), pp. 56-65.
- Bagzis, J. M., 1989. Refracturing Pays Off in Rangely Field. *World Oil*, 209 (5), pp. 39-44.

- Bai, T., and D. D. Pollard, 2000. Fracture Spacing in Layered Rocks: A New Explanation Based on the Stress Transition. *Journal of Structural Geology*, 22, pp. 43-57.
- Barton, C. A., and M. D. Zoback, 1990. Self-similar Distribution of Macroscopic Fractures at Depth in Crystalline Rock in the Cajon Pass Scientific Drillhole. In: Rock joints. Barton, N., O., and O. Stephansson (eds.). *International Symposium on Rock Joints*, pp. 163-170.
- Barton, C. A., and M. D. Zoback, 1992. Self-Similar Distribution and Properties of Macroscopic Fractures at Depth in Crystalline Rock in the Cajon Pass Scientific Drill Hole. *Journal of Geophysical Research*, B, 97(4), pp. 5181-5200.
- Barton, C. C., and P. A. Hsieh, 1989. Physical and Hydrological Flow Properties of Fractures. In: Environmental, Engineering, and Urban Geology in the United States. Field Trip Guidebook for the 28th International Geological Congress, Volume 2. Hanshaw P. M. (ed.). *American Geophysical Union*, Washington, 36 p.
- Becker, A., and M. R. Gross, 1996. Mechanisms for Joint Saturation in Mechanically Layered Rocks –An Example from Southern Israel. *Tectonophysics*, 257, pp. 223-237.
- Belfield, W. C., 1998. Incorporating Spatial Distribution into Stochastic Modeling of Fractures: Multifractals and Lévy-stable Statistics. *Journal of Structural Geology*, 20, pp. 473-486.
- Belfield, W. C., and J. P. Sovich, 1995. Fracture Statistics from Horizontal Wellbores. *Journal of Canadian Petroleum Technology*, 34 (6), pp. 47-50.
- Benavides, L., 1956. Notas sobre la Geología Petrolera de Mexico. In: Symposium sobre Yacimientos de Petróleo y Gas, *XX Congreso Geológico Internacional*. Tomo III. E. J. Guzman (ed.). Mexico, pp. 350-562.
- Berg, R. R., 1962. Mountain Flank Thrusting in Rocky Mountain foreland, Wyoming. *Geological Society of America Bulletin*, 52, pp. 1445-1486.
- Berkowitz, B., and P. M. Adler, 1998. Stereological Analysis of Fracture Network Structure in Geological Formations. *Journal of Geophysical Research*, 103, pp. 15339-15360.

- Berkowitz, B., and A. Hadad, 1997. Fractal and Multifractal Measures of Natural and Synthetic Fracture Networks. *Journal of Geophysical Research*, 102, pp. 12205-12218.
- Bogdonov, A. A., 1947. The Intensity of Cleavage as Related to the Thickness of Beds. *Soviet Geology*, 16, pp.102-104.
- Bonham, L. C., 1957. Structural Petrology of the Pico Anticline, Los Angeles County, California. *Journal of Sedimentary Petrology*, 27(3), pp. 251-264.
- Bonnet, E., O. Bour, N. E. Odling, P. Davy, I. Main, P. Cowie, and B. Berkowitz, 2001. Scaling of Fracture Systems in Geological Media. *Reviews of Geophysics*, 39(3), pp. 347-383.
- Borgos, H. G., P. A. Cowie, and N. H. Dawers, 2000. Practicalities of Extrapolating One-dimensional Fault and Fracture Size-frequency Distributions to Higher-dimensional Samples. *Journal of Geophysical Research*, 105, pp. 28377-28391.
- Bowker, K. A., and W. D. Jackson, 1989. The Weber Sandstone at Rangely Field, Colorado. In: Petrogenesis and Petrophysics of Selected Sandstone Reservoirs of the Rocky Mountain Region. Coalson, E. B., S. S. Kaplan, C. W. Keighin, Ch. A. Oglesby, and J. W. Robinson (eds.). *Rocky Mountains Association of Geologists*, pp. 65-80.
- Bowker, K. A., and P. J. Shuler, 1991. Carbon Dioxide Injection and Resultant Alteration of the Weber Sandstone, Rangely Field, Colorado. *American Association of Petroleum Geologists, Bulletin*, 75(9), Tulsa, pp. 1489-1499.
- Burroughs, S. M., and S. F. Tebbens, 2001, Upper-Truncated Power Laws in Natural Systems. *Pure and Applied Geophysics*, 158, pp. 741-757.
- Camerlo, R. H., 1998. Geometric and kinematic evolution of detachment folds, Monterrey Salient, Sierra Madre Oriental, Mexico. Masters Thesis, *The University of Texas at Austin*, 399 p.
- Castaing, C., M. A. Halawani, F. Gervais, J. P. Chilés, A. Genter, B. Bouguine, G. Ouillon, J. M. Brosse, P. Martin, A. Genna, and D. Janjou, 1996. Scaling Relationships in Intraplate Fracture Systems Related to Red Sea Rifting. *Tectonophysics*, 261, pp. 291-314.

- Chamberlin, T. C., 1910. The Appalachian Folds of Central Pennsylvania. *Journal of Geology*, 18, pp. 228-251.
- Clark, M. B., S. L. Brantley, and D. M. Fisher, 1995. Power-law Vein Thickness Distributions and Positive Feedback in Vein Growth. *Geology*, 23, pp. 975-978.
- Clift, S. J., F. E. Abegg, K. S. Aslesen, T. M. Laroche, R. G. Stanley, and S. E. Laubach, 1997. Predicting Fracture Cementation in Permian Sandstone, Pakenham (Wolfcamp) Field, Terrell County, Texas. In: Permian Basin Oil and Gas Fields; Turning Ideas into Production. DeMis, W. D. (ed.), *West Texas Geological Society*, 97-102, p. 99.
- Conklin, J., and C., Moore, 1977. Environmental Analysis of the Lower Cretaceous Cupido Formation, Northeast Mexico. In: Cretaceous Carbonates of Texas and Mexico, D. G. Bebout and R.G. Loucks (eds.). Bureau of Economic Geology, Report of Investigations 89, *The University of Texas at Austin*, pp. 302-323.
- Corbett, K., M. Friedman, and J. Spang, 1987. Fracture Development and Mechanical Stratigraphy of Austin Chalk, Texas. *American Association of Petroleum Geologists, Bulletin*, 71(1), pp. 17-28.
- Das Gupta, U., 1978. A Study of Fractured Reservoir Rocks, with Special Reference to Mississippian Carbonate Rocks of Southwest Alberta. Ph.D. Thesis. *University of Toronto*, 261 p.
- Davis, G. H., and S. J. Reynolds, 1996. Structural Geology. *John Wiley & Sons, Inc.*, 776 p.
- Davy, P., 1993. On the Frequency-Length Distribution of the San Andreas Fault System. *Journal of Geophysical Research*, 98, pp. 12141-12151
- Demicco, R. V., and L. A. Hardie, 1994. Sedimentary Structures and Early Diagenetic Features of Shallow Marine Carbonate Deposits. *Society of Economic Paleontologists and Mineralogists, Atlas Series*, 1, 265 p.
- De Voto, R. H., B. L. Bartleson, C. J. Schenk, and N. B. Waechter, 1986. Late Paleozoic Stratigraphy and Syndepositional Tectonism, Northwestern Colorado. In: New Interpretations of Northwest Colorado Geology. D. S. Stone and K. S. Johnson (eds.). *Rocky Mountain Association of Geologists, Symposium*, Denver, pp 37-50.

- Diaz, T., R. Mixon, G. E. Murray, A. Weidie, and J. Wolleben, 1959. Mesozoic Stratigraphy and Structure, Saltillo-Galeana areas, Coahuila and Nuevo León. *South Texas Geological Society*, Guidebook, 106 p.
- Dunham, R. J., 1962. Classification of Carbonate Rocks According to Depositional Texture. In: Classification of Carbonate Rocks, W. E. Ham (ed.). *American Association of Petroleum Geologists*, Memoir 1, pp. 108-121.
- Dunne, W. M., and A. J. Caldanaro Jr., 1997. Evolution of Solution Structures in a Deformed Quartz Arenite: Geometric Changes Related to Permeability Changes, *Journal of Structural Geology*, 19(5), pp. 663-672.
- Dutton, S. P., and B. J. Willis, 1998. Comparison of Outcrop and Subsurface Sandstone Permeability Distribution, Lower Cretaceous Fall River Formation, South Dakota and Wyoming, *Journal of Sedimentary Research*, 68 (5), p. 890-900.
- Einstein, H. H., and G. B. Baecher, 1983. Probabilistic and Statistical Methods in Engineering Geology. *Rock Mechanics and Rock Engineering*, 16, pp. 39-72.
- Embry, A. F., III, and J. E. Klován, 1972. Absolute Water Depth Limits of Late Devonian Paleoecological Zones, *Geologische Rundschau*, 61(2), pp. 672-686.
- Ericsson, J. B., H. C. McKean, and R. J. Hooper, 1998. Facies and Curvature Controlled 3D Fracture Models in a Cretaceous Carbonate Reservoir, Arabian Gulf. In: Faulting, Fault Sealing and Fluid Flow in Hydrocarbon Reservoirs. Jones, G., Q. J. Fisher, and R. J. Knipe (eds.). *Geological Society, London*, Special Publications, 147, pp. 299-312.
- Eyal, Y., M.R.Gross, T. Engelder, A. Becker, 2001. Joint Development During Fluctuation of the Regional Stress Field in Southern Israel. In: Paul Hancock Memorial Issue. Dunne, W. M., Stewart, I. S., Turner, J. P. (eds.). *Journal of Structural Geology*, 23 (2-3), p. 279-296.
- Fischer, M. P., M. R. Gross, T. Engelder, and R. J. Greenfield, 1995. Finite Element Analysis of the Stress Distribution Around a Pressurized Crack in a Layer Elastic Medium: Implications for the Spacing of Fluid-driven Joints in Bedded Sedimentary Rock. *Tectonophysics*, 247, pp. 49-64.

- Fisher, M. P., and P. B. Jackson, 1999. Stratigraphic Controls on Deformation Patterns in Fault-related Folds: A Detachment Fold Example from the Sierra Madre Oriental, Northeast Mexico. *Journal of Structural Geology*, 21, pp. 613-633.
- Folk, R. L., 1962. Spectral Subdivision of Limestone Type. In: Classification of Carbonate Rocks. W. E. Ham (ed.). *American Association of Petroleum Geologists*, Memoir, 1, pp. 62-84.
- Folk, R. L., 1980. Petrology of Sedimentary Rocks. *Hemphill Publishing Company*, Austin, 184 p.
- Friedman, M., 1969. Structural Analysis of Fractures in Cores from Saticoy Field, Ventura County, California. *American Association of Petroleum Geologists*, Bulletin, 53 (2), pp. 367-389.
- Fryberger, S. G., 1979. Eolian-Fluviatile (Continental) Origin of Ancient Stratigraphic Trap for Petroleum in Weber Sandstone, Rangely Oil Field, Colorado. *The Mountain Geologist*, 16(1), pp. 1-36.
- Fryberger, S. G., and M. H. Koelmel, 1986. Rangely Field: Eolian System-Boundary Trap in the Permo-Pennsylvanian Weber Sandstone of Northwest Colorado. In: New Interpretations of Northwest Colorado Geology. Stone, D. S., and K. S. Johnson, (eds.), *Rocky Mountains Association of Geologists*, pp. 129-150.
- Geldon, A. L., 1986. Hydrostratigraphic Characterization of Paleozoic Formations in Northwestern Colorado. In: New Interpretations of Northwest Colorado Geology. Stone, D. S., and K. S. Johnson, (eds.), *Rocky Mountains Association of Geologists*, pp. 265-281.
- Gillespie, P. A., C. B. Howard, J. J. Walsh, and J. Watterson, 1993. Measurement and Characterization of Spatial Distributions of Fractures. *Tectonophysics*, 226, pp. 113-141.
- Gillespie, P. A., J. D. Johnston, M. A. Loriga, K. L. W. McCaffrey, L. L. Walsh, and L. Watterson, 1999. Influence of Layering on Vein Systematics in Line Samples. In: Fractures, Fluid Flow, and Mineralization. K. J. W. McCaffrey, L. Lonergan, and J. J. Wilkinson (eds.). *Geological Society of London*, Special Publication, 155, pp. 35-56.
- Gillespie, P. A., J. J. Walsh, J. Watterson, C. G. Bonson, and T. Manzocchi, 2001. Scaling Relationships of Joint and Vein Arrays from The Burren, Co.

- Clare, Ireland. In: Paul Hancock Memorial Issue. Dunne, W. M., I. S. Stewart, J. P. Turner (eds.). *Journal of Structural Geology*, 23 (2-3), pp. 183-201.
- Goldhammer, R. K., 1999. Mesozoic Sequence Stratigraphy and Paleogeographic Evolution of Northeast Mexico. In: Mesozoic Sedimentary and Tectonic History of North-Central Mexico. Bartolini, C., J. L. Wilson, and T. F. Lawton (eds.). *Geological Society of America*, Special Paper, 340, Boulder, pp. 1-58.
- Goldhammer, R. G., P. J. Lehman, R. G. Todd, J. L. Wilson, W. C. Ward, and C. R. Johnson, 1991. Sequence Stratigraphy and Cyclostratigraphy of the Mesozoic of the Sierra Oriental, Northeast Mexico: *Society of Economic Paleontologists and Mineralogists*, Gulf Coast Section, 85 p.
- Gomez, L., J. Gale, S. Ruppel, and S. Laubach, 2001. Fracture Characterization Using Rotary-drilled Sidewall Cores: An Example from the Ellenburger Formation, West Texas. In: The Permian Basin: Microns to Satellites, Looking for Oil and Gas at all Scales. Viveiros, J. J. and S. M. Ingram (eds.). *West Texas Geological Society*, Symposium, pp. 81-90.
- Griffith, A. A., 1920. The Phenomena of Rupture and Flow in Solids. *Philosophical Transactions of the Royal Society of London*, Series A, 221, pp. 163-198.
- Gross, M. R., 1993. The Origin and Spacing of Cross Joints: Examples from the Monterrey Formation, Santa Barbara Coastline, California. *Journal of Structural Geology*, 15(6), pp. 737-751.
- Gross, M. R., and T. Engelder, 1995. Strain Accommodated by Brittle Failure in Adjacent Units of the Monterey Formation, U.S.A.: Scale Effects and Evidence for Uniform Displacement Boundary Conditions. *Journal of Structural Geology*, 17, pp. 1303-1318.
- Gross, M. R., M. P. Fisher, T. Engelder, and R. J. Greenfield, 1995. Factors Controlling Joint Spacing in Interbedded Sedimentary Rocks: Integrating Numerical Models with Field Observations from the Monterey Formation, USA. In: Fractography: Fracture Topography as a Tool in Fracture Mechanics and Stress Analysis. M. S. Ameen (ed.). *Geological Society of London*, Special Publication 92, pp. 215-253.

- Grotzinger, J. P., 1986. Cyclicity and Paleoenvironmental Dynamics, Rocknest Platform, Northwest Canada. *Geological Society of America*, Bulletin 97, pp. 1208-1231.
- Gudmundsson, A., 1987. Geometry, Formation and Development of Tectonic Fractures on the Reykjanes Peninsula, Southwest Iceland. *Tectonophysics*, 139, pp. 295-308.
- Hamlin, S. H., S. J. Clift, S. P. Dutton, T. F. Hentz, and S. E. Laubach, 1995. Canyon Sandstones –A Geologically Complex Natural Gas Play in Slope and Basin Facies, Val Verde Basin, Southwest Texas. Report of Investigations No. 232. Bureau of Economic Geology, *The University of Texas at Austin*, 74 p.
- Hamlin, H. S., 1999. Syn-orogenic Slope and Basin Depositional Systems, Ozona Sandstone, Val Verde Basin, Southwest Texas. Ph.D. Dissertation, *The University of Texas at Austin*, 135 p.
- Handin, J., R. V. Jr. Hager, M. Friedman, and J. N. Feather, 1963. Experimental Deformation of Sedimentary Rocks under Confining Pressure; Pore Pressure Tests. *American Association of Petroleum Geologists*, Bulletin, 47 (5), pp. 717-755.
- Handin, J., Friedman, M., Logan, J. M., Pattison, L. J., and Swolfs, H. S., 1972. Experimental Folding of Rocks under Confining Pressure; Buckling of Single-Layer Rock Beams. Flow and Fracture of Rocks, *Geophysical Monograph*, 16, pp. 1-28.
- Hansen, W. R., P. R. Rowley, and P. E. Carrara, 1983. Geologic Map of Dinosaur National Monument and vicinity, Utah and Colorado. Department of the Interior, *U.S. Geological Survey*.
- Hansen, W. R., 1986. History of Faulting in the Eastern Uinta Mountains, Colorado and Utah. In: New Interpretations of Northwest Colorado Geology. Stone, D. S., and K. S. Johnson, (eds.). *Rocky Mountains Association of Geologists*, pp. 5-18.
- Harris, J. F., G. L. Taylor, and J. L. Walper, 1960. Relation of Deformational Fractures in Sedimentary Rocks to Regional and Local Structure. *American Association of Petroleum Geologists*, Bulletin, 44, pp. 1853-1873.

- Hatton, C. G., I. G. Main, and P. G. Meredith, 1993. A Comparison of Seismic and Structural Measurements of Scaling Exponents During Tensile Subcritical Crack Growth. *Journal of Structural Geology*, 15, pp. 1485-1495.
- Hatton, C. G., I. G. Main, and P. G. Meredith, 1994. Non Universal Scaling of Fracture Length and Opening Displacement. *Nature*, 367, pp. 160-162.
- Heffer, K. J., and T. G. Bevan, 1990. Scaling Relationships and Natural Fractures: Data, Theory and Applications. *Society of Petroleum Engineers*, Europec 90, paper #20981. The Hague, pp. 367-376.
- Hefner, T. A., and K. T. Barrow, 1992. Rangely Field -U.S.A., Uinta/Piceance basins, Colorado. In: Structural traps –VII. Beaumont, E. A., and N. H. Foster (eds.). *American Association of Petroleum Geologists*. Treatise of Petroleum Geology, Atlas of Oil and Gas Fields, A-25, pp. 29-56.
- Henderson, J. R., C. MacLean, I. G. Main, and M. G. Norman, 1994. A Fracture-Mechanical Cellular Automaton Model of Seismicity. *Pure and Applied Geophysics*, 142, pp. 545-565.
- Hervey, J. R., and A. C. Iakovakis, 1991. Performance Review of a Miscible CO₂ Tertiary Project: Rangely Weber Sand Unit, Colorado. *Society of Petroleum Engineers*. Reservoir Engineering, 6(2), pp. 163-168.
- Hestir, K., J. P. Chilés, J. Long, and D. Billaux, 1987. Three Dimensional Modeling of Fractures in Rock: From data to a Regionalized Parent-Daughter Model. In: Flow and Transport Through Unsaturated Fractured Rock. D. D. Evans, and T. J. Nicholson (eds.). *American Geophysical Union*, Washington, Geophysical Monograph, 42, pp. 133-140.
- Hild, G. P., and R. K. Wackowski, 1998. Results of the Injection Well Polymer Gel Treatment Program at the Rangely Weber Sand Unit, Rangely, Colorado. In: Improved Oil Recovery, Part 1. *Society of Petroleum Engineers*. Proceedings of the 11th Symposium, paper SPE #39612, Tulsa, pp. 93-105.
- Hobbs, D. W., 1967. The Formation of Tension Joints in Sedimentary Rocks: An Explanation, *Geological Magazine*, 104, pp. 550-556.
- Holail, H., K. C. Lohmann, and I. Sanderson, 1988. Dolomitization and Dedolomitization of Upper Cretaceous Carbonates: Bahariya Oasis, Egypt. In: Sedimentology and Geochemistry of Dolostones. V. Shukla and

- P. A. Baker (eds.). *Society of Economic Paleontologists and Mineralogists*, Special Publication 43, pp. 191-207.
- Hoover, J. J., and H. W. Rauch, 1989. The Effects of Lineaments on Gas Well Yield from Devonian Shales and Siltstones in North Central West Virginia. In: *Proceedings of the Appalachian Basin Industrial Associates*. Shumaker, R. C. (compiler), Fall Meeting, 16, p. 185-216.
- Huang, Q., and J. Angelier, 1989. Fracture Spacing and its Relation to Bed Thickness. *Geological Magazine*, 126(4), p. 355-362.
- Hudson, J. A., and S. D. Priest, 1979. Discontinuities and Rock Mass Geometry, *International Journal of Rock Mechanics, Mining Science, and Geomechanics Abstracts*, 16, pp. 339-362.
- James, N. P., 1984. Shallowing-upward Sequences in Carbonates. In: *Facies Models*, Walker R. G. (ed.). *Geoscience Canada Reprint Series 1*, St. Johns, Newfoundland, Canada, pp. 213-228.
- Jensen, J. L., L. W. Lake, P. W. M. Corbett, and D. J. Goggin, 1997. Statistics for Petroleum Engineers and Geoscientists. *Prentice Hall Petroleum Engineering Series*, New Jersey, 390 p.
- Ji, S. and K. Saruwatari, 1998. A Revised Model for the Relationship Between Joint Spacing and Layer Thickness. *Journal of Structural Geology*, 20 (11), pp. 1495-1508.
- Johnston, J. D., 1994. Fractal Geometries of Filled Fracture Systems -Scaling of Mechanism. In: *Fault Population*. *Geological Society, London*. Tectonic Studies Group Special Meeting, Extended Abstracts Volume, Edinburgh, pp. 64-66.
- Johnston, J. D., and K. J. W. McCaffrey, 1996. Fractal Geometries of Vein Systems and the Variation of Scaling Relationships with Mechanism. In: *Scaling Laws for Fault and Fracture Populations; Analyses and Applications*. Cowie, P. A., R. J. Knipe, I. G. Main, and S. F. Wojtal (eds.). *Journal of Structural Geology*, 18 (2-3), pp. 349-358.
- Kendall, C. G. S. C., A. S. Alsharhan, and G. L. Whittle, 1995. The Flood Recharge Sabkha Model Supported by Recent Inversions of Anhydrite to Gypsum in the UAE Sabkhas. In: *Quaternary Deserts and Climatic Change*. Alsharhan, A. S., K. W. Glennie, G. L. Whittle, and C. G. S. C.

- Kendall (eds.). *International Conference on Quaternary Deserts and Climatic Change*, Al Ain, United Arab Emirates, pp. 29-42.
- Kleist, R., S. A. Hall, and I. Evans, 1984. A Paleomagnetic Study of the Cretaceous Cupido Limestone, Northeast Mexico: Evidence for Local Rotation within the Sierra Madre Oriental. *Geological Society of America, Bulletin*, 95, pp. 55-60.
- Kobluk, D. R., and M. J. Risk, 1977. Micritization and Carbonate-Grain Binding by Endolithic Algae. *American Association of Petroleum Geologists, Bulletin*, 61 (7), pp. 1069-1082.
- Koch, G. S. Jr., and R. F. Link, 1971. Statistical Analysis of Geological Data. *Dover Publications, Inc.*, New York, 438 p.
- Koelmel, M. H., 1986. Post-Mississippian Paleotectonic, Stratigraphic, and Diagenetic History of the Weber Sandstone in the Rangely Field Area, Colorado. In: Paleotectonics and Sedimentation. J. A. Peterson (ed.). *American Association of Petroleum Geologists, Memoir*, 41, pp. 371-396.
- Kulander, B. R., S. L. Dean, and B. J. Ward Jr., 1990. Fractured Core Analysis. Interpretation, Logging, and Use of Natural and Induced Fractures in Core. *American Association of Petroleum Geologists, Methods in Exploration Series*, 8., Tulsa, 88 p.
- Lachenbruch, 1961. Depth and Spacing of Tension Cracks. *Journal of Geophysical Research*, 66, pp. 4273-4292.
- Ladeira, F. L., and N. J. Price, 1981. Relationship Between Fracture Spacing and Bed Thickness. *Journal of Structural Geology*, 3(2), pp. 179-183.
- Lander, R. H., and O. Walderhaug, 1999. Porosity Prediction Through Simulation of Sandstone Compaction and Quartz Cementation. *American Association of Petroleum Geologists, Bulletin* 83, pp. 433-449.
- Lander R. H., J. F. W. Gale, S. E. Laubach, and L. M. Bonnell, 2002. Interaction Between Quartz Cementation and Fracturing in Sandstones. *American Association of Petroleum Geologists, Annual Meeting Abstracts*, Houston.
- Larsen, R. J., and M. L. Marx, 1987. An Introduction to Probability and its Applications. *Prentice-Hall Inc*, New Jersey, 404 p.

- Larson, T. C., 1975. Geological Considerations of the Weber Sandstone Reservoir, Rangely Field, Colorado. *Rocky Mountains Association of Geologists*, Symposium, pp. 275-279.
- Laubach, S. E., 1988. Subsurface Fractures and their Relationship to Stress History in East Texas Basin Sandstone. *Tectonophysics*, 156 (4), pp. 495-503.
- Laubach, S. E., 1989. Paleostress Directions from the Preferred Orientation of Closed Microfractures (Fluid-Inclusion Planes) in Sandstone, East Texas Basin, U.S.A., *Journal of Structural Geology*, 11 (5), p. 603-611.
- Laubach, S. E., 1991. Fracture Patterns in Low-permeability-sandstone Gas Reservoir Rocks in the Rocky Mountain Region. Rocky Mountain Regional/Low Permeability Reservoirs Symposium and Exhibition, April 15-17, Denver, CO. *Society of Petroleum Engineers of AIME*, Richardson, TX., pp. 501-510.
- Laubach, S. E., 1992. Fracture Networks in Selected Cretaceous Sandstones of the Green River and San Juan Basins, Wyoming, New Mexico, and Colorado. In: Geological Studies Relevant to Horizontal Drilling in Western North America. W. Schmoker, E. B. Coalson, and C. A. Brown (eds.). *Rocky Mountains Association of Geologists*, pp. 115-127.
- Laubach, S. E., 1996. Fracturing and Diagenesis as Coupled Processes. *Geological Society of America*, 28th Annual Meeting, Abstracts with Programs, 28 (7), pp. 136-137.
- Laubach, S. E., 1997. A Method to Detect Natural Fracture Strike in Sandstones. *American Association of Petroleum Geologists*, Bulletin 81(4), Tulsa, pp. 604-623.
- Laubach, S. E., 1999. Fracture Quality Analysis, Status Report. Presented at the Annual Meeting of Industrial Sponsors of the Fracture Research and Application Consortium, Bureau of Economic Geology. *The University of Texas at Austin*. <http://www.beg.utexas.edu/indassoc/fraccity/index.htm>
- Laubach, S. E., and C. M. Tremain, 1991. Regional coal fracture patterns and coal bed methane development. In: Rock Mechanics as Multidisciplinary Science: Rogiers, J. C (ed.). Proceedings of the 32nd U.S. Symposium, Rotterdam, A. A. Balkema, p. 851-859.

- Laubach, S. E., and Milliken, K. L., 1996. New fracture Characterization Methods for Siliciclastic Rocks. In: Rock Mechanics Tools and Techniques. Aubertin, M., F. Hassani, H. S. Mitri (eds.). Proceedings of the 2nd North American Rock Mechanics Symposium; NARMS '96, a Regional Conference of ISRM; Montreal, Canada, pp. 1209-1213.
- Laubach, S. E., R. A. Marrett, J. E. Olson, and A. R. Scott, 1998. Characteristics and Origins of Coal Cleat: A Review. *International Journal of Coal Geology*, 35, pp. 175-207.
- Laubach, S. E., R. Marrett, and J. Olson, 2000. New Directions in Fracture Characterization. *The Leading Edge*, 19 (7), p. 704, 706, 708, and pp.710-711.
- Laubach, S. E. and A. Schwartz, unpublished. Weber Sandstone Fracture Quality Assessment, Rangely Field, Colorado. Bureau of Economic Geology. *The University of Texas at Austin*.
- Laslett, G. M., 1982. Censoring and Edge Effects in Areal and Line Transects Sampling of Rock Joint Traces. *Mathematical Geology*, 14 (2), pp. 125-140.
- Lehmann, C., D. A. Osleger, and I. P. Montañez, 1998. Controls on Cyclostratigraphy of Lower Cretaceous Carbonates and Evaporites, Cupido and Coahuila Platforms, Northeastern Mexico. *Journal of Sedimentary Research*, Section B: Stratigraphy and Global Studies, 68 (6), pp. 1109-1130.
- Lerche, I., and W. Narr, 1986. Estimating Subsurface Fracture Density in Core: Effects Resulting from Variable Fracture Spacing. *Society of Petroleum Engineers*. Formation Evaluation, pp. 249-258.
- Lorenz, J. C., and R.E. Hill, 1991. Subsurface Fracture Spacing: Comparison of Inferences from Slant/Horizontal Core and Vertical Core in Mesaverde Reservoirs. *Society of Petroleum Engineers*. Rocky Mountain Regional Meeting and Low-Permeability Reservoirs Symposium, Denver, paper #21877, pp. 705-716.
- Lucia, F. J., and Major, R. P., 1994. Porosity Evolution Through Hypersaline Reflux Dolomitization. *International Association of Sedimentologists*, Special Publication, 21, pp. 325-341.

- Mallory, W. W., 1975. Middle and Southern Rocky Mountains, Northern Colorado Plateau, and Eastern Great Basin Region. In: Paleotectonic Investigations of the Pennsylvanian System in the United States. McKee, E. D., and E. J. Crosby (eds.). *U. S. Geological Survey*, Professional Paper, 853-N, 349 p.
- Main, I. G., T. Leonard, O. Papasouliotis, C. O. Hatton, and P. G. Meredith, 1999. One Slope or Two?. Detecting Statistically Significant Breaks of Slope in Geophysical Data, with Application to Fracture Scaling Relationships. *Geophysical Research Letters*, 26, pp. 2801-2804.
- Mandal, N., S. K. Deb, and D. Khan, 1994. Evidence for a Non-linear Relationship between Fracture Spacing and Layer Thickness. *Journal of Structural Geology*, 16 (9), pp. 1275-1281.
- Mandelbrot, B. B., 1982. The Fractal Geometry of Nature. *Springer-Verlag*, New York, 499 p.
- Marrett, R., 1996. Aggregate Properties of Fracture Populations. In: Scaling Laws for Fault and Fracture Populations; Analyses and Applications. Cowie, P. A., R. J. Knipe, I. G. Main, and S. F. Wojtal, (eds.). *Journal of Structural Geology*, 18 (2-3), pp. 169-178.
- Marrett, R., 1997. Permeability, Porosity, and Shear-wave Anisotropy from Scaling of Open Fracture Populations. In: Fractured Reservoirs: Characterization and Modeling Guidebook. T. E. Hoak, A. L. Klawitter, and P. K. Blomquist (eds.). *Rocky Mountain Association of Geologists*, Denver, pp. 217-226.
- Marrett, R., 2000. Advances in Quantitative Fracture Scaling. Presented at the Annual Meeting of Industrial Sponsors of the Fracture Research and Application Consortium. Bureau of Economic Geology, *The University of Texas at Austin*. <http://www.beg.utexas.edu/indassoc/fraccity/index.htm>
- Marrett, R., 2001. Spatial Architecture of Fracture Arrays. Presented at the Annual Meeting of Industrial Sponsors of the Fracture Research and Application Consortium, Bureau of Economic Geology, *The University of Texas at Austin*. <http://www.beg.utexas.edu/indassoc/fraccity/index.htm>
- Marrett, R., and R. Allmendinger, 1990. Kinematic Analysis of Fault Slip Data. *Journal of Structural Geology*, 12(8), pp. 973-986.

- Marrett, R., and S. E. Laubach, 1997. Diagenetic Controls on Fracture Permeability and Sealing. *International Journal of Rock Mechanics and Mining Sciences*, 34 (3-4), paper #204.
- Marrett, R., O. Ortega, and C. Kelsey, 1999. Extent of Power-law Scaling for Natural Fractures in Rock. *Geology*, 27(9), pp. 799-802.
- Marrett, R. and M. Aranda-García, 1999. Structure and Kinematic Development of the Sierra Madre Oriental Fold-Thrust Belt, Mexico. In: Stratigraphy and Structure of the Jurassic and Cretaceous Platform and Basin Systems of the Sierra Madre Oriental, Monterrey and Saltillo Areas, Northeastern Mexico, A Field Book and Related Papers. *South Texas Geological Society*. Special Publication for the Annual Meeting of the American Association of Petroleum Geologists and the SEPM Society for Sedimentary Geology, San Antonio, pp. 69-98.
- Marrett, R., J. L. Wilson, and W. Ward, 1999. Stratigraphy and Structure of Jurassic and Cretaceous Rocks of the Sierra Madre Oriental, Northeastern Mexico. In: Stratigraphy and Structure of the Jurassic and Cretaceous Platform and Basin Systems of the Sierra Madre Oriental, Monterrey and Saltillo Areas, Northeastern Mexico, A Field Book and Related Papers. *South Texas Geological Society*. Special Publication for the Annual Meeting of the American Association of Petroleum Geologists and the SEPM Society for Sedimentary Geology, San Antonio, pp. 5-68.
- Marrett, R. and Laubach, S., 2001. Fracturing During Diagenesis. In: Genesis and Controls of Reservoir-Scale Carbonate Deformation, Monterrey Salient, Mexico, Marrett, R. (ed.). Field Trip Guidebook 28, Bureau of Economic Geology, *The University of Texas at Austin*, pp. 109-123.
- Mauldon, M., W. M. Dunne, and M. B. Jr. Rohrbaugh, 2001. Circular Scanlines and Circular Windows: New Tools for Characterizing the Geometry of Fracture Traces. *Journal of Structural Geology*, 23, pp. 247-258.
- McCaffrey, K. J. W., J. D. Johnston, and M. A. Loriga, 1994. Variation of Fractal Dimension in Vein Systems. In: Fault Populations. P. A. Cowie, I. G. Main, and R. Knipe (eds.). *Tectonic Studies Group*, Special Meeting, Edinburgh, pp. 103-105.
- McCoy, R. M. and S. A. Young, 1992. Sagebrush Associated with Lineaments Shows Influence of Hydrocarbon Microseepage in High Production Areas of the Altamont-Bluebell oil field. In: Hydrocarbon and mineral resources of the Uinta Basin, Utah and Colorado. Fouch, T. D., V. F. Nuccio, T. C.

- Jr. Chidsey (eds.). *Utah Geological Association*, Publication 20, pp. 135-142.
- McQuillan, H., 1973. Small-scale Fracture Density in Asmari Formation of Southwest Iran and its Relation to Bed Thickness and Structural Setting. *American Association of Petroleum Geologists*, Bulletin 57, pp. 2367-2385.
- Milliken, K. L., 1994. Cathodoluminescence Textures and the Origin of Quartz Silt in Oligocene Mudrocks, South Texas. *Journal of Sedimentary Research*, A64 (3), pp. 567-571.
- Milliken, K. L. and S. E. Laubach, 2000. Brittle Deformation in Sandstone Diagenesis as Revealed by Cathodoluminescence Imaging with Application to Characterization of Fractured Reservoirs. In: Cathodoluminescence in Geosciences. Pagel, M., V. Barbin, P. Blanc, and D. Ohnenstetter (eds.). *Springer-Verlag*, pp. 225-244.
- Mitchum, R. M. Jr., and J. C. Van Wagoner, 1991. High Frequency Sequences and their Stacking Patterns: Sequence Stratigraphic Evidence of High Frequency Eustatic Cycles. In: The Record of Sea Level Fluctuations, K. T. Biddle, and W. Schlager (eds.). *Sedimentary Geology*, 70, pp. 131-160.
- Moldovanyi, E. P. and K. C. Lohman, 1984. Isotopic Recognition of Successive Cementation Events within the Phreatic Environment, Lower Cretaceous Sligo and Cupido Formations. In: A Field Guide to Upper Jurassic and Lower Cretaceous Carbonate Platform and Basin Systems, Monterrey-Salttillo Area, Northeast Mexico. Wilson, J. L., W. Ward, and J. Finneran (eds.). *Society of Economic Paleontologists and Mineralogists*, Gulf Coast Section, pp. 52-63.
- Monroy-Santiago, F., S. E. Laubach, and R. Marrett, 2001. Preliminary Diagenetic and Stable Isotope Analyses of Fractures in the Cupido Formation, Sierra Madre Oriental. In: Genesis and Controls of Reservoir-Scale Carbonate Deformation, Monterrey Salient, Mexico. Marrett, R. (ed.). Field Trip Guidebook 28, Bureau of Economic Geology, *The University of Texas at Austin*, pp. 83-107.
- Moros, J. G., 1999. Relationship Between Fracture Aperture and Length in Sedimentary Rocks. Masters Thesis. *The University of Texas at Austin*. 120 p.

- Morrow, D. W., 1982. Diagenesis 2; Dolomite Part 2, Dolomitization Models and Ancient Dolostones, *Geoscience Canada*, 9 (2), pp. 95-107.
- Mueller, M. C., 1991. Prediction of Lateral Variability in Fracture Intensity Using Multicomponent Shear-Wave Surface Seismic as a Precursor to Horizontal Drilling in the Austin Chalk. *Geophysical Journal International*, 107, pp. 409-415.
- Narr, W., 1991, Fracture Density in the Deep Subsurface; Techniques with Application to Point Arguello Oil Field. *American Association of Petroleum Geologists*, Bulletin, 75 (8), pp. 1300-1323.
- Narr, W., 1993. Deformation of Basement in Basement-Involved, Compressive Structures. In: Laramide Deformation in the Rocky Mountain Foreland of the United States. Schmidt, C. J., R. B. Chase, and E. A. Erslev, (eds.). *Geological Society of America*, Special Paper, 280, pp. 107-124.
- Narr, W., 1996. Estimating Average Fracture Spacing in Subsurface Rock. *American Association of Petroleum Geologists*, Bulletin 80(10), pp. 1565-1586.
- Narr, W. and J. Suppe, 1991. Joint Spacing in Sedimentary Rocks. *Journal of Structural Geology*, 13, pp. 1037-1048.
- Narr, W., and J. Suppe, 1994. Kinematics of Basement-Involved Compressive Structures. *American Journal of Science*, 294, pp. 802-860.
- Nelson, R. A., 1985. Geologic Analysis of Naturally Fractured Reservoirs: Houston, *Gulf Publishing*, 320 p.
- Nelson, R. A., 1987. Fractured Reservoirs: Turning Knowledge into Practice. *Journal of Petroleum Technology*, pp. 407-414.
- Nelson, R. A., and S. Serra, 1995. Vertical and Lateral Variations in Fracture Spacing in Folded Carbonate Sections and its Relation to Locating Horizontal Wells. *The Journal of Canadian Petroleum Technology*, 34 (6), pp. 51-56.
- Nicol, A., J. J. Walsh, and J. Watterson, 1996. Fault Size Distributions—Are They Really Power-law?. *Journal of Structural Geology*, 18, pp. 191-197.
- Novoa, E., V. Mount, and J. Suppe, 1998. Map-view Interference of Monoclinial Folds. *Journal of Structural Geology*, 20 (4), pp. 339-353.

- Odling, N. E., 1992. Network Properties of a Two-dimensional Fracture Pattern. *Pure and Applied Geophysics*, 138, pp. 95-114.
- Odling, N. E., 1997. Scaling and Connectivity of Joint Systems in Sandstones from Western Norway. *Journal of Structural Geology*, 19(10), pp.1257-1271.
- Odling, N. E., P. Gillespie, B. Bourguine, C. Castaing, J. P. Chiles, N. P. Christensen, E. Fillion, A. Genter, C. Olsen, L. Thrane, R. Trice, E. Aarseth, J. J. Walsh, and J. Watterson, 1999. Variations in Fracture System Geometry and Their Implications for Fluid Flow in Fractured Hydrocarbon Reservoirs. *Petroleum Geoscience*, 5, pp. 373-384.
- Olson, J. and D. D. Pollard, 1989. Inferring Paleostresses from Natural Fracture Patterns; a New Method. *Geology*, 17 (4), pp. 345-348.
- Olson, J. E., and D. D. Pollard, 1991. The Initiation and Growth of En Échelon Veins. *Journal of Structural Geology*, 13(5), pp. 595-608.
- Onasch, C. M., 1990. Microfractures and their Role in Deformation of a Quartz Arenite from the Central Appalachian Foreland, *Journal of Structural Geology*, 12 (7), pp. 883-894.
- Ortega, O., R. Marrett, S. Hamlin, S. Clift and R. Reed, 1998. Quantitative Macrofracture Prediction Using Microfracture Observations: A Successful Case Study in the Ozona Sandstone, West Texas. Extended Abstract. *American Association of Petroleum Geologists*. Annual Meeting Extended Abstracts, Salt Lake City, p. A503.
- Ortega, O., and Marrett, R., 2000. Prediction of Macrofracture Properties Using Microfracture Information, Mesaverde Group Sandstones, San Juan Basin, New Mexico. *Journal of Structural Geology*, 22 (5), pp. 571-588.
- Ouillon, G., C. Castaing, and D. Sornette, 1996. Hierarchical Geometry of Faulting. *Journal of Geophysical Research*, 101, pp. 5477-5487.
- Padilla y Sánchez, R., 1985. Las Estructuras de la Curvatura de Monterrey, Estados de Coahuila, Nuevo León, Zacatecas y San Luis Potosí. *Revista del Instituto de Geología de la Universidad Autónoma de México*, 6, pp. 1-20.

- Pascal, C., J. Angelier, M.-C. Cacas, and P. L. Hancock, 1997. Distribution of Joints: Probabilistic Modeling and Case Study near Cardiff (Wales, U.K.). *Journal of Structural Geology*, 19, pp. 1273-1284.
- Pettijohn, F. J., 1957. Sedimentary Rocks. *Harper and Row Publishers*, New York, 747 p.
- Pickering, G., J. M. Bull, and D. J. Sanderson, 1995. Sampling Power-law Distributions. *Tectonophysics*, 248, pp. 1-20.
- Pineau, A., 1985. Echantillonnage des espacements entre fractures; une distribution exponentielle negative troquée. *Comptes-Rendus de l'Académie des Sciences, Paris*, II, 301, pp. 1043-1046.
- Pollard, D. D., and P. Segall, 1987. Theoretical Displacements and Stresses Near Fractures in Rock: With Applications to Faults, Joints, Veins, Dikes, and Solution Surfaces. In: *Fracture Mechanics of Rock*. B. Atkinson (ed.), *Academic Press*, London, pp. 277-349.
- Price, N. J., 1966. Fault and Joint Development in Brittle and Semibrittle Rocks. *Pergamon Press*, Oxford, 176 p.
- Price, N. J. and J. W. Cosgrove, 1990. Analysis of Geological Structures. *Cambridge University Press*, New York, 502 p.
- Priest, S. D., and J. A. Hudson, 1976. Discontinuity Spacing in Rock. *International Journal of Rock Mechanics, Mining Science, and Geomechanics Abstracts*, 13, pp.135-148.
- Priest, S. D., and J. A. Hudson, 1981. Estimation of Discontinuity Spacing and Trace Length Using Scanline Surveys. *International Journal of Rock Mechanics Mining. Science, and Geomechanics Abstracts*, 18, pp. 183-197.
- Railsback L. B., and L. M. Andrews, 1995. Tectonic Stylolites in the "Undeformed" Cumberland Plateau of Southern Tennessee. *Journal of Structural Geology*, 17(6), pp. 911-915.
- Raleigh, C. B., J. H. Healy, and J. D. Bredehoeft, 1972. Faulting and Crustal Stress at Rangely, Colorado. In: *Flow and Fracture of Rocks, Geophysical Monograph*, 16, pp. 275-284.

- Ramsay, J. G., 1980. The Crack-Seal Mechanism of Rock Deformation. *Nature*, 284, pp. 135-139.
- Ramsay, J., and M. Huber, 1987. Modern Structural Geology. Volume 1: Strain Analysis. Volume 2: Folds and Fractures. *Academic Press*, New York, 307 p.
- Rauch, H. W., 1984. Use of Lineaments as Exploration Tools for Natural Gas and Ground Water in Martin County, Kentucky. In: Remote Sensing for Exploration Geology. Morris-Jones D. R. and J. J. Cook (chairpersons). *Proceedings of the International Symposium on Remote Sensing of Environment*, Third Thematic Conference; Colorado Springs, Volume 1, pp. 249-250.
- Reed, R. M., and S. E. Laubach, 1996. The Role of Microfractures in the Development of Quartz Overgrowth Cements in Sandstones: New Evidence From Cathodoluminescence Studies. *Geological Society of America*. Abstracts with Programs, Annual Meeting, p. A-280.
- Reid, R. P., and I. G. Macintyre, 2000. Microboring versus Recrystallization: Further Insight into the Micritization Process. *Journal of Sedimentary Research*, 70(1), pp. 24-28.
- Renshaw, C. E., and J. C. Park, 1997. Effect of Mechanical Interactions on the Scaling of Fracture Length and Aperture, *Nature*, 386, pp. 482-484.
- Rives, T., M. Razack, J.-P. Petit, and K. D. Rawnsley, 1992. Joint Spacing: Analog and Numerical Simulations. *Journal of Structural Geology*, 14, pp. 925-937.
- Rives, T., K. D. Rawnsley, and J.-P. Petit, 1994. Analogue Simulation of Natural Orthogonal Joint Set Formation in Brittle Varnish. *Journal of Structural Geology*, 16 (3), pp. 419-429.
- Rouleau, A. and J. E. Gale, 1985. Statistical Characterization of the Fracture System in the Stripa Granite, Sweden. *International Journal of Rock Mechanics, Mining Sciences and Geomechanics Abstracts*, 22, pp. 353-67
- Sanderson, D. J., S. Roberts, and P. Gumiel, 1994. A Fractal Relationship Between Vein Thickness and Gold Grade in Drill Core from La Codosera, Spain. *Economic Geology*, 89, pp. 168-173.

- Sheldon, R. P., 1963. Physical Stratigraphy and Mineral Resources of Permian Rocks in Western Wyoming. *U.S. Geological Survey, Professional Paper* 313-B, 273 p.
- Scholle, P. A., 1978. A Color Illustrated Guide to Carbonate Rock Constituents, Textures, Cements, and Porosities. *American Association of Petroleum Geologists, Memoir* 27, Tulsa, 241 p.
- Scholz, C. H., 1995. Fractal Transitions on Geological Surfaces. In: Barton C. C., and P. R. La Pointe (eds.). *Fractals in the Earth Sciences. Plenum Press*, New York, pp. 131-140.
- Segall, P., and D. D. Pollard, 1983. Joint Formation in Granitic Rock of the Sierra Nevada. *Geological Society of America, Bulletin*, 94, pp. 563-575.
- Sen, Z., and A. Kazi, 1984. Discontinuity Spacings and RQD Estimates from Finite-Length Scanlines. *International Journal of Rock Mechanics and Mining Sciences and Geomechanics Abstracts*, 21, pp. 203-212.
- Silliphant, L. J., T. Engelder, and M. R. Gross, 2002. The State of Stress in the Limb of the Split Mountain Anticline, Utah: Constraints Placed by Transected Joints. *Journal of Structural Geology*, 24 (1), pp. 155-172
- Sinclair, S. W., 1980. Analysis of Macroscopic Fractures on Teton Anticline, Northwestern Montana. Masters Thesis, *Texas A&M University*, College Station, 102 p.
- Smith, L. A., 1985. Micritization by Boring, Infilling and Primary Micritic Carbonate in Modern and Ancient Carbonate Allochems. Masters Thesis, *University of Illinois, Urbana*, 50 p.
- Snow, D. T., 1969. Anisotropic Permeability of Fractured Media. *Water Resources Research*, 5, pp. 1273-1289.
- Snow, D. T., 1970. The Frequency and Apertures of Fractures in Rock: *International Journal of Rock Mechanics and Mining Science*, 7, pp. 23-40.
- Sowers, G. M., 1972. Theory of Spacing of Extension Fracture. *Engineering Geology. Case Histories*, 9, pp. 27-53.

- Stearns, D. W., and M. Friedman, 1972. Reservoirs in Fractured Rock. In: Stratigraphic Oil and Gas Fields. *American Association of Petroleum Geologists*, Memoir 16, pp. 82-106.
- Stone, D. S., 1986. Rangely Field Summary. 2. Seismic Profile, Structural Cross Section, and Geochemical Comparisons. In: New Interpretations of Northwest Colorado Geology. D. Stone (ed.). *Rocky Mountain Association of Geologists*, Denver, pp. 226-228.
- Stowell, J. F. W., A. P. Watson, and N. F. C. Hudson, 1999. Geometry and Population Systematics of a Quartz Vein Set, Holy Island, Anglesey, North Wales. In: Fractures, Fluid Flow, and Mineralization. McCaffrey, K. J. W., L. Lonergan, and J. J. Wilkinson (eds.). *Geological Society, London*, Special Publication, 155, pp. 17-33.
- Suppe, J., 1985. Principles of Structural Geology. *Prentice-Hall*, New Jersey, 537 p.
- Swan, A. R. H. and M. Sandilands, 1995. Introduction to Geological Data Analysis. *Blackwell Science*, Oxford, 446 p.
- Terry, R. D., and G. V. Chilingar, 1955. Summary of "Concerning some additional aids in studying sedimentary formations," by M. S. Shvetsov. *Journal of Sedimentary Petrology*, 25, pp. 229-234.
- Terzaghi, R., 1965. Sources of Error in Joint Surveys. *Geotechnique*, 15, pp. 287-303.
- Vermilye, J. M., and C. H. Scholz, 1995. Relation Between Vein Length and Aperture. *Journal of Structural Geology*, 17(3), pp. 423-434.
- Waechter, N. B., and W. E. Johnson, 1986. Rangely Field: Pennsylvanian-Permian Paleostucture and Stratigraphy as Interpreted from Seismic Data in the Piceance Basin, Northwest Colorado. In: New interpretations of Northwest Colorado Geology, Stone, D. S., and K. S. Johnson, (eds), *Rocky Mountains Association of Geologists*, pp. 51-64.
- Walker, R. G., 1979. Facies Models. *Geological Association of Canada*. Reprint Series 1, 211 p.
- Walmann, T., A. M. Sørensen, J. Feder, T. Jøssang, and P. Meakin, 1996. Scaling Relations for the Lengths and Widths of Fractures. *Physics Review Letters*, 77, pp. 5393-5396.

- Warburton, P. M., 1980. A Stereological Interpretation of Joint Traces Data, *International Journal of Rock Mechanics, Mining Science, and Geomechanics Abstracts*, 17, pp.181-190.
- Westaway, R., 1994. Quantitative Analysis of Population of Small Faults. *Journal of Structural Geology*, 16, pp.1259-1273.
- Wilkins, S. J., M. R. Gross, M. Wacker, Y. Eyal, and T. Engelder, 2001. Faulted Joints: Kinematics, Displacement-Length Scaling Relations and Criteria for their Identification. In: Paul Hancock Memorial Issue. Dunne, W. M., I. S. Stewart, and J. P. Turner (eds.). *Journal of Structural Geology*, 23 (2-3), pp. 315-327.
- Wilkins, S. J., and M. R. Gross, (in press). Normal Fault Growth in Layered Rocks at Split Mountain, Utah: Influence of Mechanical Stratigraphy on Dip Linkage, Fault Restriction and Fault Scaling. *Journal of Structural Geology*.
- Wilson, J.L., W. Ward, and J. Finneran, 1984. A Field Guide to Upper Jurassic and Lower Cretaceous Carbonate Platform and Basin Systems, Monterrey-Salttillo Area, Northeast Mexico: *Society of Economic Paleontologists and Mineralogists*, Gulf Coast Section, 76 p.
- Wojtal, S., 1986. Deformation within Foreland Thrust Sheets by Populations of Minor Faults. *Journal of Structural Geology*, 8, pp. 341-360.
- Wojtal, S. F., 1996. Changes in Fault Displacement Populations Correlated to Linkage Between Faults. In: Scaling Laws for Fault and Fracture Populations; Analyses and Applications. Cowie, P. A., R. J. Knipe, I. G. Main, and S. F. Wojtal, (eds.). *Journal of Structural Geology*, 18 (2-3), pp. 265-280.
- Wong, T. F., J.T. Fredrich, and G. D. Gwanmesia, 1989. Crack Aperture Statistics and Pore Space Fractal Geometry of Westerly Granite and Rutland Quartzite: Implications for an Elastic Contact Model of Rock Compressibility. *Journal of Geophysical Research*, 94, pp. 10267-10278.
- Wu, H., and D. D. Pollard, 1992. Propagation of a Set of Opening-Mode Fractures in Layered Brittle Materials under Uniaxial Strain Cycling. *Journal of Geophysical Research*, 97, pp. 3381-3396.

- Wu, H., and D. D. Pollard, 1995. An Experimental Study of the Relationship Between Joint Spacing and Layer Thickness. *Journal of Structural Geology* 17, pp. 887-905.
- Young, D. H., 1962. Statistical Treatment of Experimental Data. *McGraw-Hill Book Company, Inc.*, New York, 172 p.
- Zhao, P. and S. Ji, 1997. Refinement of Shear-Lag Model and its Applications. *Tectonophysics*, 279, pp. 37-53.

Vita

Orlando José Ortega Pérez was born in Caracas, Venezuela, on March 26, 1966, to José del Pino Ortega Rodríguez and Josefa Candelaria Pérez de Ortega. Orlando graduated from high school in 1983, and entered the Universidad Central de Venezuela (UCV) in 1984. He obtained a degree in Geological Engineering in 1990 receiving the José Félix Rivas National Award for Academic Excellence, the highest honor awarded in Venezuela to a recently graduated student. After his graduation, Orlando continued taking graduate courses at the UCV, where he also taught an undergraduate-level course in Geology Field Methods. In 1990 he joined the Department of Exploration in Petróleos de Venezuela (PDVSA), where he worked as an Exploration Geologist for five years. In the spring of 1995 he was admitted to The University of Texas at Austin and obtained a Masters of Science in Geological Sciences in Fall 1997. Orlando continued working at UT towards a Ph.D. degree in Structural Geology with emphasis on natural fracture characterization. Orlando José Ortega Pérez is author or co-author of 16 publications in professional journals and professional conference proceedings.

Permanent address: 1407 Cloverleaf Dr., Austin, Texas 78723.

This dissertation was typed by the author.